Towards the trapping of single potassium atoms in optical tweezers

PROSENJIT MAJUMDER

MAJUMDER, PROSENJIT (2022) Towards the trapping of single potassium atoms in optical tweezers. Doctoral thesis, Durham University.

Towards the trapping of single potassium atoms in optical tweezers

Prosenjit Majumder

This thesis presents the development of a toolbox for trapping ^{39}K atoms in a magneto optical trap with the future vision of trapping a single atom in an optical tweezer. Such technique promise with potential applications in the fields of quantum computation, quantum information, quantum simulation, and precision measurement. In this work, we studied spectroscopic of two different transition of ^{39}K then we trap ^{39}K in a MOT, which is a small step toward optically trap a single ^{39}K atom in a tweezer.

In second chapter, we present a summary of the theoretical framework relating to laser cooling and trapping. Also include detail description of the energy level structure and challenges for cooling potassium.

In third chapter, we demonstrated a laser frequency stabilization technique. We include theoretical understanding along with the experimental results. We compare the D_1 and D_2 transitions of $4S \to 4P$ line of ^{39}K by various experimental parameters.

In fourth chapter, we present a history pre-cooling of alkali atoms is necessary. We also explain our experimental apparatus require for the required for laser cooling. Then we discuss the laser system used for the experiments along with the alignment technique for laser beam and AOMs alignment to control the frequencies. We also characterized and setup the tapered amplifier to increase the laser beam power.

And in chapter five, we present the optimization and characterization the different experimental parameters of the pyramid MOT to produce as much as bright MOT as possible.

In chapter sixth, we present details of the theoretical framework required to understand the absolute absorption of $4S \to 5P$ transition of ^{39}K along with the experimental results. For future extension, to study the precision measurements to identify the Rydberg states of cold ^{39}K atoms. And in order to cool down ^{39}K atoms beyond Doppler cooling limit, one can use degenerate Raman sideband cooling via the $4S_{1/2} \to 5P_{1/2}$transition.

Finally, in last chapter, we discuss the immediate future experiment in order to achieve a single atom in an optical tweezer. Therefore, after slowing down

the atoms in pyramid chamber as we did for ^{39}K, one can trap ^{39}K atoms in a 3D-MOT in the science chamber, then using optical tweezers with a specific wavelength, one can trap ^{39}K single atom in optical tweezers.

Towards the trapping of single potassium atoms in optical tweezers

Prosenjit Majumder

A thesis submitted in partial fulfilment
of the requirements for the degree of
Doctor of Philosophy

Department of Physics
Durham University

October 2021

Contents

List of Figures

List of Tables

Declaration

I confirm that no part of the material offered has previously been submitted by myself for a degree in this or any other University. Where material has been generated through joint work, the work of others has been indicated.

Prosenjit Majumder

Durham, October 2021

This work could not have been carried out without the guidance and support of a vast number of people.

My first thanks must go to my supervisor Prof. Simon Cornish who provided me with the opportunity to work in his group and to study cold atom physics which had first intrigued me as an undergraduate. I greatly appreciate the work he has done in reading through the various drafts of this thesis and for the suggestions and comments which have crystallized my understanding. And I like to thanks my second supervisor Prof. Ifan Hughes for any kind of official work and emotional support at any point of time and any topic.

I would like to thank the many members of our team member, especially Dr. Philip David Gregory and Dr. Ana Rakonjac, their prowess and understanding of experimental physics was critical in getting the experiment to where it is today. In addition, Dr. Avinash Kumar and Dr. Steve Hopkins gave me the best introduction to the experiment possible, and I am indebted for all of their hard work and patience.

The rest of 'Cornish Division' have been equally helpful. Alex Guttridge, Zenghkun Fu has been a huge help in all things technical, while Oliver Wales, Rahul Sawant and Sarah Bromley was always willing to solve problems regardless of how many times per day. The current group of Mew Ratkata, Jacob Blackmore, Jack Segal, Andrew Innes, Stefan Spence, Vincent Brooks, Lewis McArd, Kali Wilson, Alexandros Alampounti have all been of great help, not least in the creation of some really delicious baked goods.

The whole of QLM has been fantastic, always providing a friendly and supportive place to work for international student like me. Furthermore, I am extremely grateful to Steve Lishman and the rest of the mechanical workshop for their understanding and excellent work throughout this project.

I am eternally grateful to my friends both old and new. First of all I must thank Shams Galib, Amit Gajbhiye and Tamal Sarkar, they are always been my close friend for the longest time. You have always been there for me and, whether it's just for a quick meet at the pub or in house, even a holiday in India, you never fail to make me feel better about life, huge thanks those music, and kegs of beer. I am also thankful for the University College for the membership and any kind of social help.

Finally, I have thank my Mum, my Dad, Wife, my brother and sister for their reassurance and encouragement throughout my 4 years in Durham. Without them I am not sure where I would be.

Chapter 1

Introduction

Since the laser was developed 60 years ago, [1, 2], the area of atomic physics has changed dramatically. The new sources of extremely monochromatic light have advanced much more accurate spectroscopy of atoms and molecules. Therefore, the capability of cooling and trapping atoms in the micro-Kelvin temperature utilising lasers were developed. This work headed to the honour of Nobel Prize in Physics to S. Chu, C. Cohen-Tannoudji and W. D. Phillips 1997 [3–5].

Building upon these key developments, we have observed considerable advancements in the domain of quantum simulation, where an artificial system can be developed and studied to investigate tricky many-body real-world puzzles. Over recent years, two neutral particle systems have emerged as encouraging and interesting platforms for quantum simulation: atoms excited to Rydberg states and ultracold polar molecules. Here in this introductory chapter, we review the necessary techniques to manipulate neutral atoms and molecules for the quantum simulations. These include quantum gas microscopes and arrays of optical tweezers. We also discuss the recent accomplishments in the field of quantum many-body science using these platforms.

The approach of quantum simulation, i.e. the application of an artificial quantum system to investigate another system, was first conceptualized by Feynman and is now possible with the state of the art experiment [6]. More generally, like chemists design new compounds with useful properties, physicists may build artificial quantum materials that exhibit interesting properties such as magnetism and superconductivity. The properties of such materials may then be explored by varying the parameters of the quantum simulator.

1.1 Optical tweezers

Before trapping a single atom in optical tweezers, it is essential to understand the working principle of optical tweezers. In 1970 the optical scattering and gradient forces observed by Arthur Ashkin [7] and awarded the Nobel Prize in Physics for this development in 2018. Each photon of the laser beam carries momentum $\rho = h/\lambda$ (where h is Planck's constant and λ is the wavelength), and the momentum can be changed by reflection or refraction. When light moves between different optical medium, due to different refractive indices, the photons changes the angle and velocity, which can be described using Snell's law,

$$n_1 \sin\theta_1 = n_2 \sin\theta_2, \tag{1.1}$$

where n_1 and n_2 are the refractive indices of the two respective media and θ_1 and θ_2 are the incidence and refraction angle respectively.

Therefore if a laser beam hits atoms due to reflection and refraction, there will be a momentum change of the light. Due to conservation of momentum (Newton's second law), there is a change in momentum on the atoms and an optical force acting on the atoms, which can be described using the Fresnel Equations.

When the atom in the center of a laser light (the laser reaches the atom when it is perpendicular to the plane), the atom experiences a little reflection and no refraction, which indicate $\sin\theta_1 = \sin\theta_2 = 0$ even though refractive indices are different. If the atom moved slightly to one side, the laser beam is no longer perpendicular to the atom; hence, refraction occurs along with some reflection. Therefore, the refraction will cause the beam to change its direction, due to Snell's law as the refractive index of the atomic medium is higher than the air, this changes the velocity (hence the momentum $\bar{p} = m\bar{v}$, m is the mass of the atom and v is the velocity of the atoms within laser

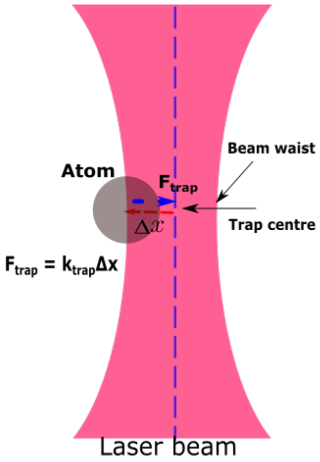

Figure 1.1: Picturization of an optical trapping force with a constant k_{trap}. The trap's restoring force (F_{trap}) acting on a trapped atom, which follows Hookes' law and the force also depend on the distance between the atom and the trap centre (Δx).

beam) of the laser beam. Therefore, the force experienced by the atom is F ($\bar{F} = \frac{d\bar{p}}{dt} = m\frac{d\bar{v}}{dt} = m\bar{a}$). Therefore, if the photon in the laser beam experience a force, there must be a force acting on the atom according to Newton's third law. As a results, a reaction force pushes the atom back to its original equilibrium position so that the momentum is conserved as presented fig.1.1 This force acts like a restoring spring force, which is as follows,

$$F_{trap} = -\kappa_{trap}\Delta\bar{x}, \tag{1.2}$$

where κ is the optical trap stiffness, and Δx is the displacement of the atom with respect to the trap center. It is negative because it is a restoring force acting in the opposite direction to the trapped atom's motion, i.e. away from the trap center.

The single atom can be loaded in optical tweezers, the atom loading in an optical trap depends on the collisional blockade regime (which is going to be present with great details), generated by intense, inelastic, light-assisted collisions among the pair of atoms in the optical trap, which was first created by [8]. Recently, huge progress made in the field of manipulation of single-atom trapping using optical tweezers. A spatial light modulator (SLM) to create a comprehensive, two-dimensional (2D) pattern of optical tweezers and trap many single atoms at once with 50-60% probability directly from a magneto-optical trap (MOT) [9, 10]. Then the trap atoms can be rearranged by a collection of walking optical tweezers controlled by a set of crossed acousto-optical deflectors (AODs) to random points in 2D. Recently, Prof. Mikhail D. Lukin group at Harvard University trapped 256 programmable single atoms by optical tweezers [10, 11]. Here we concentrate on the construction of the optical system needed to trap individual potassium atoms in an optical tweezers. In the longer term, this will feed into two research directions - Rydberg excitation and the creation of KCs molecules.

1.2 General properties of Rydberg atoms

To make atoms not more interacting at a distance larger than a micrometre, they need to be excited to its Rydberg states. And this is the states with the large principal quantum number (n). The Rydberg atoms feature two important properties, (i) the Rydberg atoms lifetime increase if the principal quantum number rises, typically scaling as $\sim n^3$, which is much larger than the actual transitions, i.e. ~ 100 μs limit for $n \approx 50$. And (ii) Rydberg atoms possess large dipole moments in between two consecutive principal quantum states with opposite parity. This leads to a considerable interaction strength V, for example for $n = 50$ at 5 μm separation, the interaction strength is like $V/h \geq 1$ MHz (h is Planck constant) [11].

The nanoscale condensed material with spin 1/2 particles magnetic structure is simulated with neutral Rydberg alkali atoms, which is confined in holographic 2D arrangements of microtraps with arbitrary geometries [12]. However, few atoms can be excited to its Rydberg states of high principal quantum number $n \geq 50$ in an ensemble of atomic cloud, where inter-atomic separation R of few micrometres. Classically in Rydberg atom behave like an electric dipole ($\mathbf{d}$) due to separation between nucleus and electrons. And dipole-dipole interaction ($\mathrm{H}_{dd} \sim d_1.d_2/4\pi\epsilon_0 R^3$) between to Rydberg atoms enhance quite strongly compared to neutral atoms in their ground state, which can be utilized a qubit for quantum computing [13] or can be used in spin Hamiltonian [11, 14, 15].

1.2.1 Quantum simulation

In real materials, it is very hard to understand the correlation between the electronic spin. Therefore the quantum simulation approach is a promising platform help us to engineer and design an artificial condensed matter system, which is effectively isolated from the thermal environment and easy to access local observable remotely. In recent past few cold atom laboratories studies the spin model - like many-body localization phenomena [16], quantum thermalization [17], propagation of correlations in quantum systems [18], topological quantum matter with ultracold gases [19] and two-dimensional neutral atom qubit array [20, 21].

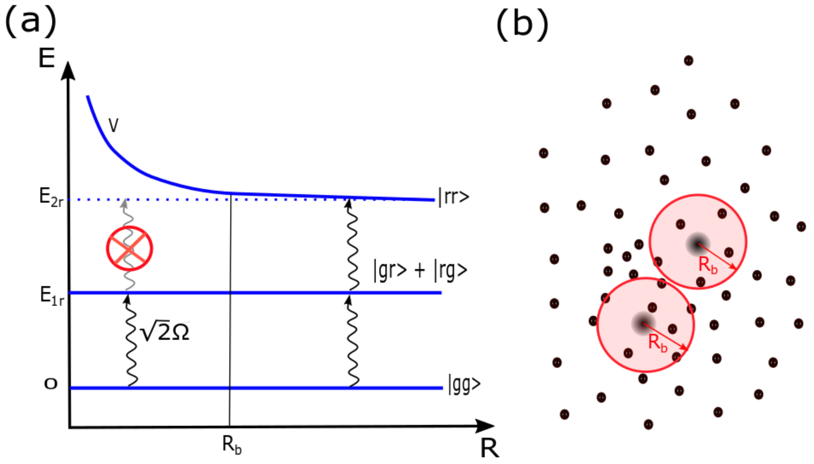

Figure 1.2: Representation of Rydberg blockade effect. (a) Two atoms with decreasing inter-atomic distance R, due to van der Waals interaction (V) between states, the doubly-excited state $|rr\rangle$ is shifted. Two atoms cannot be excited simultaneously; the atoms behave independently from each other, when laser driving strength Ω between $|g\rangle \leftrightarrow |r\rangle$ transition weaker then interaction shift. While the distances smaller than the blockade radius R_b, the excitation of Rydberg states $|rr\rangle$ is no longer resonant and produced a entangle state, $|gg\rangle \leftrightarrow \frac{1}{\sqrt{2}}(|rg\rangle + |gr\rangle)$ and the transition is driven by Rabi coupling $\sqrt{2}\Omega$. (b) Blockade sphere in an ensemble of atoms, for isotropic interactions.

The quantum gates can be realized using two strongly coupled interacting Rydberg atoms through the Rydberg blockade effect, and the idea first proposed by [22, 23]. Two atoms can be transported from their electronic ground-state $|g\rangle$ to a higher Rydberg level $|r\rangle$ with a specific Rabi frequency Ω, due to dipole-dipole interaction the Rydberg states $|rr\rangle$ also shifted

($V = C_6/R^6$), which is known as van der Waals shift. Hence the Rydberg blockade regime can be defined as $\hbar\Omega \ll V$. And the doubly-excited state $|rr\rangle$ is adequately moved apart from the resonance to prevent the simultaneous excitation of the pair of atoms by resonant laser, as presented in figure 1.2. Therefore, the ground-state $|gg\rangle$ is only linked to the entangled state, i.e. $\frac{1}{\sqrt{2}}(|gr\rangle + |rg\rangle)$, the entangled states achieved by the individual Rydberg excitation symmetrically delocalized on the pair of atoms, including an increased coupling $\sqrt{2}\Omega$. Those behaviors are seen with pair of atoms [24, 25], then soon generation of entangled states and quantum gate observed by [26]. The blockade regime can be realized with many atoms experimentally in optical tweezers [27], and in the optical lattice [28].The Rydberg atom problem can be mapped into a quantum Ising spin pattern by investing the coherent laser field run as an external B-field serving on the states $|g\rangle$, $|r\rangle$ and the van der Waals shift as an Ising coupling [29].

The dipole-dipole interaction also allows implementations and realization of XY- Hamiltonian: while the spin-1/2 particle in pair of dipole-coupled Rydberg levels (which are ↑ and ↓) induced by microwave and the dipole-dipole communication is resonant and assumes the formation of an XY ('flip-flop') coupling $J(\sigma_1^x\sigma_2^x + \sigma_1^y\sigma_2^y)$. Although it appears to be only a tiny expansion of the Ising coupling, it leads to entirely various features because Pauli matrices $\sigma^{x,y,z}$ do not commute. If we consider a pair of atoms, which directs to a spin-exchange oscillation among the pair degenerate states $|\uparrow\downarrow\rangle$ and $|\downarrow\uparrow\rangle$, hybridized by the dipole-dipole coupling, which can further be viewed as a spin-excitation bouncing from one Rydberg atom to different atom, as witnessed by [30] with three Rydberg atoms.

One of the long term goals of this work is to develop a tool of quantum simulation with the ^{39}K Rydberg atoms, as done by [31].

1.3 Why Cold Molecules?

An individual atom has a small magnetic dipole moment, and also excited states have a short lifetime, which is a disadvantage of an atomic system. However, polar molecules allow an interesting middle path in between, because the electric dipole moments are higher than the comparable magnetic moments possible in atoms, and also offer chemically steady species, which indicate the promising long lifetimes. As a consequence, many real-life applications as ultracold chemistry [32], many-body physics [33], precision measurement [34], and quantum simulation [35] become possible using ultracold polar molecules platform. Also, arrangement of ultracold molecules present a promising unique platform for quantum computation, and quantum information [36], quantum memory [37].

In this thesis, we also have a scope to develop a tool for trapping ^{39}K atoms in an optical trap with the future vision of creating a single ultracold polar ^{39}K^{133}Cs molecule in an optical tweezer.

1.4 Molecules cooling mechanism

Fortunately, direct atom cooling is an easy technique used, but it is very hard to cool down molecules directly. Laser cooling is particularly relevant to a tiny number of atomic species where a closed atomic transition among pairs of states exists, like alkali atoms. But molecules usually have a highly complicated energy level than atoms, which include rotational and vibrational levels. Hence, it is tricky to get good transitions for cooling and repump. Still, laser cooling of particular molecules has become feasible by choosing transitions with convenient Franck-Condon factors, where simply a tiny number of states are populated subsequent multiple scattering methods, and considerable improvement has been performed in this area in the last several years [38, 39].

Direct cooling of molecules as we discuss, the straightforward cooling of molecules is very difficult. The molecules are often cooled with a sequence of different procedures for producing steam of molecular beam, slowing, and cooling is employed. In the beginning, an origin of molecules can be generated in a thermal beam; by applying various and testified slowing techniques, one can decrease their original velocity and enable restriction of the molecules in a trap. Buffer gas-cooled sources can be placed straight into a static magnetic trap and produce the molecule by sympathetically cooling via collisions with a cold atomic gas [40]. Sisyphus cooling, a procedure well recognised for atoms, has also been employed to trapped and cool molecules[41]. Multiple methods have also been advanced to slowdown a beam of molecules to a velocity where they can be placed into a trap, like shifting electric [42] or magnetic [43] fields, or a changing optical potential [44] can be utilised to eliminate kinetic energy from the molecules. Still, the procedures have the benefit of being commonly applicable; the temperatures attained with these methods are in a range within a few mK to K.

Until now, the numerous spectacular advancement has been seen in the trapping of molecules directly in SrF [45], CaF [46, 47] and YO [48] system. The highly diagonal Franck-Condon factors play an essential purpose in cooling down the molecules directly. In this process, several extra photons scattering on the MOT cooling transition before decaying into a different state. Those decay can be controlled by an array of repump lasers related to the branching ratios particular to the molecule. After the molecules are restrained in an MOT, then molecules can be cooled into the ultra-cold temperature applying blue detuned molasses [49]. Even trapping CaF molecules in tweezers [39].

Indirect cooling of molecules is a remarkably thriving strategy to create ultracold molecules in high phase-space density for different species. In the indirect technique, the ultracold molecules can be created by cooling individual atoms separately and then associating them to form molecules. Due to high phase-space density atomic mixture sample, the produced molecules also in the high phase-space density, as there is no heating due to the association method. In recent past, by applying magneto-association across a Feshbach resonance [32] ultracold molecules were created in high-lying vibrational levels close to threshold energy. Because of the coherent nature of magneto-association, molecules in an optical lattice can be regulated association and dissociation with significantly higher efficiency [50]. Subsequently, the weakly-bound molecules later are shifted to the rovibrational ground state of a molecular potential employing STIRAP, with efficiencies surpassing 90% [51–55] in single-pass. Therefore, the sequence of magneto-association and the STIRAP is a remarkably successful and effective technique for producing ground-state molecules.

Alternatively using the photo-association [56] technique one can create ultracold molecules in high-lying vibrational levels close to the threshold energy. During this optical association method, associated atoms absorbed a resonant photon and then excited to a bound molecular state. One can produce ground state molecules by careful choice of photo-association transition. This method has already been applied to create molecules in their rovibrational ground state like Cs_2 and LiCs system as presented in the following work [57, 58].

1.5 Why KCs Molecules?

The critical feature of diatomic molecules that we intend to utilize is holding a noble permanent electric dipole moment. This characteristic is only obtainable in ultracold heteronuclear molecules produced in the rovibrational ground state. Those molecules create an electric dipole moment in their spin-singlet electronic ground state. In the spin-singlet $S = 0$ and so there is no spin to have a direction in the ground state that involves no magnetic dipole moment raised from electronic spin.

In order to produce any molecules, it is necessary to identify either an experimentally accessible broad interspecies Feshbach resonance or effective optical coupling to the molecular states. Therefore, the original prophecy of positions of interspecies Feshbach resonance is significantly essential. However, consistent calculations can be performed utilising the molecular potentials achieved from the spectroscopic spectrum, like for $^{39}K^{133}Cs$ molecules the inter-species Feshbach resonance can be found in [59, 60].

Other achievable polar molecules that signify the importance and investigated in the lab like RbCs [51–54, 61] and KRb [62]. Ultracold KCs molecules are fascinating to investigate due to the three most significant fundamental features: (*i*) KCs molecules can be displayed as bosonic and fermionic molecules because, in the natural abundance of potassium, three steady potassium isotopes exist in the environment: pair of bosonic ^{39}K (93.258 %); ^{41}K (6.730 %); and individual fermionic isotope ^{40}K (0.012%) [63]. (*ii*) both possess a permanent electric dipole moment of 1.92 Debye, which is relatively higher when compared to other stable molecules. And at last, (*iii*) both atoms are steady on reactive collisions, driving to fewer trap lacks. In addition, the chemical reaction 2KCs $\rightarrow$ K_2 + Cs_2 cannot obtain while there is collision among a couple of KCs molecules.

1.6 Thesis Overview

In this thesis, we focus on the ground work for spectroscopy for two different transitions of ^{39}K and construction of the tools and techniques needed for cooling and trapping of ^{39}K isotope, with the future vision of trapping an array of single Rydberg ^{39}K atom for quantum simulations and in extension a single ultracold polar ^{39}K^{133}Cs molecule in an optical tweezer. This thesis is structured in the subsequent chapters:

In chapter 2, we present a summary of the theoretical framework relating to laser cooling and trapping, to understand the outcomes exhibited in this thesis. Also include detail description of the energy level structure and challenges for cooling potassium.

In chapter 3, we demonstrated a laser frequency stabilization technique i.e modulation transfer spectroscopy. We include theoretical understanding along with the experimental results. We compare the D_1 and D_2 transitions of $4S \rightarrow 4P$ line of ^{39}K by discussing pump and probe, temperature, beam intensities and polarization dependency.

In chapter 4, we present a history pre-cooling of alkali atoms is necessary. We also explain our experimental apparatus require for the required for laser cooling. Here we select the optical frequencies in order to trap ^{39}K in a pyramid MOT chamber. Then we discuss the laser system used for the experiments along with the alignment technique for laser beam and AOMs alignment to control the frequencies. We also characterized and setup the tapered amplifier to increase the laser beam power. And at the end, we present the assembly and characterization of magnetic coils and describe our detection technique.

In chapter 5, we present the optimization and characterization of the pyramid MOT. For characterization, first, we varied polarization angle of pyramid MOT beam (cooling + repump beam) and produced a MOT within the chamber, then optimized the MOT beam intensities (cooling and repump beam) and pyramid chamber temperature. After that we optimize the shim coils in three different directions as a function of quadrupole field gradient and at the end we optimize cooling and repump detuning and produce as much as bright MOT as possible.

In chapter 6, we present details of the theoretical framework required to understand the absolute absorption of $4S \rightarrow 5P$ transition of ^{39}K along with the experimental results. For future extension, to study the precision measurements to identify the Rydberg states of cold ^{39}K atoms using 405 nm optical transition, as presented in [64] with thermal ^{39}K atoms. And in order to cool down ^{39}K atoms beyond Doppler cooling limit, one can use degenerate Raman sideband cooling via the $4S_{1/2} \rightarrow 5P_{1/2}$transition [65].

In chapter 7, we discuss the immediate future experiment in order to achieve a single atom in an optical tweezer. Therefore, after slowing down the atoms in pyramid chamber as we did for ^{39}K, one can trap ^{39}K atoms in a 3D-MOT in the science chamber, then using optical tweezers with a specific wavelength, one can trap ^{39}K single atom in optical tweezers.

In this thesis, we covered a comprehensive spectrum of topics in atomic and molecular physics. But a detailed discussion of the specific individual subject proposed is exceeding the range of a particular PhD thesis. Consequently, a review of the critical background theory is given through the respective chapter's relevant details. In chapter 3, the theoretical Dr Heung-Ryoul Noh and the final polarization data obtained in the lab by Andrew Innes. And at last, the study done by the curious scholar is guided through suitable references for related articles and comprehensive review papers.

Chapter 2

Laser cooling and trapping principles

The methods utilized in laser cooling, trapping, Bose−Einstein condensation Rydberg physics or in ultracold molecule experiments are thoroughly documented and broadly obtainable in the literature. More precisely, Rydberg excitation and molecules experiments require ultracold ensembles of atoms as a starting point. Here in this chapter, we report the basic theory of laser cooling and pay appropriate consideration to the challenges of cooling potassium atoms. We will exclusively discuss the theoretical aspect, leaving the reader to gather additional details from the respective references.

2.1 Atom-Light Interaction

In 1980's remarkable work done by Hänsch [66], Schawlow [67], Wineland and Itano [68]. The mechanism to cool down the atoms cloud using atom−light interactions can be explained semi-classically if we assume an atom as a two-level quantum arrangement, which interacts by a coherent classical field. The basic concept presented in figure 2.1. After absorbing the atoms' photon energy, the atom jumps from the ground state into a specific higher excited state due to energy conservation. The atomic velocity also changes due to the conservation of the system's momentum by one recoil speed in the laser beam propagation direction. Therefore, atom's recoil momentum due to photon's momentum can be written as, $p = \hbar k$, where $\hbar$ is Planck constant and $k(= 2\pi/\lambda)$ photon's momentum wave number. The corresponding recoil velocity of the atom written as, $v_{rec} = h/\lambda M$, where λ is the laser's wavelength, and the atomic mass is M. Therefore, the momentum energy change produces a push on the atoms in the laser beam's direction.

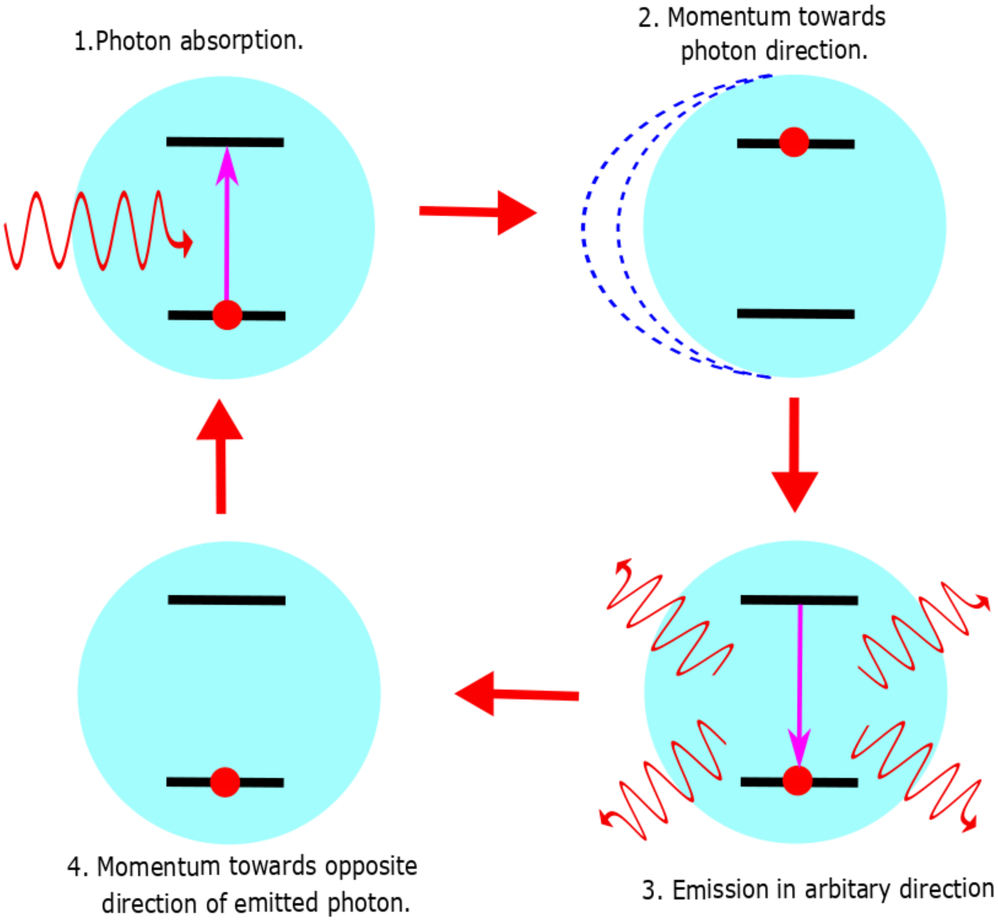

Figure 2.1: The mechanism shows that the decelerate of atoms can possible with radiation pressure. After absorbing a photon, the atom jumps to an excited state from its ground state presented in (1). Due to conserve this system's absolute momentum, each atom recoils in that same incoming photon's direction, as shown in (2). Due to the excited state's short lifetime, spontaneously emitting the photons in all direction while the atom spontaneously decays to its ground state as presented in (3), after the atom returning the ground state, the sequence starts again, as shown in (4). Therefore spontaneously emitted photons momentum kicks average overall direction is zero; this cyclic process momentum transfer eventually slowed down the atom. This figure is adapted from [69].

The excited states' lifetime limited because of that, the excited atom can finally collapse to its original state spontaneously. In this process, a photon with atomic recoil energy is released in a stochastic direction. In this way, over numerous absorptions and emission sequences, no resultant force acts on the atoms from the emission; only the directional force from absorption by the atoms remains. Considering the laser light propagating with wave vector $\vec{k}$ with frequency ω, and detuned $\delta = \omega - \omega_0$, from the resonance, exclusively motionless atoms feel this identical detuning from each laser light. From the moving atoms, the Doppler effect drives the modification of laser frequency as follows,

$$\omega^{'} = \omega - \vec{k}.\vec{v} = \omega_0 + \delta - \vec{k}.\vec{v}. \tag{2.1}$$

With red detuned, i.e., the laser beams with negative detuning, the atoms will preferably absorb photons from the counter−propagate beam with respect to the atom's motion.

The excited state population can be determined by working on the particular two-level system and by solving steady-state optical Bloch equations, which is as follows,

$$\rho_{excited} = \frac{\Omega^2/4}{\delta^2 + \Omega^2/2 + \Gamma^2/4}, \tag{2.2}$$

where Ω and Γ is decay rate and the Rabi frequency. It's been noted that the intensity of the laser field I, which can be related to Rabi frequency of the laser as follows,

$$I = \frac{2\Omega^2 I_{sat}}{\Gamma^2}, \tag{2.3}$$

while I_{sat} define as the saturation intensity, and $R = \Gamma\rho_{excited}$ is the photon scattering rate. After coupling, the scattering rate and the momentum change because of photon absorption. Therefore that scattering force can be formulated as follows,

$$\vec{F} = \frac{\hbar\vec{k}\Gamma}{2} \frac{I/I_{sat}}{1 + I/I_{sat} + 4\delta^2/\Gamma^2}. \tag{2.4}$$

We contemplate a couple of counter−propagating laser lights along a specific beam axis, this is the changing in detuning due to the Doppler shift for a moving atom by $\pm kv$ velocity. Therefore, atoms experience a net force on them, which is as follows,

$$\vec{F}_{\pm} = \vec{F}(\delta - kv) - \vec{F}(\delta + kv).$$

$$\vec{F}_{\pm} = \frac{\hbar\vec{k}\Gamma}{2}\Big[\frac{I/I_{sat}}{1 + 2\frac{I}{I_{sat}} + 4(\frac{\delta - kv}{\Gamma})^2} - \frac{I/I_{sat}}{1 + 2\frac{I}{I_{sat}} + 4(\frac{\delta + kv}{\Gamma})^2}\Big]. \tag{2.5}$$

In this equation, $2I/I_{sat}$ term is the denominator values results from two beams with intensity I. In this regime, the Doppler shift is much less than linewidth. Therefore equation 2.5 can be approximated as follows,

$$\vec{F}_{\pm} \approx \frac{8\hbar k^2\delta}{\Gamma}\frac{I/I_{sat}}{\Big[1 + 2I/I_{sat} + 4(\delta/\Gamma)^2\Big]^2}v = -\alpha v. \tag{2.6}$$

where the Doppler coefficient represents as α, the frictional force $F_{\pm}$ is in the opposite direction to the motion of the atom, while the laser beam is red detuned from resonance. Figure 2.2 presents the resultant force experience by the atoms due to a set of counter−propagating laser light on a flying atom.

The earlier mentions equation implies the atoms that are not moving will continue at rest due to no resultant force working on the atoms, but in reality, atoms moving with speed **v**; thus, the Doppler effect has been seen and need to take into account. Hence atoms with various velocities seeing modified laser beam frequencies lead to non−zero radiation pressure force exercising.

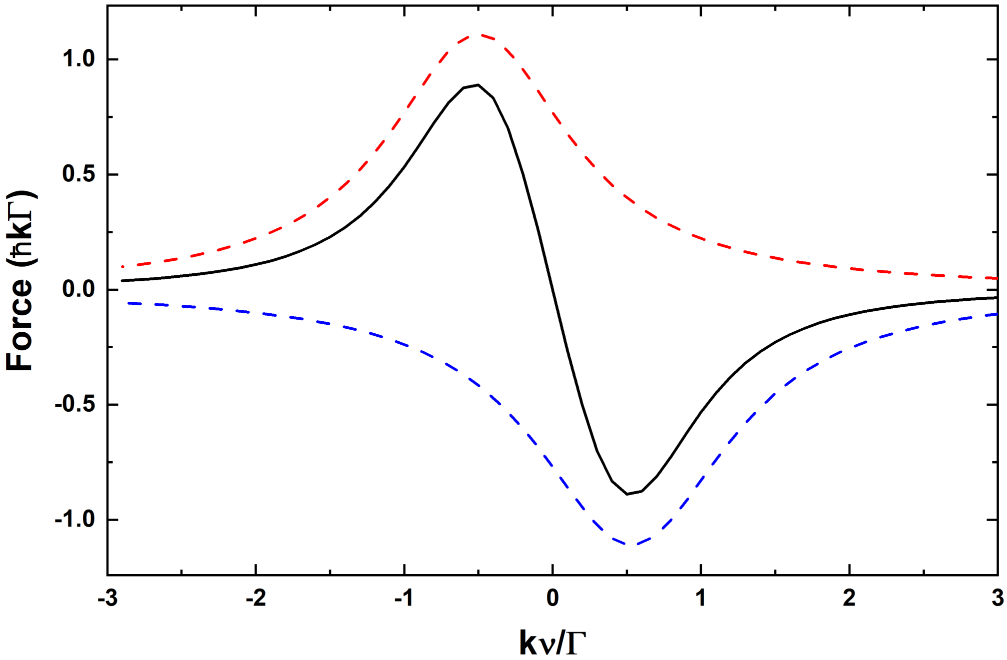

Figure 2.2: The scattering force vs atomic velocity plotted in one dimension (1D). The black curve displays the resultant force excited on the flying atom with the velocity v provided by detuned (i.e. $\delta = -\Gamma/2$) individual pair counter−propagating beams in the plot signified for $I/I_{sat} << 1$. The plot's red and blue trajectories represent forces acting on the atoms due to the specific laser light. While the atom becomes a negative velocity, the optical force acts repulsive and conversely for opposite velocity. And the force is frictional against the atomic motions.

2.1.1 The Doppler cooling

A one dimensional optical molasses presented in equation 2.6 can be generalised in three dimension (3D) by incorporating the situation produced by three pairs of beams, and the damping coefficient in the denominator, to become,

$$\alpha_{3D} = -\frac{8\hbar k^2 \delta}{\Gamma} \frac{I/I_{sat}}{\{1 + 2.3I/I_{sat} + 4(\delta/\Gamma)^2\}^2}. \tag{2.7}$$

The above equation is only can be seen as an approximation. As indicated by [70], there is a certain probability of photon absorption from one beam followed by a spontaneous emission through a different beam.

Due to the arbitrary character of spontaneous emission, the damping force contributes to the cooling rate of $-\alpha v^2$. The heating also occurs where individual momentum punch of $\hbar k$ is a component regarding a stochastic tour in momentum space. Therefore, the mean square momentum increases by $\hbar^2 k^2$ in every level [71, 72]. Consequently the mean square momentum variation with respect to time is presented by,

$$\frac{d\langle p^2 \rangle}{dt} = 2\hbar^2 k^2 R = 2D_p, \tag{2.8}$$

where D_p defined as the momentum diffusion coefficient. There is heating associated with the momentum diffusion at the rate of $\hbar^2 k^2 R/m = D_p/m$, in N dimensions the scattering rate can be define as follows,

$$R = \frac{\Gamma}{2} \frac{2NI/I_{sat}}{(1 + 2NI/I_{sat} + 4\delta^2/\Gamma^2)}. \tag{2.9}$$

In stable thermal equilibrium, the cooling and heating rates are equal. Therefore, it's no harm to apply the equilibrium theorem [71] to determine the thermal energy of the atomic gas as follows,

$$k_B T = \frac{D_p}{3\alpha_{3D}} = \frac{\hbar \Gamma_P^2}{8|\delta|}\left(1 + 4\frac{\delta^2}{\Gamma_P^2}\right), \tag{2.10}$$

where $\Gamma_P = \Gamma\sqrt{1 + 6I/I_{sat}}$ is define as power broadened linewidth in 3D, k_B is Bolztmann's constant, and T is the temperature of the atomic cloud. The minimum temperature for a given laser the intensity can be written as $T_m = \hbar\Gamma_P/2k_B$, where $\delta = -\Gamma_P/2$ is the detuning. One can achieve the lowest temperature using the Doppler cooling mechanism, which is called Doppler temperature [5, 73, 74] as follows, where the $I/I_{sat} \ll 1$

$$T_D = \frac{\hbar\Gamma}{2k_B}. \tag{2.11}$$

For ^{39}K and ^{133}Cs the Doppler limits are 145 [75] and 126 μK [76] respectively.

2.1.2 Sub-Doppler cooling

In order to produce ultracold and quantum gases, the sub−Doppler laser cooling is a crucial technique for neutral atoms [4]. To increase the Doppler limited phase space density of MOT/ cloud, which motivates us to apply other cooling schemes like optical molasses [77], most notably via the mechanism known as Sisyphus cooling [78–80]. The fundamental law is that a pair of individual frequency counter-propagating red detuned laser light with circular polarization causes a spatially changing energy shift in the atoms. Atoms in various Zeeman sublevels encounter multiple shifts in energy levels so that the resultant optical pumping of atoms from higher potential energy sub-levels into lowest energy sub-levels [81]. Therefore, the optically pumped atoms propagate from the area wherever its potential energy is lowest, the possible energy transfer to kinetic energy and the possibility of absorbing a photon gains.

In details, Fig. 2.3 shown the mechanism in a simple system consisting of one ground state $J = 1/2$ and one $J^{'} = 3/2$ excited state. The counter-propagating interfering beams create periodic polarization gradients, which cause a spatially periodic change in the magnetic sub-level of the atoms. The atoms experience the periodic potential in such a way that it's the maximum for one level and the minimum for another level. After that, an optical pumping back and forth between the sub-levels, the atoms at the potential peak absorbed a circularly polarized beam (photon) and spontaneously decayed back to a lower-lying atomic sub-level after releasing high energy photons. Then the atom at the lower sub-level continuously moves towards the next potential maxima, then again transferred back to the original position by releasing a higher energy photon. This mechanism process occurs until the atom reaches the potential minimum.

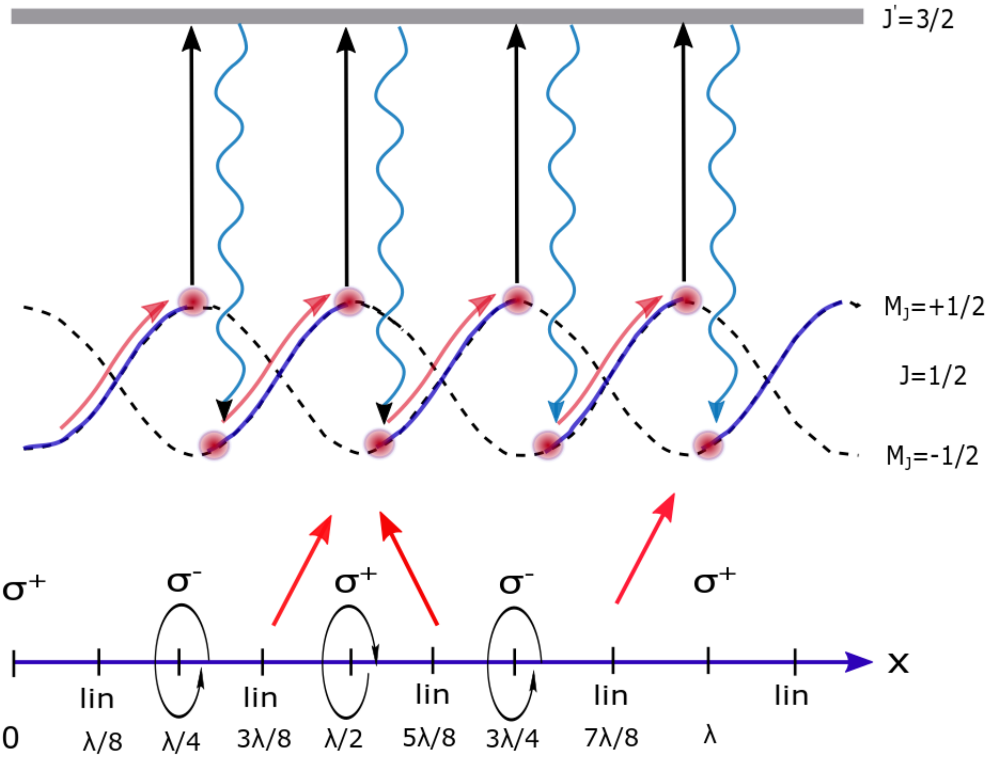

Figure 2.3: Schematic diagram of Sisyphus cooling mechanism. From $x = 0$ the atom in the $M_J = +1/2$ state started moving along its potential curve til it arrive $x = \lambda/4$ (with σ^- polarization) and atom is excited to $|J^{'} = 3/2, M_J = -1/2\rangle$ state by absorbing photon and then simultaneously decays back to the $|J = 1/2, M_J = -1/2\rangle$ state via spontaneous emitted higher energy photon and atom finally in minimum potential within the $M_J = -1/2$ state. Then the atom again claim up the energy hill until it gets pumped reverse into $M_J = 1/2$ at $x = \lambda/2$ (while $\sigma^{\pm}$ polarization) by absorbing photon.

The sub−Doppler cooling mechanism is effective, particularly if natural linewidth Γ is less than the hyperfine splitting Δ of excited states, like in the case of Cs, Na and Rb, for $\Delta \sim \Gamma$, heating effect or photon reabsorption [82] occurs. Unfortunately, the bosonic potassium isotopes fall into this class [83]. Landini *et al*. [75] adapt their sub-Doppler cooling to account for this.

Therefore the sub-Doppler cooling mechanism, Zeeman sublevels need to take into consideration theoretically [78], which leads to a significantly larger force for small atomic velocities, directing into temperatures significantly below than then Doppler limit approaching the recoil limit,

$$T_r = \frac{(\hbar k)^2}{2k_B m}, \tag{2.12}$$

where the angular wave number $k = 2\pi/\lambda$ of the absorbed laser beam. For example ^{39}K and ^{133}Cs the recoil limits are 418 nK [63] and 180 nK [84] respectively. The most profound observation is the sub−Doppler temperatures are dependent on laser detuning δ.

2.2 Optical frequencies

The basic theory of laser cooling is conceptualized for a two-level system, but in real atoms always hold a more complex multi-level electronic level structure, the single valence electron of the alkali metals makes life relatively simpler, which making this family especially useful cooling targets. A closed atomic transition is required to laser cool and trap atoms in an optical trap continuously. Due to complexity of the atomic structure the cooling decay into another state that do not interact with the laser light anymore. Such 'dark'states no longer cool down the atoms and atoms lost for ever. The key features of laser cooling is therefore to find the transition with minimum leakage to dark states or to drive back into the cooling cycle using a repump beam. For example, cooling and trapping ^{39}K atoms in a optical trap, the (D$_2$: $S_{1/2} \rightarrow P_{3/2}$) lines are commonly used by 767 nm wavelength laser system. In this scheme the cooling occur on the $F = 2 \rightarrow F = 3$ transition, for which electric dipole selection rules forbid any transitions except decay back to the $F = 2$ ground state. However, sometime atoms also can off resonantly excite on the $F = 2 \rightarrow F = 2$ transition then decay back to the dark $F = 1$ hyperfine ground state, in that case repumping light need to be employed. Figure 2.4 highlights the relevant hyperfine structure and optical transitions used for our experiment. To successfully cooling down atoms needs the perfect laser frequencies to be regulated to < 1 MHz, which is much less than the cooling and repumping lines natural linewidth.

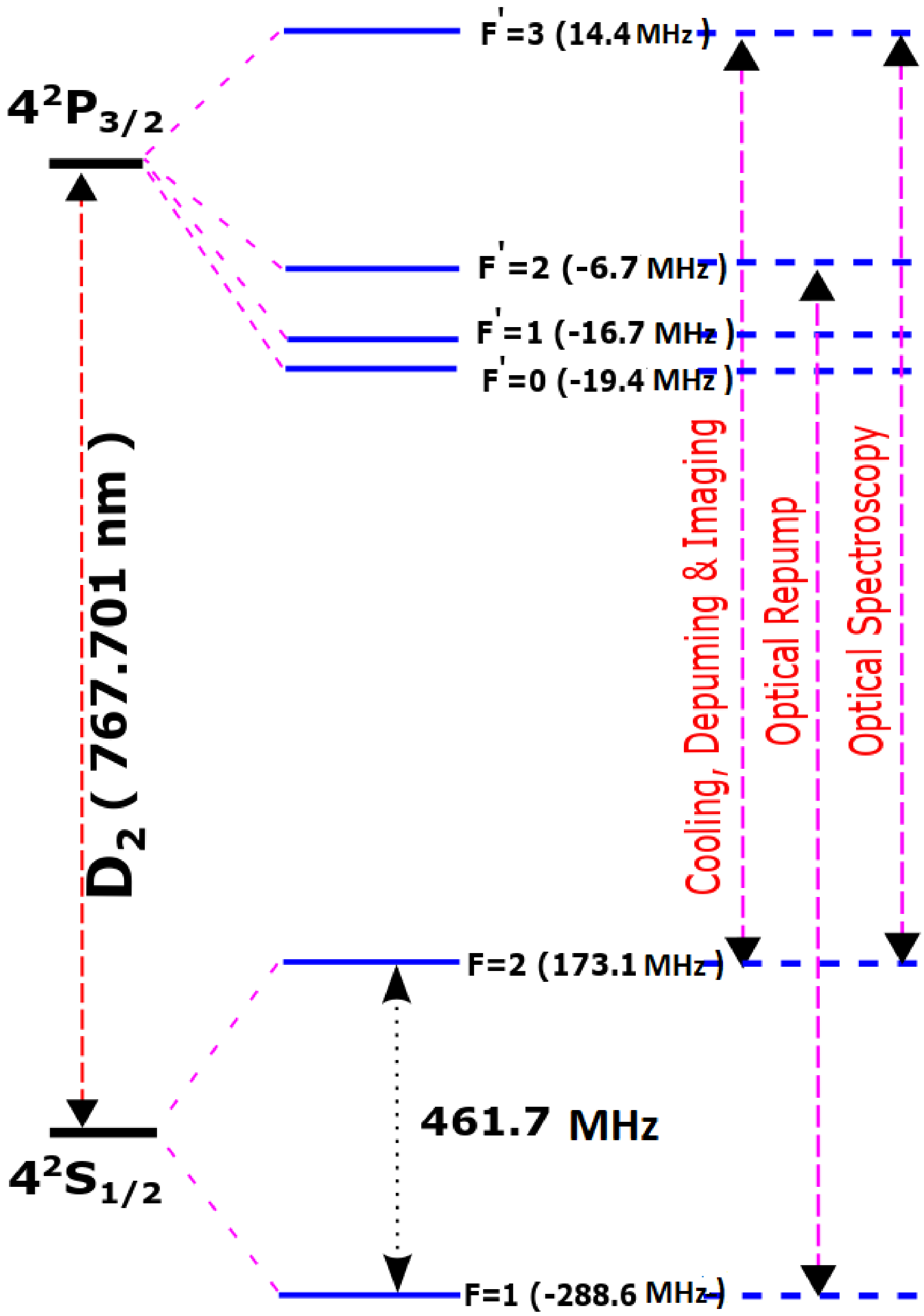

Figure 2.4: Hyperfine structure of D_2 lines in ^{39}K isotope (frequencies are not to scale) in their ground and first electronic excited states. The arrows designate the laser transitions utilised in the experiment for cooling, repump and spectroscopy.

These transitions occur at 389.28 THz for 39K also the laser frequency need be constant to $\sim 10^{-8}$. Therefore, this higher-order stability demands the laser's effective frequency stabilization utilizing a nice error signal to serve as a frequency reference; we used another spectroscopic beam on the $F = 2 \rightarrow F = 3$ transition.

To understand the important of the decay process to the dark states need to examine the number of photon scattering occur before off-resonant loss to the dark state with respect to how many scattering events required for cooling. The frequency difference among the $F = 2 \rightarrow F = 2$ and $F = 2 \rightarrow F = 3$ is $\Delta = 21.1$MHz which is slimier as the detuning $|\delta| \sim 2 - 4\Gamma \approx 12 - 24$ MHz for cooling beam, now using the equation 2.9 give us the relative scattering rate as,

$$\frac{R^{cooling}_{scatter}}{R^{off-res}_{scatter}} = \frac{1 + 4((\Delta + \delta)/\Gamma)^2 + I/I_{sat}}{1 + 4(\delta/\Gamma)^2 + I/I_{sat}} \tag{2.13}$$

The relative scattering rate is plotted in fig. 2.5 as function of intensity for different detuning.

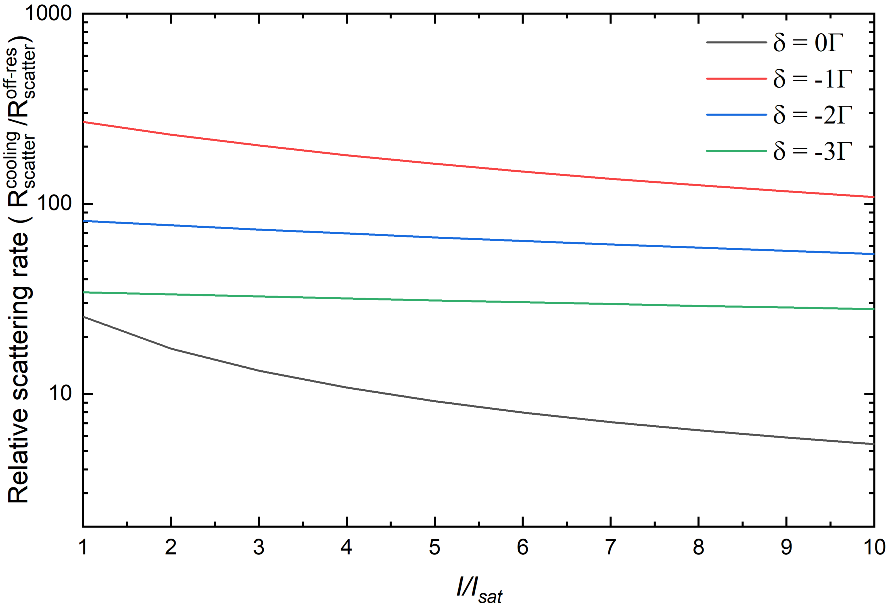

Figure 2.5: The relative scattering rate as a function of normalized intensity (I/I_{sat}) for four different detuning (δ).

A typical K-MOT operates with $\delta = 2 - 3\Gamma$, the scattering rate associated with those detuning is approximately 30 - 90. A typical ^{39}K atoms with capture velocity $v_c \approx 50$m/s has momentum Mv_c absorbs $\hbar k_L$ momentum per photon, therefore it requires approximately $Mv_c/\hbar k_L \approx 4 \times 10^4$ number of photon to be absorbed in order to fully slowed down. Therefore, the majority of the atoms would fall out of the cooling cycle before slow down, which reduced the capture rate and atoms number in the MOT.

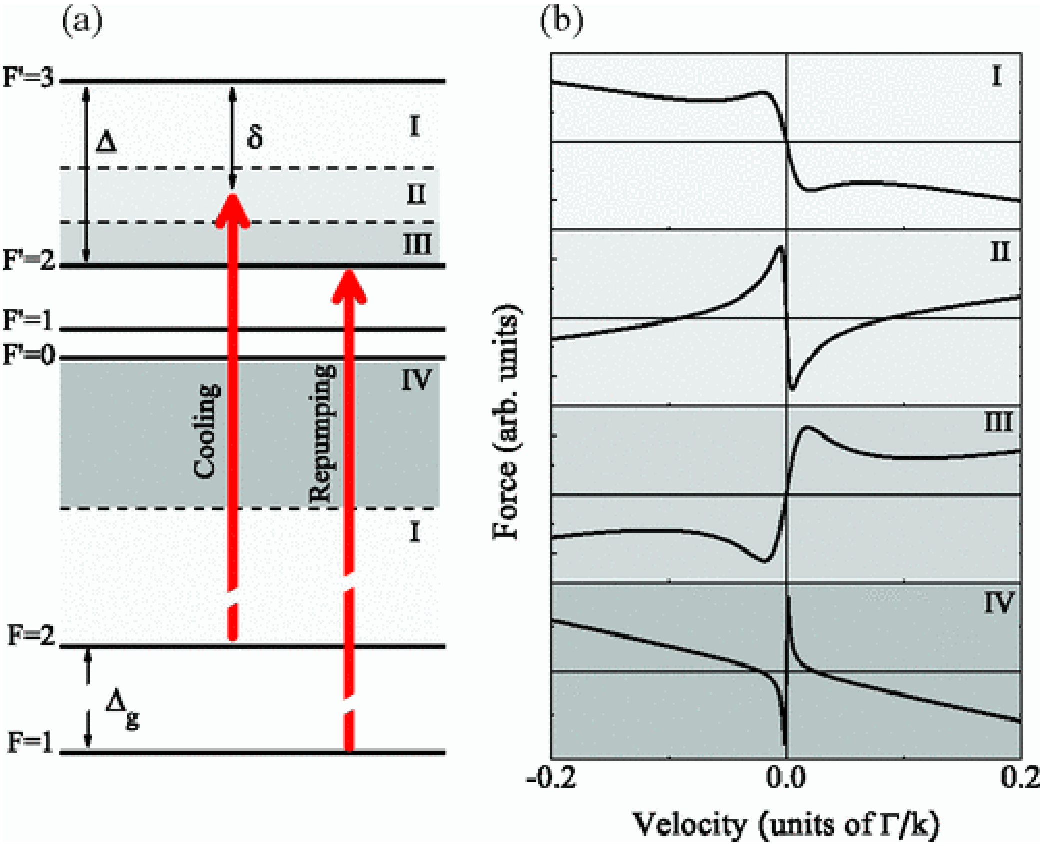

Figure 2.6: The schematic diagram for operating areas for Doppler and sub−Doppler cooling of bosonic potassium atoms. (a) The excited state of the energy level structure, the Δ and δ are defined as total hyperfine splitting and cooling detuning, and Δ_g denotes as ground state splitting. In (b), estimated cooling forces in the different regime of the hyperfine energy level as a function of the atomic velocity. This picture is adapted from [75].

In the labs, experiments are usually performed at a much higher atomic density with sufficiently large detunings $\delta \gg \Gamma$, this condition occurs to maintain the scattering rate of the photons with the particular atoms is minimum in a way that the cooling process does not disturb by the spontaneously emitted photons [82]. To cool down the atomic cloud requires red detuned laser beams from one of the hyperfine transition. The frictional forces are dependent upon the detunings for the Doppler and sub−Doppler cooling. It has been found in [75] that the sub−Doppler cooling is uniquely effective in domains of type I and II. Furthermore, the Doppler cooling is effective in the areas of type I and IV, as shown in figure 2.6.

Therefore, the above discussion indicates that the bosonic potassium sub−Doppler cooling mechanism works extremely near the resonance. Also, the heating from photon re-absorption may be more significant in this region. In the case of $\delta \gg \Delta$, the velocity capture area is shallow.

2.3 The magneto-optical trap (MOT)

In the previously discussed cooling technique, cold atoms accumulate in the interaction region of the beams; without any confinement of the area, atoms are diffused within seconds. While new atoms entering the region will be cooled, therefore the density of cold atoms in the intersection region remain higher but without any confinement, severely limits the density that can be achieved. Thus, both cooling and trapping atoms require a spatial dependence radiation pressure force, which can be accomplished by adding a weak magnetic field to cause Zeeman splitting the multilevel atomic transition. The frictional force is spatially working on the atoms to confined atoms on the trap's centre. Therefore, introducing a quadrupole field outside of the MOT chamber can create a zero field on the chamber's centre. Furthermore, a Zeeman energy shift also introduced with the atom's energy levels by the quadrupole magnetic field. The field easily can be created by using two copper coil in the anti−Helmhotz configuration, which generates a linear magnetic field gradient.

2.3.1 Zeeman Interaction

The weak magnetic field generated by the quadrupole coils used to split the atomic energy via the Zeeman effect, $E_Z = \mu_F B$, where $\mu_F = g_F \mu_B m_F$ and the g_F arise from the projection of J onto F, which for $J = 1/2$ is simply given by, $g_{F_\pm} = \pm\frac{1}{2I+1}g_J$ creates an imbalance in the radiation force from counter propagating laser light that is dependent on position. The counter-propagating laser light must have opposite-handed circular polarizations so that they interact with different atomic transitions in such a way that an increase in magnetic field strength takes one beam closer to resonance and the other one further away. A one dimensional example shown in figure 2.9. Replacing δ in equation 2.6 and now we get $\delta \pm (kv + \beta z) = \omega - \omega_0 \pm (kv + \beta z)$, where $\beta\hbar z = (g^{'}m^{'} - gm)\mu_B B^{'}z$ is the energy shift of a transition resonance, directly leads to [85],

$$F_{MOT} \backsimeq -\alpha v - \frac{\alpha\beta}{k}z, \tag{2.14}$$

valid only for $\beta z \lesssim \Gamma$. This formula can be extended to the three dimensions with careful selection of beam polarizations as in figure 2.10. Therefore, magneto-optical trapping is a very robust technique to capture and trap alkali atoms like potassium, caesium, rubidium, etc.

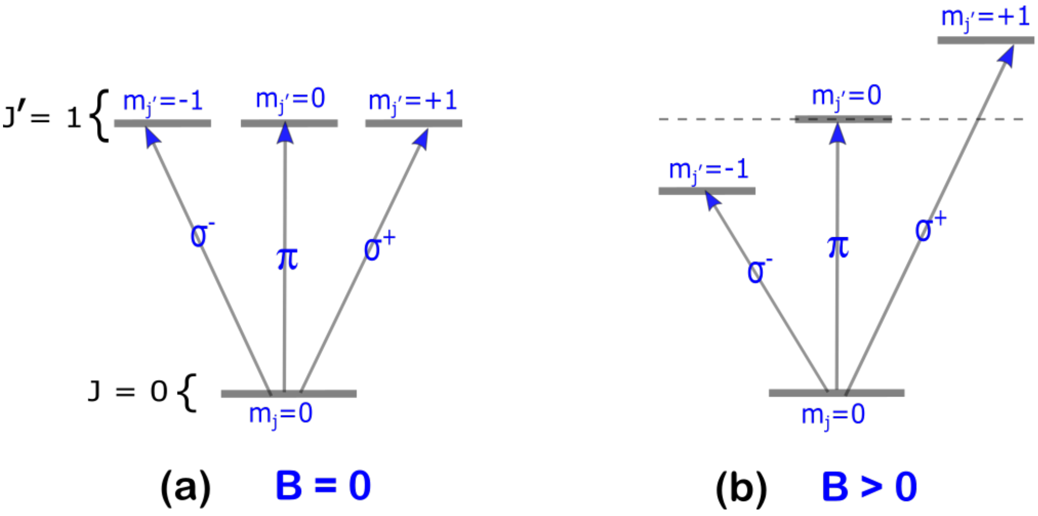

Figure 2.7: The Zeeman effect for a $J = 0 \longrightarrow J = 1$ transition: (a) presenting three magnetic sub-levels of the excited state, which is degenerate in absence of B-field; (b) the degeneracy lifted by applying non-zero magnetic field.

In figure 2.7 present one example of a transition from a $J = 0$ ground state to a $J = 1$ excited state. In the excited state includes three-fold degeneracy of its magnetic sublevels i.e. $m_J = -1, 0, +1$, which can be lifted by applying a magnetic field. Due to conservation of angular momentum i.e. selection rules, the transitions from the ground state to excited state $\Delta m_J = m_J - m_J$ only possible by photons with particular spin projections, for example $\Delta m_J = +1$ only possible with a photon with a spin projection onward the quantization axis (represented by the magnetic field B) of $m_S = +1$ and its called σ^+ transition. Similarly, for $\Delta m_J = -1$ transition requires a photon with $m_S = -1$, which is called σ^- transition. And finally, for the $\Delta m_J = 0$ transition requires a photon with $m_S = 0$ (parallel to the B-field), which is called π transition. Therefore, by employing different photon polarization require for the transitions, combined with the differences in transition frequency due to the Zeeman effect, atoms can be subjected to a position-dependent cooling force that causes trapping.

2.3.2 Zeeman effect on the atomic transitions

Following the appearance of a B-field, the Zeeman energy concerning the two excited states (i.e. D_1 and D_2) can be expressed by the Breit−Rabi equation [86]. The equation is given below (i.e in equation 2.16) and plotted for potassium in Figure 2.8,

$$E(J) = -\frac{hv_{HFS}}{2(2I+1)} - g_I \mu_B m_F \pm \frac{1}{2} hv_{HFS} \times \left(1 + \frac{4m_F}{2I+1} x + x^2\right)^{1/2}, \quad (2.15)$$

where

$$x = \frac{(g_J + g_I)\mu_B B}{hv_{HFS}}. \quad (2.16)$$

The values for potassium of the gyromagnetic factors (g_J and g_I), the hyperfine splitting (v_{HFS}) and the nuclear spin (I) are given in Table 2.1.

Name	Symbol	Value
Ground State Hyperfine Splitting	v_{HFS}	461.701 MHz
Nuclear Spin	I	3/2
Nuclear Gyromagnetic Ratio	g_I	-0.00014193489(12)
Electron Gyromagnetic Ratio	$g_J(4^2S_{1/2})$	2.00229421(24)
	$g_J(4^2P_{1/2})$	2/3
	$g_J(4^2P_{3/2})$	4/3
Planck's Constant	h	6.626069 $\times 10^{-34}$ J.s
Bohr magneton	μ_B	9.27400915$\times 10^{-24}$ J.T^{-1}

Table 2.1: Potassium-39 atomic structure constants required for the calculation of the Breit-Rabi equation. All the numerical value is taken from [88].

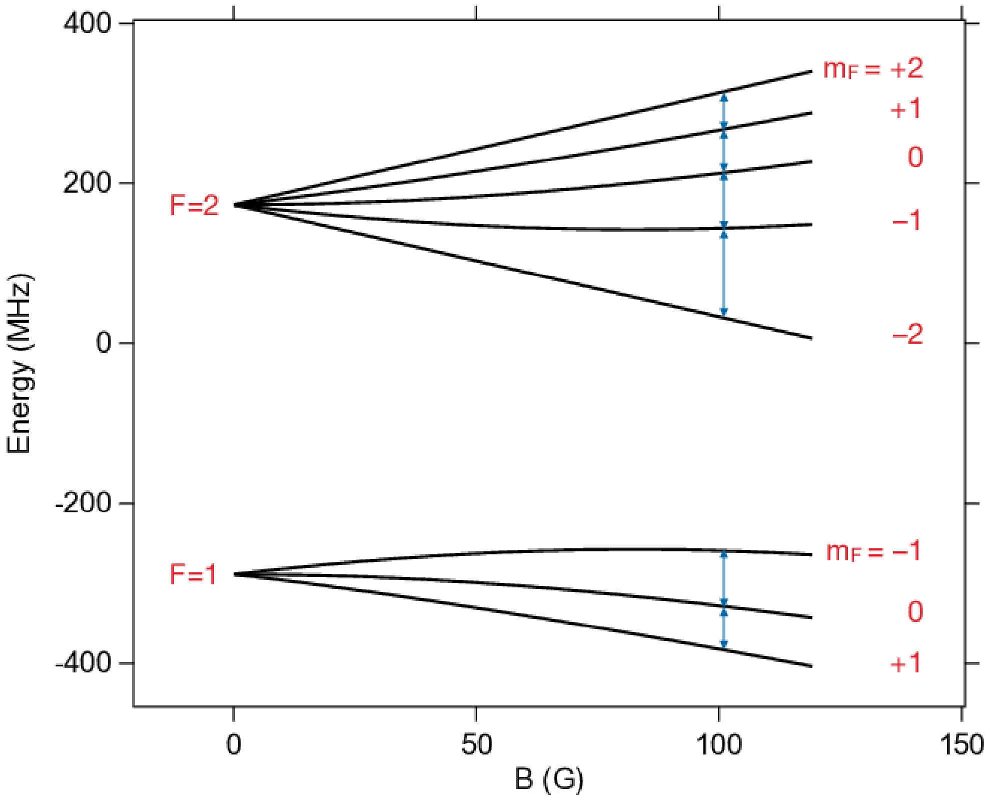

Figure 2.8: Hyperfine structure of the ground state 4^2 $S_{1/2}$ levels of ^{39}K in magnetic field. The blue arrow indicates $\Delta m = 1$. The figure is taken from [87].

2.3.3 One dimensional MOT

The atomic MOT achieved with the combined effect of cooling and trapping, to understand it properly, first consider the one-dimensional case, in which the magnetic field simply varies linearly with the position as shown 2.9. If a red detuned right-hand circular polarized laser beam with frequency ω_L is directed onward the $+Z$ direction, and it will drive σ^- transition within the region of $z < 0$, since the B-field is antiparallel to the propagation path of the beam. The laser beam resonance where the Zeeman splitting causes the transition frequency to be ω_L. In another case, when $z > 0$, the B-field is parallel to the propagation direction of the beam, so it drives σ^+ transition. Still, the B-field gradient increases the detuning, which reduces the rate of photons absorption.

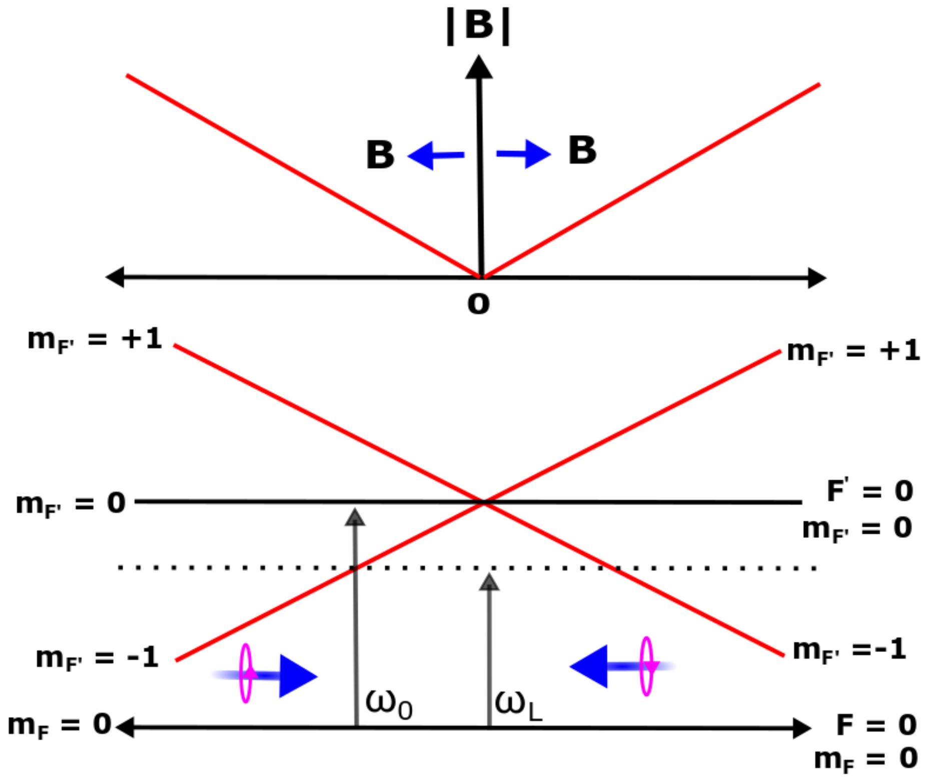

Figure 2.9: Simple Schematic for a magneto-optical trap for a singlet ground state and triplet excited state. In principle, as the atoms move away from the centre the Zeeman shift tunes them towards resonance with the restoring beam and out of resonance with the opposite beam producing a net restoring force. The two opposite polarised light works on the $\Delta m = \pm 1$ transition.

In same-way, for identical right-hand polarization laser beam propagating along the $-z$ direction drives the σ^- transition in the region $z > 0$ and for σ^+ transition for $z < 0$, with a resonance in the $z > 0$ region when the Zeeman shift makes the σ^- transition frequency equal to ω_L. Therefore, at present of both beam, the force on the atom due to the beam propagating towards $+z$ exceeds that of the counter-propagating beam in the region $z < 0$, and vice versa, therefore, the net force on the atom is always directed towards the $z = 0$ position. The result is that atoms are cooled and pushed towards the $B = 0$ position where the forces from the two beams cancel out, and there is no net force and form one dimensional MOT.

We used the convention of defining the polarization from the point of view of the source, right-hand circularly polarized laser beam has spin projection $m_S = +1$ in the direction of propagation, and left-hand circularly polarized laser beam has spin projection $m_S = -1$.

2.3.4 Three dimensional MOT

With the extension of one dimensional MOT, the three dimensional MOT involves three orthogonal pair of a counter-propagating laser beam with an appropriate B-field. The B-field configuration commonly used is the spherical quadrupole, which is provided by a coaxial set of coils in the anti-Helmholtz arrangement, as shown 2.10. The B-field is directed towards the central $B = 0$ point in the transverse (x, y) plane, while the field on-axis is directed away from the $B = 0$ point, which requires laser beams of opposite handedness for the axial and transverse directions to produce the correct configuration for an MOT.

Apart from the beams opposite polarization, the direction of axial and transverse field also differ in their respective B-field gradients. The gradient in the transverse (x and y) directions are equal, but the axial (z) component has to be opposite direction with a double in magnitude,

$$\frac{dB_x}{dx} = \frac{dB_y}{dy} = -\frac{1}{2}\frac{dB_z}{dz} \tag{2.17}$$

The opposite polarity requires the beam polarization along the z-axis to be reversed for the x and y-axis. The greater axial magnitude means that the restoring force is twice as large along the z-axis. The above equation is derived from the Maxwell equations.

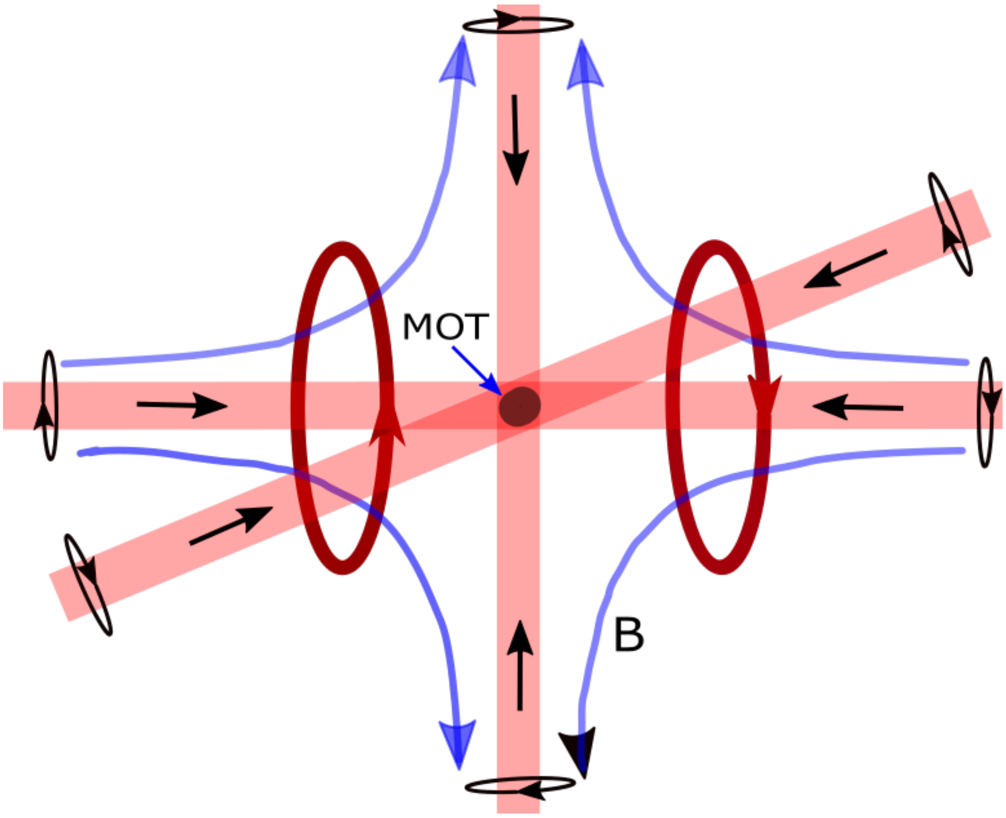

Figure 2.10: Schematic diagram of MOT in three dimensions array. Three mutually orthogonal counter-propagating pairs of laser beams pointed toward the trap centre and unique field's zero generated by specific quadrupole magnetic coils. The beam polarisations must need to be opposite to each other. The laser beams are red-detuned from the cycling transition to cooling and trapping the atoms. A repumping light must also be present in a real system to pump the atoms from the dark state.

Equation 2.14 presents the weak magnetic field that causes a position dependence of the Doppler cooling. The right B-field and laser beam polarization will drive atoms to the zero of the B-field. It is important to note that the field is too weak to cause trapping by itself and just has the effect of introducing the spatially-varying Zeeman splitting. A full description of the MOT is a complex endeavour; however, the critical MOT dynamics can be captured using simple expressions.

Element (Phase)	A	B	C	T_M (K)
K (Solid) K (Liquid)	4.961 8.233	- 4646 - 4693	0 - 1.2403	336.8
Rb (Solid) Rb (Liquid)	4.857 8.316	- 4215 - 4275	0 - 1.3102	312.6
Cs(Solid) Cs (Liquid)	4.711 8.232	- 3999 - 4062	0 - 1.3359	301.6

Table 2.2: Included the values of constants in equations 6.23. In order to make a comparison, we have mentioned three different alkali metals with their natural abundance of potassium, rubidium and caesium, are widely used in cold atom physics. We have also enclosed the melting point of respective alkali metal.

2.4 Vapour pressure and number density

The knowledge of vapour pressure and atomic number density is essential for thermal vapour cells and cold atomic cloud. For example, At room temperature ^{39}K has low vapour pressure and atomic number density; therefore, we need to thermally heat the cell sufficiently high to get a significant absorption signal. The Antoine equation [89] represents a relation between vapour pressures as a function of temperature, which is as follows,

$$\log_{10} \mathrm{P(atm)} = \mathrm{A} + \frac{\mathrm{A}}{\mathrm{T(K)}} + \mathrm{C} \cdot \log_{10} \mathrm{T(K)}, \tag{2.18}$$

here A, B and C define as material and state-dependent constants given in the following summary [90],

Now if we consider the above mentioned gases as Ideal gas we can write,

$$\mathrm{PV} = \mathrm{nRT} \tag{2.19}$$

here n, V, and R define as mole's number, volume and molar gas constant respectively. While, $n = \mathrm{N/N}_A$, and N is defined as the total number of atoms furthermore N_A is unique Avogadro number. So now ideal gas relation becomes,

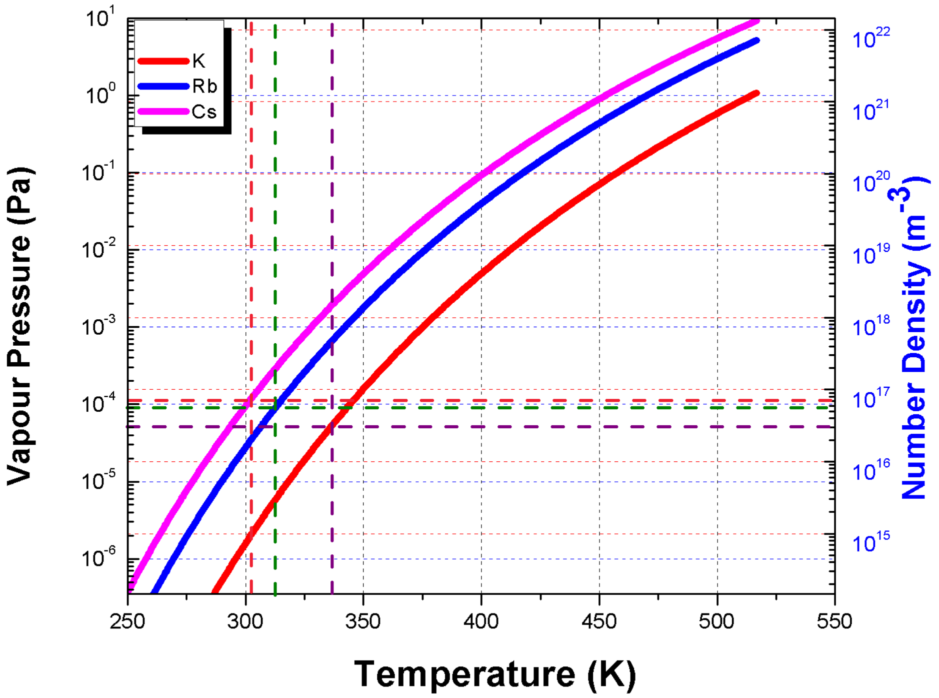

Figure 2.11: Comparison of K (red) vapour pressure and number density with respect to temperature along with Rb (blue) and Cs (pink). The intersection of horizontal and vertical violate, green and pink lines represents the melting point of K, Rb and Cs respectively, as mentioned in table 2.2. Here we convert atmospheric pressure to pascal with 1 atm = 101325 pa.

$$\frac{\mathrm{N/N_A}}{\mathrm{V}} = \frac{\mathrm{P(T)}}{\mathrm{RT}} \Longrightarrow \frac{\mathrm{N}}{\mathrm{V}}(=\mathrm{N_D}) = \frac{\mathrm{P(T)}}{\mathrm{T}} \cdot \frac{\mathrm{N_A}}{\mathrm{R}} = \frac{\mathrm{P(T)}}{\mathrm{k_B T}}, \tag{2.20}$$

where $\mathrm{N_D}$ is number density and $\frac{\mathrm{N_A}}{\mathrm{R}} = \frac{1}{\mathrm{k_B}}$, $\mathrm{k_B}$ is Boltzmann constant.

Now we can numerically plot vapour pressure and number density as a function of temperature, which is as follows in figure 2.11.

Compared to the alkali mentioned above metals, the vapour pressure of potassium is lower at the same temperature, so to achieve a reasonable vapour pressure, we need to heat the cell. For example, we heated up at least 100 °C to get the reasonable absorption spectrum for 4S → 5P transition, while for Rb and Cs, the room temperature is sufficient. The cell was placed inside a rectangular copper box (Because copper is a good thermal conductor of heat) as shown in figure 6.7 heated up with the resistive heater.

2.5 Why Potassium ?

The most abundant of potassium atomic sample consists ^{39}K, ^{40}K and ^{41}K isotope with the natural abundances of 93.2581%, 0.0117% and 6.7302% respectively. Hence ^{39}K, and ^{41}K both are bosonic isotope with nuclear spin $I = 3/2$, whereas ^{40}K is the fermionic isotope with nuclear spin $I = 4$. Therefore, bosonic and fermionic combination make potassium a unique candidate to study Bosonic-Fermionic interactions.

Due to small hyperfine splitting of the ^{39}K hyperfine manifold, if we detune the cooling beam as required for the laser cooling, we actually bring the detuned laser light closer to resonance with the non$-$cycling transitions, which make ^{39}K more difficult to cool down efficiently. Therefore, in the ^{39}K system pumping rate into the $|F = 1\rangle$ state is quite rapid. Therefore, the repumping light must be about as intense as the cooling light, be detuned from the repumping transition and must be counter-propagating as it now provides a considerable amount of the force. Cooling and repumping in this scenario start to lose meaning but will continue to be used for descriptive convenience. As indicated in figure 2.6, the Doppler and sub-Doppler only efficient in specific detuning, which is unique compare to another alkali atom-like Rb and Cs. Farther more, our experiment demonstrated that a ^{39}K MOT might be formed by using only cooling and repump light on the same polarization.

2.6 Optical properties potassium

In atomic physics experiments, potassium is very attractive due to its natural abundance. There are two bosonic isotopes which are ^{39}K and ^{41}K and also a fermionic isotope ^{40}K. As we have discussed before, another reason for using it is the easy accessibility of cheap semiconductor laser systems at the D$_1$ and D$_2$ transitions wavelengths.

The valence electron of potassium has an electronic orbital ($\vec{L}$) and spin

($\vec{S}$) angular momentum. And due to spin-orbit coupling, the total angular momentum becomes $\vec{J}$ of the atom, hence the spin-orbit coupling causes fine structure splitting of the energy states. Therefore, two ground and multiple excited states are represented as $^2S_{1/2}$ and $^2P_{1/2}$, $^2P_{3/2}$ respectively. As we know, because of the interplay between the nuclear spin $\vec{I}$ and the total angular momentum $\vec{J}$, the hyperfine structure becomes relevant.

$$\vec{F} = \vec{J} + \vec{I}, \tag{2.21}$$

here F is defined as a quantum number and the values of F bounds $(J - I) \leq F \leq (J + I)$. As we discussed before, the nuclear spin for ^{39}K and ^{41}K is $I = 3/2$ and for ^{40}K it is $I = 4$. Due to the strength of the hyperfine coupling. The size of the nuclear magnetic moment is more relevant in the Zeeman splitting. Therefore, the hyperfine frequency shifts because of interaction between total electron and nuclear spin is provided as,

$$\Delta v_{hf} = \frac{1}{2}KA + \frac{3}{2}\frac{K(K+1) - 4I(I+1)J(J+1)}{2I(2I-1)2J(2J-1)}B \tag{2.22}$$

here $K \equiv F(F+1) - I(I+1) - J(J+1)$, the hyperfine constants defined as A and B, all constant presented in table 2.3.

Isotope	Nat. abundance (%)	I	State	F	A (MHz)	B (MHz)
^{39}K	93.2581	3/2	$^2S_{1/2}$	1,2	230.868	$--$
			$^2P_{1/2}$	1,2	28.85	$--$
			$^2P_{3/2}$	$0-3$	6.093	2.786
^{40}K	0.0117	4	$^2S_{1/2}$	9/2,7/2	-285.731	$--$
			$^2P_{1/2}$	7/2–9/2	-34.52	$--$
			$^2P_{3/2}$	5/2–11/2	-7.59	-3.5
^{41}K	6.7302	3/2	$^2S_{1/2}$	1,2	126.999	$--$
			$^2P_{1/2}$	1,2	15.245	$--$
			$^2P_{3/2}$	$0-3$	3.363	3.351

Table 2.3: Hyperfine constants for three individual isotopes for ground $4^2S_{1/2}$ and excited states $4^2P_{1/2}$ and $4^2P_{3/2}$ energy levels. The values are obtained from ref.[91, 92]

As we discussed before, the hyperfine splitting is narrow, as shown in figure 3.2. From this energy level, in the diagram, it is clear that the Doppler linewidth ($\Delta\omega_D = 2\pi \times 390$MHz at 300K) and the ground state splitting for ^{39}K are of a similar magnitude. On the other hand, the excited state splitting is very small, comparable to the natural linewidth (5.956 MHz and 6.035 MHz) for D_1 and D_2 lines respectively [63].

2.7 Practical Implementation and Summary

The magneto-optical trapping an excellent method to laser cool alkali atoms to sub-millikelvin temperature, a typical MOT can cool atoms in the order of 10^{10} atoms within a second and confined them to a cloud of few millimetres size, which is an excellent starting point to study the cold atomic physics. However, the initial temperature may not sufficient for many cold atom experiments. Therefore, the temperature of the optical molasses can be achieved an order of magnitude lower by using the sub-Doppler cooling scheme as discuss 2.1.2, which can be used for atom interferometry and Rydberg excitation experiments directly. Furthermore, to achieve quantum degeneracy, the temperature needs to be reduced further using an evaporative cooling scheme. In this method, the temperature approximately reduces another order of magnitude below the sub-Doppler temperature, which is helpful for Bose-Einstein fermionic condensates and ultracold molecular physics.

The atom loading of an MOT and the collisional losses due to background collisions are directly proportional to the vapour pressure. Therefore, the high vapour pressure requires rapid loading at the cost of a short lifetime of the trapped atoms. On the other hand, the low vapour pressure allows long interaction times but with long experimental cycles. The experimentalist solved this problem by using a two-chamber system. All the cooling, trapping and probing of the MOT occurs in a low pressure ‘science’ chamber, in this way, one can keep the atoms isolated from background gases, which increases the lifetime of the atoms; on the other hand, the MOT is initially loaded by a low-velocity atomic flux generated in a neighbouring ‘source’ chamber, for example, pyramid chamber. In the next chapter 4, we design and discuss cold-atom sources by using a pyramid chamber are outlined.

Chapter 3

Modulation transfer spectroscopy of potassium D transitions

Atomic physics experiments, particularly laser cooling [93] experiments, require a frequency stabilized laser light source including residual frequency fluctuations that are considerably lower than the transition linewidth (which is typically a several MHz for the D_1/D_2 transitions in alkali metal atoms). There are several well-established techniques to achieve a zero-crossing spectrum that can be utilized for laser frequency stabilization, which are sub-Doppler spectroscopy techniques named saturated absorption spectroscopy (SAS) [94] and polarization spectroscopy (PS) [95]. Other commonly employed techniques include the dichroic atomic vapour laser locking scheme (DAVLL) [96, 97], frequency modulation spectroscopy (FMS) [98], and modulation transfer spectroscopy (MTS) [99].

Here we present an experimental investigation of modulation transfer (MTS) spectroscopy of D_1 and D_2 line of natural abundance ^{39}K. Our results are compared to theoretical simulations provided by Dr. Heung-Ryoul Noh at Department of Physics, Chonnam National University, South Korea. The MTS spectrum first was studied using hot Cesium atoms [100] in 2001 by Bertinetto *et al.* Then the MTS spectrum for Rubidium atoms (D_2 line) [101] was characterized by Zhang *et al* in 2003. The MTS spectrum normally requires a cycling transition but also can appear without closed cycling transition in the two-level system [102], which is demonstrated by Li *et al* in 2011 and in 2016 Zhan *et al.* extensively studied in the non-cyclic crossover transition in Lithium [103] system. In the case of potassium atom, people mainly use the D_2 transition to lock the laser [104] but nowadays the D_1 transition getting more attention for trapping and cooling of ^{39}K atoms using gray molasses [105], still no one has discussed the accurate theoretical treatment and characterization of the MTS spectrum for the D_1 line in ^{39}K.

Modulation transfer spectrum is Doppler-free due to standing wave created in between the pump and probe beams as both beams coming from the opposite direction and interact with the atoms in a non-linear fashion. The main advantages of MTS are that (a) it has a flat background at zero and (b) is usually dominated by a single closed transition. We observed in the case of the D_2 transition that the MTS spectrum is dominated by a real atomic transition (i.e F = 2 → F = 1,2,3) as compared to the cross-over and other transitions. But in the case of D_1 transition, we find a big MTS signal (in terms of amplitude and slopes) for the ground-state crossover transition (i.e F $= [1 \leftrightarrow 2] \rightarrow$ F$' = 1$). Both optical processes can be understood theoretically; both of the transitions can be model by the Optical Bloch equations and the Four Wave mixing process (FWM), which will present systematically.

In this chapter, we investigate and compares the MTS spectrum for both the D_1 and D_2 transitions in figure 3.4, by investigating the dependency of the MTS spectrum on the pump and probe beam, intensities and also different polarization configurations. We examine different polarization sequences such as linear parallel polarization (lin||lin), perpendicular (lin⊥lin) polarization, equivalent circularly polarizations configuration (define as L^+ - L^+ or $L^- - L^-$) and oppositely circular polarization (define as $L^+ - L^-$ or $L^- - L^+$) for both the D_1 and D_2 transitions.

3.1 Saturated Absorption Spectroscopy

In this segment, we will explain the Lamb dip or saturated absorption spectroscopy. The resonant laser light passes within a thermal cell containing an atomic sample and is detected by a photodiode. When the resonant laser beam propagates through a gas of atoms, the intensity I of the laser light modifies; this change in intensity can be calculated via the number of photons scattered by the atoms per unit volume, which the following equation can express,

$$\frac{dI}{dz} = -\hbar\omega\gamma_p n, \tag{3.1}$$

where z is defined as the path of propagating of laser light within the thermal vapour cell, ω is defined as laser frequency and n is the atomic density inside the cell. The scattering rate at low beam intensity (in the weak probe regime) can be defined as,

$$\gamma_p = (\frac{s_0}{1+s_0})\Big(\frac{\gamma/2}{1+(2(\omega-\omega_0)/\gamma')^2}\Big), \tag{3.2}$$

here ω_0 is defined as transition frequency from ground state to excited state, the saturation parameter on the resonance defined by $s_0 = (I/I_s)$, $I_s = \pi\gamma hc/3\lambda^3$ is the saturation intensity on resonance, $\gamma^{'}$ is defined as the power-broadened linewidth (where $\gamma^{'} = \gamma\sqrt{1+s_0}$), and λ defined as transition wavelength. Therefore, equation 3.1 can be formulated as follows,

$$I(z) = I_0 e^{-\alpha z}, \tag{3.3}$$

where $\alpha = \sigma_{eg} n L(\omega)$ ($L(\omega)$ is defined as laser detuning from the atomic resonance, which is a Lorentzian function, σ_{eg} and n define as a scattering cross-section, absorption coefficient respectively). Now the scattering cross-section can be expressed as follows,

$$\sigma_{eg} = \frac{\hbar\omega\gamma}{2I_s} = \frac{3\lambda^3}{2\pi}. \tag{3.4}$$

Assuming atoms are moving in arbitrary directions in the vapour cell with velocities, which can be represented by the Maxwell distribution $dn(v)$. In this thesis, we will only discuss the v_z components, i.e. the direction of laser beam propagation.

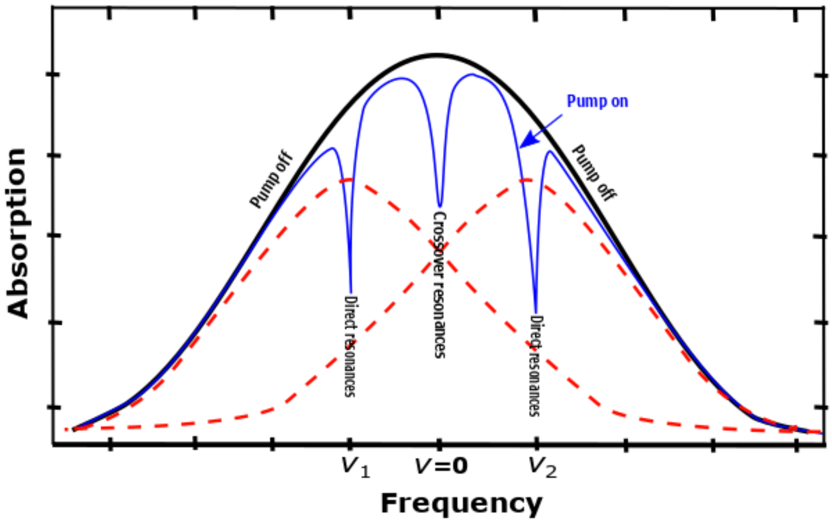

Figure 3.1: Example of absorption coefficient vs laser frequency at any multi-level systems. The black Bell-shaped curves are with the pump off, while red dotted Bell curves represent the individual transitions. And the blue curve is with the pump beam on.

The sub-Doppler outline of a spectrum in saturated absorption is thoroughly presented in [106, 107]. A weak probe beam and a relatively strong pump light overlap within the thermal cell in the sub-Doppler method. The atoms with zero group velocity are resonant at the intersection of both lights only on the resonance frequency. The intense pump light has transferred the atomic population from the ground to the excited state. Therefore, the decreased ground state population can be detected by using a weak probe light. So, the absorption decreases in the probe light close resonance can be detected, called the Lamb dips in the Doppler background. Normally for any alkali atomic system, we can see two ground states and multiple excited states and their saturated absorption spectrum have many Lamb dip, including crossover transitions. These crossover features arise whenever there are sufficient atoms whose Doppler shifts are precisely half the frequency separation among two transitions because the pump and probe light are counter-propagating and the atom will see them Doppler shifted by equal and opposite amounts. If the laser frequency is precisely halfway (in middle) between the two transitions with respect to the lab rest frame, the atom will encounter both pump and probe as acting on resonance, shown in 3.1 figure. In section 3.5 we experimentally demonstrate Lamb dip for the D_1 and D_2 transition in potassium.

3.2 Four wave Mixing process

The modulation transfer spectroscopy can can be explained in terms of the Four-Wave mixing (FWM) process. In the MTS process there are two frequency components of the laser beam, i.e. pump beams with sidebands. The pump light (plus sideband) interacts with the probe light through the third-order susceptibility (χ^3) and creates a fourth frequency as a sideband of the probe beam. This modulation process involves a few specific frequencies that make MTS a perfect scheme for the four-wave mixing process. Here we explain in detail the precise laser frequencies involved in this process, which is shown in figure 3.2.

Within our thermal cell, atoms are interacting with both probe and pump lights and the atoms flying with a velocity of v along the propagation direction of the pump light, see the light Doppler shifted in frequency (kv, k defined as wave vector $k = 2\pi/\lambda$). And the resonant frequency ω_0, with respect to laser frequency the expression kv get modified. The pump carrier frequency ω_1 with the two sidebands, the oscillation frequencies become $\omega_1 \pm \Omega$ and the probe frequency is ω_2 after the probe beam is modulated by the pump beam, which produces new photons with frequency $\omega_2 \pm \Omega$. This interplay can be explained relating the figure 3.2. We also consider the decay channels as defined as the decay rate of Γ and decay rate of other different states of Γ_1; hence, we consider the total excited state decay rate defined as Γ.

3.3 Basic theory

Here we summarizing the theory performed by Noh in supplying the calculations, which can be found in detail in the following papers [99, 108]. We recognise a two-level atomic system with excited and ground states, expressed

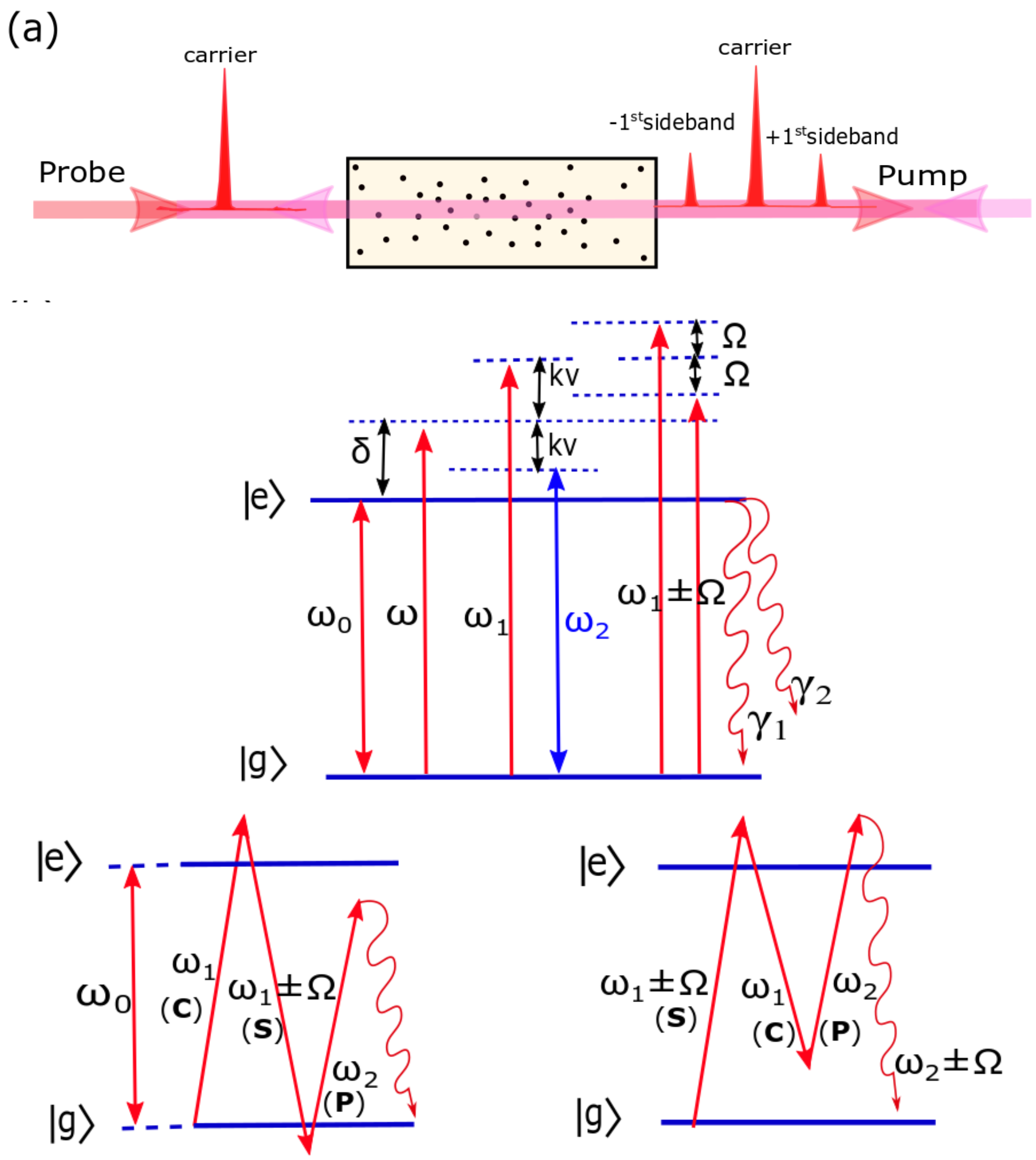

Figure 3.2: (a) A simple diagram of modulation transfer spectroscopy. (b) Energy level diagram of a two-level atomic system along with a non-cycling transition. (c) and (d) diagrams to understand the non-linear interaction (four wave mixing) process in the modulation spectrum.

by ket vectors $|e\rangle$ and $|g\rangle$ respectively. Therefore, the atomic system can be represented via the known optical Bloch equation as [99],

$$\dot{\rho} = -(i/\hbar)[H_0 + V, \rho] + \dot{\rho}_{sp}, \tag{3.5}$$

here the density matrix operator defined as ρ and the ground state atomic Hamiltonian is represented as $H_0 = \hbar\omega_0|F_e, m_e\rangle\langle F_e, m_e|$ and $\dot{\rho}_{sp}$ terms represent the matrix elements of spontaneous emission, which can be represented as follows,

$$\dot{\rho}_{sp} = \begin{pmatrix} -\Gamma\rho_{e,e} & -\frac{\Gamma}{2}\rho_{e,g} \\ -\frac{\Gamma}{2}\rho_{g,e} & \Gamma\rho_{g,g} \end{pmatrix} \tag{3.6}$$

The matrix elements can be expressed in the following way,

$$\begin{aligned} \langle F_e, m|\dot{\rho}_{sp}|F_e^{'}, m^{'}\rangle &= -\Gamma\langle F_e, m|\rho|F_e^{'}, m^{'}\rangle, \\ \langle F_e, m|\dot{\rho}_{sp}|F_g^{'}, m^{'}\rangle &= -(\Gamma/2)\langle F_e, m|\rho|F_g^{'}, m^{'}\rangle, \\ \langle F_g, m|\dot{\rho}_{sp}|F_g^{'}, m^{'}\rangle &= \Gamma \sum_{F_e=F_g-1}^{F_e=F_g+1} \sum_{q=-1}^{+1} S_{F_{g,m}}^{F_{e,m+q}} S_{F_{g,m^{'}}}^{F_{e,m^{'}+q}} \langle F_g, m|\rho|F_g, m^{'}\rangle, \end{aligned} \tag{3.7}$$

The total decay rate from the excited to ground states defined as Γ and for $i \neq j$ $(\dot{\rho}_{sp})_{ji} = (\dot{\rho}_{sp})_{ji}$. The optical Bloch with first time dependence (i.e. equation 3.7) can be transformed into new slowly varying variables, which can be defined as $\rho_{ij} = e^{c_{ij}t}\partial_{ij}$, where $c_{ij} = -(+)\omega$, where i and j indicates the ground (or excited) and excited (or ground) states, respectively, if $c_{ij} = 0$, while i and j signifies the ground or in-excited states. Therefore, equation 3.7 is modified in the subsequent equation,

$$\dot{\partial}_{ij} = e^{-c_{ij}t}\dot{\rho}_{ij} - ic_{ij}\partial_{ij}, \tag{3.8}$$

here $\dot{\rho}_{ij}$ is defined as matrix element from equation 3.7. And in equations 3.9 the normalized transition strength in between $\mid F_e, m_e\rangle$ and $\mid F_g, m_g\rangle$ is defined as $S_{F_{g,m_g}}^{F_{e,m_e}}$ [102, 109].

The probe light is not modified during the processed MTS spectroscopy, but the pump light frequency modulates. Therefore the interaction part of the Hamiltonian can be written in the subsequent way,

$$\begin{aligned} V = \frac{\hbar}{2}(\Omega_c e^{-i\omega_1 t} + \Omega_s e^{-i(\omega_1+\Omega)t} - \Omega_s e^{-i(\omega_1-\Omega)t} \\ +\Omega_p e^{-i\omega_2 t}) \mid F_e, m\rangle\langle F_g, m \mid +h.c., \end{aligned} \tag{3.9}$$

In above equation $\Omega_i(= -\frac{d_{eg}E_i}{\hbar})$ is defined as the Rabi frequency, where $i = c, s, p$ indicates different laser carrier frequency, and $\omega_{1(2)} = \omega + (-)kv$ is the beam frequency of the carrier pump (probe) beam (while the atoms are moving with velocity v). Here d_{eg}, i.e. dipole operator, which is linked to the decay rate, which can be expressed as,

$$\Gamma = \frac{1}{3\pi\epsilon_0}\frac{\omega_0^3}{\hbar c^3}d_{eg}^2 \tag{3.10}$$

In figure 3.2 we define detunings δ_1 and δ_p, which satisfy $\omega_1 = \omega_0 + \delta_1$ and $\omega_2 = \omega_1 + \delta_p$ respectively, where $\delta = \omega - \omega_0$ is defined as the detuning. Therefore δ_1 and δ_p can be derived in terms of velocity distribution v as follows,

$$\delta_1 = \delta + kv, \qquad \delta_p = -2kv \tag{3.11}$$

If we consider three photons' interactions ∂_{ee} and ∂_{gg} has 11 different oscillation frequencies, which are 0, $\pm\Omega$, $\pm 2\Omega$, $\pm\delta_p$, $\pm(\delta_p + \Omega)$ and $\pm(\delta_p - \Omega)$, similarly for ∂_{eg} has 20 oscillation frequencies, i.e 0, $-\delta_p$, $-\delta_p \pm \Omega$, $-\delta_p \pm 2\Omega$, $+\delta_p$, $\delta_p \pm \Omega$, $\delta_p \pm 2\Omega$, $-2\delta_p$, $-2\delta_p \pm \Omega$, $\pm\Omega$, $\pm 2\Omega$, and $\pm 3\Omega$ and ∂_{ge} another 20 oscillation frequencies with $-\partial_{eg}$. All from the oscillation frequencies just mentioned, the populations only affected by 0, $\pm\Omega$ and $\pm 2\Omega$ denoted as emission and absorption for two, 1 carrier, 1 and 2 side-band photons. Furthermore, additional oscillation frequencies can be explained similarly. For simplification, we will only consider two oscillation frequencies, i.e. 0 and $\pm\Omega$; all other oscillation frequencies are not considered.

When the photon number is limited, the populations can be created via the two-photon carrier and sideband photons. Furthermore, via three-photons interaction, the probe photon provides the optical coherences (off-diagonal matrix elements). Therefore, only five oscillation frequencies matter in our entire populations, which are 0, $\pm\Omega$ and $\pm 2\Omega$. Compared to carrier oscillation frequency, sideband frequencies are weak; therefore, we can ignore 2nd-order sideband $\pm 2\Omega$. Similarly, seven oscillation frequencies (i.e. $-\delta_p \pm \Omega$, $-\delta_p$, 0, $\pm\Omega$, and $\pm 2\Omega$) are important for the excited-ground state coherences, and opposite sign for ground-excited state coherences. Therefore the population can be expressed as follows,

$$\begin{aligned}\partial_{ee} = p_1 + (p_2 + ip_3)e^{-i\Omega t} + (p_4 + ip_5)e^{-i2\Omega t} + (p_6 + ip_7)e^{-i\delta_p t} \\ +(p_8 + ip_9)e^{-i(\delta_p+\Omega)t} + (p_{10} + ip_{11})e^{-i(\delta_p-\Omega)t} + c.c.,\end{aligned} \tag{3.12}$$

$$\partial_{gg} = \partial_{ee}(p_i \to q_i), \qquad i = 1, ..., 11, \tag{3.13}$$

Now the coherences terms can be expressed explicitly as follows,

$$\begin{aligned}\partial_{eg} = (r_1 + is_1)e^{-i\delta_p t} + (r_2 + is_2)e^{i(-\delta_p-\Omega)t} \\ +(r_3 + is_3)e^{i(-\delta_p+\Omega)t} + \text{other 17 terms}\end{aligned} \tag{3.14}$$

$$\partial_{ge} = \partial_{eg}^* \tag{3.15}$$

In equation 3.12, the 17 terms which is related to $e^{-i\delta_p t}$, $e^{i(-\delta_p-\Omega)t}$ and $e^{i(-\delta_p+\Omega)t}$ are not shown. Here p, q, r and s defined later on this section.

Now, if we are inserting equations 3.14 and 3.16 into equation 3.10 we can obtain several coupled linear differential equations, as an example for $\dot{p}_1$ and $\dot{q}_1$ the equations becomes,

$$\begin{aligned}\dot{p}_1 = -\Gamma q_1 - \Omega_c s_{13} + \Omega_s s_{14} - \Omega_p s_1, \\ \dot{q}_1 = \Gamma q_1 + \Omega_c s_{13} - \Omega_s s_{14} + \Omega_p s_1,\end{aligned} \tag{3.16}$$

where s_1, $_{13}$ and s_{14} are the imaginary components of the oscillations frequencies. Therefore, from equation 3.16, we can have $\dot{p}_1 + \dot{q}_1 = 0$(i.e $p_1 + q_1 = 1$) which means the population is conserved. Therefore, using the induced dipole moments, the detected beat spectrum can be estimated as follows,

$$\begin{aligned}\langle d\rangle = Tr(\rho d) = d_{eg}S_{eg}\{(r_1 + is_1)e^{-i\delta_p t} + (r_2 + is_2)e^{i(-\delta_p-\Omega)t} \\ +(r_3 + is_3)e^{i(-\delta_p+\Omega)t} + \text{other terms} + c.c, \}\end{aligned} \tag{3.17}$$

Since the electric field, E_{sig} is created by the oscillating electric dipole, which is changed in phase by $\pi/2$ with respect to the probe field. S_{ij} is defined as relative transition strength in-between ground states and excited states.

$$\begin{aligned} E_{sig} \propto i(r_1 + is_1)e^{-i\delta_p t} + i(r_2 + is_2)e^{i(-\delta_p - \Omega)t} \\ +i(r_3 + is_3)e^{i(-\delta_p + \Omega)t} + \text{other terms} + c.c, \end{aligned} \tag{3.18}$$

This electric field is oscillating with $\omega_2 \pm \Omega$, which can be understood properly by the FWM process as presented in figure 3.2. In this coherence interaction process, the carrier frequency ω_1, sideband $\omega_1 + \Omega$ and probe ω_2 interacts with the atoms and generate a new oscillation frequency $\omega_2 \mp \Omega$, this can be understood in figure 3.2. Since the beating oscillating electric field interacts with the probe beam, the observed signal is obtained as follows, and the computed spectrum is presented in figure 3.3.

$$I_0 \mathbf{cos(\Omega t)} + Q_0 \mathbf{sin(\Omega t)} \tag{3.19}$$

where I_0 and Q_0 are the dispersive in-phase component and an absorptive quadrature component, which can be expressed as,

$$I_0(\delta_1, \delta_p, t) = S_{eg}(s_3 + s_2), \qquad Q_0(\delta_1, \delta_p, t) = S_{eg}(r_3 - r_2) \tag{3.20}$$

To obtain final results, one can integrate in-phase and quadrature parts across the transverse and longitudinal velocity distributions, which is as follows,

$$\begin{aligned} I(t) = \frac{1}{t_{av}} \int_0^{t_{av}} dt \int_{-\infty}^{\infty} dv f_D(v) I_0(\delta + kv, -2kv, t) \\ Q(t) = \frac{1}{t_{av}} \int_0^{t_{av}} dt \int_{-\infty}^{\infty} dv f_D(v) Q_0(\delta + kv, -2kv, t), \end{aligned} \tag{3.21}$$

where velocity distribution of the atoms (i.e. Maxwell-Boltzmann function) is defined as f_D,

$$f_D = (\sqrt{\pi u})^{-1} \exp[-(v/u)^2] \tag{3.22}$$

where $u(= (2k_BT/M)^{1/2})$ is defined as the most probable velocity distribution, the thermal cell temperature is defined as T, the atomic mass is defined as M and the average time to cross laser beam is $t_{av}(= (\sqrt{\pi}/2)d/u)$, where the diameter of the beam is d [110].

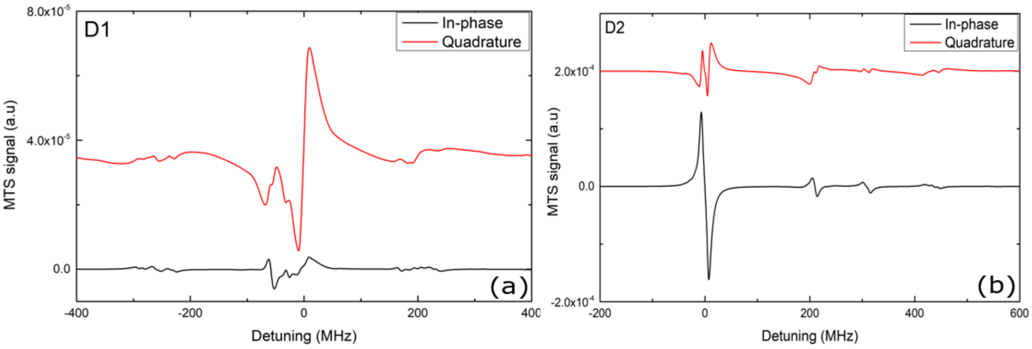

Figure 3.3: Calculated in-phase and quadrature parts of the detected MTS signal. In (a) indicate D_1 transition of potassium (^{39}K + ^{41}K) isotopes. Similarly the MTS spectrum for D_2 transition presented in figure (b). The simulation done by Heung-Ryoul Noh.

The in-phase and quadrature components of D_1 and D_2 transitions of potassium atoms. For the simulations, we used carrier, each sideband, and probe intensities of 11.8 mW/cm^2, 2.5 mW/cm^2 and 57 mW/cm^2 respectively, the thermal cell temperature was 99 degrees, beam diameter was 2 mm. The EOM modulated frequency was considered to be 6.08 MHz. The in-phase represents the MTS spectrum at phase angle = 0 degree and for quadrature component at phase angle = 90 degrees, respectively.

Before going to details spectroscopic studies we need to understand the energy level diagram (figure 3.4), where we can represent $4^2S_{1/2} = 2 \rightarrow 4^2P_{1/2} = 2$ as D_1 (i.e 770.108 nm) and $4^2S_{1/2} = 2 \rightarrow 4^2P_{2/3} = 3$ as D_2 (i.e 766.7 nm) transition respectively.

This chapter will extensively examine and describe the temperature dependence of saturation absorption and the MTS spectrum and characterize the effect of the probe beam and pump intensity on the modulated spectrum. Then we study the impact of the polarization on both the crossover transition in D_1 and for the D_2 transition, respectively.

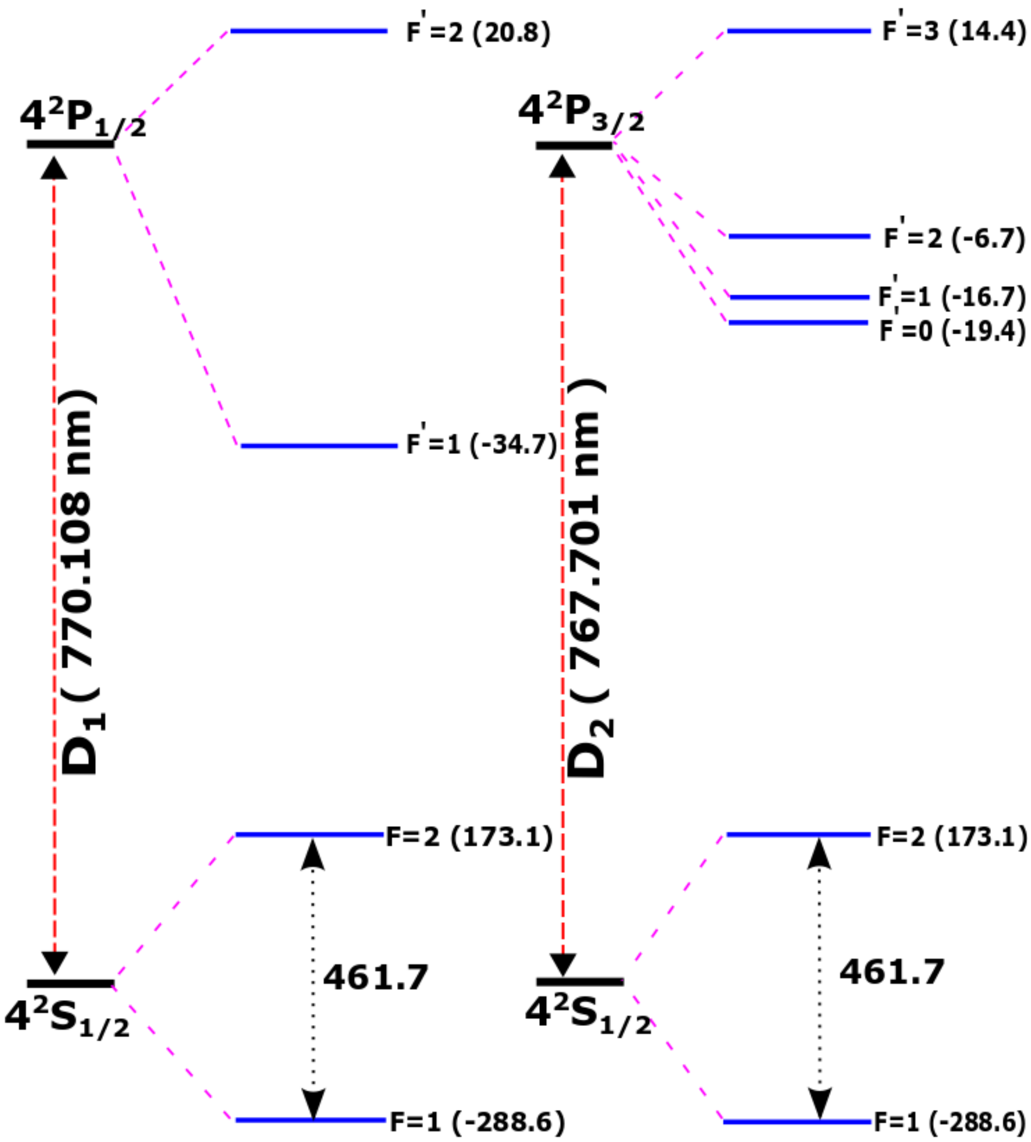

Figure 3.4: Energy level diagram for the D_1 and D_2-lines of ^{39}K, the numerical values are taken from [63].

3.4 Experimental setup

The optical layout of our experimental components for MTS spectroscopy is shown in figure 3.5. In our experiment, we used a homebuilt external cavity diode laser (ECDL) with a littrow configuration with an AR-coated laser diode (Part number:- EYP - RWE - 0790 - 04000 - 0750 - SOT0001 - 000), which can be tuned from 750 nm to 790 nm. Therefore, the D_1 and D_2 line

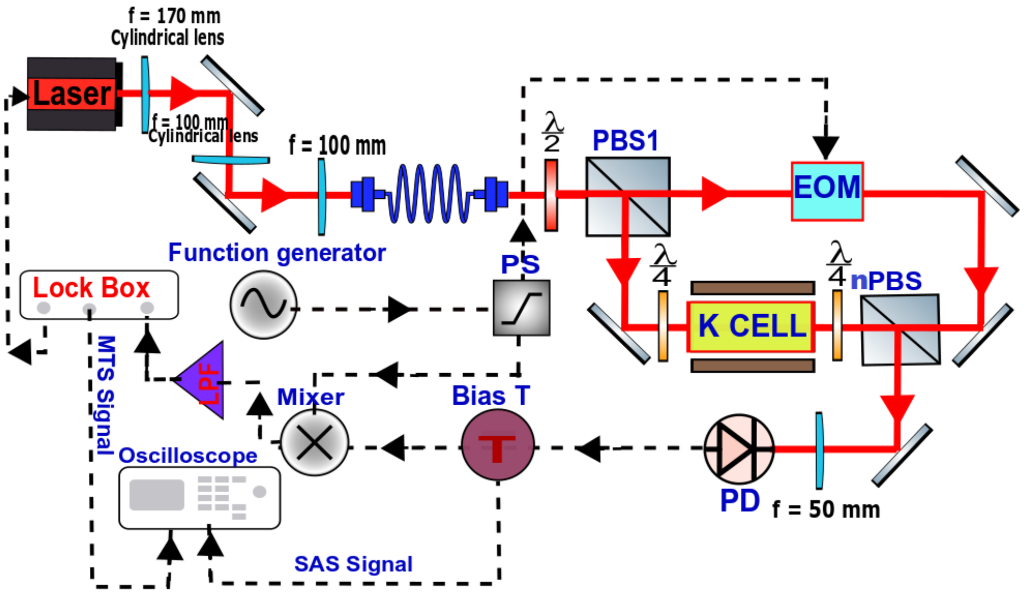

Figure 3.5: Optical setup of our MTS spectroscopic experiment. The modulation frequencies of 6.05(5) MHz and 5.85(3) MHz were used for the D_1 and D_2 transitions. The beat signal is demodulated after being detected by a fast photodiode, producing the error signal. PBS, polarization beam splitter; nPBS, non-polarization beam splitter, PD, photodiode; DBM, double-balance mixer; LP, low pass filter; PS, power splitter; EOM, electro-optic modulator.

of potassium is easily accessible by the laser diode. For D_1 transition we have 3 ± 0.2 mW laser beam power and 1.3 ± 0.2 mW for D_2 transition available for modulation transfer spectroscopy, due to the requirement of other experiments simultaneously. When the beam is passed through PBS1, it splits into two beams with specific polarization: the pump and probe beams. We can control the power of the pump and probe beam by using a half-wave plate just before the PBS1.

The 23 mm vapour cell is inside a copper cube that can be heated up to 130°C to get sufficient vapour pressure. In order to control the polarization of the pump and probe beams, one can use a half waveplate and quarter waveplate on each ends of the vapour cell. A homemade EOM modulator is used to modulate the phase of the pump beam, which can be driven by a 5.85(3) MHz rf signal generated by a digital function generator (Digimess compact H.UC-65-00, FG 100). We used a homemade fast photodiode circuit (Hamamatsu-S5971) to record the spectrum. To divide the low and high-frequency segments of the photodiode spectrum a bias-T (Mini-circuits

ZFBT-4R2GW-FT+) is used. The low-frequency component was directed towards an oscilloscope, which gives us SAS spectrum, and the higher frequency segment was mixed within a DBM (double-balanced mixer) (Mini-Circuits ZAD-1H+) and later separated by a homemade active low pass filter with a cut off frequency of 16 kHz and a gain of 178. We used a power splitter (PS) (Mini-circuits ZSC-2-1+) to synchronize the function generator and DBM with the EOM. We used a homemade EOM setup with a simple LCR circuit with a Q-factor of 15(1) [111], where L, R and C are defined as the inductance, resistance, and capacitance of the inductor, the EOM used a $LiTaO_3$ crystal.

As indicated [103], the modulation frequency should be approximately 0.7Γ, where $\Gamma = 2\pi \times 6.035$ MHz and the corresponding expected modulation frequency is 4.22 MHz. Though, in our investigation, the power broadening of the transitions makes the spectral linewidth greater than the natural linewidth. This phenomenon influences our modulation frequency, and the optimized modulation frequency also raises. However, a higher modulation frequency has a better signal to noise ratio. For these reasons, we choose modulation frequencies of 6.05(5) MHz for D_1 and 5.85(3) MHz for D_2, which is near the natural linewidth of respective transitions.

Once the MTS signal is demodulated by the mixer and low-pass filter, it's fed to the locking amplifier module, which regulates and distributes it to the laser system input. This input voltage allows access to the ECDL piezo actuator voltage by adjusting the cavity length. The voltage for this is driven by the scanning controlling unit. The error signal can be seen on an oscilloscope while scanning the frequency. We take a peak to peak amplitude and slope of the MTS spectrum directly from the oscilloscope. We also calculate the slope by fitting a straight line between two peaks using Origin. The difference between these two amplitudes/slopes is an error in the slope and amplitude.

3.5 Saturated absorption spectroscopy of the D_1 and D_2 lines of potassium

As any cold atom physics experiment starts from absorption spectroscopy, we also started with saturated absorption spectroscopy. We used a 23 mm cell (Toptica CE K 25) containing potassium isotopes in our experiment. At room temperature, we have low vapour pressure within the potassium cell; to increase the vapour pressure sufficient for experiments, we started to heat the cell and record the saturated absorption spectrum at different temperatures, using the temperature sensor to monitor the cell temperature. Our example spectra are shown in figure 3.6 for the D_1 transition and for the D_2 transition presented in figure 3.7. We also theoretically estimate the temperature inside the 23 mm vapour cell from the Doppler broadened absorption spectrum using ElecSus [112].

Our home-built ECDL laser system was used for the spectroscopy and MOT experiment presented in next chapter. The output of the laser was elliptical, therefore, two cylindrical lenses were used in perpendicular orientation to make the laser beam circular. The light coupled with the fibre and used for experiments, we used a Thorlabs camera to measure the collimated beam size $w_x = 1.7 \pm 0.02$ mm and $w_y = 1.9 \pm 0.03$ mm (along the horizontal and vertical axis) for D_1 and D_2 respectively just before entering the thermal cell.

The basic setup of our experiment is shown in figure 3.5. In saturated absorption spectroscopy, two counter-propagating pumps and probe beams interact and overlap in a potassium vapour cell. As discussed before, due to low number density and vapour pressure at room temperature, our thermal cell needs to be warmed up with a resistive heater and monitor the temperature using a thermistor. A photo-detector detects the probe beam, and the probe light gives us the SAS spectrum with Doppler background as shown in figure 3.6 for the D_1 transition. Here we can see three main Lamb dips which are A, B (B_1 + B_2) and C, while A represent $F = 2 \rightarrow F' = 1,2$ transition, B represent crossover peak $F = [1 \leftrightarrow 2] \rightarrow F' = 1,2$ transition and C is $F = 1 \rightarrow F' = 1,2$ transition respectively. Within the crossover peak two peaks are visible, they are B_1 and B_2 respectively. Due to low natural abundances of

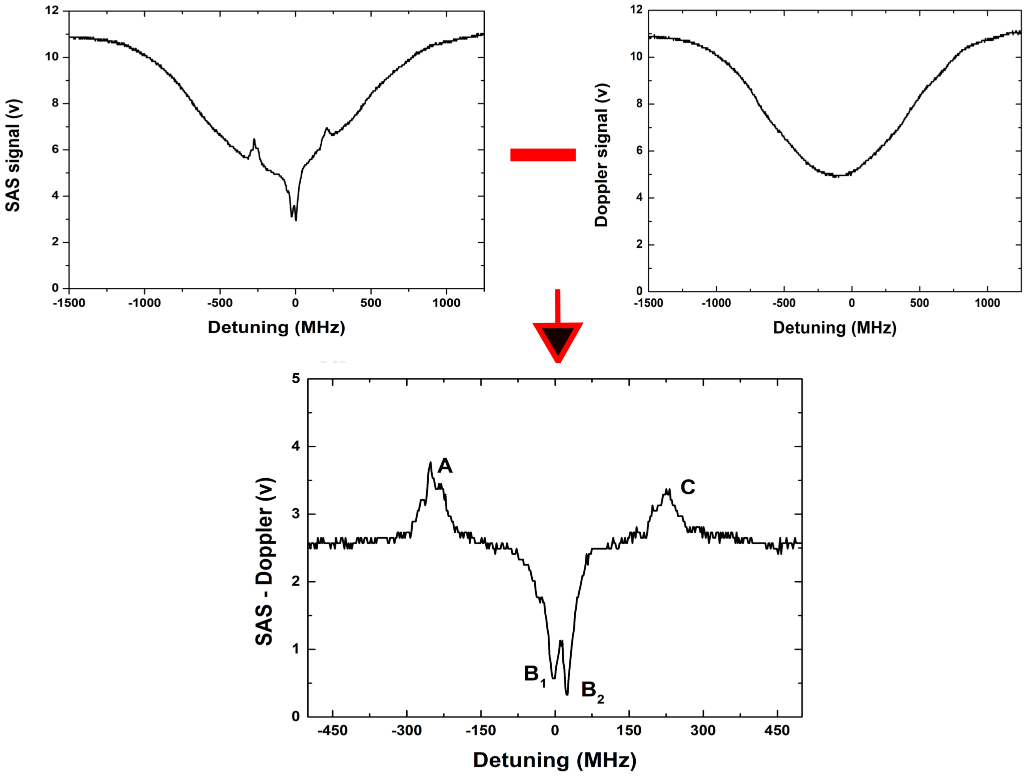

Figure 3.6: The Doppler-free SAS spectrum of D_1 transition was obtained by deducting the Doppler spectrum from the saturated absorption spectrum. The frequency axis is calibrated using a cavity signal.

the ^{40}K and ^{41}K isotopes, the contribution of ^{40}K and ^{41}K isotopes on the spectrum is not visible.

For the D_2 line in figure 3.7, here are two main features in the spectrum. Each component consists of a group of overlapping transitions, mainly in A and B. Within the typical Lamb dips, $'A'$ corresponds to $F = 2 \rightarrow F' = 1,2,3$ in addition there is crossover resonance within the individual of the excited states. Similarly, characteristic peak B includes two ground state crossover peaks within two actual transitions. Here in this spectrum, a very weak peak appears, which is coming from ^{41}K isotope.

The Doppler background of the saturation absorption spectrum strongly coupled with the temperature, through exponential dependence of the vapour pressure. For D_1 transition Lamb dip started appear from 70°C and the dip is not visible beyond 130°C 3.8, because the cell becomes optically thick on resonance, not that the line becomes broader at the higher temperature and

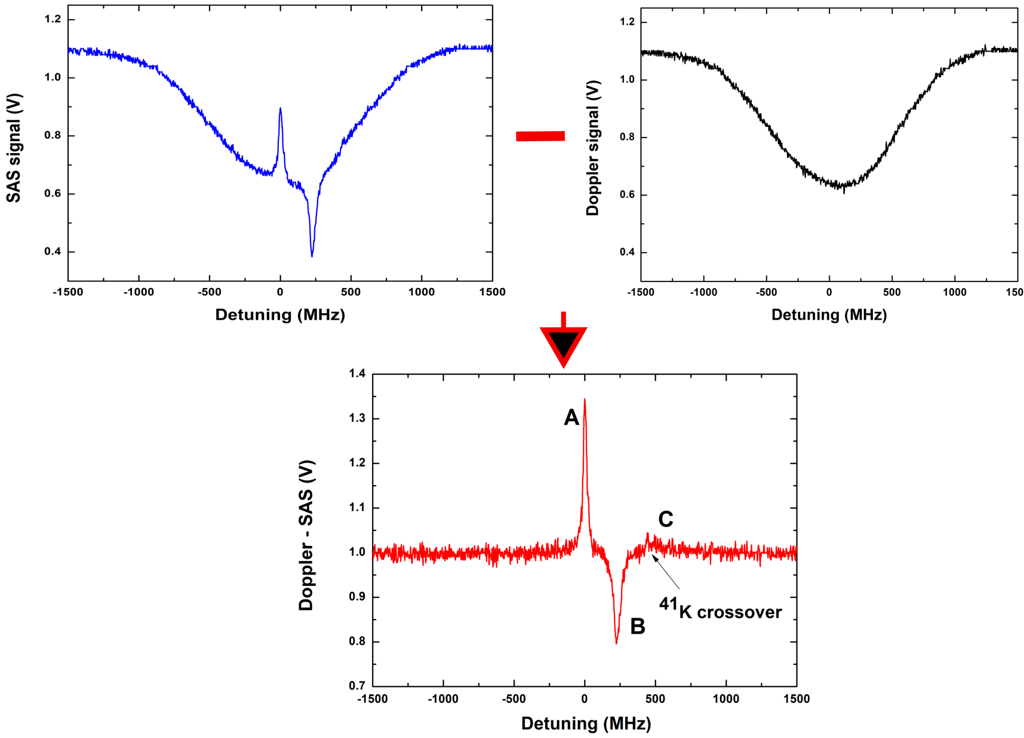

Figure 3.7: The Doppler-free SAS spectrum of the D_2 line of potassium was measured by subtracting the Doppler broadened background from the Doppler broadened SAS spectrum.

maximum Lamb-dip for features B (which is the crossover transition) around 104 ± 3°C (as we discuss in figure 3.10). But for A and C (the resonance transitions), the optimal temperature is higher than peak B. For D_2 transition the peaks started appear from 65°C, we can clearly see two narrow peaks $\bar{A}$ and $\bar{B}$, which are $\mathrm{F} = 2 \rightarrow \mathrm{F}' = 1, 2, 3$ and the crossover ($\mathrm{F} = [1 \leftrightarrow 2] \rightarrow \mathrm{F}' = 1,2,3$) transition respectively. Also we can see a small dip near 260 MHz which is corresponding to $\mathrm{F} = 1 \rightarrow \mathrm{F}' = 0, 1, 2$ of ^{39}K which is overlap with ^{41}K ground state crossover. The peaks are not visible beyond 115°C, because the cell becomes optically thick on resonance as indicated earlier. For this transition both peaks are in maximum point near 96 ± 2°C.

We take both the Doppler and sub-Doppler spectrum at the same temperature within a small time window to optimize the temperature dependence. After that, we subtract these two signals, and we end up with a flat background and narrow of A and B as shown in figure 3.6 and 3.7. After that, we fit a Lorentzian function for simplicity and extract the peak heights (Am-

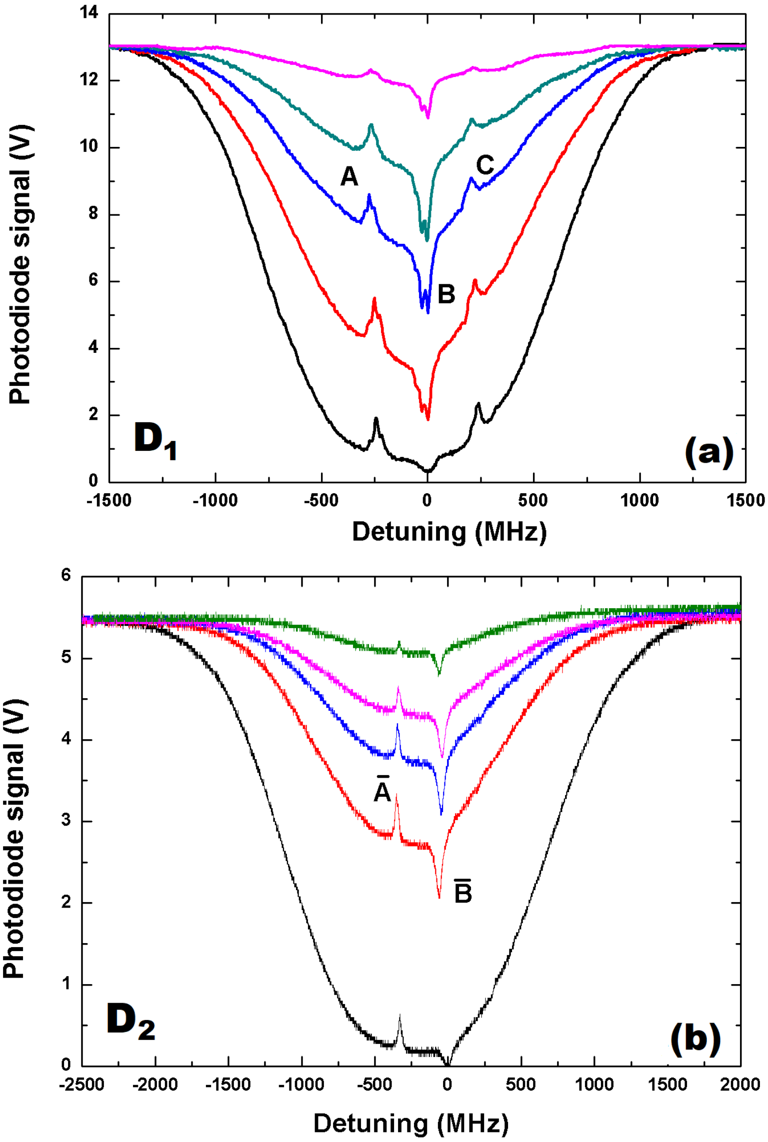

Figure 3.8: The saturated absorption spectrum at different cell temperatures. In figure (a), the D_1 line shapes are presented for different temperatures. From top to bottom, the curves represent 83, 90, 104, 119, and 129°C respectively. Similarly, in figure (b), the D_2 line shapes are presented for different temperatures. From top to bottom, the curve represent 79.5, 84.3, 90.5, 98.6, and 113.4°C respectively.

plitude). Because our MTS spectrum will appear in B peak of D_1 crossover transition and as presented in figure 3.10, within B peak we can see two peak B_1 and B_2 with the MTS spectrum generated by B_1 peak. The measured amplitude is shown in figure 3.9. We quantify the frequency axis using the cavity spectrum, which is briefly discussed in A.2.1 section. The intensity of a weak probe light travelling within a thermal cell is equivalent to exp(-αL),

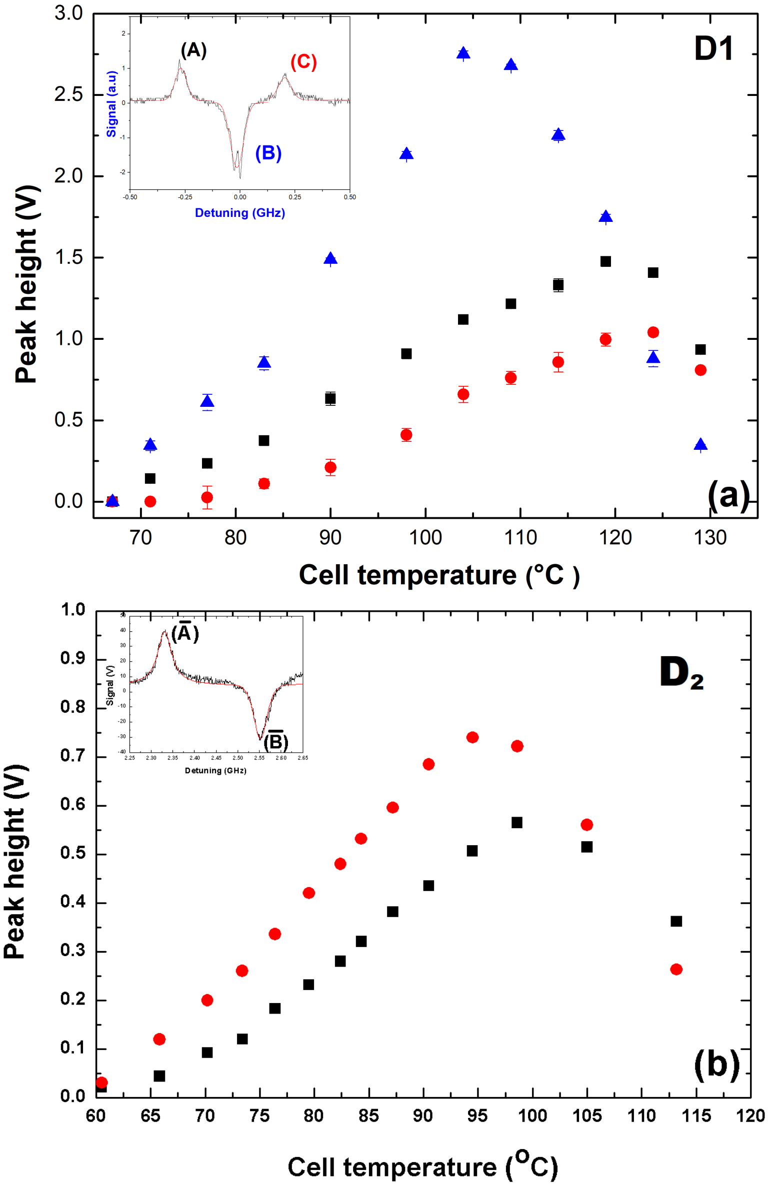

Figure 3.9: The temperature dependency of SAS features. The temperature regulated with the current passing within the resistive heater attached to the cell in the experiment. In (a) the peak amplitude or height varies with the cell temperature, the blue, black and red represent the A, B_1 and C respectively for D_1 770.1 nm transition with fixed pump and probe intensity 12.3 ± 0.04 mW/cm^2 and 5.50 ± 0.05 mW/cm^2 respectively (b) Similarly in case of D_2 767.7 nm transition features $\bar{A}$ (red data point) and $\bar{B}$ (black data point) peak amplitude or height varies with the cell temperature, while the pump and probe beam intensity was 13.7 ± 0.03 mW/cm^2 and 6.74 ± 0.01 mW/cm^2 respectively.

where α and L is defined as absorption coefficient and the length of the cell, respectively.

In figure 3.9, we show the temperature dependence of the amplitude of the peaks A, B and C for D_1 770.1 nm and D_2 767.7 nm transition. The height of the features for both transitions increase with increasing temperature and reach a maximum 104 ± 3 °C for D_1 (770.1 nm) and 96 ± 2 °C for D_2 (767.7 nm) transition respectively. If we increase the temperature further, cell becoming optically thick and not much light making it through the cell - hence the signal become smaller. In the case of other features B and C for D_1 transition and feature $\bar{B}$ in D_2 transition, it almost follows the same behaviors in terms of peak height at the higher temperature.

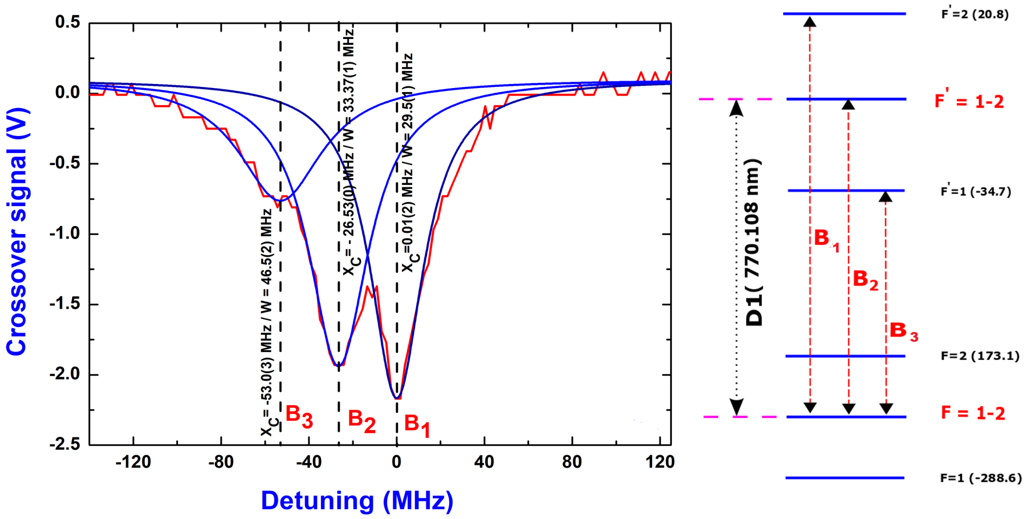

Figure 3.10: For the crossover of D1 saturated absorption spectrum three (B_1, B_2 and B_3) Lamb-dips are clearly visible, B_1 and B_2 are dominating. We fit three Lorentzian curves corresponding to the three crossover transitions shown in the figure. After fitting the Lorentzian function and estimating the peak positions, we can say that separation between $F' = 2$ to $F' = 1$ agrees with our fitted value within 4.6%.

If we concentrate on the crossover transition for the D_1 transition in figure 3.10, where two peaks B_1 and B_2 are easily visible but B_3 is weak. B_1 represents $F = [1 \leftrightarrow 2] \leftrightarrow F' = 2$, B_2 indicates $F = [1 \leftrightarrow 2] \leftrightarrow F' = [1 \leftrightarrow 2]$ and B_3 is generated from $F = [1 \leftrightarrow 2] \leftrightarrow F' = 1$ transitions respectively. We also fit Lorentzian functions and compute the peak positions as shown in figure 3.10. We find that the separation between peak B_3 and B_1 is 53.0(5) MHz. This should be compared to the separation between $F' = 1$ and $F' = 2$ which is 55.5 MHz, which is within 4.6% uncertainty of the measured value. As the B_1 and B_2 are strong peaks, we studied their temperature dependence. We found that the amplitude of both features increases linearly and reaches a maximum of around 104 ± 3°C beyond which the amplitude decreases dramatically to almost zero at 130 ± 2°C. So we found from this section that optimal temperature for D_1 and D_2 transitions are 104 ± 3°C and 96 ± 2°C respectively.

Note : − In this section when we optimize the signal for the D_1 transition as a function of temperature, the B_1 ($F = [1 \leftrightarrow 2] \rightarrow F^{'} = 2$) is the main feature for MTS spectroscopy which will be discussed in the next section. And similarly, for the D_2 transition feature, $\bar{A}$ ($F = 1 \rightarrow F^{'} = 1,2,3$) generates the dominant signal in the MTS spectrum.

3.6 Modulation Transfer Spectroscopy with $4^2S_{1/2} \rightarrow 4^2P_{1/2}$ & $4^2P_{3/2}$ Transition.

This section will discuss the impact of temperature, intensity, and the polarization of the pump and probe lights on the MTS spectrum. Figure 3.11, shows how the MTS spectrum depends on the temperature of the potassium vapor cell when the pump intensity is 36.75 ± 0.06 mW/cm^2 and the probe intensity is 22.05 ± 0.01 mW/cm^2 for the D_1 transition respectively. Similarly for the D_2 transitions pump intensity is 13.7 ± 0.05 mW/cm^2 and the probe intensity is 7.38 ± 0.01 mW/cm^2 respectively. In figure 3.12, we compute the amplitude and slope of the signal, and we can see that the temperature greatly affects the response of the MTS spectrum. For both D_1 and D_2 transition, initially the amplitude and slope increase abruptly with the increased temperature up to 104 ± 3°C for D_1, and 96 ± 2°C for D_2, then decrease dramatically. This kind of changes happens at low temperatures, the atom number is insufficient. The atom vapor density increases with temperature, at the peak position in figure 3.12, atom number keeps increasing with temperature, and we get maximum amplitude and slope of the MTS spectrum. At higher temperatures, the collisions between atoms and cell walls also reduce the efficiency of the optical pumping, which will reduces the spectrum.

All the data were taken with the same beam intensity mentioned above and

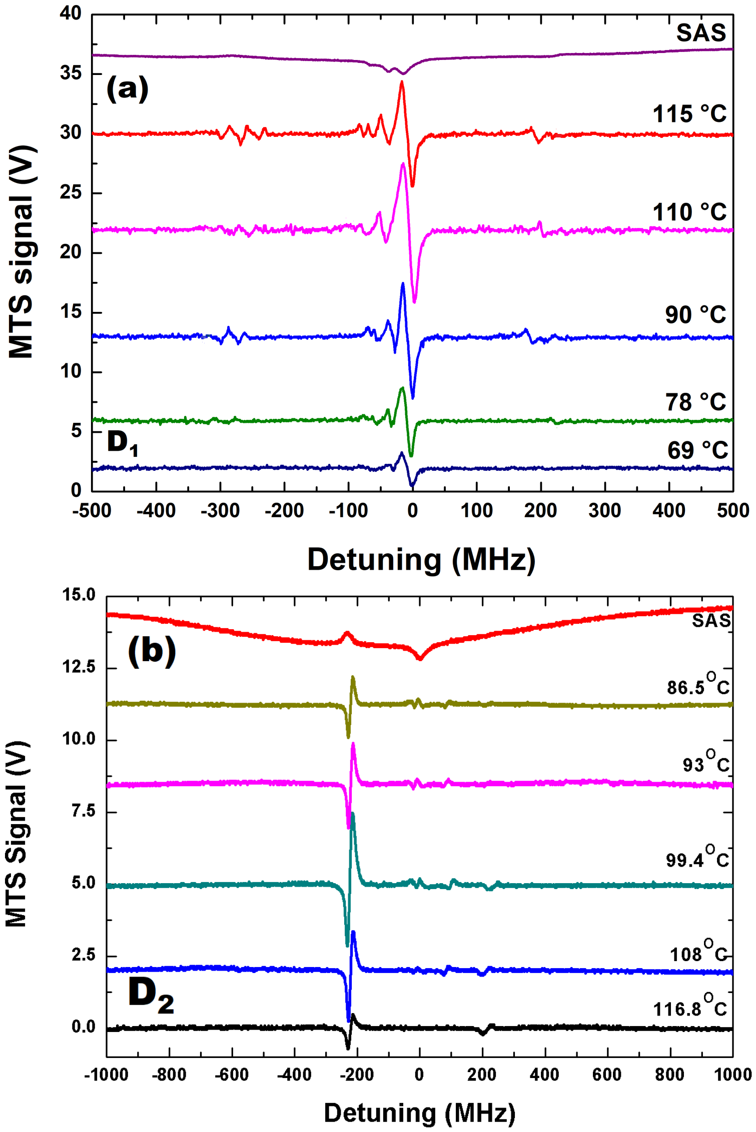

Figure 3.11: Typical modulation transfer spectroscopy with saturated absorption spectroscopy as a reference. In figure (a), the MTS spectrum studied for the D_1 transition at different vapour temperatures. From top to bottom, every spectrum represents a different cell temperature which is denoted in the plot. In (b), similarly, we studied the spectrum for the D_2 transition at different vapour temperatures; here, we also listed different spectra with different temperatures.

with a minimum interval. For the D_1 transition, the MTS spectrum compares to B_1, $F = [1 \leftrightarrow 2] \rightarrow F' = 1$ transition, which is not been reported before for ^{39}K. Before this work, only in the Li MTS spectrum [103] has the same kind of crossover transition been reported, where the incoherent process generated the spectrum. Other modulated resonance and crossover transitions in D_1

are also visible, but the dips and slopes are negligible in comparison to B_1 crossover transition. Similarly in the case of the D_2 transition, the MTS spectrum represents the $F = 2 \rightarrow F^{'} = 1, 2, 3$ transition, which is denoted as A and B corresponding to crossover $F = [1 \leftrightarrow 2] \rightarrow F^{'} =$ 1,2,3 transition. Clearly, in the spectrum, we can observe a big MTS signal associated with the cycling $F = 2 \rightarrow F^{'} = 3$ transition, which dominates the other signal. We can qualitatively confirm while comparing the saturated absorption signal with the MTS signal, we have seen the zero crossings of the MTS signal is not aligned with the centre of the saturated signal; it is shifted to higher frequency. Therefore, we expect that the MTS spectrum for the D_2 line generates from $F = 2 \rightarrow F^{'} = 3$ transition.

From the temperature dependence experiments we can conclude that for D_1 transition 104 ± 3 °C is the optimal cell temperature, similarly for D_2 transition we have the 96 ± 2°C is optimized temperature for 10 cm long potassium thermal cell. Our optimal MTS temperatures are quite similar to the optimal temperatures of the saturated absorption spectrum for our experiments.

3.7 Pump and Probe intensity optimization

The MTS spectrum depends on the pump intensity as shown in figure 3.13. For each transition, the slope and amplitude of the MTS spectrum rise with the pump power and follows the almost linear behavior at low beam intensity at constant probe intensity. For the D_1 transition the amplitude and slope peaks around 17.5 ± 0.05 mW/cm^2 and then both the amplitude and slope becomes saturated, while the constant probe intensity was 23.7 ± 0.04 mW/cm^2.

Similarly, for D_2 transition, the MTS spectrum amplitude and slope peak at 13 mW/cm^2 and then decrease dramatically. All the data was taken at constant probe intensity of 9.50 ± 0.05 mW/cm^2. For both transitions we prefer $L^+ - L^+(L^- - L^-)$ configuration of the pump and probe light to improve the MTS signal in our experiments.

In the remaining part of this part, we investigate the impact of probe intensity

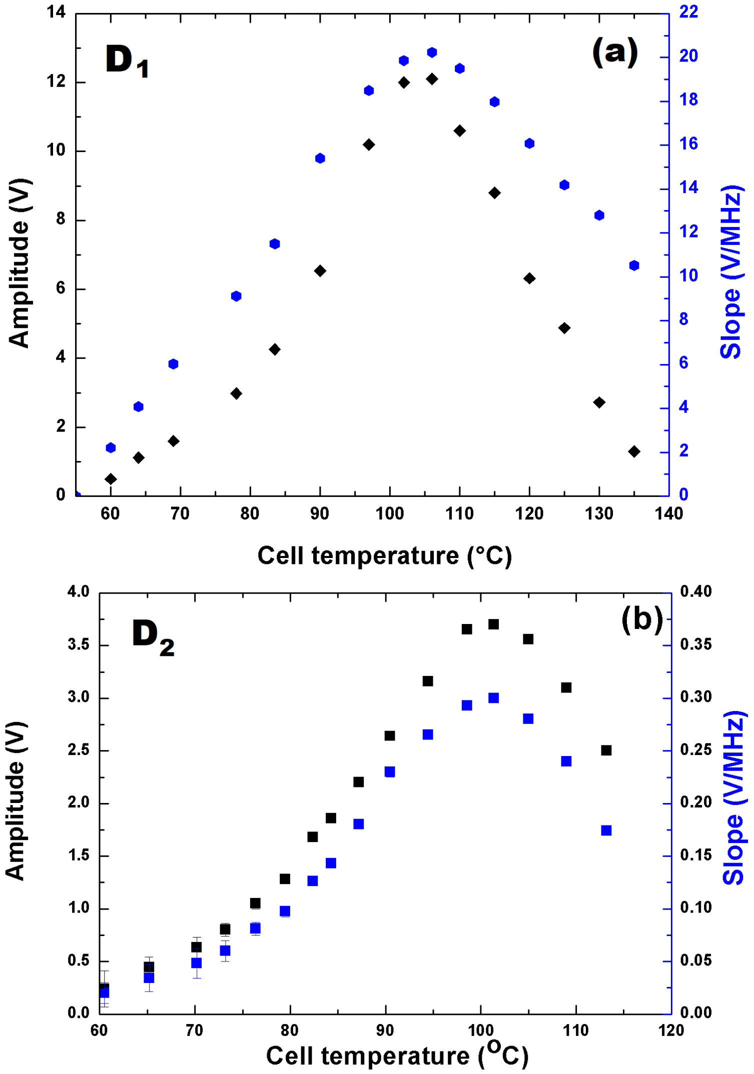

Figure 3.12: Dependence of MTS spectrum on temperature with fixed pump and probe intensity, here we only quantify the B_1 features for D_1 (crossover) and the A feature for $D_2(F = 2 \rightarrow F^{'})$. In (a) the D_1 transition amplitude and slope increases until 104 ± 3°C and then reduces dramatically. Similarly in (b) the D_2 transition, amplitude and slope increases until 96 ± 2°C and then reduces relatively fast.

on the MTS spectrum, as shown in figure 3.14. For the D_1 transition the B1 feature ($F = [1 \leftrightarrow 2] \rightarrow = 2$) generates the largest MTS signal and similarly for D_2 line the largest feature in the MTS spectrum corresponds to the main peak $\overline{A}$ corresponding to $F = 2 \rightarrow F^{'} = 3$ (expected) transition. The amplitude and slope of both signals increase linearly with the increase of the probe intensity initially. For D_1, transition peaked at $\sim 31 \pm 1$ mW/cm^2, after that the amplitude started the decline. While for D_2 transition the amplitude and

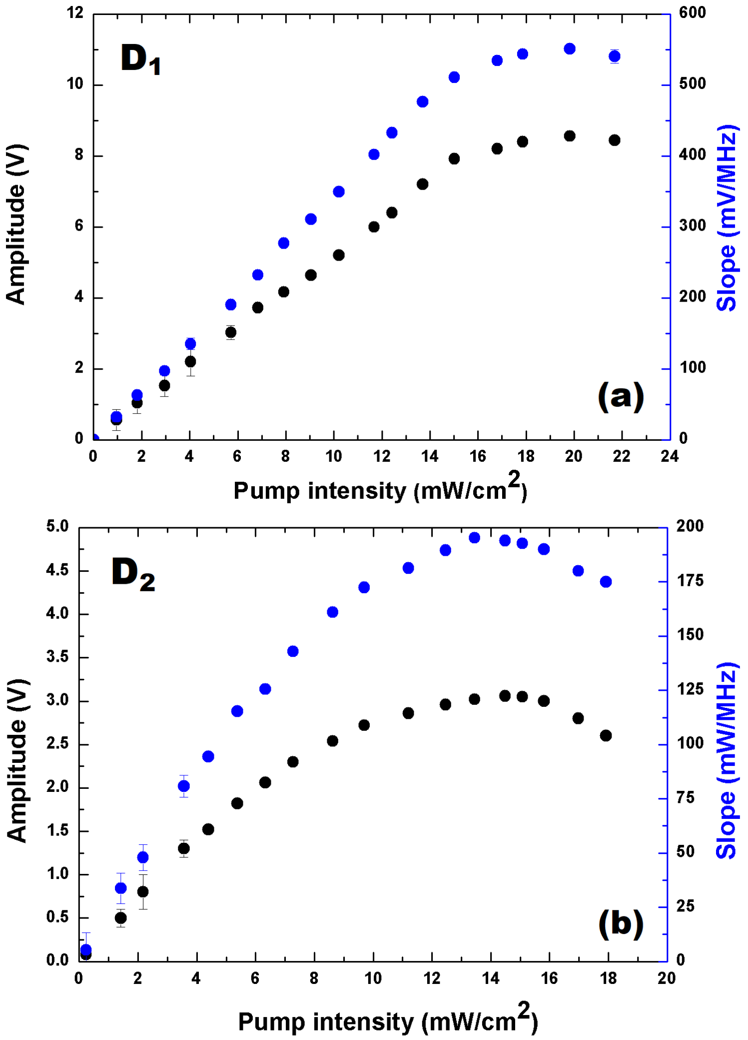

Figure 3.13: Pump intensity dependence on the MTS spectrum for constant probe intensity. (a) shows the D_1 transition with a fixed probe of 23.7 ± 0.04 mW/cm^2. (b) shows the D_2 transition with a fixed probe of 9.50 ± 0.05 mW/cm^2.

slope are almost saturated after $\sim 7 \pm 1$ mW/cm^2 probe intensity at constant pump intensity. The spectrum is dominated by a low signal-noise ratio at a lower intensity, but in higher intensity, the signal dominates the noise. Here we measure the pump and probe power just before the hot potassium thermal vapor cell. The beam size also impacts the MTS spectrum, which is not studied in this thesis. But the interested reader can find a detailed study on the Rb system in [111].

The amplitude and slope increase with the increase of laser power because of the low atom-atom collision rate and the efficiency of the four-wave mixing

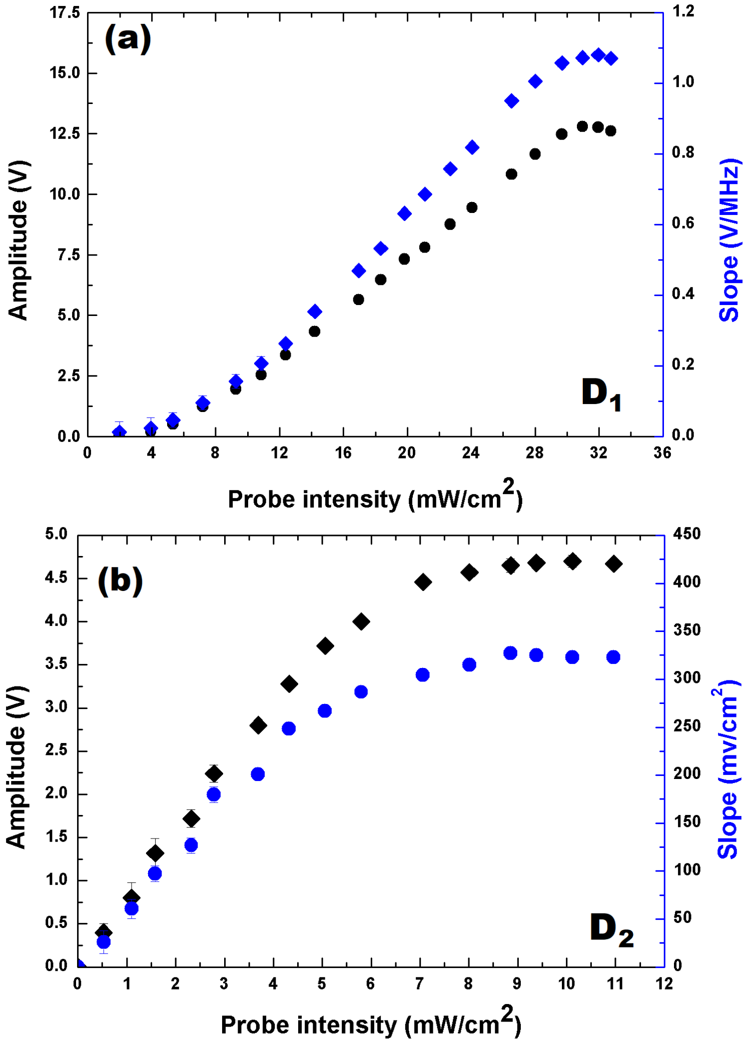

Figure 3.14: Probe intensity dependence on the MTS spectrum for constant pump intensity was kept constant. (a) shows the D_1 transition with a fixed pump intensity of 16.40 ± 0.01 mW/cm^2. (b) shows the D_2 transition with a fixed pump intensity of 11.60 ± 0.02 mW/cm^2.

Transition	Peak pump intensity (mW/cm^2)	Peak probe intensity (mW/cm^2)	Temperature (°C)
D_1	17.5 ± 0.5	31 ± 1	104 ± 3
D_2	13 ± 1	7 ± 1	96 ± 2

Table 3.1: Optimal pump and probe intensity for both D_1 and D_2 transition of ^{39}K at individual peak cell temperature.

(FWM) process increases at higher intensities. Then if we increase the probe intensity, the collision rate becomes more significant and less FWM process and end up with smaller amplitude and slope. Still, when we increase the probe intensity with constant pump intensity, we observe that after the peak position of amplitude and the slope does not change that much. Also, the pump and probe intensity will start the broadening of transition linewidth, which plays a crucial role in the MTS spectrum, i.e. the MTS amplitude and the slope decreases with increasing intensity. We quantified the optimal temperature, pump and probe intensities in table 3.1 for both transitions.

3.8 Different polarization combination

In this section, we investigate theoretically and experimentally the polarization dependency of the MTS spectrum. We examine four separate combinations of pump and probe beam such as linear polarization define as $lin \parallel lin$, $lin \perp lin$ and circular polarization define as $L^+ - L^+(L^- - L^-)$, $L^+ - L^-(L^- - L^+)$, which can be obtained by rotating $\lambda/2$ or $\lambda/4$ wave-plates on each ends of the thermal cell as shown in figure 3.5. For the modeling and for the experiments we used carrier, each sideband, and probe intensities of 11.8 mW/cm^2, 2.5 mW/cm^2 and 57 mW/cm^2 respectively, the thermal cell temperature was 99 degrees, beam diameter was 2 mm and the EOM modulated frequency was 6.08 MHz. In our experiment, $lin \parallel lin$ and $lin \perp lin$ combination can be achieved by excluding the quarter-wave plates from each side of the vapour cell by arranging proper angles of the half wave-plates to make the $lin \parallel lin$ and $lin \perp lin$ polarization configurations.

Then we re-inserted the $\lambda/4$ wave plates and removed the $\lambda/2$ wave plates. The quarter wave-plates are then rotated to provide the correct polarization configuration for $L^+ - L^+/(L^- - L^-)$ and $L^+ - L^-/(L^- - L^+)$. The results for the different configurations for both the D$_1$ and D$_2$ transitions are shown in the figure 3.15 and 3.16 respectively, which is also comparable with our theoretical study. There is a significant role of the carrier, sidebands and the probe frequencies as indicated [99, 102, 108].

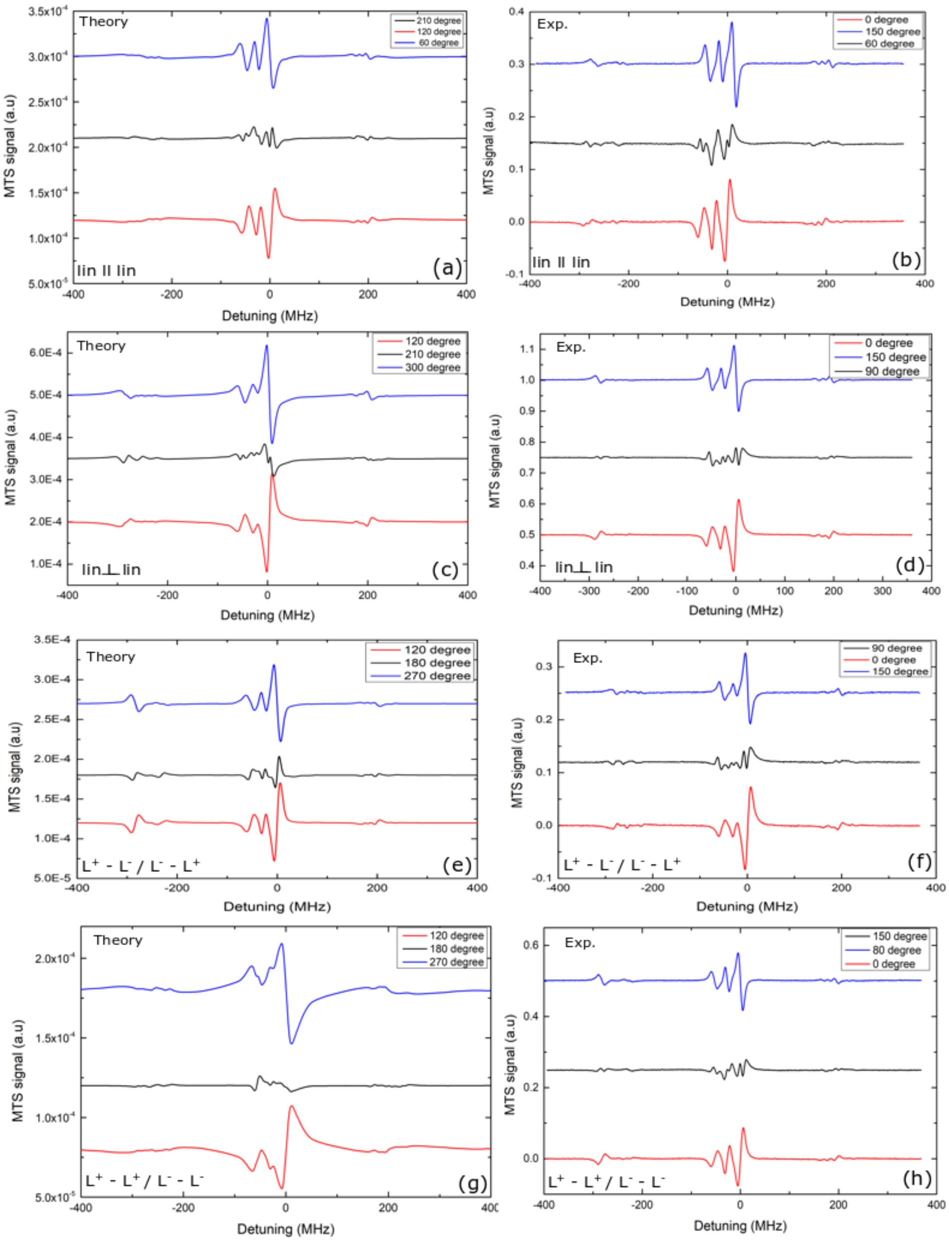

Figure 3.15: Comparison of theory and experiment for the MTS spectrum on the D1 line of ^{39}K. Different polarization configurations of the MTS spectrum, for theory and the experiments presented in (a) and (b) for $lin \perp lin$, (c) and (d) for $lin \parallel lin$, (e) and (f) for $L^{+} - L^{-}(L^{-} - L^{+})$ and finally (g) and (h) for $L^{+} - L^{+}(L^{-} - L^{-})$ respectively. In each plot relative phase are indicated by three different colours. All the fitting parameters we already discussed earlier. The simulations done by Dr. Heung-Ryoul Noh, Chonnam National University based on data and parameters suggested by the author and the data from Mr. Andrew Innes, Durham University under instruction by the author.

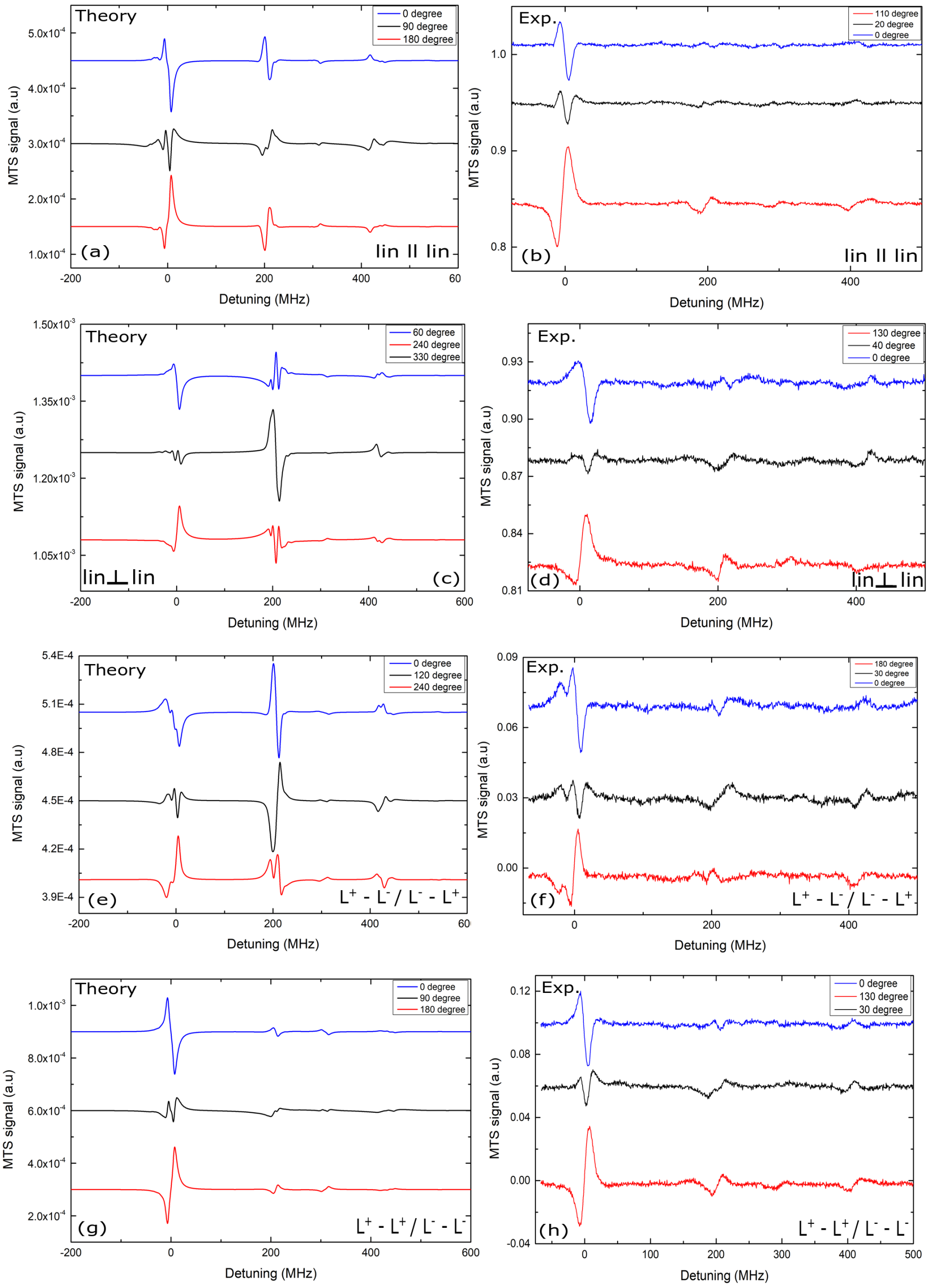

Figure 3.16: Comparison between theoretical study and our experiment for D_2 transition. Different polarization configurations of the MTS spectrum, for theory and the experiments presented in (a) and (b) for $lin \perp lin$, (c) and (d) for $lin \parallel lin$, (e) and (f) for $L^+ - L^-(L^- - L^+)$ and finally (g) and (h) for $L^+ - L^+(L^- - L^-)$ respectively from D_1 line. In each plot relative phases indicated by three different color. The simulations done by Dr. Heung-Ryoul Noh, Chonnam National University based on data and parameters suggested by the author and the data from Mr. Andrew Innes, Durham University under instruction by the author.

In the MTS spectrum shown in figure 3.15 and 3.16 both transitions depend on polarization configurations. The MTS spectrum for different polarization configurations is created by a coherent four-wave-mixing process as indicated by [99, 102, 103]. As explained in [99, 102] a long interaction leads to small amplitude and slope for crossover transition due to leakage of the population to the other states than unique ground states. In cycling transition, the big spectrum (in terms of amplitude) depends positively on the atom-light interaction time, i.e. higher signal for higher interaction time.

In every plot, the phase angle indicates our phase is really a relative phase, for example zero phase in theory might not be zero for the experiments. We choose the theory and the experimental spectrum by relating closely to each other. We found in figure 3.15, we found a good consistency within the theory and experimental results for D_2 transition in figure 3.16. Final version of the experimental polarization data taken by another PhD student in the group, Andrew Innes.

In the case of parallel polarization arrangement, both beams are linearly polarized in the same way. In this case, the dipole inter-plays among the m_F states with $\Delta m_F = 0$ permitted (only for $\vec{E}$ parallel to $\vec{B}$) where Δm_F is the difference in the magnetic sub-levels in the excited and ground states. At the same time, the direction of the E-field (associated B-field along the direction) is accepted as a quantization axis. In the case of the perpendicular polarization configuration, the probe light excites the atoms, which are in $\Delta m_F = 1$ state. On the other hand, the carrier and sideband beam excite the atoms, which are in $\Delta m_F = 0$ states.

In figure 3.15 for the D_1 line, we can see the amplitude and slope of crossover peaks $F = [1 \leftrightarrow 2] \rightarrow F^{'} = 2$ transition has maximum compared to other transitions and crossovers. In the four polarization configurations, *lin* $\parallel$ *lin* configuration is smaller than *lin* $\perp$ *lin* configuration. While in case of the $L^+ - L^-(L^- - L^+)$ polarization configuration is lower than the $L^+ - L^+(L^- - L^-)$ configuration.

Similarly in figure 3.16 the D_2 line, the maximum amplitude and slope observed in the resonance peak $F = 2 \rightarrow F = 3$, compared to other transition and crossover peaks. In four polarization combinations *lin* $\parallel$ *lin* configuration is bigger than $lin \perp lin$ configuration, which opposite in D$_1$ transition. While in case of $L^+ - L^-$ $(L^- - L^+)$ polarization configuration is lower than $L^+ - L^+$ $(L^- - L^-)$ configuration, which is similar to D$_1$ transition.

When our pump laser is tuned to F$_g$ = 2 → F$_e$ = 1, on the magnetic sublevels (i.e m$_F$ states) $|F_g = 2, m_F = 0, \pm1\rangle \rightarrow |F_e = 1, m_F = 0, \pm1\rangle$ and spontaneously collapse to $|F_g = 1, m_F = 0, \pm1\rangle$. Similarly, for lin||lin arrangement, the transition $|F_g = 1, m_F = 0\rangle \rightarrow |F_e = 1, m_F = 0\rangle$ is not allowed and $|F_g = 1, m_F = 0\rangle$ doesn't engage in the modulation transfer spectroscopic method. But for lin⊥lin configuration, each the magnetic sublevels for F$_g$ = 1 contribute to the MTS spectrum. Therefore, we can expect the crossover amplitude in the lin⊥lin arrangement is greater than the lin||lin polarization arrangement, which is agreed with our experimental results. If we tune the pump light to regulate F$_g$ = 1 → F$_e$ = 1. Then the crossover spectrum's amplitude in the lin||lin greater than lin⊥lin polarization arrangement.

In case of circular polarization configuration, the pump beam polarization with $L^-(L^+)$ all the atoms populates in $|F_g = 2, m_F = -2\rangle$ $(|F_g = 2, m_F = 2\rangle)$, if the probe beam tuned with $L^-(L^+)$, then the atoms will transfer $|F_g = 2,\ m_F = -2\rangle \rightarrow |F_e = 1,\ m_F = -1\rangle$ or $|F_g = 2\ ,\ m_F = 2\rangle \rightarrow |F_e = 1,\ m_F = 1\rangle$, which is almost closed transition and provide a big MTS spectrum. Similarly, if the probe beam polarization is $L^+(L^-)$ then the transitions involve for the MTS spectrum is $|F_g = 2,\ m_F = -2\rangle \rightarrow |F_e = 1,\ m_F = 1\rangle$ or $|F_g = 2,\ m_F = 2\rangle \rightarrow |F_e = 1,\ m_F = -1\rangle$ which is not a closed transition and we get smaller MTS spectrum with is greatly agreed with our experimental results.

In the case of D$_2$ line, the F = 2 → F$^{'}$ = 3 transition generates maximum amplitude and slope of the MTS spectrum, compared to other transition and crossover peaks. We have noticed the same kind of behavior while playing with the polarization. We have detected the maximum amplitude and slope of the MTS spectrum in $L^+ - L^+(L^- - L^-)$ polarization configuration. But we observed the amplitude and slope for F = [1 ↔ 2] → F$^{'}$ = 1 crossover in D$_1$ line much higher than F = 2 → F$^{'}$ = 3 in D$_2$ transition.

The four-wave mixing mechanism can interpret the MTS spectrum for the cycling transition. The atom population determines the amplitude and transition probability, which is known as branching ratios [113]. We can reveal that the FWM process is different in different polarization configurations, because different magnetic sublevels of the atoms are involved.

3.9 Summary

In the section 3.5 we optimize the temperature dependency with saturation absorption spectroscopy for both D_1 and D_2 transition, we found the optimal temperature for both transitions is different; for D_1 transition, the peak temperature is 96 ± 2 °C, and for D_2 transition its 104 ± 3 °C. In section 3.6 we optimize the temperature dependency of the MTS spectrum and optimize the pump and probe intensity as well. For D_1 transition the optimum pump and probe intensity are 17.5 ± 0.5 mW/cm^2 and 31.5 ± 1 mW/cm^2 respectively. For D_2 the optimum pump and probe intensities are 13 ± 1 mW/cm^2 and 7 ± 1 mW/cm^2 respectively. Next we studied the polarization effect on the MTS spectrum and we found that $L^+ - L^+$ or $L^- - L^-$ is the most favorable polarization for both transitions. Our main interest is to lock the laser, so if we locked our laser at the zero crossing of $\mathrm{F} = [1 \leftrightarrow 2] \rightarrow \mathrm{F}' = 2$ (D_1) transition, and we measure the maximum voltage fluctuation relative to the zero-crossing of the MTS spectrum measured was $\triangle \mathrm{V} = 135$ mV and in terms of frequency its 117.4(1) kHz. Similarly, for D_2 transition, after locking at zero points of the MTS spectrum, we measured the maximum voltage fluctuation $\triangle \mathrm{V} = 65$ mV, which in terms of laser frequency was 185.7(1) kHz. After locking, the fluctuation linewidth is confirmed to be much less than the natural linewidth for a larger time. For the 100% confirmation, we found ^{39}K MOT in our chamber as discussed in the next chapters.

Chapter 4

Cold-Atom Source: Experimental Equipments and Setup

For any experiment, it's crucial to understand the experimental apparatus. The optical setup thoroughly describe in this chapter, which was developed as part of previous work in Durham [76, 114–116] and used to take all the measurements that will be given in detail in Chapters 5. The methods that are highlighted in this chapter are follows,

- We explain why cold atom source is necessary for any cold atom experiments.
- A summary of cold atom sources used by different cold atom lab around the world.
- The latest optical structure, which includes utilizing acousto-optic modulators (AOMs), other optical and electronic devices for precise control of frequency and intensity of the laser light.
- Optical alignment and optimization of cooling, repump and spectroscopic AOMs .
- To increase laser beam power, we nicely aligned a tapered amplifier, which involves two optical fibres.
- Integration of vacuum chamber along with the pumping and bake-out pro-

cess.

- Optical alignment of pyramid MOT beam to increase and collimate the laser beam size.

- Magnetic quadrupole coil characterization in order to achieve the MOT.

- Magnetic shim coil assembly in order to achieve the MOT at a suitable position.

- Integration of K and Cs dispenser and detection technique of MOT fluorescence.

4.1 Important of a cold atom source

A cold-atom source is a demanding part of designs using the two-chamber system for cold-atom experiments. This chapter describes the necessary requirements for a cold-atom source. Before discussing the different principles and designs of cold atomic sources, it is critical to set out the essential requirements of a cold-atom source to load an MOT efficiently,

1. Dense flux of low-velocity atoms

A high-density atomic flux is a critical feature for loading a succeeding atomic MOT because a cold atomic source helps a higher loading rate, which allows increases in the repetition rate, signal-to-noise ratio, duty cycle, trap lifetime.

2. Low background collisions

The thermal background collision of the high-velocity atoms with cold atoms limits the number and lifetime of the atoms. Cold atoms experiments are very susceptible to high thermal background collisions, particularly like quantum gases experiments.

3. Efficient use of laser beam power

Compact homemade laser systems have restricted usable optical beam power that should be utilized as efficiently as possible, unlike experiments where optical beam power is usually not an issue.

4. Minimum deviation of the atomic source

A minimum deviation beam provides loading of an MOT to occur far from the source, which may require the vacuum system or a design feature to reduce the influence of stray magnetic fields and thermal background collision from the source of the atom.

5. Compact and Robust

The absolute size of the device is significantly crucial for many experiments; therefore, the compact size of the device is also the efficient use of space. The cold-atom source designed in this thesis is focused on generating a high flux with minimum cost and optimal use of the lab space.

The atomic source should be resistant to mechanical vibrations, variations in the local magnetic field, and optical misalignment so that it is suitable for work in real-world situations.

The MOT also depends on aperture size, the transverse velocity of the atoms, collisions with background thermal atoms will transfer kinetic energy to the cooled atoms and push them from the dense flux of low-velocity atoms flux.

4.2 Different cold atomic Source Configurations

The cold atomic MOT sources can be broadly classified first by the arrangement of optical and magnetic fields. And secondly, the geometries are used to create the optical fields. There are three separate configurations, which are 2D, $2D^+$, and 3D MOT sources.

A two-dimensional quadrupole B-field can produce a 2D-MOT source with the help of a transverse cooling scheme. The B-field is zero onward the field's axis. After cooling, the atoms are guided towards the zero-field area. Along the zero-field axis, the atoms are propagating with their initial velocity. For the 2D-MOT source, no light force is present along the axial direction. Therefore, in this case, people are pushing the atoms in the axial axis using a narrow push beam, which changes some velocity distribution of the atomic flux [117].

Source Type	Institution	Year	Species	Flux (atoms/s)	Cooling Int. (I_{sat})	Detuning ($\Gamma/2\pi$)	B-Field Grad. (G/cm)	Aperture Size (mm)	Ref.
Zeeman Slower	Harvard	2005	^{87}Rb	3.2×10^{12}	–	–	–	3	[118]
		2005	^{87}Rb	1.7×10^{12}	–	–	–	3	[118]
	Nottingham	2014	^{133}Cs	1×10^{8}	–	–	–	–	[119]
		2014	^{6}Li	7×10^{7}	–	–	–	–	[119]
Pure 2D-MOT	FOM, Amsterdam	1998	^{87}Rb	6×10^{9}	1.8	-1.7	17.7	0.8	[120]
	Stuttgart	2002	^{87}Rb	6×10^{10}	6.7	-1.9	17	6	[121]
	NPL, London	2005	^{87}Rb	2×10^{8}	1.5	-3	6	2	[122]
	JPL, Pasadena	2006	^{133}Cs	1.5×10^{10}	1.7	-1.4	14	4	[123]
2D-MOT	LKB, Paris	2002	^{87}Rb	1×10^{9}	2.5	-3	10	–	[124]
	JPL, Pasadena	2012	^{133}Cs	8×10^{9}	2.1	-1.4	15	4	[125]
	KRISS, Daejeon	2012	^{87}Rb	4.5×10^{10}	–	-2	14	4	[126]
	USTC, Shanghai	2017	^{88}Sr	1×10^{9}	1.0	-1.5	–	2	[117]
2D^{+}-MOT	FOM, Amsterdam	1998	^{87}Rb	9×10^{9}	1.8	-3	12.6	0.8	[120]
	Strathclyde	2000	^{85}Rb	7.3×10^{8}	3.0	–	–	–	[127]
	Harvard	2003	^{87}Rb	8×10^{9}	6.5	-5	21.5	1.25	[128]
	NPL, London	2005	^{87}Rb	8×10^{9}	1.5	-3	6	2	[122]
	TIFR, Mumbai	2006	^{85}Rb	1.9×10^{10}	–	-2	15	2	[129]
		2006	^{87}Rb	2×10^{10}	–	-2	15	2	[129]
3D-MOT	CNRS, Paris	1997	^{133}Cs	1×10^{6}	–	–	–	–	[130]
	INFN, Napoli	2001	^{87}Rb	7×10^{7}	3.0	-2.5	15	–	[131]
	LKB, Paris	2001	^{87}Rb	1.3×10^{8}	–	-3	15	5	[132]
LVIS	JILA, Boulder	1996	^{87}Rb	5×10^{9}	7.9	-5	5	1	[133]
	FOM, Amsterdam	1998	^{87}Rb	3.2×10^{8}	4.1	-3.3	13.6	0.8	[120]
	NIST, Boulder	2005	^{133}Cs	1×10^{10}	9.1	-1.7	7	0.5	[134]
	NPL, London	2005	^{87}Rb	8×10^{9}	1.5	-3	8	2	[122]
Pyramid MOT	Oxford	1998	^{133}Cs	1.1×10^{9}	5.4	-2	10	1 × 2	[135]
	Wisconsin	1998	^{39}K	5.3×10^{3}	7.1	-7	4	2	[136]
		1998	^{40}K	3×10^{-1}	7.1	-7	4	2	[136]
	Pisa	2001	^{133}Cs	4×10^{9}	9.1	-2.7	12	1 × 2	[137]
	JPL, Pasadena	2003	^{133}Cs	2.2×10^{9}	2.7	-2.1	–	1	[138]
		2004	^{87}Rb	1×10^{8}	0.7	-2.3	–	1	[139]
		2004	^{87}Rb	1×10^{8}	0.9	-2.1	–	1	[139]
	Durham	2008	^{87}Rb	1.8×10^{7}	2.4	-2.8	10.1	2.4 × 3	[140]
		2008	^{133}Cs	1.3×10^{7}	3.6	-2.8	10.1	2.4 × 3	[140]
Grating MOT	AFRL, New Mexico	2017	^{87}Rb	4×10^{8}	6.5	–	20	1	[141]

Table 4.1: A literature review of cold atom sources, classified by source type, also include the source characteristics and some critical parameters.

Now for the 2D$^+$-MOT source, an additional cooling beam is used compared to the 2D-MOT source configuration. But the transverse MOT beams still cool and push atoms towards the beam axis where B-field is zero; however, the longitudinal cooling provides an enormously narrower atomic velocity distribution.

The atomic flux is directed towards an axial intensity imbalance [142]. On the other hand, the 3D-MOT source, produced by a three-dimensional quadrupole magnetic field, generates a single zero B-field point and cooling and trapping in all three directions. Furthermore, the 3D-MOT source configuration is the standard MOTs employed for trapping atoms. To generate an atomic flux, one can achieve by two processes: by adding an additional push beam through the MOT or creating a 'hole' in one of the existing beams to create an intensity imbalance as in 2D$^+$-MOT, which is commonly called a low-velocity intense source (LVIS)[133]. One summary of the cold atom source is presented in table 4.1.

4.3 Cold atomic source designs

Producing many beams for both cold atomic sources and MOT includes much complexity and size to the apparatus. In an earlier chapter, we discuss that the primary MOT employed three retro-reflected independent laser beams to create the usual arrangement of three orthogonal sets of laser lights, which demands diverse optical components to individually control every beam's polarization, intensity, and direction. Therefore, the pyramid MOT source makes our life a little bit simpler because, in the case of pyramid MOT, we need only one single beam to control.

4.3.1 The Pyramid MOT (P-MOT)

The P-MOT gives us a steady and unique way to produce an ultracold atomic reservoir. It has been utilized efficiently during both single and dual-species [139, 143] investigations in the lab. As discussed before, like in a three dimensional MOT, the pyramidal MOT must also generate the same radiation field as in a six beam MOT. A pyramidal MOT only requires an individual light to create the ideal arrangement of beam polarization as a conventional three counter-propagating beam MOT. The original pyramidal MOT consisted of a big beam of LH circular or RH circular polarized light incident on a conical hollow mirror [144]. There was a tiny hole in the vertex to confine atoms and enable the transfer of atoms into the experimental MOT, or in the Science chamber [143]. The first reflection on the mirror creates a set of counter-propagating lights with inverse polarization configuration. And the 2nd reflection then generate an RH circular or LH circular polarized retro-reflected beam, and this happens in all three dimensions creating the required polarization configuration to create MOT. Figure 4.1 illustrates the setup of a pyramidal MOT.

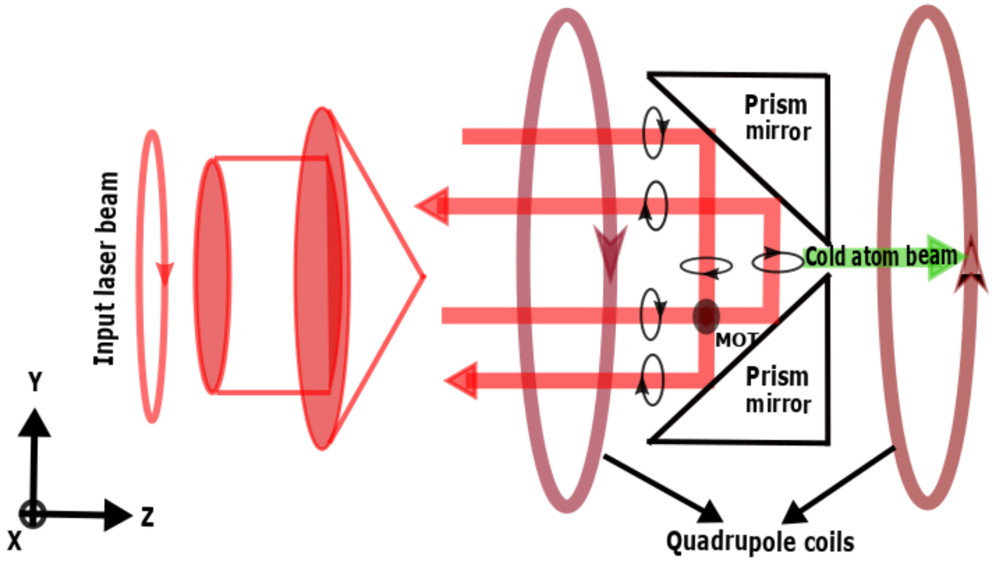

Figure 4.1: Cross-slice of unique pyramidal MOT chamber including the resulting polarization configuration.

4.4 Experimental Apparatus

The laboratory equipment consists of a dual-species MOT scheme with a giant magnetic ion pump. The alkali dispensers are the reservoir of atoms for a dual-species cold P-MOT. In this chapter we extensively discuss apparatus for pyramid MOT. The optical setup of our experiment present in fig. 4.2.

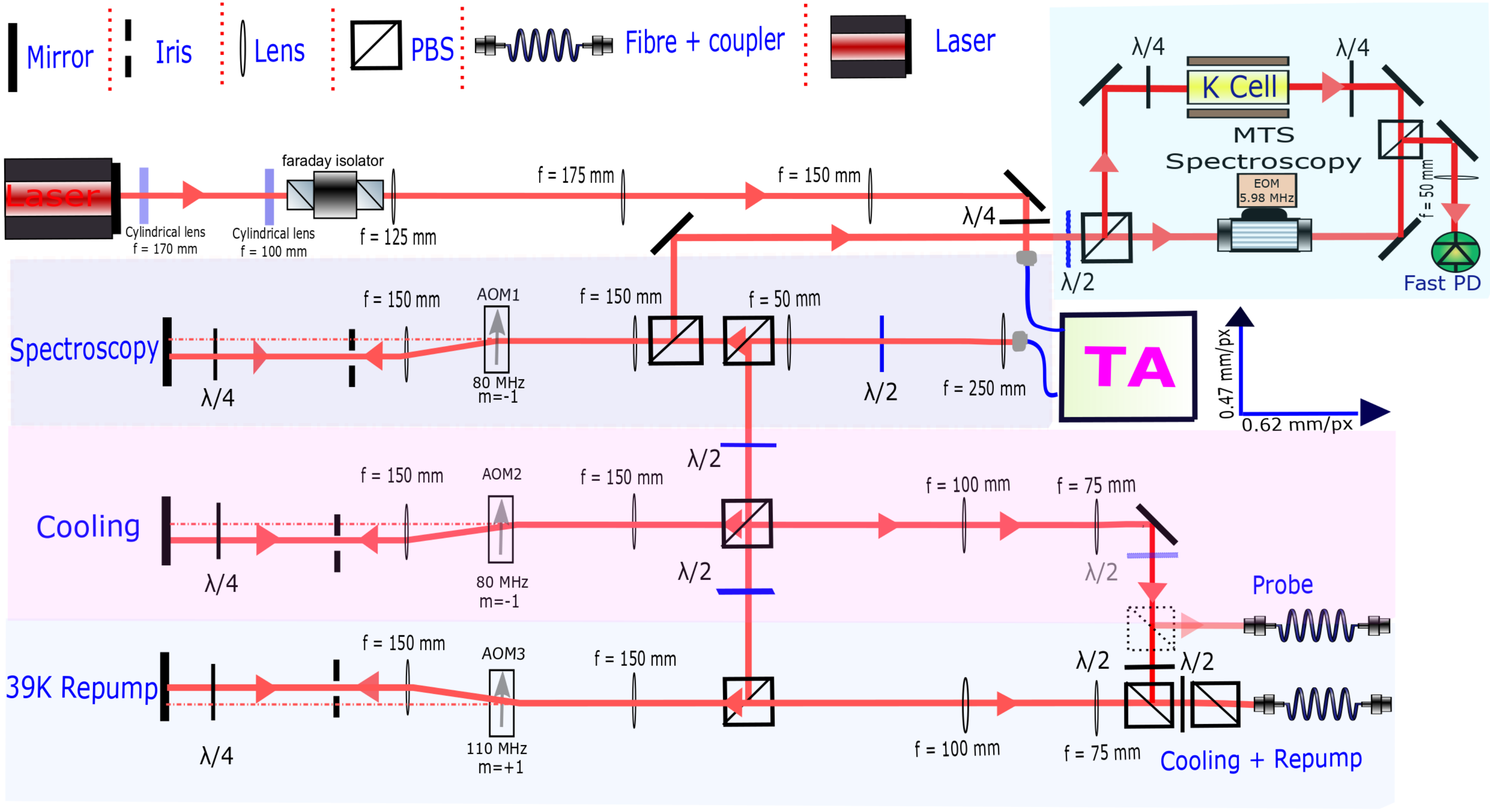

Figure 4.2: Optical diagram of the laser table. The different transition from the ground states to excited states are indicated by different colour for ^{39}K isotope. Polarization maintaining optical fibres are used for TA input and output beam from optical table to the experiment table.

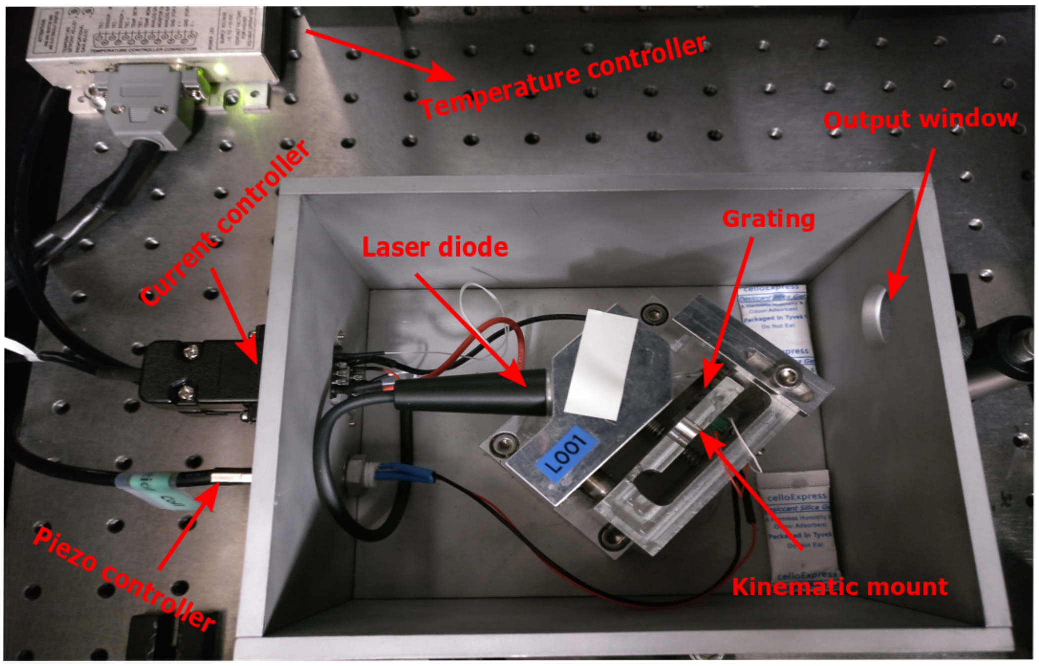

Figure 4.3: Photograph of the only homemade laser system for our experiment showing multiple internal elements.

4.4.1 Laser System

For every cold atom experiment requires a well isolated and stable laser system. In this section, we focused on home-build laser system for our P-MOT and its stability in details. For our experiment, we used one homemade external cavity diode laser (ECDL) in the Littrow configuration. The laser tuning process and the picture of our laser system presented in figure 4.3.

The laser operates around 766.7 nm wavelength, corresponding to the D_1 and D_2 line of ^{39}K isotope. Our laser is extremely stable, with narrow linewidth, and the frequency is very easily tunable to achieve MOT temperature. We used a anti-reflection GaAs semiconductor diode (Eagleyard,EYP-RWE-0790-04000-0750-SOT01-00001). The diffraction grating has been used to elongate the cavity, installed on an adjustable mirror mount. The adjustable two screws on the mirror mount are used to adjust the grating in horizontal and vertical axes. By rotating that horizontal screw, we can adjust the frequency. There is a piezoelectric transducer connecting the horizontal screw and the rear exterior of the moveable mount, which enables movement of the grating via using a potential over the piezo to investigate the laser frequency, and the vertical screw helps to adjust the 1st order response feedback to the laser diode, as shown in fig. 4.3. It needs to be set at the low value of the threshold current to achieve maximum feedback. The cavity is covered by a conducting metal shelter assembled on a plane Peltier cooler and a thermistor to measure and control the cavity's temperature. We maintained the cavity temperature around 18 ^{o}C. The Peltier and thermistor remain connected to a temperature controller to stabilise the specific cavity's temperature. A current controller (Thorlabs LDC205C) is employed to regulate the current supplied for the laser diode.

Typically our laser operates at about 178 mA laser current and produces 55 mW of output beam power. The beam generated from the diode is elliptical; therefore, we used two cylindrical lenses to fixed the ellipticity and astigmatism [145] of the beam, then the circular beam is transferred within an optical isolator (Laser 2000, I80T-4L) to bypass undesired back reflection to the diode, as in shown fig. 4.2 which shows our simplified schematic optical setup.

As indicated, the output beam from the diode is elliptical, i.e. not symmetric on both the x and y-axis. In order to make the beam profile round, we undertook the following steps,

• First, place a first cylindrical lens (L_1) of 170 mm focal length just in front of the laser and make sure the beam passes through the centre of the first cylindrical lens.

• Place the 2nd cylindrical lens (L_2) with 100 mm focal length. The separation between L_1 and L_2 is 70 mm i.e both lenses focus the beam at $\sim$ 170 mm from the lens L_1 as shown in fig. 4.4.

Here both cylindrical lenses need to be orthogonal to each other, both lenses focus the x and y-axis of the beam separately at 170 mm from the lens L_1. Now using another lens with 125 mm focal length, we can make the beam approximately collimated and symmetrical around the x and y-axis.

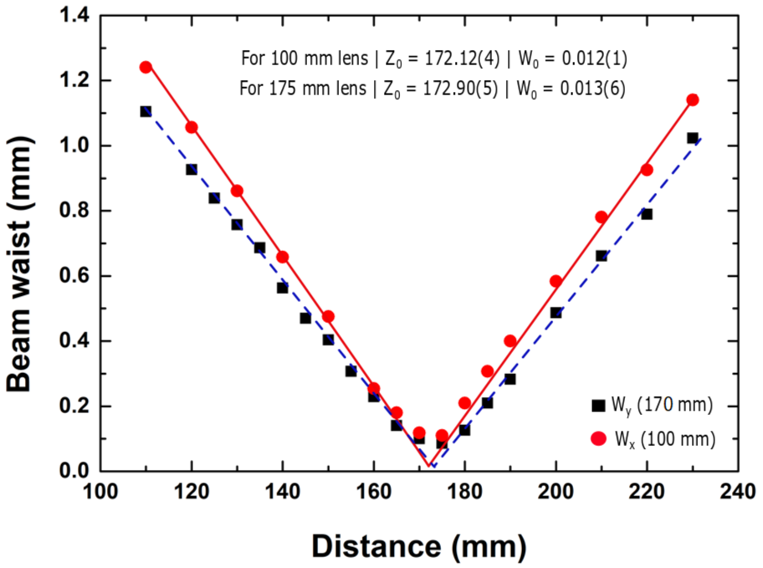

Figure 4.4: Characterization of the beam. The data points are fitted with beam profiling equations as discussed in [145, 146] to measure beam waist as a function of beam position for 100 and 170 mm cylindrical lens.

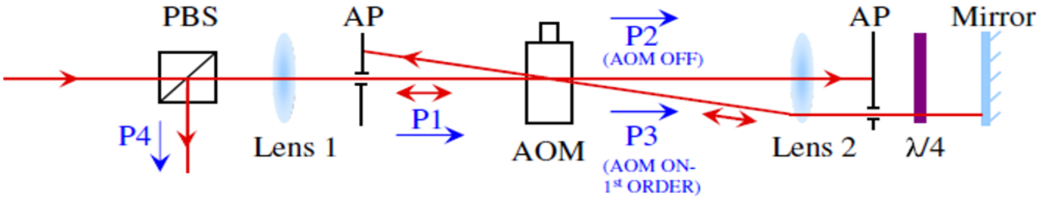

Figure 4.5: The pictorial layout of arrangement for double passed AOM device, the optical elements like AOM, PBS, AP (aperture), and $\lambda/4$ presented and P1, P2, P3, and P4 labels are beam powers at their respective locations. The figure is adapted from [147].

4.4.2 Optical alignment and optimization of AOMs

To control and modify the frequencies, intensities and direction of a laser beam, the acousto−optic modulators (AOMs) are very valuable devices. The device consists of a crystal with Bragg planes; the incoming laser beam diffracts off acoustic wavefronts and propagates within the crystal. The modulation of the incoming laser beam can be produced by modifying those acoustic waves' amplitude and frequency progressing within that crystal, so the acoustic waves change the refractive index of the crystal.

The radio frequency (RF) signal for the AOM regulated by the AOM driver

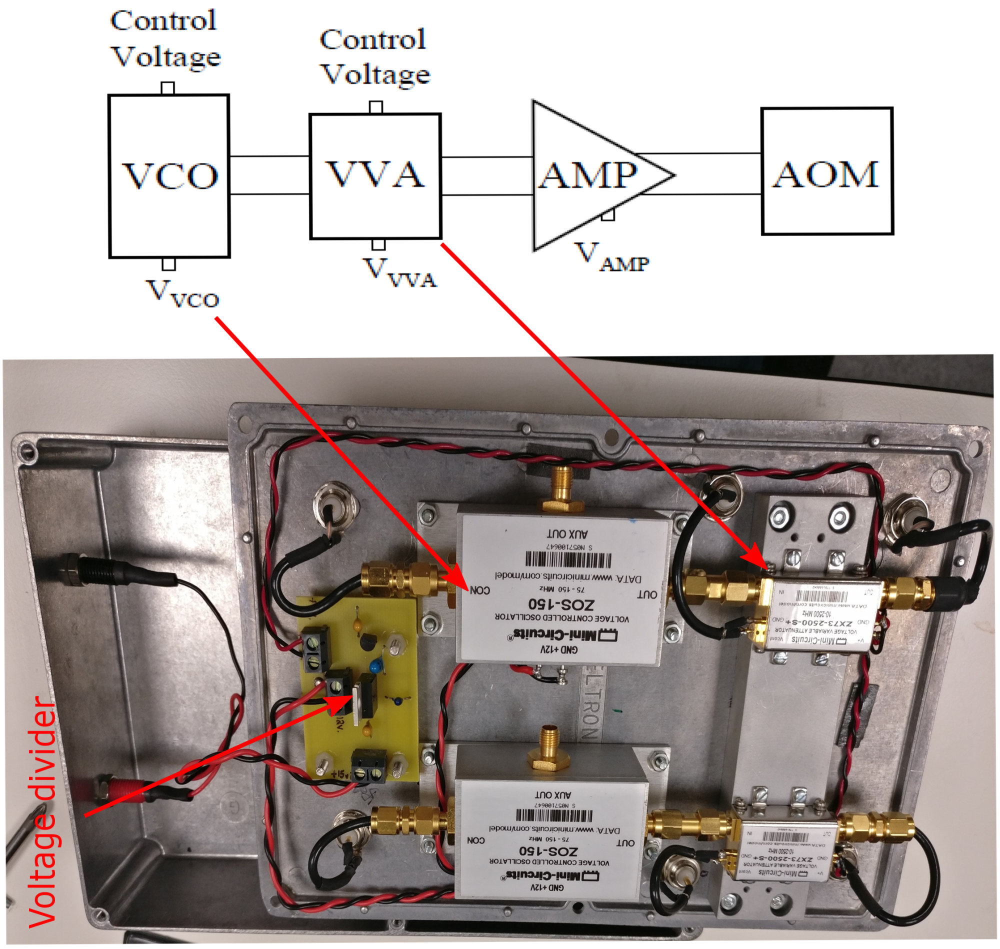

Figure 4.6: A photographic view of a simple AOM driver which is essential to drive the AOMs, the VCO, VVA, and amplifier is shown.

produced the acoustic wave. The driver is built up of three components as shown in the figure 4.6, which are Voltage Controlled Oscillator (VCO), Voltage Variable Attenuator (VVA) and an amplifier; the voltage divider divide 15 Volt into two-part for VCO (12 Volt) and VVA (3 Volt) and a simple amplifier circuit connected in between AOM and VVA, the details can be found in [147].

The AOM alignment is quite tricky as shown in figure 4.5. We align the AOMs as follows,

- First ensure the laser beam passes through a row of holes in the optical bench and after that place a PBS to make sure the beam still follows the same row of holes.

• Then place the first lens so that the laser beam crosses through the centre of the lens.

• Locate the focal point of the beam, which can be done using the knife-edge technique or Thorlabs CMOS CCD.

• Place the AOM at the focal point of lens 1, then turn on the AOM and align it for maximum first-order diffraction efficiency. Here we need to keep in mind that different AOMs have different active acoustic apertures. Typically the active aperture is of the order of 100−200 μm and for that we need a focal length of 150 to 250 mm lens. The active acoustic aperture (d), focal length F, wavelength λ and the radius of the input laser beam D following equation is,

$$d = \frac{1.27F\lambda}{D}. \tag{4.1}$$

• Then, after switching off the AOM and implant the 2nd lens at its focal point from the AOM. Simultaneously, checking the beam in the lens's central position by following the no beam spot difference regardless of the lens in place.

• Implant a $\lambda/4$ plate and a zero degree mirror after the 2nd lens, centre the quarter-wave plate on the zeroth-order beam.

• After the 1st lens, set an aperture at the point of the input beam to transmit only the zeroth-order beam.

• Here, the retro-reflected zeroth-order beam can be utilized as a guide.

• Using a power meter after the PBS (P4) and maximizing the power by fine-tuning the mirror and rotating the quarter-wave plate.

• Now, switch on the AOM and relocate the quarter-wave plate to dispatch the first-order diffracted beam. Place an aperture within the 2nd lens and the quarter-wave plate to transmit only the first-order light coming out.

• The position of the 2nd lens needs to be optimized in such a way that the beam deflection least as the AOM frequency is varied, which can be achieved by watching at the double passed laser beam an identified distance downstream. Then mark the beam's deflection for the series of AOM frequencies;

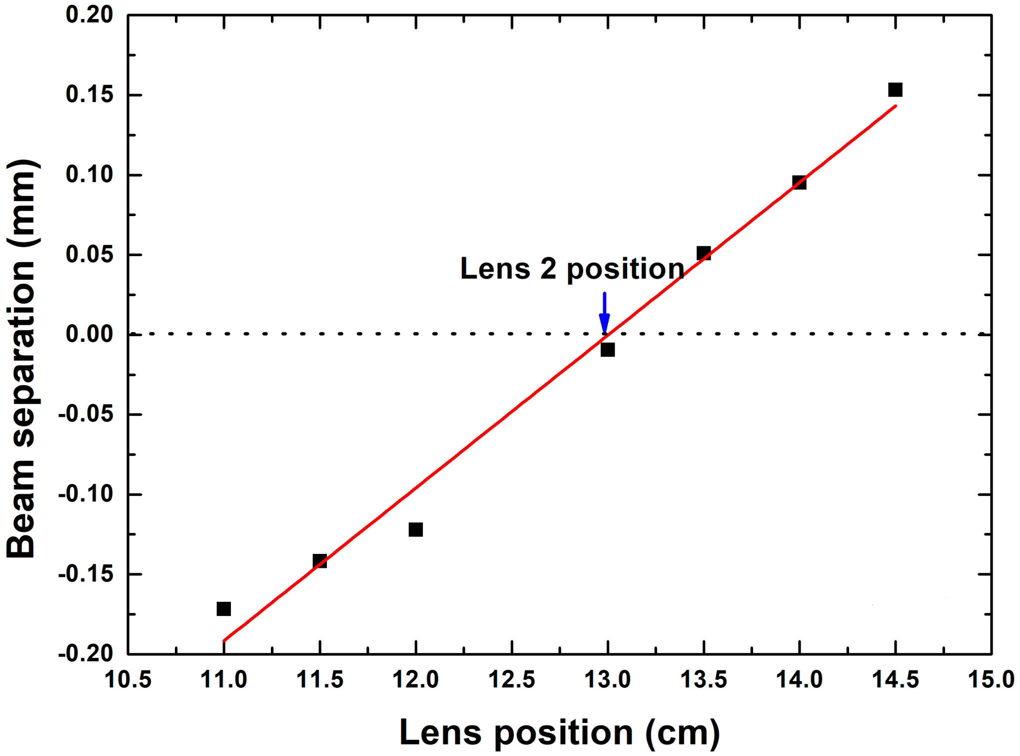

Figure 4.7: Alignment of lens 2 of double passed cooling AOM. After placing lens 2 at zero beam separation, that will make the beam position is independent of frequency, which is essential for our experiment. Here we present the optimal position of lens 2 for AOM2 i.e cooling AOM.

usually, we choose any two extensive ranges, like 110 MHz and 60 MHz, using a Thorlabs CCD to find the beam centre. The beam centre can be found after fitting the Gaussian function in Matlab. Then we plot the beam deflection (as a measured quantity) as a function of lens positions (as a set quantity). Therefore, we can find the optimal place for the 2nd lens from the plot to the point where the beam deflection (or separation) is minimum, as shown in figure 4.7.

• And finally, optimal adjustment for maximum double pass efficiency can be achieved using the retro-reflected mirror.

After aligning and optimising the AOMs, we achieve a double pass efficiency for the cooling, repump and spectroscopic AOMs of approximately 74%, 72% and 71% respectively.

For ^{39}K MOT it is very important for both beams to have the same polarization and one way to achieve same polarization for both cooling and repump beam by using a 'D' shape mirror just before adding two beam but in this way we loss fiber efficiency we only achieve 25% coupling efficiency in this process, and another way to use another cube just before adding two beam but in this process we lose 50% of cooling beam. Therefore, we choose 2nd method to add both beam.

4.5 Important optical frequencies

To control the cooling, repump and spectroscopic frequency, AOMs are normally used in cold atom physics. In case of potassium system, the laser frequencies for the experiment i.e the right AOM frequencies can be computed for cooling down the ^{39}K atoms using following two mathematical equations,

$$\Delta_C = 2 \times (f_{Aom2} - f_{Aom1}) \tag{4.2}$$

and

$$\Delta_R = 440.6 - 2 \times (f_{Aom1} + f_{Aom3}), \tag{4.3}$$

where Δ_C and Δ_R are the cooling and repumping detuning respectively and f$_{Aom1}$, f$_{Aom2}$ and f$_{Aom3}$ are the actual operating AOM frequencies.

The hyperfine splitting of D_2 transitions and our experiment's specific laser frequencies are presented in table 4.2. The detailed pictorial understanding with experimental sub-Doppler spectrum can be found in Fig. 4.8, the frequencies with detuning can be selected from the above mentioned equation. Precise knowledge and control of required detunings are produced by three AOMs for ^{39}K isotopes in our experiment.

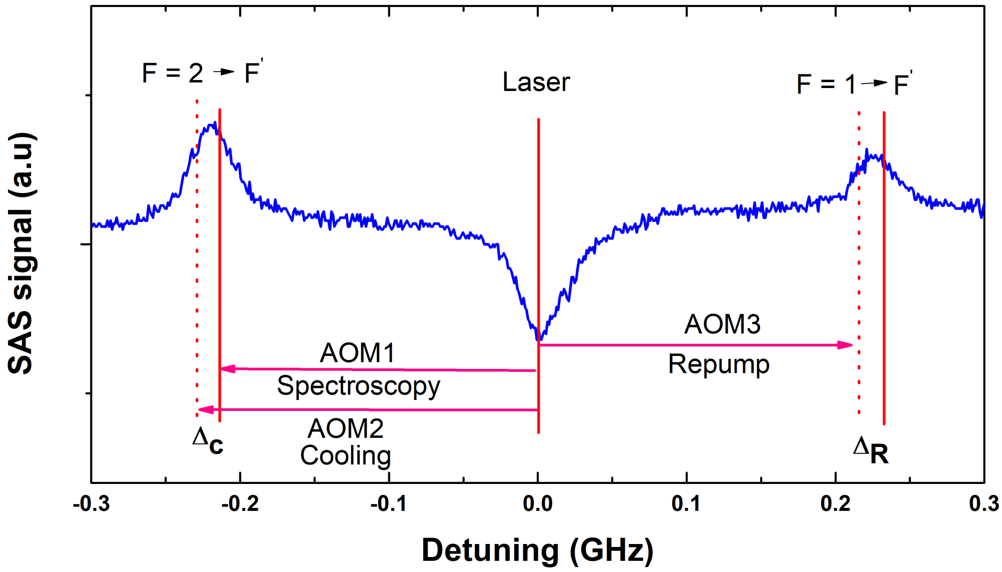

Figure 4.8: Doppler-free SAS spectrum on the D_2 transition of ^{39}K, including the estimated frequency of the different lights required for atom cooling, repumping and spectroscopy. The hyperfine splitting within $F = 1 \rightarrow F^{'} = 0,1,2$ and $F = 2 \rightarrow F^{'} = 1,2,3$ corresponding to 461.7 MHz (ground state splitting). The central dip of the signal indicates the crossover in mid-ground and excited states.

	Transition	AOM frequency	Detuning (MHz)
Optical cooling	$F = 2 \rightarrow F^{'} = 3$	88.75 MHz	-22.5(5) MHz
Optical Repumping	$F = 1 \rightarrow F^{'} = 2$	134.58 MHz	-16.6(3) MHz
Spectroscopy	$F = 2 \rightarrow F^{'} = 3$	80 MHz	0.0(8)

Table 4.2: Laser frequencies are modulated for magneto-optical trapping in our experiment. The actual cooling, spectroscopy, optical pumping and repumping frequency along with detuning and their errors show measured values presented. The optical setup presented in figure 4.2.

4.6 Tapered Amplifier

The pyramid MOT requires a high intensity $\sim 10\mathrm{I}_{Sat}$ for cooling and repump each. For typical ^{39}K MOT beams required $35\mathrm{I}_{Sat}$ total retro-reflected beam intensity but our homemade ECDL can generate a limited intensity $\sim 3.5\mathrm{I}_{Sat}$, which is not sufficient to achieve the MOT. If we focus the beam we get a much higher intensity, but the pyramid MOT needs a large beam ($I = 2P/\pi\omega^2$, I intensity and P power of the laser beam). We used a home-build tapered amplifier to increase cooling and repump beam power without modifying their linewidth and stabilization to produce sufficient laser intensity. The increased output is utilized to create the expected MOT. The tapered amplifier chip is made from GaAs semiconductor shown in figure 4.9(a). The detail of the chip can be found in [148, 149],

The GaAs TA semiconductor chip is sensitive and fragile to unexpected seed power changes, injection current, temperature and mechanical collapses. Additionally, the producing beam power can significantly vary for slight variations in injection current, seed power, temperature and polarization of seed light; for a TA only horizontal polarized light is needed to make it work efficiently. We used Thorlabs LCD24C current controller, which provides a maximum current of 4 A with approximately 0.1% accuracy. On a typical working day, the TA chip worked at less than 1 A current and produced a sizeable amount of optical power $\sim$ 1 W. The significant power simultaneously creates lots of thermal energy, which must be cool down to prevent damage within a minute. A Peltier is laid down under the GaAs semiconductor TA chip frame by a copper base squeezed within those pair metallic surfaces to cool down rapidly. A thermistor (Thorlabs-TH010K) is placed in the chip structure to monitor the chip temperature. The temperature associated with the Peltier and thermistor can be controlled using a controller complement (Thorlabs, TEDE 200C). To increase the chip's life, TA needs to operate in low current and low seed power (like a minimum current $\sim$ 10 mW and a maximum $\sim$ 30 mW of seed power as specified in the user manual).

The optical setup of our homemade TA is shown in figure 4.10. The F220APC-780 fibre coupler is used for input light; then, the light goes through a Thorlabs optical isolator (IO-5-780-VLP) because of the back reflection rear surface of the chip into the lasers, which might affect the performance. Then using a telescope of 3 : 1 we reduced the beam size and made the beam size optimal for the injection beam and we made sure the injecting polarization is horizontal by using a polarizing cube just before injecting. The output beam is elliptical, and we make the beam circular by employing a cylindrical lens with a focal distance of 40 mm as in figure 4.9 (b) and 4.10. We use the output Faraday isolator with 85% efficiency (Thorlabs, IO-5-780-HP, isolation 38-44 dB) to block unwanted retro-reflected light be-

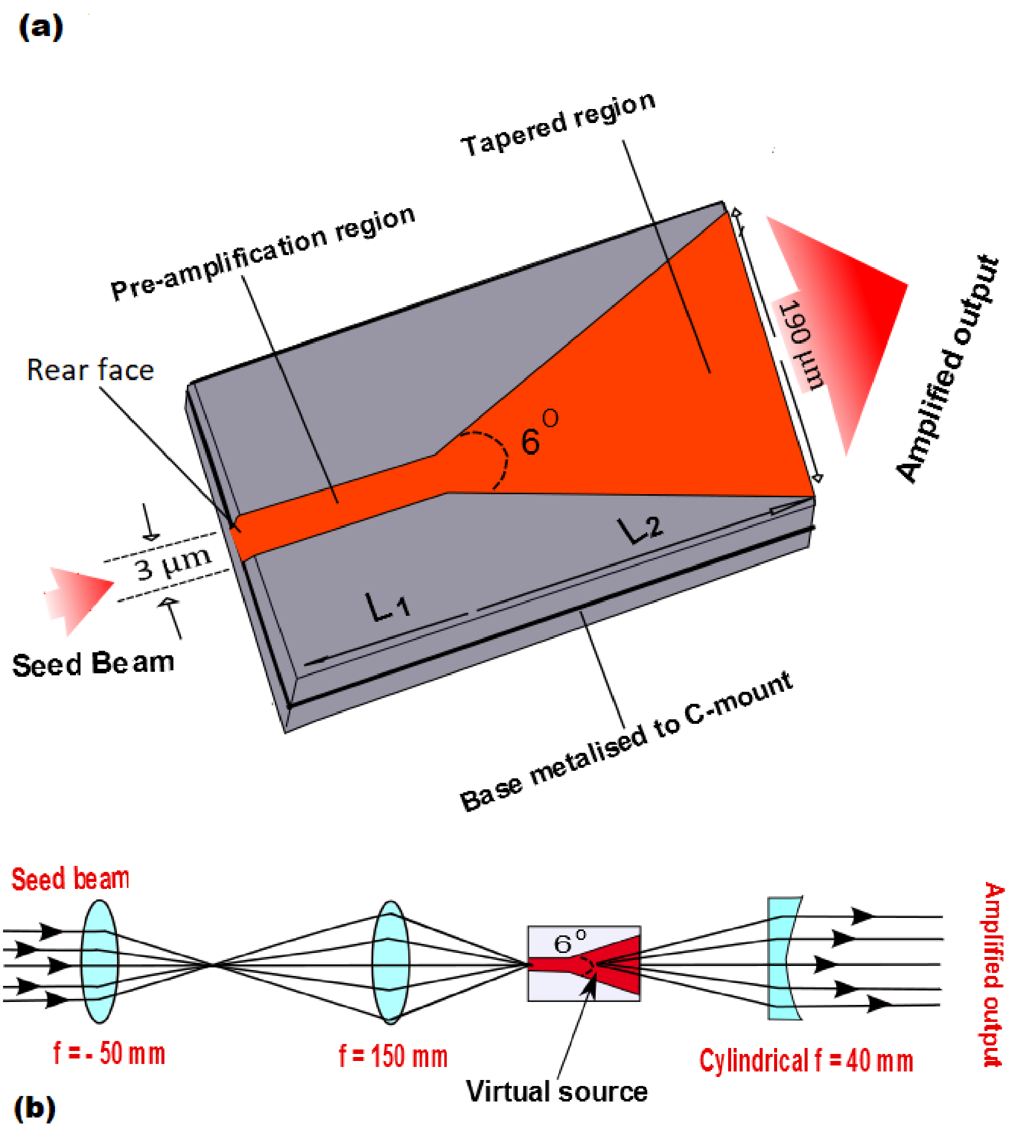

Figure 4.9: (a) A clear schematic representation of semiconductor-based GaAs chip called a tapered amplifier. In (a) the pre-amplifier and tapered regions' lengths in the chips are defined as L_1 and L_2. And the angle between the pre-amplifier and tapered area is $\theta = 6^0$ to satisfy the complete tapered zone with optical intensity arising from the pre-amplifier area. (b) The unique top representation of the trapping amplifier chip structure presents the XZ plane's output beam's virtual source. At the chip's rear surface, the seed beam is focused with a lens with a focal distance of -50 and 150 mm, respectively, and output end one cylindrical lens of 40 mm focal distance is employed to collimate the elliptical light.

cause the chip is very sensitive to the back reflection of the light, which may commence to permanent harm on the chip. Therefore, we utilise a telescope to adjust the size according to the output coupler (F220APC - 780) and the quarter-waveplate employed to maintain the output fibre's polarisation.

Light amplification is mainly controlled by the incoming seed beam power, seed coupling, and TA injection current. In the case of weaker seed power and inadequate coupling with higher injection power, reduce the lifetime of the TA chip. In fig. 4.11 (a) we show the change in output beam power as a function of seed power at a fixed current of 1.2 A. Output power rises approximately linearly with seed power (< 6), and then it seems to saturate after 8 mW seed power. Because of the limited power available from our ECDL, we only can measure up to 13 mW seed power. Figure 4.11 (b) represents the variation of producing power as a function of injection current at fixed seed power 13 mW. For our experiments, we are operating our TA at 13 mW seed power at 1.2 A of injection current, which produced ~ 300 mW of output power from polarization maintaining, single-mode output fibre.

4.7 Pyramid MOT chamber

Beams of slow atoms are helpful for many experiments, including ultracold molecules, atomic interferometry, atom optics, and precision measurement experiments. So, in general, the Pyramid MOT has two objectives; firstly to pre-cool and accumulate atoms from an atomic vapour reservoir and secondly, send the pre-cooled atomic cloud to the area of the science chamber for further experimental direction. The compact Pyramid MOT was first introduced by Jha and co−worker [143] with a well collimated single laser light reflected by mirrors in a corner cube configuration, then this Pyramid-shaped MOT was constructed in Oxford to produce a continuous and robust source of slow pre-cooled atoms [139, 150]. Details can be found in earlier discussion.

The Pyramid chamber consists of four separate mirrors; the mirrors are in the form of an inverted pyramid with a gap at the centre and a couple of coils in anti-Helmholtz configuration, which produces approximately 8.5 G/cm at the trap centre at 16 A quadrupole current. The mirror arrangement of the pyramid MOT chamber is shown in figure 4.12 (b). The mirrors are surrounded by three shim coils positioned in North−South (N-S), East−west

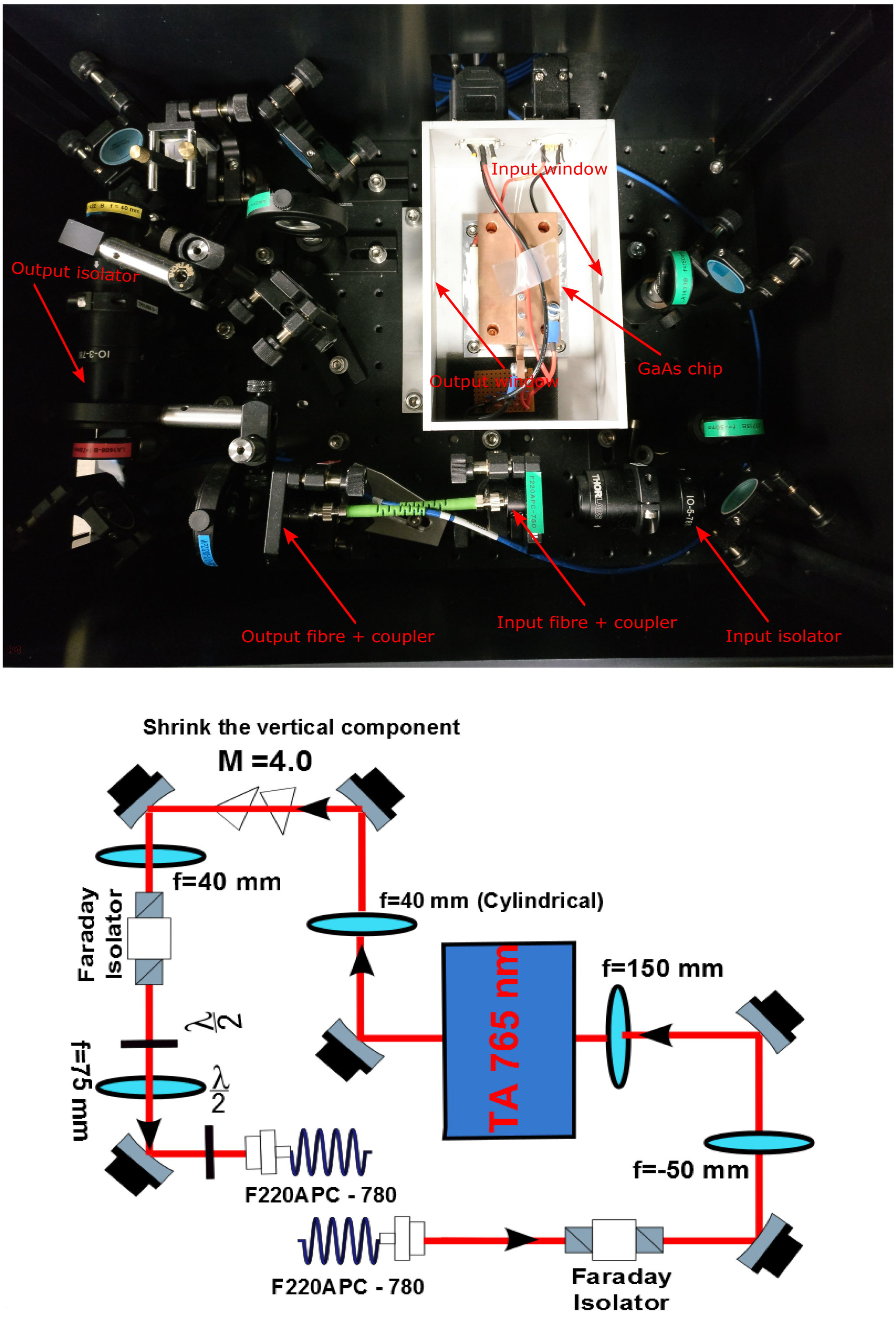

Figure 4.10: In the top, the photograph of tapered amplifier setup in the optical table for our experiments and in the bottom a simple schematic of the tapered amplifier optical setup.

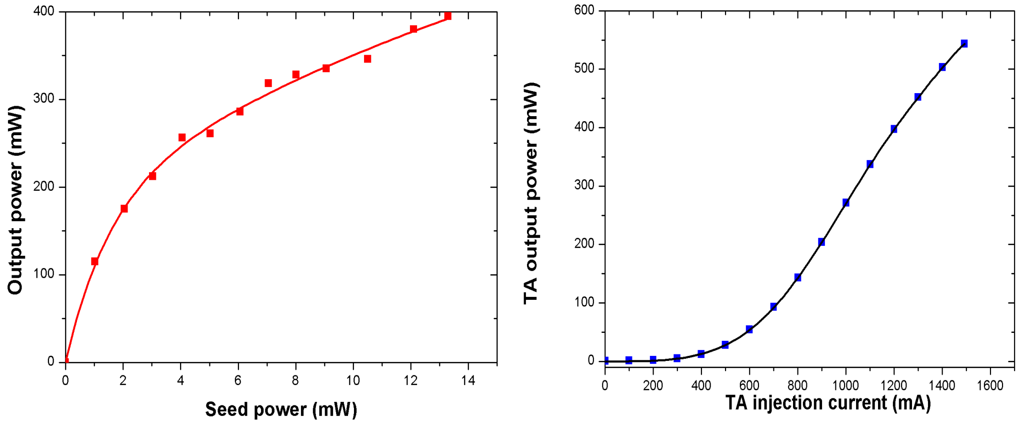

Figure 4.11: Tapered amplifier system's characterisation. In (a) variation of output beam power as a function of seed laser power in a steady injection current of 1.2 A. The data reveals a saturation in output power comes into the picture after six mW of input seed laser power. (b) Modification of the produced laser beam power as a function injection current at fixed seed power of 13 mW. All the errors in the data points are tiny and measured from the power meter's accuracy (Thorlabs PM100D) with 0.5% accuracy.

(E-W) and up-down directions. The Pyramidal MOT mirrors are installed within the vacuum chamber. Each reflecting surface of the pyramid serves as a mirror and is coated with a broadband dielectric in order to achieve the same reflectivity for both right-handed polarization and left-handed polarization of the beam. While a big incoming laser light is thrown around the centre of the pyramid, six counter-propagating lights are automatically generated, and the beam configuration and polarization are equivalent to a conventional six-beam MOT. Normally the operational parameters are optimized by fluorescence signals but in our case, the MOT fluorescence is small and had a large background reflection from the pyramid mirrors, therefore, we optimize our MOT empirically by seeing MOT present or not in the camera.

The dimension of pyramidal mirror inverted configuration with 60 mm × 60 mm square bottom, and 30 mm length. The optics do not meet at the pyramid top, giving a rectangular aperture of $\sim 2.4 \times 3.0$ mm, also mirror made up of two tetrahedral prism and two planer chisel prism mirrors respectively, kept in such a position that the mirrors can clip with the stainless steel as shown in fig. 4.12 (b). All three sets of counter-propagating beams with opposite polarization of the laser beam create an MOT inside our vacuum chamber discussed and presented in fig.4.1 with great details.

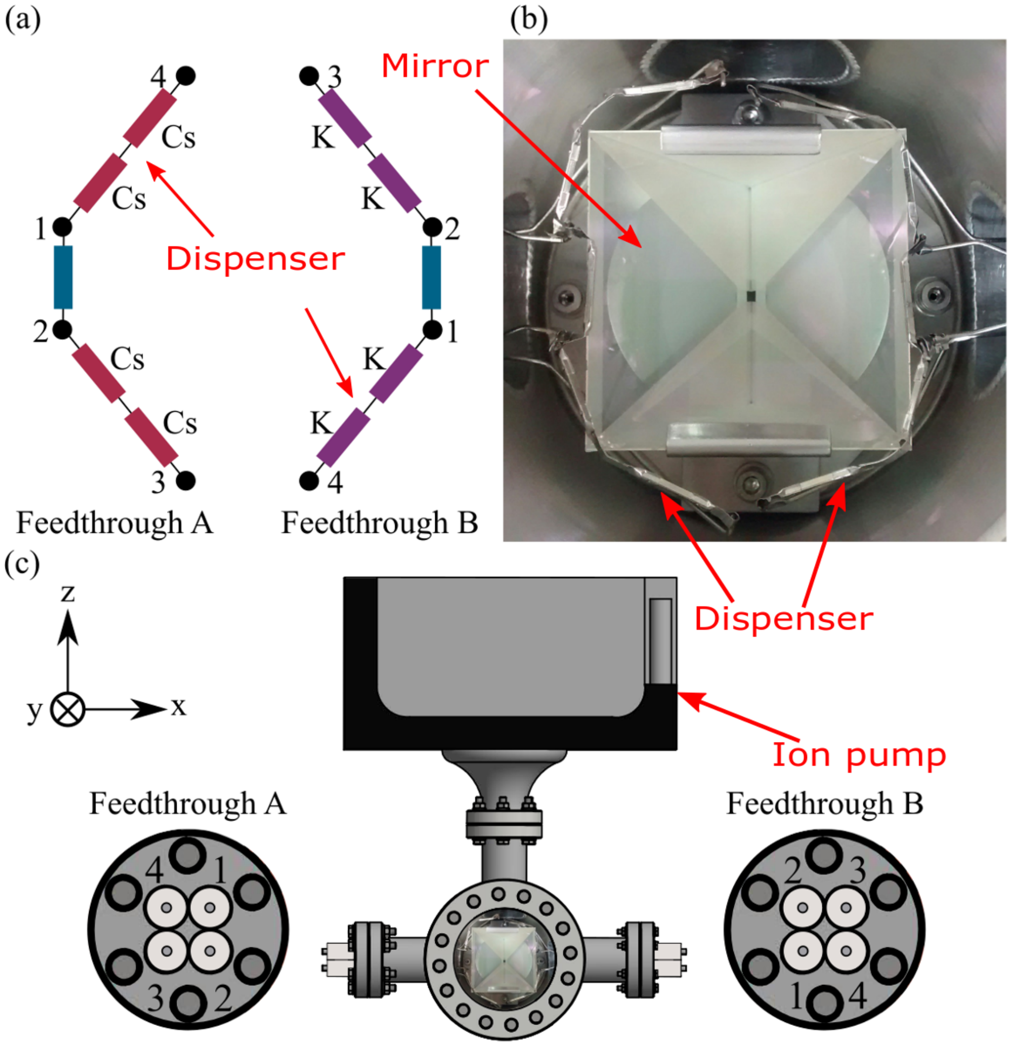

Figure 4.12: Figure (a) shows dispenser orientation within the vacuum chamber around the pyramid mirror. Pyramid mirror assembled shown in figure (b). Feedthrough B is connected to the K dispensers and feedthrough A is connected to Cs dispenser as shown in (c). The front representation of the P-MOT chamber including the ion pump is presented in the figure.

4.7.1 Alkali-metal Dispensers

The reservoir for our experiments is a collection of two ^{39}K and ^{133}Cs alkali metal dispensers mounted on both sides of the pyramid optics within our equipment as shown in figure 4.12 (a). Generally, dispensers are electrically coupled through spot-welding of a thick 1 mm stainless steel atomic reservoir. Each stainless steel rod are twisted on a different inner end of ultra-high vacuum feedthrough, as presented in figure 4.12 (b). 3 $\leftrightarrow$ 2 and 1 $\leftrightarrow$ 4 in feedthrough B are connected to the K dispenser and 4 ↔ 1 and 2 ↔ 3 in feedthrough A are connected to the Cs dispenser as shown in figure 4.12 (c). Individual feedthrough is attached through four cylindrical connectors so that the potential can be applied over every dispenser separately. Throughout the experiment, the individual species dispenser is worked continuously at $2.5 < I < 4$ A; meanwhile, sometimes with larger currents of 4.5 A applied only for 40/50 second during our experiment to enhance atom numbers in the MOT. Here low current regulation guarantees the durability of the dispenser joining point.

4.7.2 Vacuum chamber baking and pumping

The vacuum chamber used in our experiment was designed and assembled by our previous PhD students. It is shown in figure 4.12 (b) and 4.13. Initially, the vacuum chamber is pumped out by a turbomolecular pump supported with a roughing pump, which was produced by Paul Griffin *et al.* [151]. The residual gases in the chamber during the first day of pumping out of the chamber are mainly water vapour, nitrogen, carbon dioxide, and carbon monoxide. These gases are commonly absorbed by the stainless steel chamber wall. After pumping out overnight, the pressure reached $\sim 10^{-7}$ mBar, which is higher than the base pressure achievable by the pumping rig. The base pressure is a realistic estimate of the lowest pressure that the pumping rig can reach. The pressure of the system would tend towards the actual base pressure of the pumping rig as trapped gases are slowly released from the walls of the chamber and undergo molecular flow towards the pump. In general, this can take weeks, possibly even years depending on the size of the chamber without any heating. To reach the base pressure in a reasonable amount of time, the chamber is baked at 200 °C to increase the out-gassing rate. It is also sometimes advantageous to degas the element of the ion pump while the system is still warm. The chamber is baked for three days and cooled down again. At this point, the pressure of the arrangement has been decreased by a further two orders of magnitude. The dominant contaminant of the system is now light molecules, such as hydrogen, which are not pumped away effectively by the turbo-pump. Ion pumps, in comparison, do pump these lighter gases efficiently allowing for lower base pressures to be achieved. Therefore once the system is cooled, the ion pump is activated, and the chamber is separated from the turbo-pump. Therefore, the measured pressure of the chamber rapidly reaches $\sim 10^{-10}$ mBar.

Source of out-gassing The ultra-high vacuum (UHV) pressure requires a chamber that produces minimum gas particles, Such particles are generate by several mechanisms [152, 153],

✓ Diffusion: take out the gas from within a material to the outer surface.

✓ Desorption: previously adsorbed gas comes out from the surface.

✓ Permeation: in this process, gases adsorb onto an exterior surface and then diffuses through the inner material and coming out from the inner surface.

✓ Vapourisation: due to temperature, particles of material come out as a gas phase; these particles are the material's vapour pressure.

These methods are collectively termed outgassing and, coupled with real and virtual leaks, limit the possible base pressure. Diffusion and desorption can be considerably decreased through implementing a bake-out of the vacuum operation, whereby the system is heated to 100 – 400 °C throughout primary pumping.

4.7.3 Pyramid MOT beam alignment

The pyramid MOT is sensitive to the laser beam alignment and polarization, therefore it is necessary to align very carefully and choose the right polarization as presented in 4.13 (a). We correct the polarization with the following steps,

• First, just before the fiber output we placed a polarizing beam splitter (PBS) and rotated the PBS to give minimum transmission.

• Then we inserted a quarter wave-plate and find a polarizing angle where the beam power is minimum.

• And after finding the right polarization angle of minimum beam power, rotate the quarter waveplate by 45° from the minimum power, which gives us exactly 1/2 of the maximum beam power and make our beam completely

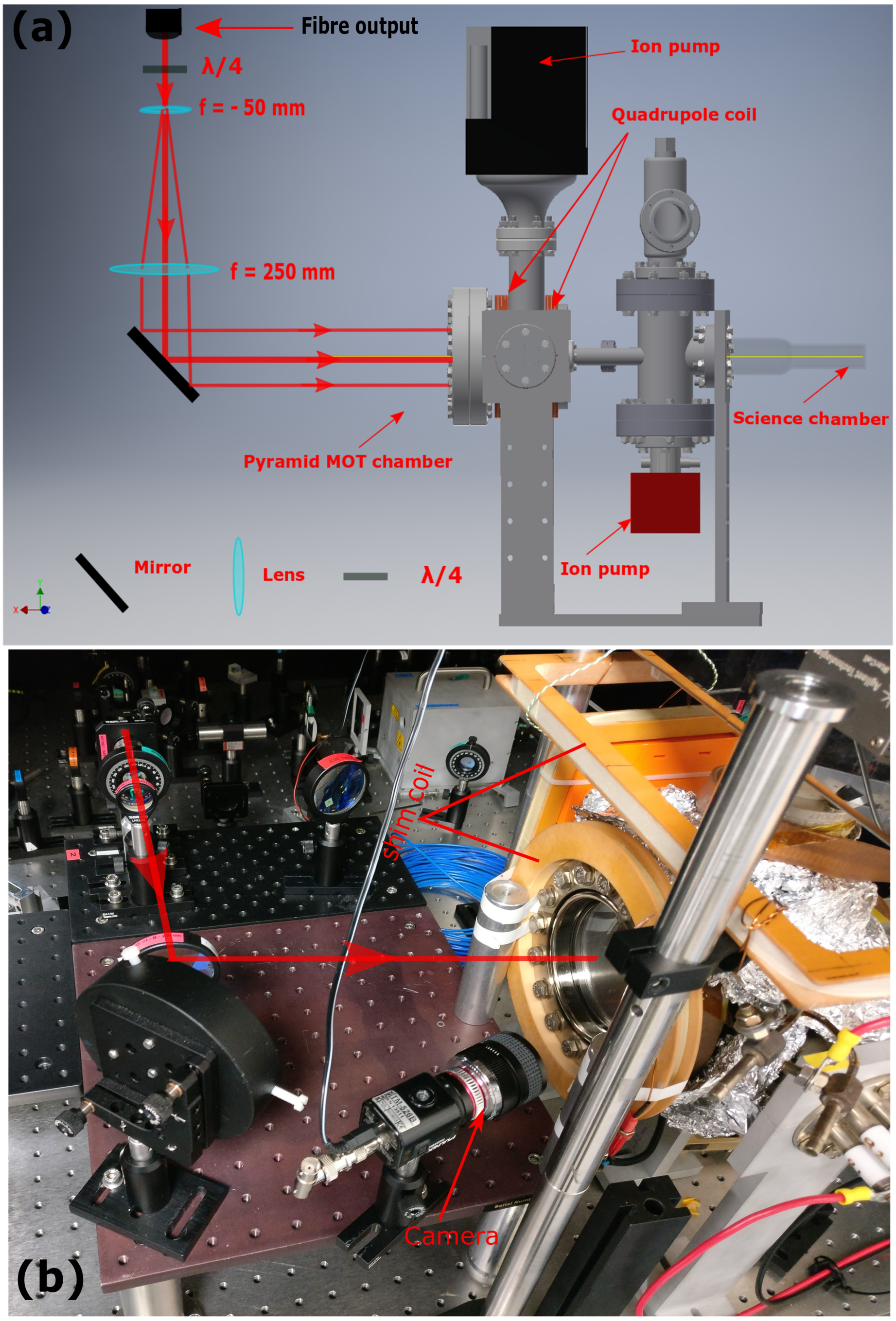

Figure 4.13: A simple inventor drawing of our vacuum chamber for the trapping in figure (a). The actual setup of the vacuum chamber in the optical table presented in figure (b).

circularly polarized.

We found the optimal polarizing angles are 159° or 339° in order to get a MOT from our setup.

By adjusting a big single circularly polarized beam above the mirror parts, three orthogonal beams coupled by opposite polarization similar to that of a standard six beam MOT are created. Therefore, ^{39}K pyramid MOT can be accomplished by easily regulating a single beam comprising cooling and repump light for ^{39}K. The alignment of the beam is relatively tricky; therefore, one can align the beam in the following way:

- First measure the height of the centre of the pyramid with respect to the breadboard. Make a note of this number and mark a line on a beam block at exactly this height.

- Then set the output of the collimator to be perfectly horizontal.

- After that adjust the height of the collimator to be the same as the centre of the pyramid.

- Now insert the first lens of the telescope such that the beam position marked on a beam block down-stream is not altered.

- Repeat the previous alignment method for the second lens of the telescope, often this is more sensitive with the first lens removed – if we are doing this we need to put a collar on the first lens.

- Then adjust the separation of the two lenses to produce a well collimated beam.

- After that cut out a piece of paper/card to fit exactly inside the viewport of the pyramid. Make sure the centre of the circle is marked – easiest to draw a cross on it from the circumference. It is also useful to draw some concentric circles on the target as well to help get the beam centred and beam collimated.

- Now place the target paper/card in the viewport and position the large mirror such that the large collimated beam is centred on the viewport and centred on the mirror.

- Then remove the target and look where the reflections from the pyramid mirror are going.

- Adjust the angle of the mirror such that the reflections are visible at the fibre collimator.

- Replace the target and move the mirror base to recentre the beam on the target.

• At the end we repeat the process until the beam is centred on the target and the reflections are aligned back onto the collimator.

The beam from the P-MOT fibre comprises 34.6(4) mW and 32.0(1) mW for cooling and repumping beams for ^{39}K. The collimated (employing a Thorlabs F810APC-780 collimator) laser beam radius, i.e. $1/e^2$, is 3.1(3) mm and crosses within an achromatic quarter-wave ($\lambda/4$) plate (Casix WPA1212-700-1000 nm). To optimize the beam size, we used a telescope with two lenses of the focal length of -50 mm and 250 mm respectively; to expand the beam size by a factor of ~ 5. After that, we are using a 100 mm diameter two-inch mirror to reflect the big laser beam within a window of the vacuum chamber and then the beam incident on the pyramid mirrors, as shown in fig. 4.13. We used $\sim 5\text{I}_{sat}$ for each cooling and repump beam respectively, which is comparable as we found in literature [136].

4.7.4 Magnetic coils

We present the B-field produced by the coils as a function of axial length (along the z-axis). If we consider a set of twin circular coils separated by a few cm, the field can be revised as a second-order equation as follows,

$$B(z) = B_0 + \beta z + \frac{\gamma}{2} z^2 \tag{4.4}$$

where the bias field at the center is B_0 at the center of the coil set in Gauss (G), $B_0 = 0$ for the two of anti-Helmholtz coils, β and γ represent the magnetic field gradient and curvature respectively, which can be represented in G cm^{-1} and G cm^{-2} respectively. Those field parameters depend on the current flowing within the coil set. Therefore, the bias field, gradient, and curvature of the field coil couple is further commonly parameterized as G A^{-1}, G cm^{-1} A^{-1} and G cm^{-2} A^{-1} respectively. The B$-$field is estimated by using a Hall probe.

A set of anti-Helmholtz coils (which can be water-cooled) produce the required B-field of 8.5(4) G/cm for a magneto-optical trap at 16 A quadrupole current. Initially two shim coils, one circular and one rectangular are used in our experiment, the coils are powered using a DC power supply. The quadrupole coils are 130 mm and 70 mm from the centre of the chamber, the number of turns is 20 ± 1. We simulate the magnetic field using Matlab in figure 4.14 (a).

Magnetic coils	Parameter	Values	Units
Pyramid MOT	Field gradient (β)	0.55(4)	G cm^{-1} A^{-1}
Pyramid shim N−S	Bias field (B_0)	1.82(3)	G A^{-1}
Pyramid shim E−W	Bias field (B_0)	0.94(1)	G A^{-1}

Table 4.3: We parameterized the magnetic fields for all coils employed in the atom trapping equipment.

To modify the zero B-field position inside our vacuum chamber, the shim coils are being utilized. Outside of the north end of the pyramid chamber, one shim coil is centred around the circular chamber window, named N-S shim coil, which is 95 (2) mm from the centre of the pyramid MOT chamber. In the east front of the chamber (E-W shim coil) is 135(3) mm from the centre of the trap (and in the up-down directions one as a rectangular shim coil, which is added later to improve the pyramid MOT signal) as shown in figure 4.14 (a). The parameters are presented in table 4.3. In our experiment, we run the coils at currents of $-3 < I < 4$ A; using the relevant shim coil, it is satisfactory to transfer the zero-field position utilizing the generated magnetic field; therefore, using specific shim coils, we can relocate the trap centre over the entire volume of 6 cm width and 3 cm depth in between the pyramidal mirror within the vacuum chamber. In a typical experiment like this, the shim coils are utilised to place the MOT centre straight across the gap in a particular pyramid centre in the non-existence of a retro-reflected axial MOT light which causes an optical force inequality. Therefore, the imbalance of radiation pressure forces shifts the atoms from the pyramid chamber to the science chamber for future experiments. Thus, the pyramid MOT is only used to slow down the atoms, making the higher density of atomic ensemble in the 3D MOT in the science chamber.

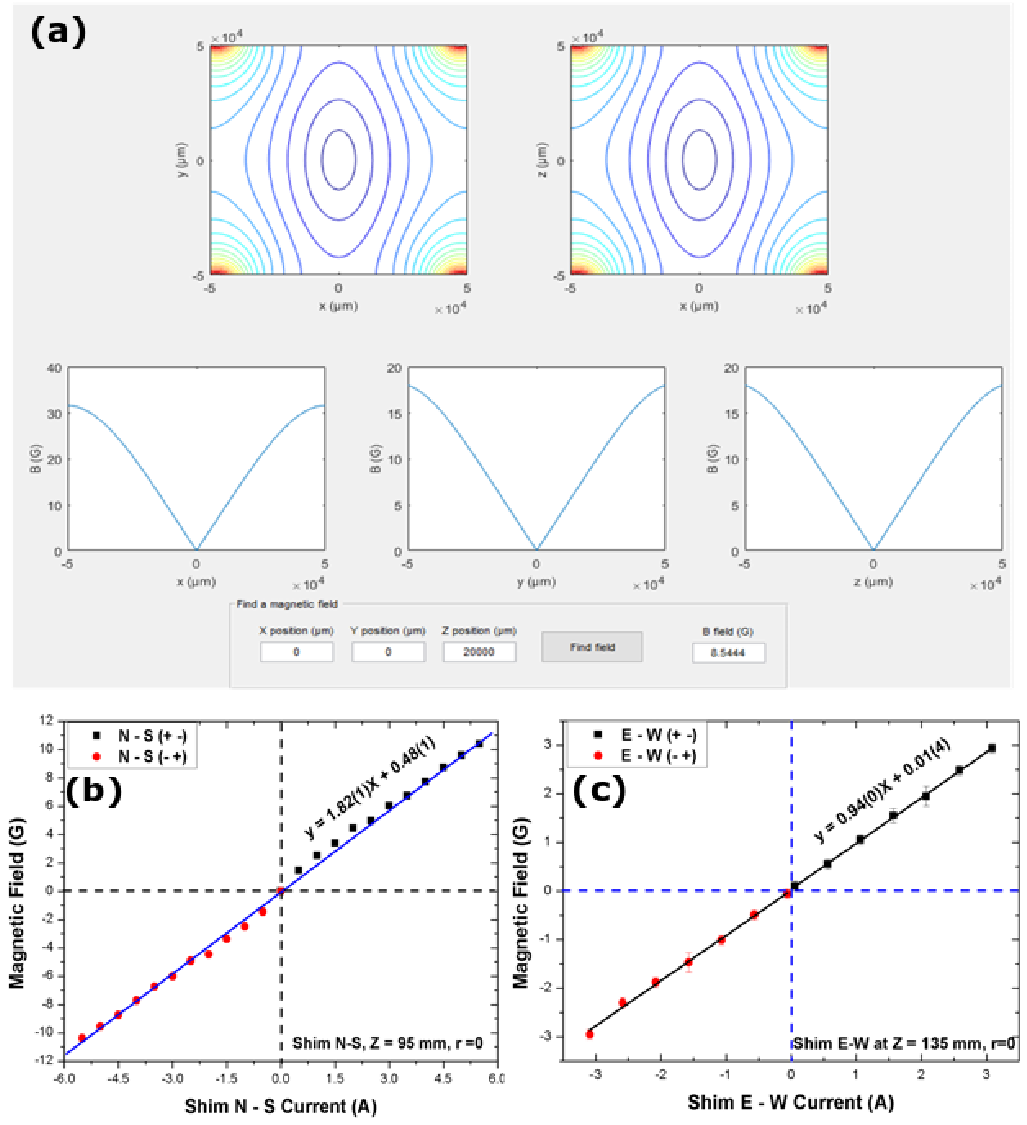

Find a magnetic field

X position (µm): 0

Y position (µm): 0

Z position (µm): 20000

B field (G): 8.5444

Figure 4.14: Quadrupole magnetic field simulation for magneto−optical trapping guided by equation 4.4 in figure (a). Measured B-field as a function of shim current for N-S and E-W shim coils respectively in figure (b) and (c).

4.8 Detection

After trapping atoms in the MOT, the fluorescence radiated from the ensemble of cold atoms; using a single lens, one can detect fluorescence using a photodiode to control experiments and calculate the number of the atoms within the MOT. Therefore, this non-destructive characteristic mechanism is beneficial throughout optimization and tracking the achievement of the apparatus.

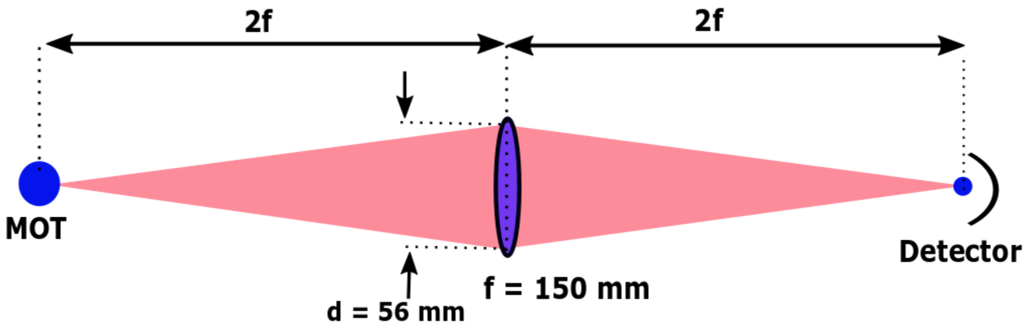

Figure 4.15: The fluorescence imaging technique from the cloud of atoms from inside the MOT chamber. A big 2 inch lens with 56 mm diameter, of focal length 150 mm has been used to collect the fluorescence. And the fluorescence was detected by a photo-detector.

One 2-inch with 56 mm diameter and 150 mm focal length lens has been used to obtain a part of the MOT fluorescence coming through a solid angle. It focuses the beam onto a large area of photodiodes (Thorlabs DET36A) as shown in figure 4.15. Still, due to the small detectable fluorescence signal and considerable background reflection, it's hard to detect a signal with Thorlabs DET36A photodiodes from the pyramid mirror.

But in place of Thorlabs DET36A photodiode, we placed a CMOS Camera (Thorlabs DCC1545M) and took two pictures simultaneously, one picture with the MOT and another picture was taken without the MOT. After subtracting the two pictures, we can detect a weak signal. Therefore, our MOT characterization presented with details in the next chapter.

Chapter 5

Results: Optimization and Characterization

To study ultracold atomic physics with a moderate lifetime, we need to trap the alkali atoms in a low-pressure chamber to minimize the background collision between the atoms. It is crucial to load the trap the atoms with higher efficiency for the experiments like Bose-Einstein condensations [154, 155], where long trap lifetimes and a large sample of atoms are necessary for efficient evaporative cooling.

In the previous chapter 4 we describe a tool to produces well collimated cold atomic sources and in this chapter reports the optimization of the pyramid MOT. Two popular methods for trapping atoms in an MOT directly from atomic vapour [156] using thermal atomic beam, and Zeeman slower [157]. Both processes add a considerable number of atoms untrapped inside the vacuum chamber, causing pressure within the chamber, also depositing untrapped atoms on the chamber walls. Therefore, the untrapped atoms are a potential source of background collision that leads to a short lifetime and decay process. Furthermore, making an ultracold atomic ensemble loaded from the MOT in the low-pressure range is necessary for lifetimes of tens of seconds, one way to optimally trap ultracold atoms from the source of the cold collimated atomic beam, which is passed through the pyramid hole. The slow atomic beam efficiently captured in the science chamber; in this process, one can minimize the background collisions resulting in a trap of a

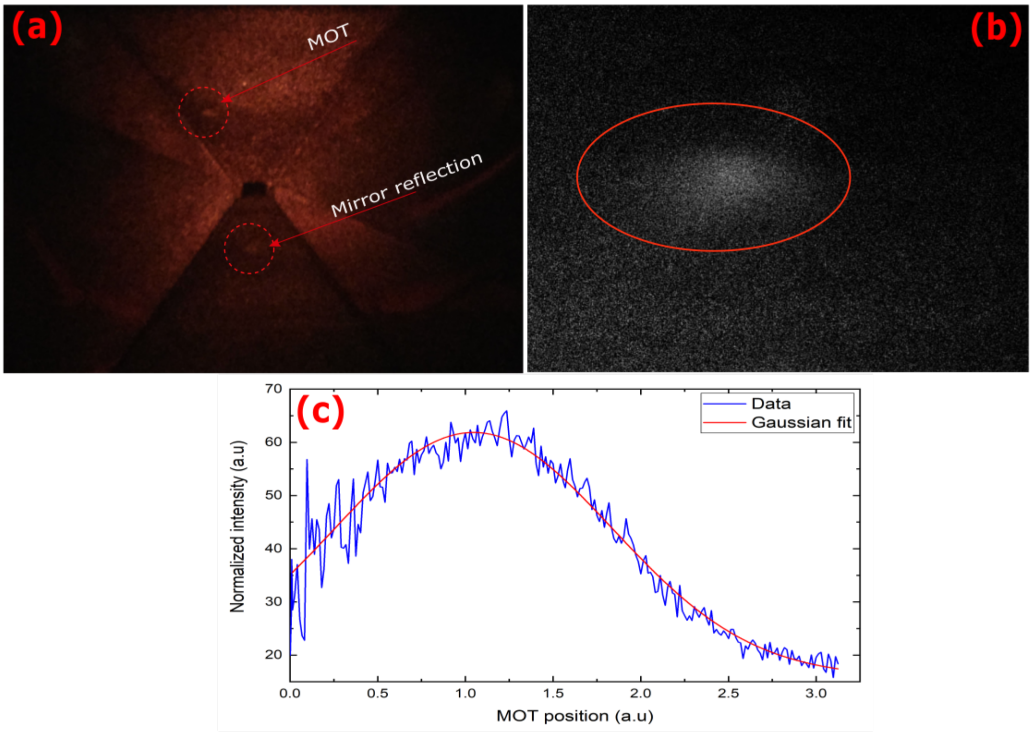

Figure 5.1: In (a), a photograph of an MOT, the mirror reflected image is also visible within the chamber. In (b) background-subtracted image of our potassium MOT within the pyramid chamber and figure (c) normalized MOT signal detected by the camera, which is fitted with Gaussian profile.

high number of atoms in high space density with a higher lifetime.

We also produced cold atomic flux using a pyramid chamber and the produced MOT within the chamber can be seen in picture 5.1 (a), the background-subtracted image presented in 5.1 (b), we also include normalized detected MOT signal, and our pyramid MOT happened to be too faint, it can be seen by the camera, but due to huge background reflection of MOT beam, it is hard to detect and distinguish the atoms with the cost of any exposure time; therefore, we optimized our results empirically, we got a very small photodiode signal (few mV) with highest possible gain and if we convert it in terms of atom's number using equation 2.19 we approximately get $\sim 10^2 - 10^4$ number of atoms due to limited laser power, which is also reported in [136]. To get the maximum number of atoms within an MOT, every correlated parameter needs to be optimized as follows.

5.1 MOT beam polarization optimization

The fundamental measurable parameter to be optimized for the cooling and pumping laser beam polarization, which is easily fixed employing a single achromatic quarter-wave plate for any atomic species like ^{39}K. In the previous chapter, we discussed how one could align a pyramid MOT beam carefully. We also indicate that the ^{39}K isotope is highly dependent on the polarization of the MOT beam; therefore, we optimized the beam in terms of polarization; we used a polarizing beam splitter to make our both beam perfectly circular, as we discussed in section 4.7.3, we found circular polarization angles around 160° or 340°, and the results are as follows, in figure 5.2(a), as discussed, we are limited with atoms number and back reflection, after checking whether the MOT is visible or not in the full spectrum of quarter-wave plate angle; we categorized the MOT into three categories which are MOT, faint MOT and no MOT.

Now when we rotate the quarter wave-plate and detect the fluorescence by a camera, we found the brightest MOT around approximately 160° or 340°, (which indicate our beam is perfectly circular polarized), which is also well agreed with the polarization selection process as discussed in 4.7.3, we also found faint MOT near both sides of MOT regime as shown in figure 5.2 (a) and we found no MOT beyond those angles of quarter wave-plate, which means the beams are not anymore circularly polarized. Further extends as presented in figure 5.2 (b), our analysis by plotting MOT beam power as a function of deviation from perfect circular polarization. Therefore we found approximately ± 5° deviation of circular polarization angle is the optimal angle to get an MOT for our experiments, where the beam is perfectly circular and the atoms are pumped efficiently. And approximately ±8° both side of the ± 5°, the beam was not perfectly circular, which indicate atoms are not pumped efficiently.

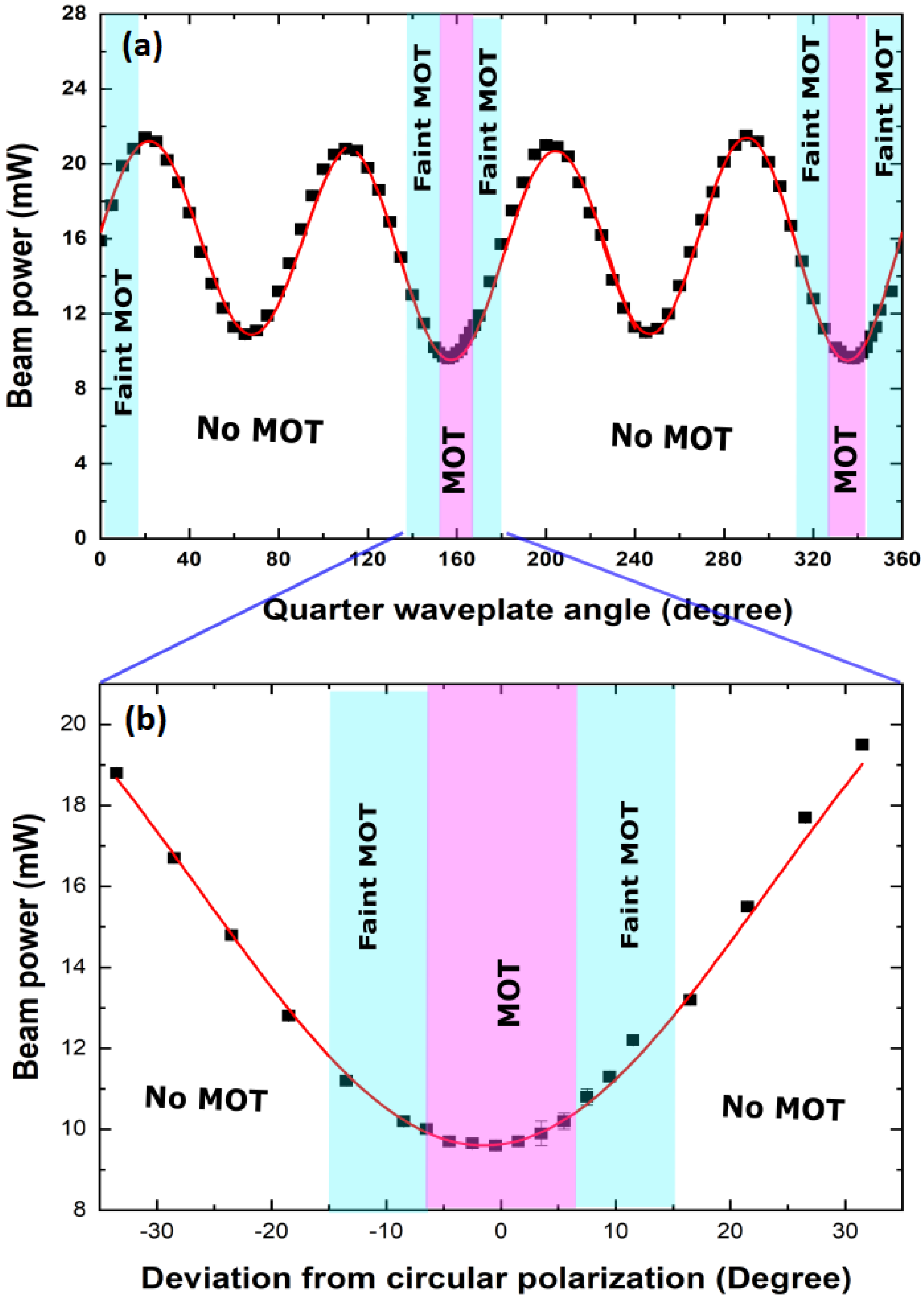

Figure 5.2: In figure (a), we check the circular polarization in the full spectrum of quarter wave-plate angle. The MOT categorized into three categories, which are MOT, faint MOT and no MOT with a different colour. In figure (b), we further extend our characterization by plotting MOT beam power as a function of deviation from perfect circular polarization; the data was taken with $\sim 4\mathrm{I}/\mathrm{I}_{sat}$ for both cooling and repumped beam.

5.2 MOT intensity optimization

Usually, the consequences of the pyramid MOT beam intensity on the loading rate of the 3D MOT are examined in the cold atom experiments, which is beyond our present experiments. We optimize pyramid MOT directly from the pyramid chamber in the investigation, as we have a weak MOT signal.

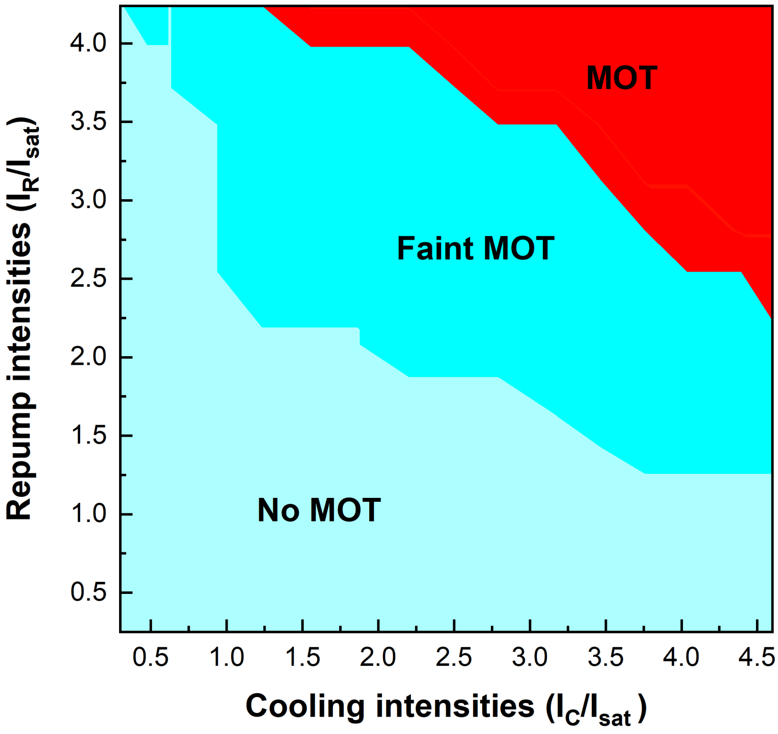

Figure 5.3: Repump beam intensities as a function of cooling beam intensities, both intensities were normalized by saturation intensity of D_2 transition of ^{39}K isotope. Three different colours represent big MOT, weak MOT and no MOT visible within the MOT chamber.

This section, we investigate the repump intensities as a function of cooling intensities, both intensities are normalized by saturation intensity (I_{Sat} = 1.75 mW.cm^{-2}) of the D_2 transition of ^{39}K isotope as shown in figure 5.3. Here we identified three regimes with different colours, the red colour regime where we found relatively big MOT, then in the cyan colour regime, the MOT was relatively less bright but more visible than regime red, and in the rest of the regime, the MOT is not visible. Therefore due to limited beam intensity we can't go beyond $\sim 4I/I_{sat}$ (where beam waist is $\sim$ 15.5 mm).

The optimal beam power is presented in table 5.1.

Here we observed increment of coupling and repumping intensities the MOT started to appear; initially, the MOT was faint then if we increase more cooling and repumping beam power, we observe relatively bigger MOT. We can say, increase in repumping intensity prevents achieving low temperatures at relatively higher density, and the temperature does not depends on the repump intensity at low density, which indicates the role of reabsorption of spontaneously emitted photons within the atomic cloud [158].

5.3 MOT chamber temperature optimization

The pyramid chamber has been simultaneously kept heated using a heating tape produced by silicon. The heating was important to guarantee that most of the released potassium would deliver it to the six-way cross working as a pyramid MOT before deposit in the coolest area of the MOT chamber. As we present at 2.11, the potassium solid in form at room temperature, therefore it is important to heated up to produce sufficient vapour pressure and atomic number density to capture atom in the optical trap.

In this section, we examined the temperature of the pyramid MOT chamber as a function of quadrupole field gradient due to the fact that the number of the atoms/MOT size was strongly dependent on the quadrupole field gradient, while the dispenser ran at 3.5 A as presented in figure 5.4. As we discussed before, the red regime indicates MOT; in the cyan colour regime, the MOT was relatively small, compared to regime red and the rest of the regime the MOT is not visible.Without any heating, even though the dispensers across and the chamber were rightly attached, the temperature at the centre of the chamber was found to only be ∼ 23°C, which was significantly lower. At constant quadrupole field gradient (beyond 6.5 G/cm), we found faint MOT and MOT (cyan and red colour regime the MOT) where atoms have favourable vapour pressure and number density to form an MOT but after 90 °C vapour pressure and number density increases and due to random high velocity of atoms, the atom-atom collision increase and the lifetime of the atoms reduced resultant faint MOT and NOT MOT after 110

°C.

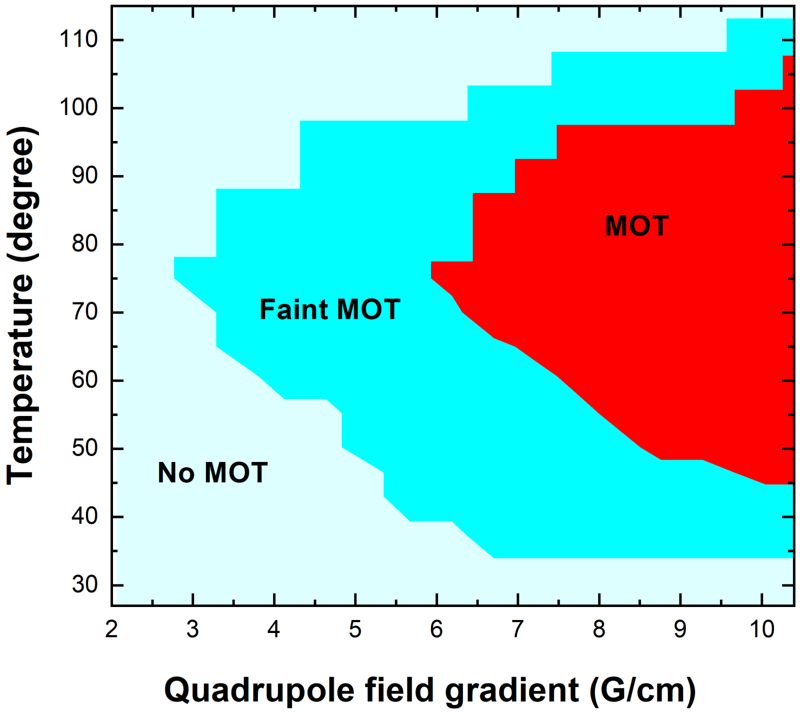

Figure 5.4: Vacuum chamber temperature as a function of the quadrupole field gradient. As indicated earlier three different colours define MOT (red),faint MOT (cyan) and no MOT.

The heaters were placed around the windows of the pyramid MOT chamber, near adequate to its middle. We changed the temperature of the heaters and observed the temperature just above the centre of the chamber employing a thermocouple as close to the centre of the chamber as possible. Each time we turned the set temperature of the heaters, we waited for 45 minutes before catching images of the MOT so that the operation could approach thermal equilibrium. From the data, we can conclude that the optimal temperature for our experiment was $\sim 75 \pm 3$ °C. Similar kind of experiment also reported in [159].

5.4 Magnetic field optimization

Along with the parameters mentioned earlier, the magnetic field parameters are the key affecting parameters for the pyramid MOT performance for any species, including bosonic ^{39}K. Three magnetic shim coils (section 4.7.4) installed to create magnetic fields in the direction of E−W, N−S and Up−down (the pictorial view shown in fig. 4.13) enable individual control of the transverse (horizontal), axial and Up−Down (vertical) positions of MOT respectively. Therefore, the magnetic field enables the MOT to be horizontally and vertically positioned in the aperture at the pyramid apex. The range of translation of the MOT centre is equivalent to the employed magnetic field, by a steady proportionality reliant on the pyramid MOT coil B−field gradient. The ^{39}K pyramid MOT flux hugely depends on the magnetic field (B-field) i.e. the transverse position centre with quadrupole coil gradient of 8.5(3) G cm^{-1} is presented in figure 5.5. Remark the different ranges across which the achieved flux is a maximum. This highest regularity symbolizes that inside captured atoms ensemble is uniquely above the aperture at the pyramid apex. While the captured flux decreases to half this maximum value, only half of the pyramid MOT cloud is above the pyramid apex. Due to radiation pressure imbalance, the cloud enters into the 3D−MOT chamber.

In this section, we note that the MOT was visible or not within the chamber at different shim fields at constant quadrupole field gradient and constant dispenser current, which is 3.5 A. As indicated earlier, the different colour in the plots defines different MOT sizes. In figure 5.5 (a) E−W shim field i.e transverse (horizontal) field as a function of quadrupole field gradient. The optimal parameter for the transverse field was $-0.25 < B_{EW} < 1$ G and E − W i.e transverse (horizontal) field. In figure 5.5 (b) Up−Down shim field, i.e. transverse (vertical) field as a function of quadrupole field gradient, here we observed a big MOT within a small range of shim field with comparison to E−W shim field, the optimal parameter for the vertical B−field was $\pm -0.5 < B_{EW} < 0.5$ G, therefore without a vertical shim coil field the MOT was well visible. Likewise, In figure 5.5 (c) N−S shim field, i.e. axial shim field with respect to quadrupole field gradient, here we can observe some part of the MOT suddenly disappear due to radiation pressure imbalance at the apex of the pyramid MOT chamber. The optimal parameter, axial shim B−field varying with quadrupole field gradient, but we can approximately say that the optimal axial shim B−field was $\pm\ 5.5 < B_{EW} < 6.5$ G. From all

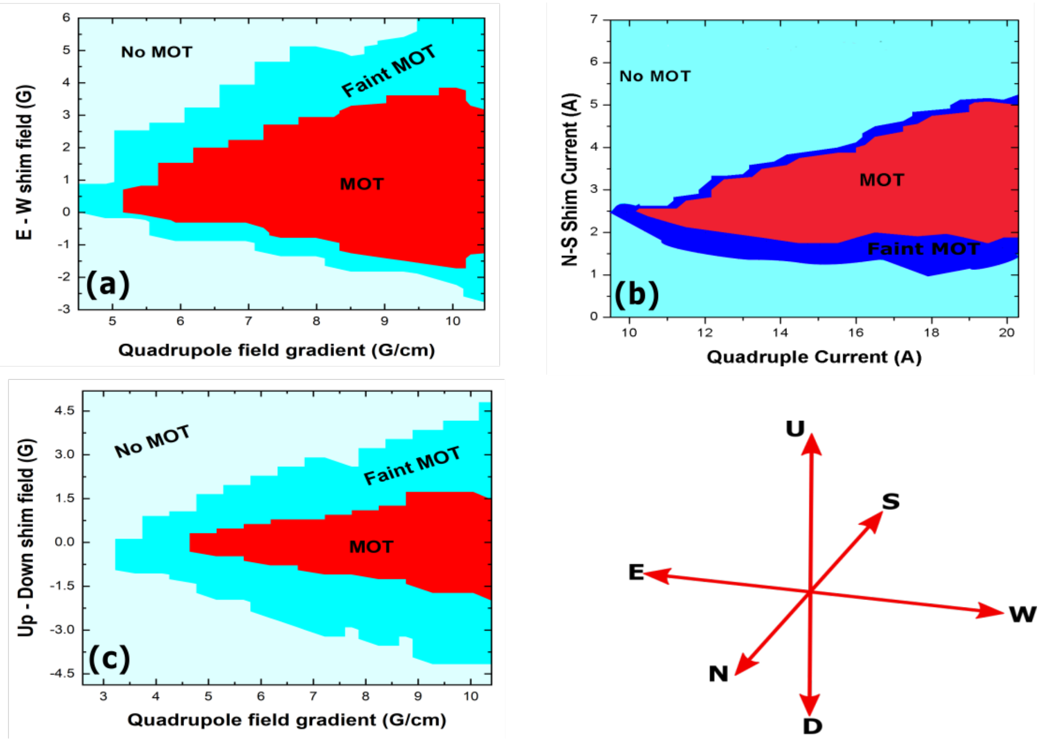

Figure 5.5: In figure (a) E−W shim i.e transverse (horizontal) field as a function of quadrupole field gradient. In figure (b) Up−Down shim field, i.e. transverse (vertical) field as a function of quadrupole field gradient and in figure (c) N−S shim field, i.e. axial field with respect to quadrupole field gradient. In figure (a) and (b), three different colour, red, cyan, and light cyan, represent MOT, faint MOT and no MOT. In figure (c), red, blue, and light cyan colour represent MOT, faint MOT, and no MOT.

shim field the optimal quadrupole field gradient was 10.5(4) G/cm, which is also realized by the previous experiment within our group [160].

5.5 Cooling and repump beam detuning optimization

In principle, the cooling and repump laser beams' frequencies were optimized to achieve the most significant atom number in the three dimensional MOT. But in our case, we tried to optimize MOT directly from the pyramid MOT chamber. The AOM controlled the frequencies (as discussed in section 4.4.2) and was used to change the detunings over a spectrum of frequencies. Subsequently, a loading period of several seconds for every detuning collection,

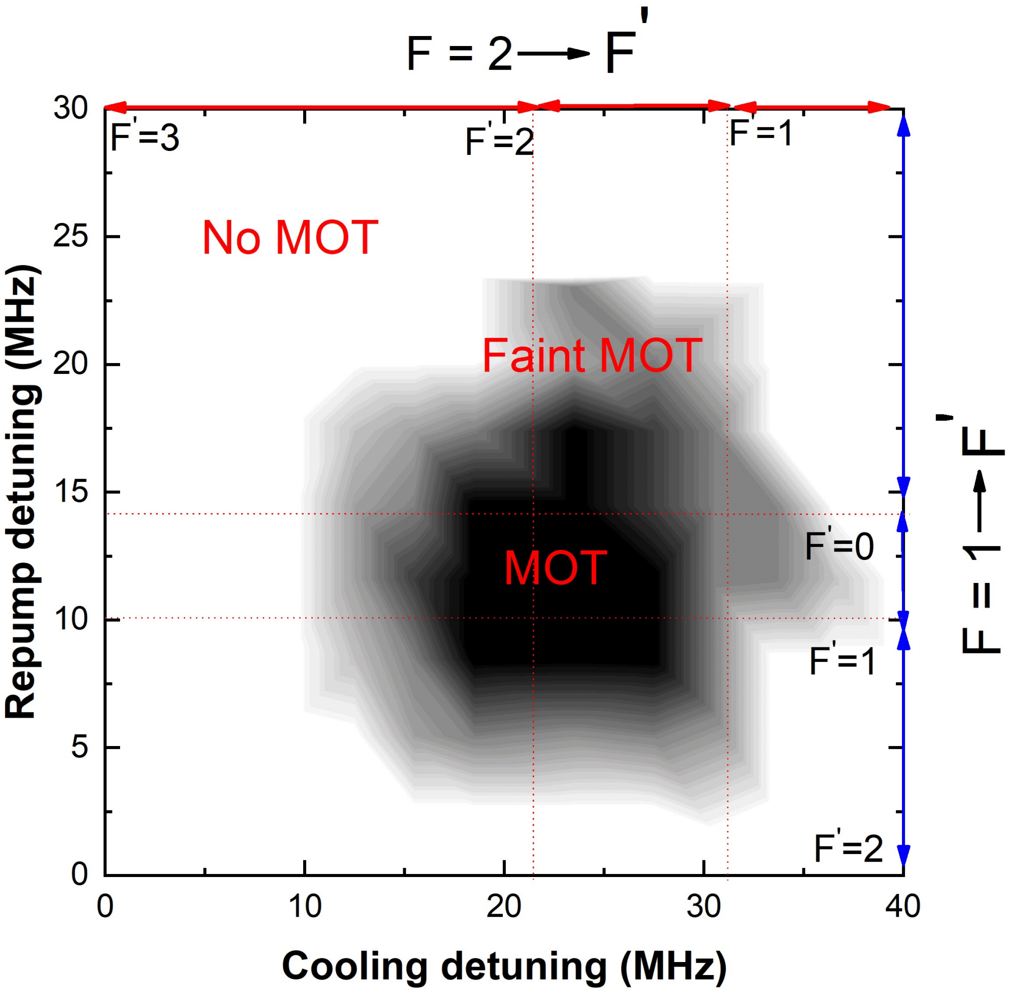

Figure 5.6: Pyramid MOT as a function of the cooling and repump frequencies. The red regions show the maximum number of atoms; the atom number decreases, shown as a weak MOT and too faint for the camera presented as no MOT. The data were taken with 33.5(4) mW and 31.2(3) mW cooling and repump beam power, respectively, the shim field value was 6.5 G, 1 G and 0.5 G for N-S, E-W and Up-Down shim fields, respectively, the quadrupole field gradient was 10.5(4) G/cm and the chamber temperature was 70(2)°C. Both axes are also comparable with actual atomic transitions.

a picture of the MOT was captured with the help of a CCD and categorized the MOT in three sections, i.e. MOT, faint MOT and No MOT as presented in figure 5.6.

Due to the laser detuning are evolving, the excited state fraction also changes, i.e. the fluorescence rate per atom. Due to a considerable number of points, the data were obtained over a moderate timescale (roughly several minutes). So to eliminate any long-term fluctuations from each set of detunings was rearranged. The outcomes are presented in Figure 5.6. For each cooling detuning, we vary repump detuning across the frequency spectrum. We also indicate different hyperfine transitions for cooling and repump in the figure 5.6. Doppler cooling occurs when the laser frequencies are tuned below the transitions frequencies, where the atoms experience optical frictional forces, as shown in equation 2.6. If we consider the Zeeman sub-levels of the atoms, a much higher frictional force arises, as presented in equation 2.11. As described in figure 2.4, the Doppler cooling is efficient in regime I and IV, but we found MOT almost all across the transitions. The optimum detunings can be found within range of $-\ 30 < \Delta_C < -\ 18.5$ (negative sign coming from directional cooling AOM) and $7.5 < \Delta_R < 20$ MHz for the cooling and repump laser beams respectively, which approximately match with various potassium experiments [161–163].

Parameters	Values	Units
Cooling detuning Δ_c	$-\ 30 < \Delta_C < -\ 18.5$	MHz
Repump detuning Δ_R	$7.5 < \Delta_R < 20$	MHz
Cooling beam power	33.5(4) (Max. available)	mW
Repump beam power	31.2(3) (Max. available)	mW
Quadrupole field gradient	10.5(4)	G cm^{-1}
N−S shim field	$5.5 < B_{NS} < 6.5$	G
E−W shim field	$-0.25 < B_{EW} < 1$	G
Up−Down shim field	$-0.5 < B_{UD} < 0.5$	G
Chamber temp.	$\sim 75 \pm 3$	°C
Approximate atoms number	$\sim 10^2 - 10^4$	Atoms

Table 5.1: A review summary of optimized values of every parameter fixed to achieve ^{39}K MOT within our vacuum chamber.

Due to our setup's limitations, the frequencies utilized for the cooling and repump beams are identical as [163] for our pyramid MOT. However, additional experiments working with the correct frequencies to optimize every MOT individually have found that the best frequencies for individual MOT may vary insignificantly. As we indicate in figure 2.6 indicates four different frequency regime where MOT detuning is optimum [75] but in our case, we don't see such regime of frequencies due to our experiment's empirical nature; our future experiments with 3D−MOT maybe leads us to such kind of results.

In summing up, we can regularly begin loading the ^{39}K MOT by arranging laser intensities, frequency detunings, and the B-field into the resulting optimized values summarized in the chart 5.1. It is crucial to note that due to limitations of our pyramid MOT setup, the optimized frequencies for cooling and repumping may differ slightly as compare [161–163], which may be due to the fact that other experiments operating with the freedom to optimize their MOT with more stander optical method. The future and accurate investigation for pyramid can be done by detecting a high atomic flux after adding a glass cell at the end of the pyramid chamber, where we optically detect atomic flux coming out from the pyramid chamber as [164, 165].

Chapter 6

Absolute absorption on the 405 nm transition: Towards Rydberg excitation.

Physics in thermal vapour cells is one of the exciting fields of research and many applications nowadays, including atomic spectroscopy [166], quantum memory [167], magnetometry [168] and many more. Therefore, the information of absorptive and dispersive features of atomic vapour is fundamental.

If the transition is not closed, then the atom can rapidly collapse back to the lower ground state from the excited state, which signifies off−resonance by a specific probe light beam, while the atom will no longer be able to absorb photons from the probe beam. In the case of a powerful probe light, the atoms mostly in the excited states or have decayed to their lower off-resonance states, and we gets a modified absorption signal because of the medium's optical modification; therefore, the probe beam is not considered as a weak probe beam. Siddons *et al.* [169] extensively studied the Doppler-broadened absorption by the weak probe beam, which is resonant with rubidium D transition, and they fitted their absorption profile with a theoretical framework which is adapted from Zentile *et al.* named as ElecSus [112].

We can use ElecSus to determine potassium's optical properties, the atom of interest in this thesis. Potassium is widely used in cold atom physics, and D_1 and D_2 transitions of potassium are used for a different type of cooling and trapping [158, 170–172] respectively.

6.1 Energy level structure

The energy level structure of 4S → 5P transitions of ^{39}K isotopes are shown in figure 6.1. The isotope variation for D_2 transition has not been studied before so we assume isotope shift for ^{40}K is 235 MHz and for ^{41}K is 454.2 MHz respectively and we used this value to modify ElecSus code, because the atomic structure of 4S → 5P transition is comparable to 4S → 4P transition. Also, an increment in the principal quantum number does not modify the system's angular parts.Let's consider the radial distribution in terms of the 4P and 5P ground states. We can expect a shorter hyperfine splitting, as 5P is the outermost electronic arrangement of the atoms and the interaction between the electron and nucleus is smaller than 4P states. Hence, the expectation value of the electrons' position for the 5P state is larger than the 4P state. For 4S → 5P D_1 and D_2 transitions the saturation intensities and linewidths are 58.8 mW/cm^2, 57.6 mW/cm^2, $\Gamma/2\pi = 170.3$ kHz and $\Gamma/2\pi = 184.6$ kHz respectively [173].

Utilizing the selection rule (i.e. $\Delta F = 0, \pm 1$ [174]),after considering the D_1 line, the excited population's can decay into any of the ground states; hence, these transitions are called open transitions. But in the case of D_2 transition the scenario is different, if we consider the transition $F = 2 \rightarrow F' = 3$, then atoms exclusively decay back to an identical ground state, which is called closed transitions. Hence the D_2 transition includes both closed and open transitions. Assuming the weak-probe part for a closed transition to be greater intensity than an open transition, as atoms cannot be optically pumped into an off−resonant state.

To calculate the saturation intensity for 5P states, we have to take care of all possible decay channels [177, 178]. The transition strength depends on $\Gamma^{1/2}$, so it is clear that we have to heat the cell much higher than 4S → 4P to increase the number density and vapour pressure to see a sufficient transmission profile, including a suitable signal to noise ratio. And the typical order of cell temperature is higher than 100°C.

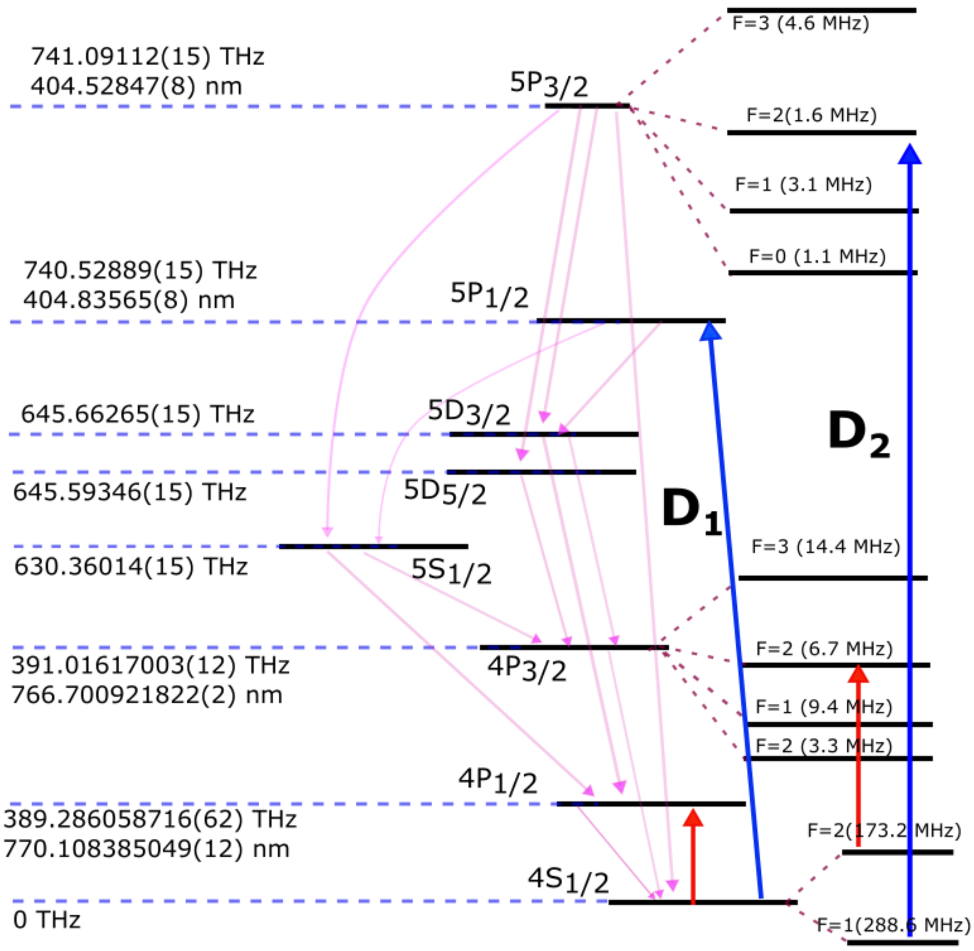

Figure 6.1: Level diagram of D_1 and D_2 transitions of ^{39}K with their natural abundances, along with possible decay path to other states. The numerical data are obtained from [91, 172, 173, 175, 176].

6.1.1 Saturation of optical transition

Here we define saturation parameter S, which describe the physical phenomenon of which is provided through a light field of strength Ω_{pr} and the beam detuning δ_{pr}, the mathematical expression is as following,

$$\mathrm{S} = \frac{\Omega_{\text{pr}}^2/2}{\delta_{\text{pr}}^2 + (\Gamma/2)^2}. \tag{6.1}$$

After substitution the saturation equation 6.1 from the Bloch equations in steady-state A.39, A.40 and A.42 we get,

$$\tilde{\mathrm{u}}_{\mathrm{ss}} = \frac{\delta_{\mathrm{pr}}}{\Omega_{\mathrm{pr}}} \cdot \frac{\mathrm{S}}{1+\mathrm{S}}, \tag{6.2}$$

$$\tilde{\mathrm{v}}_{\mathrm{ss}} = \frac{\Gamma}{2\Omega_{\mathrm{pr}}} \cdot \frac{\mathrm{S}}{1+\mathrm{S}}, \tag{6.3}$$

$$\tilde{\mathrm{w}}_{\mathrm{ss}} = -\frac{1}{2} \cdot \frac{1}{1+\mathrm{S}}. \tag{6.4}$$

The maximum population in the steady state is $\rho_{\mathrm{aa}} = 1/2$ i.e the populations of $|b\rangle$ and $|a\rangle$ (appendix-A) are identical and the saturation equation is such that $S \to \infty$, $\tilde{w}_{ss} \to \infty$. On the resonance, the saturation parameter S_0 is provided by,

$$S_0 = \frac{2\Omega_{\mathrm{pr}}^2}{\Gamma^2} \equiv \frac{\mathrm{I}_{\mathrm{pr}}}{\mathrm{I}_{\mathrm{Sat}}} \tag{6.5}$$

I_{Sat} is known as saturation intensity, which can be defined as the photon energy ($\hbar c/\lambda$) per unit time (lifetime $1/\Gamma$) per unit area and the absorption, the cross-section is generally λ^2.

$$\mathrm{I}_{\mathrm{Sat}} = \frac{2\pi^2 \cdot \hbar \cdot \Gamma \cdot \mathrm{c}}{3\lambda^3} \tag{6.6}$$

Our point of interest is ^{39}K 4S → 5P transition, the situation is quite different, hence equation 6.6 is not applicable to calculate the saturation intensity because the 5P state may collapse to alternative states as shown in figure 6.2, so we have to consider all possible decay path which is as follows,

$$\Gamma_{\mathrm{T}} = (\Gamma_{5\mathrm{P}\to4\mathrm{S}} + \Gamma_{5\mathrm{P}\to5\mathrm{S}} + \Gamma_{5\mathrm{P}\to3\mathrm{D}_{3/2}} + \Gamma_{5\mathrm{P}\to3\mathrm{D}_{5/2}}). \tag{6.7}$$

After taking care of all the possible decay path the final saturation intensity of ^{39}K 4S → 5P line [178, 179] is as follows,

$$\mathrm{I}_{\mathrm{Sat}} = 2\pi\frac{\mathrm{hc}}{\lambda^3}\frac{\Gamma_{\mathrm{T}}^2}{\Gamma_0}\frac{1}{1.58}. \tag{6.8}$$

where Γ_{T} defined as total linewidth of the transition and Γ_0 is the linewidth just along 4S → 5P transition and $\left(\frac{1}{1.58}\right)$ is a consequence of all the possible decay from the 5P state. And for ^{39}K 4S → 5P transition, the saturation intensity and decay rates are 58.8 mW/cm^2, 57.6 mW/cm^2, $\Gamma/2\pi = 170.3$ kHz and $\Gamma/2\pi = 184.6$ kHz for D_1 and D_2 lines respectively [173]. Different lifetime due to wave function overlap of different hyperfine structure.

If we label the maximum intensity of the incident light field defined as sufficient weak for weak probe regime as I_{wp}, this weak probe regime for ^{39}K is many orders of quantity smaller than saturation intensity I_{Sat} for the ^{39}K 4S → 5P line [178]. If we consider two probe beams, one is a large probe beam, and another is a small probe beam. The travelling time over the wider beam is enough larger than the smaller beam, and because of that, the scattering effects are more crucial. This represents that the larger probe beam I_{wp} is lower than the smaller beam. The effect of the beam parameter has been extensively studied in rubidium by Sherlock and Hughes [180].

From equation A.42 and 6.47 we can calculate the scattering rate R, which is as following,

$$\mathrm{R}(\mathrm{I}_{\mathrm{pr}}, \delta_{\mathrm{pr}}) = \Gamma \rho_{\mathrm{aa}} = \frac{\Gamma}{2} \cdot \frac{\mathrm{S}_0}{1 + \mathrm{S}_0 + (2\delta_{\mathrm{pr}}/\Gamma)^2}. \tag{6.9}$$

This expression of scattering is one of the important results of the Optical Bloch equation.

6.1.2 Complex refractive index of the atomic medium

The refractive index of the atomic medium can be defined as real and imaginary parts, which are n_R and n_I respectively, which can be obtained from the well known Maxwell's equations,

$$n = n_R + n_I. \tag{6.10}$$

The real and imaginary part corresponding to,

$$n_R = 1 + \frac{\chi_{\mathrm{R}}}{2}. \tag{6.11}$$

$$n_I = \frac{\chi_{\mathrm{I}}}{2}. \tag{6.12}$$

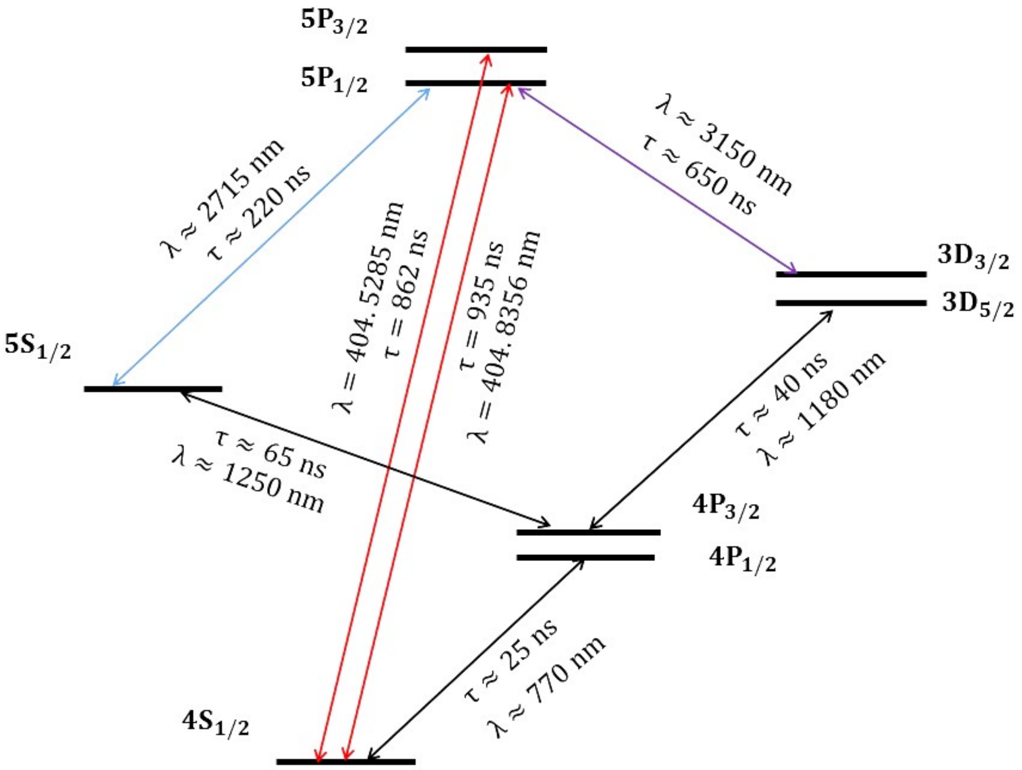

Figure 6.2: Energy levels diagram associated with possible decay path along with decay rate from the 5P state to ground states 4S. The numerical data for decay time and wavelength between the states are taken from the following papers [173, 181–184].

Now substituting equations A.52 and A.53 into the equations 6.11 and 6.12 and we get,

$$n_R(\delta_{\mathrm{pr}}) = 1 - \frac{\mathrm{Nd}_{\mathrm{ba}}^2}{2\epsilon_0\hbar}\left(\frac{\delta_{\mathrm{pr}}}{\delta_{\mathrm{pr}}^2 + (\Gamma/2)^2 + \Omega_{\mathrm{pr}}^2/2}\right) \tag{6.13}$$

and

$$n_I(\delta_{\mathrm{pr}}) = \frac{\mathrm{Nd}_{\mathrm{ba}}^2}{2\epsilon_0\hbar}\left(\frac{\Gamma/2}{\delta_{\mathrm{pr}}^2 + (\Gamma/2)^2 + \Omega_{\mathrm{pr}}^2/2}\right) \tag{6.14}$$

The above equations are particular cases of well known Kramers-Kronig relations, which describe the absorption (which is an imaginary component of the refractive index) and dispersion (which is a real component of the refractive index) properties of a dielectric medium through the complex refractive indices. In general, both real and imaginary complex refractive indices are shown in figure 6.3. In the two-level atomic system, the imaginary compo-

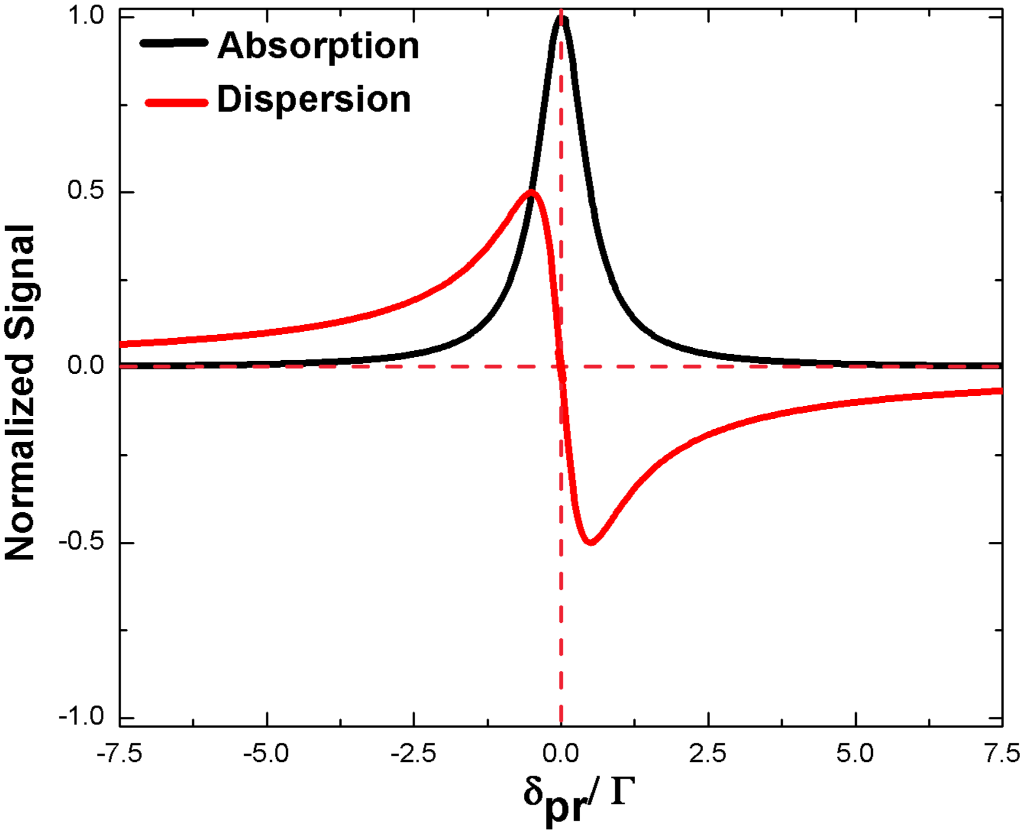

Figure 6.3: The normalized absorption coefficient $(n_I(\delta_{pr})/n_I(\delta_{pr}=0))$ and dispersion coefficient $(n_R(\delta_{pr})-1)/n_R(\delta_{pr}=0))$ of the optical medium, consists of a two-level atom. In this particular example, $\Gamma \gg \Omega_{pr}$ is framed with respect to detuning, which is normalized by decay rate (Γ) of the atoms from an excited state to ground state.

nent of the refractive index represents the absorption of the medium, which has a Lorentzian line shape.

The above particular example of Kramers−Kronig associations for a Lorentzian pattern, which can be commonly expressed as,

$$n_R(\omega) = 1 + \frac{1}{\pi}\int_0^\infty \frac{\omega' n_I(\omega')}{\omega'^2 - \omega^2} d\omega' \tag{6.15}$$

$$n_I(\omega) = -\frac{\omega}{\pi}\int_0^\infty \frac{\omega' n_R(\omega') - 1}{\omega'^2 - \omega^2} d\omega' \tag{6.16}$$

The real part of the reflective index at specific frequency depends on the entered frequency spectrum of the imaginary part of the reflective index and vice-versa. This phenomena has unique implications for pulse propagation in a dispersive optical medium.

6.1.3 Doppler broadening spectroscopy

Doppler broadening is a physical phenomenon of broadening spectral lines due to the Doppler shift because of kinetic energy distribution, i.e. non-zero velocity distribution of atoms and molecules. The atomic transitions that are not resonant with the light beam can communicate with the field if the velocity of atoms or molecules Doppler shifts into the resonance.

Consider an atom in the rest frame resonant with a light field with frequency ω_{ab}, and absorb a photon by the atom with frequency ω_{pr} in the laboratory frame. Then the observer can detect the following frequency,

$$\omega_{pr} = \omega_{ab}\left(1 \pm \frac{v}{c}\right). \tag{6.17}$$

The atom in a gaseous medium chaotically moves in all directions because of which are we able to see Doppler−broadening spectral line shape, and this line shape reflects ensemble distribution of velocities along the Z-axis and the velocities between v_z to $v_z + dv_z$ is obeyed Maxwell-Boltzmann distribution in thermal equilibrium T which can be express in the following way,

$$N_i(v)dv = \frac{N_i}{v_s\sqrt{\pi}} exp\left[-\left(\frac{v}{v_s}\right)^2\right] dv, \tag{6.18}$$

where $v_s = \sqrt{\frac{2k_BT}{m}}$ is most probable velocity of the atoms with mass m and k_B is Boltzmann constant. Equation 6.17 give us,

$$dv = \frac{c}{\omega_{ab}} d\omega_{pr}. \tag{6.19}$$

After substituting equation 6.18, into equations 6.19 and we get the number of atoms in the interim of ω_{pr} to $\omega_{pr} + d\omega_{pr}$ shift with absorption frequency ω_{ab} as following,

$$N_i(\omega_{pr})d\omega_{pr} = \frac{cN_i}{\omega_{ab}v_s\sqrt{\pi}} exp\left[-\left(\frac{c\left(\omega_{pr} - \omega_{ab}\right)^2}{\omega_{ab}v_s}\right)\right] d\omega_{pr}. \tag{6.20}$$

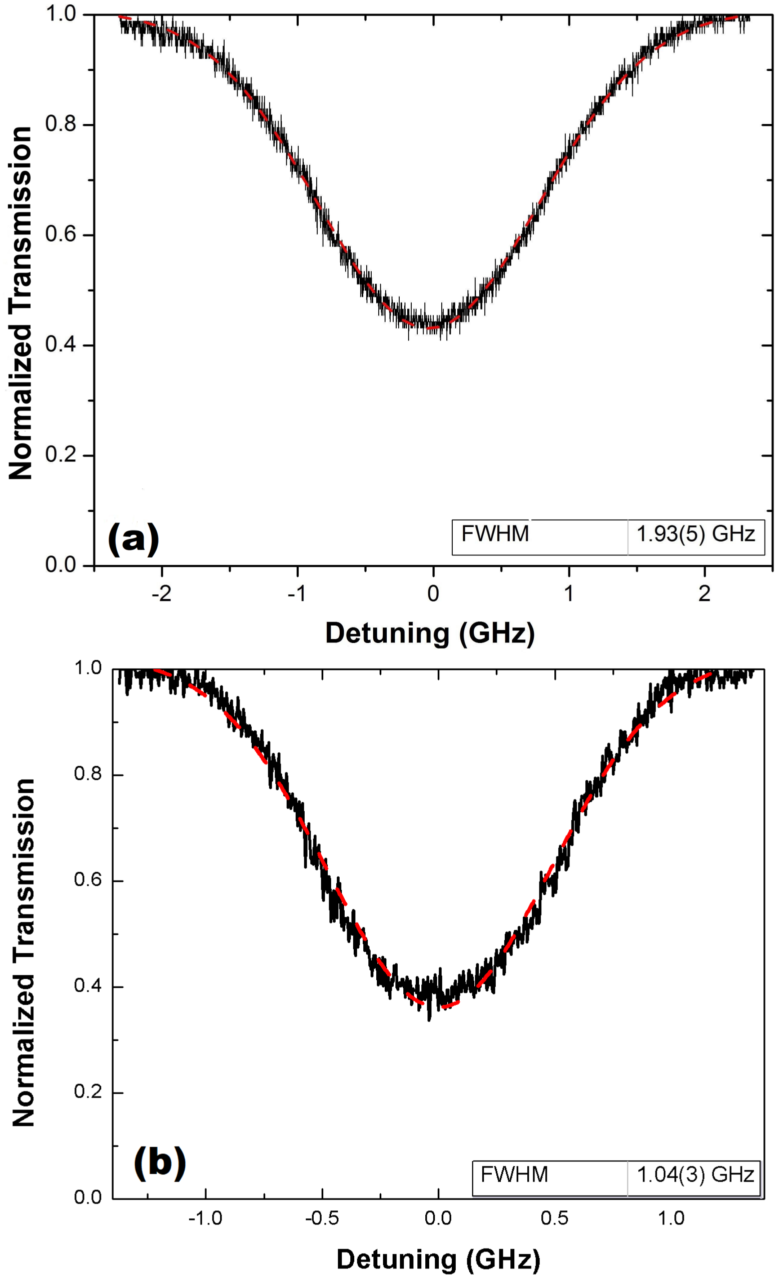

Figure 6.4: Normalized transmission as a function of detuning on the 10 cm vapour cell of natural abundance potassium (^{39}K) in the weak probe regime. Fitted with Gaussian function denoted as red dashed lines. Figure (a) represents 4S → 5P D_2 transition with 1.48 $\times 10^{-3}$ I_{Sat} probe intensity at 110.5 °C cell temperature and the FWHM is 1.93(5) GHz. Similarly in figure (b) represent 4S → 4P D_2 transition with 4.8 $\times 10^{-3}$ I_{Sat} probe intensity at 53.5 °C cell temperature and FWHM is 1.04(3) GHz.

From equation 6.20 it is trivial to determine that the FWHM (Doppler width) is following,

$$\Delta\omega = \left(\frac{2\omega_{pr}}{c}\right) \cdot \sqrt{2\ln 2\left(\frac{k_b T}{m}\right)}. \tag{6.21}$$

The equation 6.21 tells us that Doppler width is reliant on the angular frequency of probe field. After calculating the ratio of Doppler widths for the two transitions (assuming the same temperature) using the equation 6.21. And we found $\frac{\Delta\omega_{405}}{\Delta\omega_{767}} \sim 1.90(2)$ and comparing with the ratio of experimental results the ratio was $\frac{\Delta\omega_{405}}{\Delta\omega_{767}} \sim 1.86(5)$, therefore our theory agreed with our experimental results. The experimental spectrum presented in the following figure 6.4, in the example of potassium, the ground state hyperfine splitting, which is 461.7 MHz, is shorter than the Doppler width. The D_2 and D_1 transitions taken with 23 mm and 75 mm cell length respectively, because of that we have to different cell temperature.

We know that the emitted (transmitted) or consumed radiation power $P(\omega)d\omega_{pr}$ is correlated to the atomic density $\mathrm{N_i(\omega_{pr})d\omega_{pr}}$, and gives us the following intensity profile,

$$I(\omega_{pr}) = I_0 exp\left[-\left(\frac{c(\omega_{pr}-\omega_{ab})}{\omega_{ab}v_s}\right)^2\right]. \tag{6.22}$$

This is the intensity Gaussian profile detected by the calibrated photodiode.

6.2 Absolute absorption on the 4S → 5P transition

This section will demonstrate and explain the atomic structure of potassium on the 4S → 5P line with the theoretical transmission spectra computed with our theoretical model. We are going to report the experimental setup with great details and the procedure of the experiments. The results for estimating the transmission of a probe beam within a 10 cm hot potassium thermal cell containing a natural abundance of potassium vapour are shown and discussed.

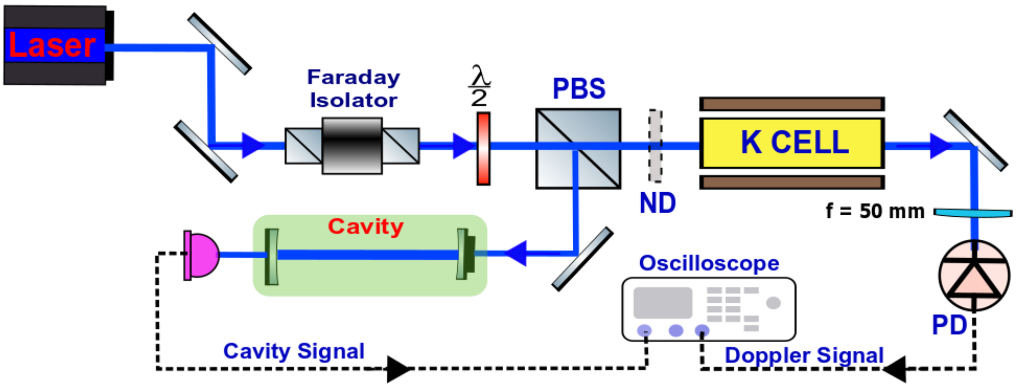

Figure 6.5: Schematic layout of our experimental setup. The laser beam from an external cavity diode laser (ECDL) is passed within an optical isolator (OI) and passes through a $\lambda/2$ wave plate and then a polarizing beam splitter (PBS). Single beam sends to a cavity (Etalon) to calibrate the frequency axis. In contrast, another beam sent through an ND filter then to a hot potassium vapour cell and focused using a 50 mm lens onto a photodiode (PD), both cavity and detected signal by PD and visible in the oscilloscope.

6.3 Experimental details

This subsection will explain the experimental procedure and the details of results for the absolute absorption of Doppler broadening spectroscopy of the 4S → 5P D line transition using a 10 cm hot thermal cell which contains a natural abundance of potassium. In this experiment, we used a home built ECDL in Littrow configuration with an output of 1.2 mW power, which produced a light field passed through an optical Faraday isolator and passes through a half-wave plate than a polarizing beam splitter (PBS) to produce a probe light. The schematic diagram of the experimental setup is in the figure 6.5.

The reflected beam from PBS sent to a Thorlabs SA200−3B scanning Fabry-Perot cavity, which has 1.50 ± 0.01 GHz free spectral range used for frequency axis calibration. Another part of the beam is sent to a 10 cm thermal vapour cell as a probe beam, the probe intensity control using a neutral density filter (ND) just before the vapour cell. The probe beam focused with f = 50 mm lens into a photodiode (PD). The PD produced a voltage equivalent to the incident intensity of the beam, with a PD circuit combined with a low-pass filter circuit to eliminate higher-frequency turbulence. Great attention was exercised to guarantee the cell was at thermal balance with the copper cube

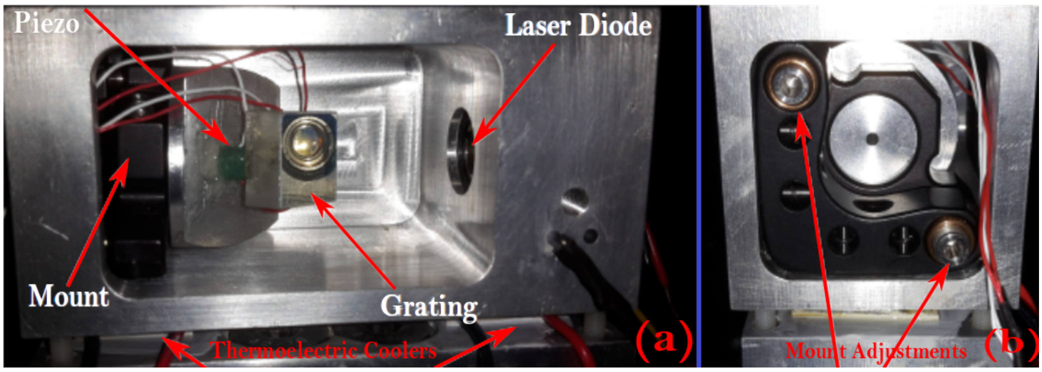

Figure 6.6: Photographs of the blue laser system employed in our experiments, where figure (a) displays the output face and (b) show the back end of our laser.

surround. A thermocouple is used in between the vapour cell and copper surrounds to monitor and record the temperature of the potassium vapour.

6.3.1 Laser system

Extended Cavity Diode Lasers (ECDL) are commonly used for atomic physics experiments due to the affordable and dependable method of producing a few mW of single-mode tunable laser output power, but some short-wavelength ECDL quite challenging to build and stabilize. Figure 6.6 is a typical image of our blue laser in Littrow configuration. This laser system consists of a laser diode (Thorlabs DL5146 - 101S - 405 nm) with an aspheric collimating lens (Thorlabs C671TME - 405 nm), reflective Holographic Grating with 3600 mm^{-1} (Thorlabs GH13 - 36U - UV), and a kinematic mount (Thorlabs KM05) to fine adjust laser cavity length, two Thorlabs AE0203D04F piezoelectric actuators and control/maintain the temperature of two multi comp thermoelectric coolers regulated through a Wavelength Electronics temperature controller (MPT 2500 series). Inside picture 6.6(a), we can notice that the grating is installed on the pair of piezoelectric actuators applying epoxy glue. This grating is fixed on the mirror install as presented in the picture 6.6(b), which provides grating to modify the grating angle. The grating was installed in such a way that the grating lines were vertical to the optical table, and the long axis of the laser light generated by the laser diode was parallel to the lines. And the whole extended cavity lies on the pair of thermoelectric coolers.

6.3.2 Tuning procedure

This particular laser tuning procedure was slightly tricky; at first, the output laser light was linked to a Fabry−Perot cavity (Thorlabs SA200) and a wavelength meter (HighFinesse WS−5). We have set our set position for the temperature controller at 1.00731 V, and the equivalent laser temperature was 20°C. In the grating, the vertical and horizontal directions are coupled, which leads to an iterative method to align the laser in the following ways,

✓ First, the laser current was fixed to merely under the threshold current.

✓ Employing a power meter or by eye, and the vertical alignment of the grating was modified to maximize the laser's producing power. Repeat this process many times by reducing the laser current by small steps to get a minimum threshold current.

✓ The scanning Fabry−Perot cavity was employed to check the laser was in single mode or not. If the cavity signal is contained peaks as presented in figure A.2, we can assume the beam is single-mode; thus, we can be confirmed that vertical alignment is finely adjusted.

✓ We were then using a wavelength meter, we measured or recorded the wavelength of the laser beam.

✓ We can change the wavelength using the horizontal mount adjusting screw slightly to get the desired wavelength.

✓ In the end, we used a heated potassium vapour cell along with a wavelength meter to examine the laser was on the atomic transition or not. If we see a Doppler broadening signal in a digital oscilloscope at the required wavelength, we can conclude that our laser was on the transition.

✓ Suppose we have any mode hop near the spectrum. In that case, we can slightly change the temperature of the laser diode using the temperature controller. The temperature change only changes the tiny amount of wavelength of our laser, and we get mode to hop free spectrum.

The procedure mentioned above was repeated many times until the desired wavelength arrived. Remark that the required wavelength was only achieved for a particular laser diode current only over the threshold current (normally, the required wavelength appears at different laser current even as well beyond the threshold current). Beyond this current, our laser does not remain in the single-mode. We believed this kind of behaviour, because of the diode not holding an AR coating, which leads to a standard laser output power on the transition was ∼ 1.2 mW.

The laser was scanned over a triangular potential ramp ∼ 4 V at 12 Hz (which is generated by a Thandar function generator) to a piezo stack actuator via Thorlabs piezo controller, which allows us to manage ∼ 6 GHz scanning range just before a mode hop/jump which is generous enough to examine some entire Doppler broadened spectrum.

6.3.3 Integration of vapour cell

Integration of vapour cell within a compact copper box is really important because, as we mentioned, we need to heat the vapour cells sufficiently high to increase the vapour pressure within the cell. In figure 6.7 our 10 cm potassium vapour cell were within a copper box to heat the cell evenly, the copper box consists of two-part, and it can be attached using two screws. The cell was evenly heated using the four resistive heaters on both sides of the individual copper box, which can heat the cell from room temperature to 130°C evenly. The copper blocks both consist of two-beam windows (holes) in both ends, from where the laser beam can enter and exit in the copper box. In between the copper box and table, a thermal insulator has been placed on insulating the copper box from the rest of the table. A small hole was made to insert a thermo-couple and monitor the temperature in the top. Since the holes are the coolest area of the cell, the potassium is condensed frequently at the window of the thermal cell. This problem is fixed by heating the windows by attaching two resistive heaters continuously for a few days. The photodiode signal was registered using a digital oscilloscope (Gw Instek GDS 2014) to read the Doppler broadened profile. And the cavity peaks were employed to transform the measured time scale to frequency, which is discussed in the following subsection A.2.1 with great details.

The weak probe regime was set using a variable ND filter just before the thermal cell one can also change the intensity of the probe light incident on the thermal cell typically from 1×10^{-4} $I_{Sat} \rightarrow 1 \times 10^{1}$ I_{Sat} as mentioned

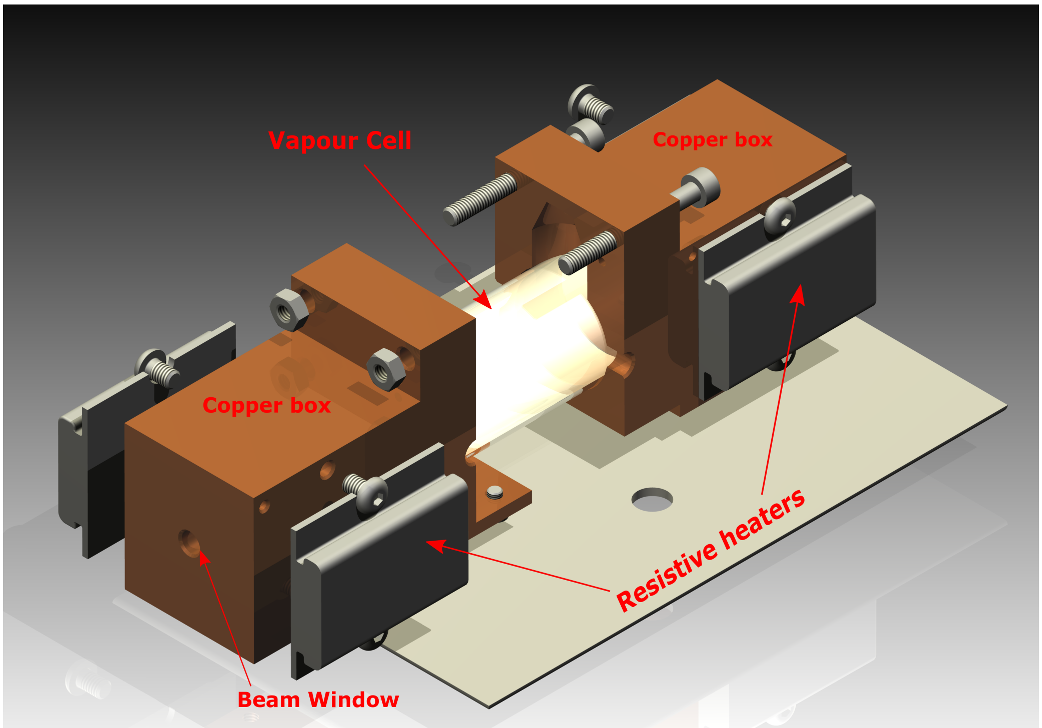

Figure 6.7: A CAD sketch of the hot potassium cell created by a previous QLM PhD scholar Micheal Köppinger.

in figure 6.5 and measured the transmission. The spectrum was taken and mean over many times at the least transmission spectrum. We measured the probe beam waist using the knife−edge technique just before the cell and fitted the data using Origin 8.6. The incident intensity was computed by measuring the power of the probe light. We took all the data when the cell came under thermal equilibrium. In the end, the Doppler spectrum was fitted with the data using the ElecSus program to examine the quality of the theoretical model as well as to estimate the temperature of the atoms.

6.4 Experimental results and discussion

6.4.1 The weak probe regime in D lines

For our future experiments, we gave the most important on D_2 transition, and we compare it with D_1 transition. In figure 6.8, we have measured the least transmission of a probe light with respect to incident intensity, which

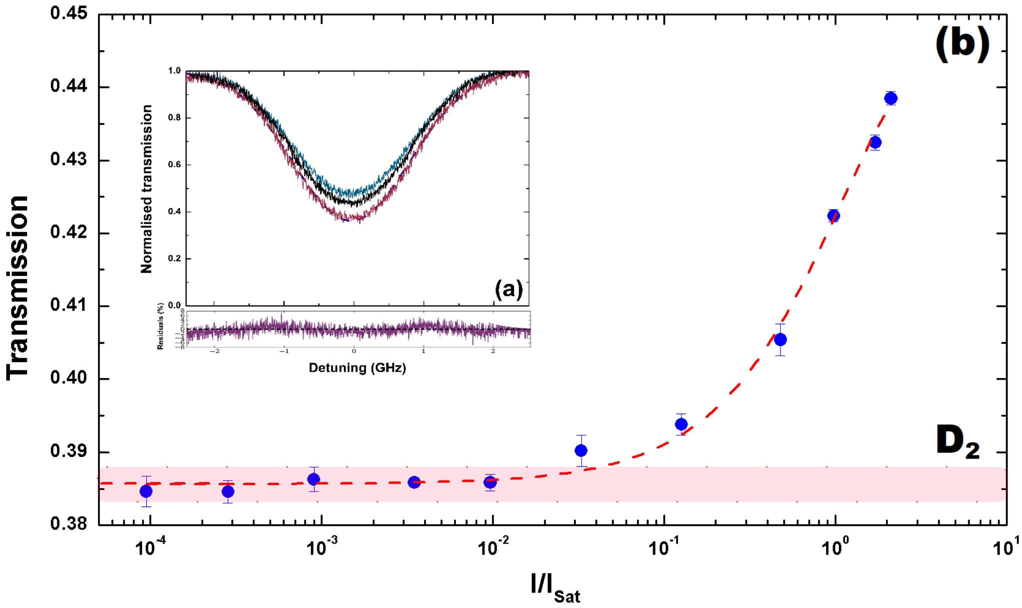

Figure 6.8: In plot (a), the transmission is a function of detuning. The multiple colours represent different probe intensities; refer to the main text for details. The brown weak probe data point fitted with ElecSus and residuals is included below. In plot (b) the probe intensity which is normalized by saturation intensity (I$_{Sat}$ = 57.6 mW/cm^2) for a natural abundance potassium, which is resonant with D$_2$ line of 4S → 5P transition. The data was taken at 110.5°C measured temperature. The pink shaded area is a weak probe regime prediction of ElecSus, and the red dashed line is exponential fitting for greater visualisation of the trend of the data points.

is normalized with saturation intensity with D$_2$ atomic transition. Each blue points represent the least transmission of probe light with size $w_x = 1.95 \pm 0.002$ mm and $w_y = 1.84 \pm 0.003$ mm and passed within a hot vapour cell of temperature 110.5°C.

The plot 6.8 (a) indicates the minimum transmission with respect to detuning. The non-identical colours (brown, black and blue) represent individual probe intensities where I$_{brown}$, I$_{black}$ and I$_{blue}$ corresponding to incident intensity of the order of 1.48×10^{-3}I$_{Sat}$, 2.03×10^{-1}I$_{Sat}$ and 8.61×10^{-1}I$_{Sat}$ respectively. The experimental red spectrum is fitted with the adapted ElecSus program, mentioned as black dashed line in figure 6.8(a) and the residuals of fitting are also presented in the figure. The residuals for the fitting data reveal the quality of the model and its indication that the ElecSus is effortlessly versatile to predict transmission spectrum at the higher principal quantum number and other alkali metals like Rb and Cs, respectively. At higher intensity, the data point is relatively noisy compared to low probe intensity, and at the higher probe intensities, the photodiode was saturated. This indicates the dependence of signal−to−noise ratio on the experimental equipment.

The figure 6.8(b) presents the minimum transmission as function of probe intensity which is normalized with the saturation intensity (i.e $\mathrm{I}_{\mathrm{Sat}}$ = 57.6 mW/cm^2) and we observed the incident intensity enter in the weak probe part at the $\sim 1\times10^{-2}$ I/$\mathrm{I}_{\mathrm{Sat}}$ and the decrease of incident intensity does not change the transmission profile, the shaded regime are ElecSus predicted weak probe regime. We fit the data point with an exponential function in order to see the clear trend of the data point.

Figure 6.9 represents the D_1 transition as we just mention the D_2 line and the figure reveals a similar kind of pattern indicates that the weak probe regime is $\sim 5 \times 10^{-2}$ I_{Sat}. Again, in 6.9(a) shows transmission at the three different incident intensities, black, red and blue colours represent the transmission spectrum. And the $\mathrm{I}_{\mathrm{black}}$, $\mathrm{I}_{\mathrm{red}}$ and $\mathrm{I}_{\mathrm{blue}}$ corresponding to incident intensity of the order of 2.05 $\times10^{-3}\mathrm{I}_{Sat}$, $1.87\times10^{-1}\mathrm{I}_{\mathrm{Sat}}$ and $6.47\times10^{-1}\mathrm{I}_{\mathrm{Sat}}$, since the intensity difference between $\mathrm{I}_{\mathrm{red}}$ and $\mathrm{I}_{\mathrm{blue}}$ is small, so the spectra almost superpose with each other. The residuals of theoretical fitting to the black data points show the quality of the theoretical prediction. In this experiment, there is a large dependence of signal−to−noise ratio on experimental equipment, as we have just discussed above.

Figure 6.9(b) indicates the minimum transmission as function of probe intensity which is normalized with the saturation intensity (i.e $\mathrm{I}_{\mathrm{Sat}}$ = 58.8 mW/cm^2) and we have observed the incident intensity enter in the weak probe regime at the $\sim 5\times10^{-2}$ $\mathrm{I}_{\mathrm{Sat}}$ and a decrease of in incident intensity does not alter the transmission spectrum as we have shown in figure 6.8(b) the red shaded regime indicates ElecSus predicted weak probe regime. We fitted the experimental blue data point with exponential function to trace the data point for better visualization as we discuss for D_2 transition.

In the case of D_2 transition Δ_1 and Δ_2 are unknown for ^{40}K and ^{41}K isotope as shown in figure 6.1. For our ElecSus modeling, we assume the isotope shifts for D_2 transition is similar to isotope shifts of D_1 line of 4S → 4P transition,

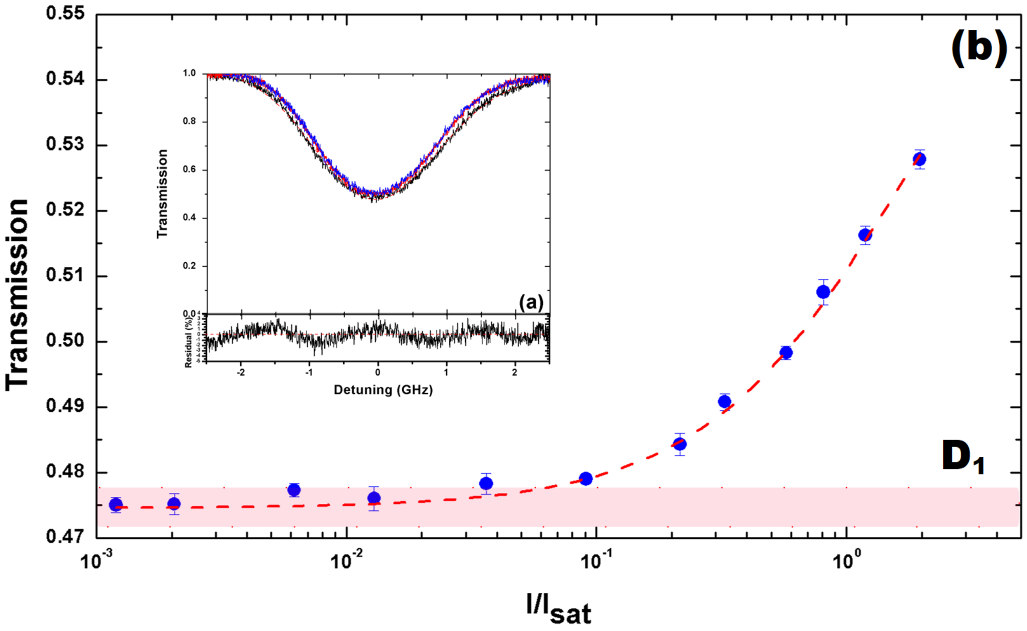

Figure 6.9: In plot (c) the transmission as a function of detuning for D$_1$ lines of 4S → 5P transition. The different colours (black, red and blue) represent individual probe intensities. Here, the black data point in the weak probe part, fitted with the ElecSus and residuals, is presented below .n plot (d) the probe intensity which is normalized by saturation intensity (I_{Sat}=58.6 mW/cm^2) for a natural abundance potassium thermal cell resonant with D$_1$ line. Specific data was taken at 123.5°C measured temperature. The pink shaded region is a weak probe regime prediction of ElecSus, and the red dashed line is for visualization of data points.

which are $\Delta_1 = 235$ MHz and $\Delta_2 = 454.2$ MHz respectively, which is in the order of MHz. By running the simulations assuming our guess was accurate, the shift in transmission spectra because of variation in isotope shift was set to not be previously measured because of the feeble isotope abundance of ^{40}K and ^{41}K and laboratory turbulence. Hence our ElecSus fitting on the D$_2$ transition was produced employing the D$_1$ transition isotope shifts of 4S → 4P transition. By looking at residuals in figure 6.8, 6.9. and 6.10 it is clear that our approximation is justified.

6.4.2 Temperature Dependent D line

In figure 6.10 we have plotted the normalized transmissions of D$_1$ and D$_2$ transitions with different cell temperatures at their respective weak probe regime. Figure 6.10(i) presents the transmission line on the D$_2$ transition line at 95.5 ± 0.6°C, 110.5 ± 0.5°C and 122.8 ± 0.4°C respectively, which can be identified by black, red and blue data points. We compute the RMS error between theory and experiment of the order of $\sim 10^{-3}$ for all three data point and the corresponding probe intensities are 1.95×10^{-3} I_{Sat}, 1.48×10^{-3} I_{Sat} and 2.13×10^{-3} I_{Sat} respectively. Similarly for D_1 transition as shown in figure 6.10(ii) shows transmission spectra at 93.5 ± 0.5°C, 109.5 ± 0.5°C and 123.8 ± 0.3°C respectively in the order of blue, red and black. The rms errors among theory and experiments of the order of $\sim 10^{-3}$ which was similar as D_2 and the corresponding probe intensities are 2.05×10^{-3} I_{Sat}, 2.01×10^{-3} I_{Sat} and 2.13×10^{-3} I_{Sat}, respectively. The individual residuals for these three unique temperatures are presented under the central figure 6.10. The temperature of the vapour cell was estimated after fitting the experimental data with ElecSus and the limitations of fitting due to an imperfect linearization of the frequency scan due to an inadequate scan range creating a limiting quantity of cavity peaks; hence, the fitting method is susceptible to the scan linearization. For example, in the case of rubidium, the sub−Doppler spectroscopy is employed to produce multiple frequency labels to linearize the scan [185]. Though, our linearization technique seems to be significantly better, as manifested in the character of the residuals of the fits.

The residuals on the fitting for the low-temperature transmissions on each plot are more significant than that of the additional fits, we considered due to a small gradient of least transmission concerning temperature and also because of a less percentage of absorption at a weaker temperature because of the lower number density. Hence the S/N ratio on the estimation of the minimum transmission is less than that of the different estimations, which drives to a significant error on the adapted temperature as the minimum transmission is the most susceptible portion of the signal. Hence, at adequately higher temperatures and experimental accuracy, the ElecSus displays an accurate thermometric instrument.

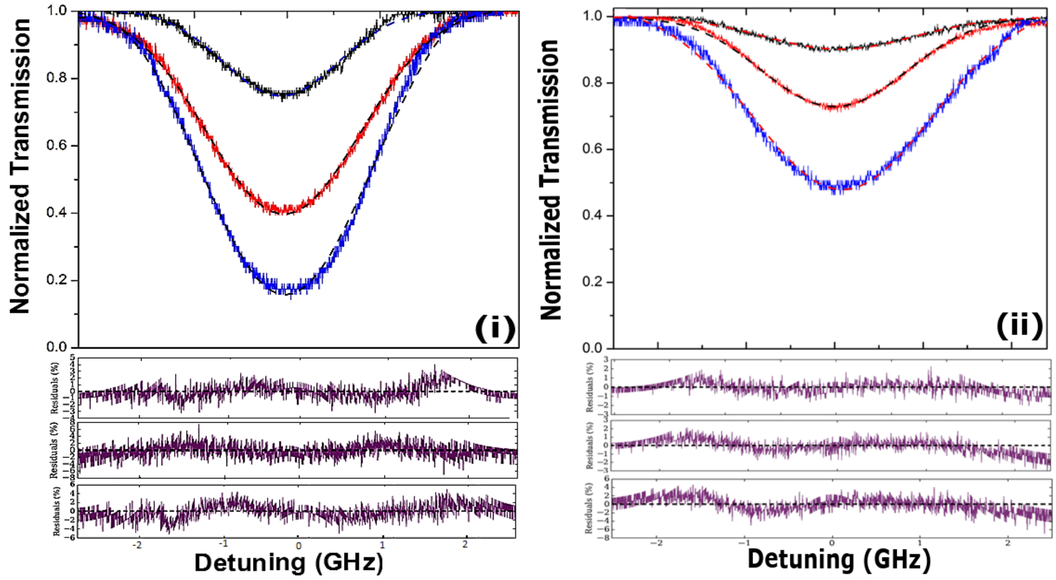

Figure 6.10: Graphical representation of the least probe transmission as a function of the temperature of potassium thermal cell, the beam resonant with the D_2 (i) and the D_1(ii) lines. The theoretical fitting by ElecSus indicates by black dashed line inside the data points. In plot (i) presents the transmission spectrum on the D_2 transition at 95.5 ± 0.6 °C, 110.5 ± 0.5 °C and 122.8 ± 0.4 °C respectively, which can be identified by black, red and blue data points. In plot (ii) notes transmission line on the D_1 line of the transition at the 93.5 ± 0.5 °C, 109.5 ± 0.5 °C and 123.8 ± 0.3 °C respectively in the order of blue, red and black colour respectively. The residuals for each temperature are shown below.

6.5 ElecSus as a thermometric tool

It is challenging to measure the actual temperature of the atoms inside the hot vapour cell directly because it is clear that we cannot place our thermal probe inside the vapour cell. Typically in everyday measurement, we measure the temperature of the glass cell and consider thermal stability achieved within the atoms and glass of the cell. This experiment process is not the most precise and efficient because the atomic temperature is not calibrated with the probe beam and the thermal connection within the cell and probe. Hence, in this section, we will present a detailed approach for achieving accurate atomic temperature using the Doppler broadening transmission outline. Similar kinds of studies have already been done, and we closely follow the following article [178].

As we see in equation A.53, the absorption coefficient is proportionate to the atomic number density. The number density is also very sensitive to the transmission, and the number density varies exponentially in temperature, and the most important is the line centre transmission, which is particularly susceptible to temperature. This fact creates ElecSus potentially valuable as a thermometric tool. In figure 6.11, the red data points represent the temperature measured by fitting transmission spectra to ElecSus and the black data point shows which corresponding experimental measurement temperature measured by the thermocouple directly. In the figure 6.11 we can see a temperature offset between thermocouple and ElecSus predicted temperature, which is problematic when we try to measure the exact temperature of the atoms. Inside both plots, in figure 6.11 we have plotted the fitted temperature (T_F) predicted by our model and the estimated thermocouple temperature (T_T). In the fitting a consistent offset among the fitted temperature and the thermocouple temperature, the gradient (m) and offset (c) within two temperatures present in table 6.1. We assume to recognise a gradient of $m = 1$ and the fixed offset among all data points if there was a calibration error of the thermocouple. We can expect the calibration error because the thermocouple measured a hotter temperature just outside the cell. After all, the copper block was hotter than the cell.

Our determined gradient and offsets agree with this within error; therefore, the error in data indicates the calibration deviation of the thermocouple and bad thermal connection among the cell and thermocouple. This data tells us that the ElecSus is a robust tool to measure the temperature of atomic vapours where straightforward measurement is not possible. In the figure 6.1, it's been seen that the error in T_F is not fixed due to the minimum transmission having a changing gradient with temperature. For example, at the transmission of ~ 0.9, while the gradient of transmission with temperature is much less than ~ 0.5. Hence the error in the fitting temperature is more prominent at low absorption, but at a higher temperature at near-total absorption, the fitting error was small.

]

Transition	Plot	m	c(°C)
$4S_{1/2} \rightarrow 5P_{1/2}$ (D_2)	(a)	1.00 ± 0.006	2.48 ± 0.02
$4S_{1/2} \rightarrow 5P_{3/2}$ (D_1)	(b)	0.98 ± 0.004	2.52 ± 0.08

Table 6.1: The calculated value of the gradient and offsets from the inside plots in figure 6.11.

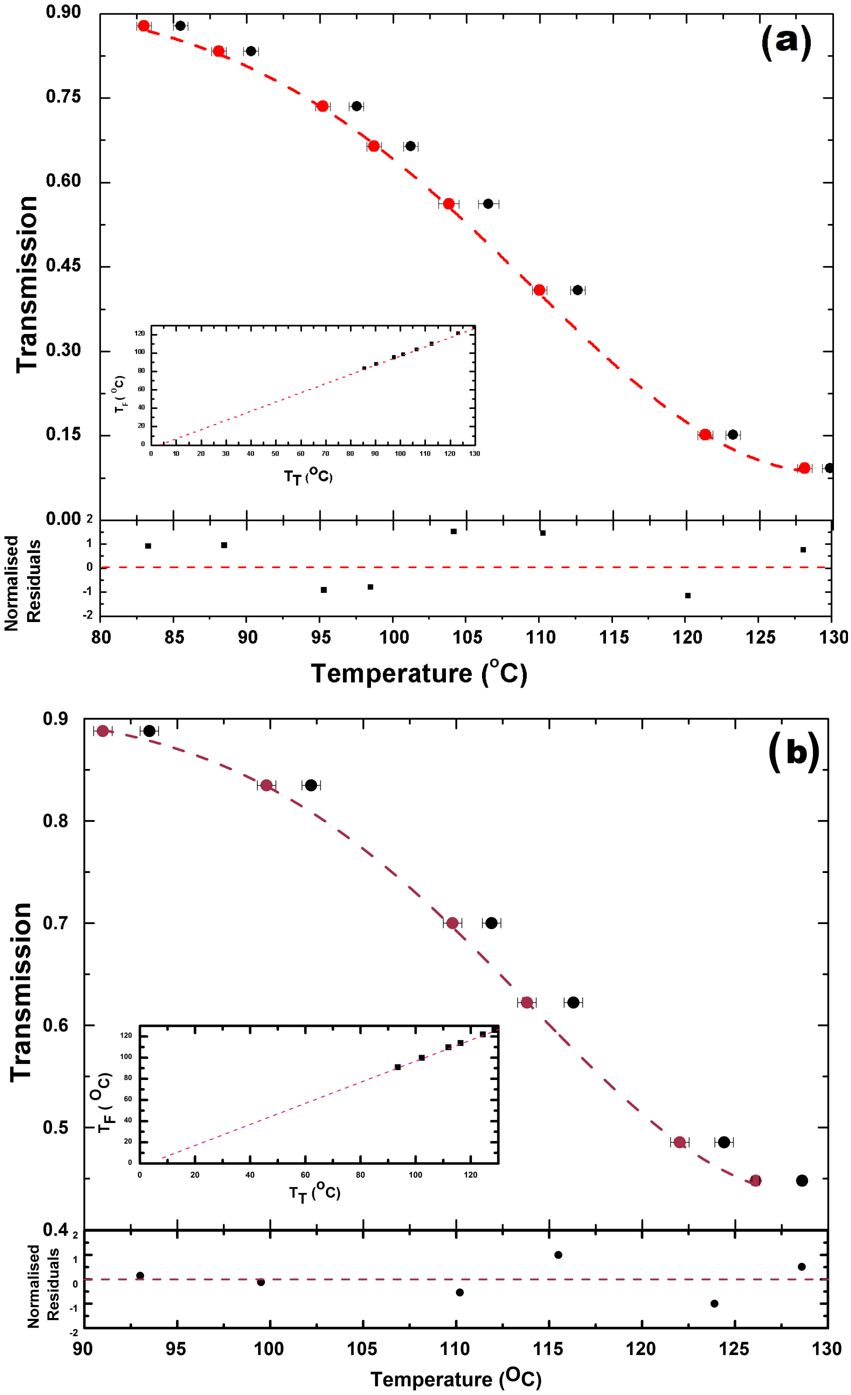

Figure 6.11: Theoretical minimum transmission calculate using ElecSus (Red dashed line) with the experimental measurement with D_2(a) and D_1(b) resonant light field of 4S → 5P atomic transition. The temperature of the red data point is calculated by fitting measured transmission spectra to ElecSus, and the black data point is the temperature measured by the thermocouple. We have also included the normalised residuals of the red data point below. Inside the plot, we show a plot of the fitted temperature and the thermocouple temperature.

In our experiment, the error is dominated by noise on the measured voltage. The main contribution of noise is coming from laser, photodiode and oscilloscope. Our weak probe beam power is in an nW regime; therefore, noise from other light sources is susceptible in our experiments, and we have to take care of these problems. As discussed earlier, to reduce noise, we believe it's good to use a higher quality photodiode and oscilloscope. By implementing the above discussion, we are capable to reduce the noise on the determined voltage and the error in the temperature, which increases the precision of ElecSus as a thermometric tool. In figure 6.1 we may see that the residuals for all of the plots are generally positive because the minimum transmission is estimated by considering a mean at the base of the transmission spectra to exclude noise. This mean uses tiny additions from points that are only beyond the minimum, and the mean is shifted in significantly higher than the predicted value.

6.6 Rydberg states excitation

Rydberg atoms, where an excited atom has individual or more than one electrons in a higher principal quantum number (n) states. As Rydberg atoms are extremely large, it has large polarizability, which introduced strong, controllable dipole-dipole interaction, which is scale as $\sim n^4$ and long radiative lifetimes scale as $\sim n^3$. Just mention properties are beneficial to make neutral atomic qubits, which is the building block of quantum gates. The most commonly used for Rydberg excitation are alkali atoms. Recently experimentalist typically explores Cs [186, 187] and Rb [188, 189], but K [64, 190] has rarely studied.

Usually, the two-photon excitation with the typically normal excitation scheme (where $\lambda_C < \lambda_P$) regularly reported in thermal cell and the cold ensemble of atoms [191]. But in the K system, the EIT spectrum can generate utilizing two-photon excitation with an inverted ladder-type arrangement, i.e. $\lambda_P < \lambda_C$, where the wavelength of the probe beam (404.5 nm) is significantly less than the coupling beam (990 nm).

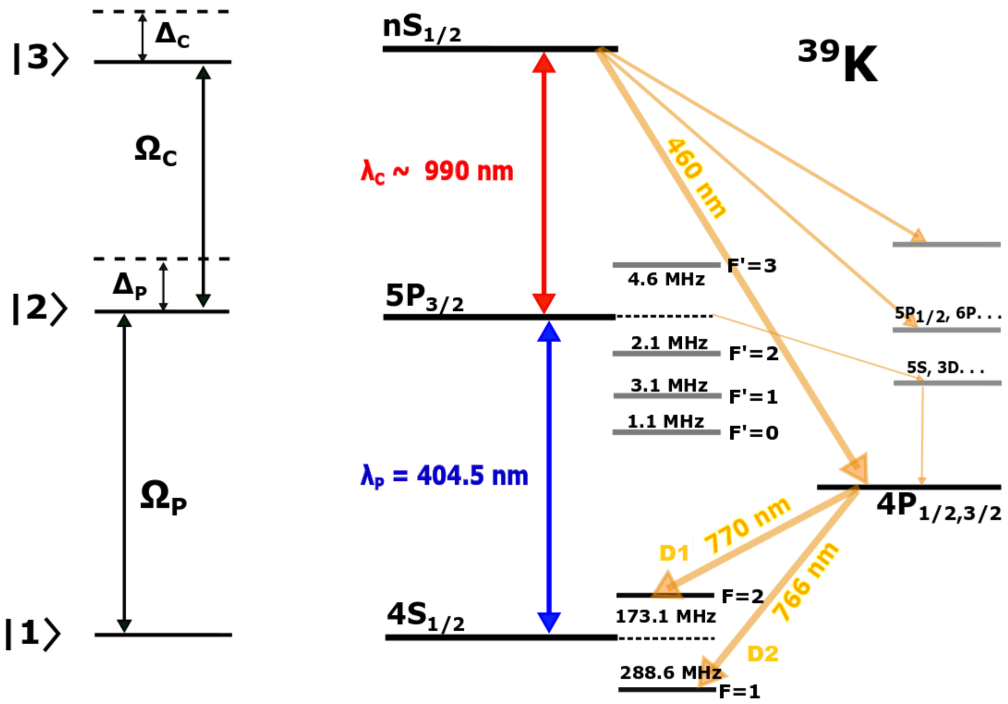

Figure 6.12: Energy level diagram for two-level excitation scheme to excite ^{39}K atoms to its *ns* Rydberg levels using inverted ladder scheme, where the probe and pump beams are 404.5 nm and 990 nm, with Rabi frequencies Ω_P and Ω_C respectively. It presents the $4S_{1/2}$ ground state, $5P_{3/2}$ is the intermediate state and the $nS_{1/2}$ is the Rydberg state, and other alternative decay channels are also presented. The diagram is adopted from [190].

The two-photon excitation is a coherence process due to the coherent interaction between the probe and coupling lasers beam with atoms. The ladder-type EIT have the advantage compare to electromagnetically induced absorption (EIA) [192, 193], or Autler-Townes splitting effect (ATS) [194] because EIT generates high-resolution Rydberg spectroscopy signal and provide a direct optical detectable signal for the highly excited Rydberg states [195]. By solving the density matrix of the optical Bloch equations, one can model the Inverted ladder system as [190]. In the numerical calculations, it is very important to include all the additional decay channels as presented in figure 6.12. Both inverted and non-inverted schemes, the EIT features appear, when $\Delta_C + \Delta_P = (\omega_P - \omega_C)v/c$ is satisfied and the wavelength ratio also influences the size and width of the transparency window.

6.7 Outlook

Here in this chapter, we have investigated the absolute Doppler broadening absorption of a probe light, which is resonant with 4S → 5P transition line. Thek weak probe section was estimated for a 10 cm hot potassium thermal cell by changing the incident probe intensity and measuring the minimum transmission. For 4S → 5P transition, we have resolved the weak probe regime $< 10^{-2}$ I/I_{Sat} for D_2 and D_1 transitions respectively. We also found an exceptional agreement of weak probe beams among ElecSus and experimental estimations with different temperatures on both transitions with RMS error $\sim 10^{-3}$. Finally, we discussed the prospects of Rydberg excitation employing the 4S → 5P transition in an an inverted ladder scheme.

Chapter 7

Outlook: Future direction and conclusion

The technique for the preparation of cold ^{39}K atoms using a pyramid magneto optical trap has been studied and presented in great detail, closely following the articles [196, 197] and our technique has two main purposes, which is followings,

✓ To develop the laser systems and locking needed to produce a MOT such that they could then be integrated into the main experiment.

✓ To test the pyramid MOT functions at 767 nm such that in the future it could be integrated into a second generation apparatus.

On the other hand ultracold Cs already been investigated by [198]. For Rydberg excitation, the next step is to combine the potassium source with a Cs MOT and then load both atoms into optical tweezers. This provides the basis for Rydberg excitation and there are interesting perspectives in using two intra-species like ^{85}Rb and ^{87}87Rb [199, 200]. Interestingly, for the Rydberg excitation it is not necessary to cool down the atoms in their ground state.

On the other hand to trap a single molecule like ^{39}K^{133}Cs, the ensemble of atoms need to cool down more to its quantum degeneracy regime; therefore, we aim to pursue a pioneer strategy similar to that demonstrated for NaCs in [201–203] at Harvard, also for Rydberg excitation with ^{39}K or ^{133}Cs require ultracold ground-state atomic ensemble. Therefore, after getting the pyramid

MOT within the chamber, the following steps need to be taken to produce an ultracold ensemble of ^{39} K/^{133}Cs atom.

7.1 Future direction

The next step is to integrate the pyramid MOT into a next-generation tweezer apparatus to produce 3D-MOT ^{39}K atomic species and load atoms in the optical tweezers, which is the foundation of any future experiments like single molecules or Rydberg excitation. We have already shown that our pyramid MOT works for Rb and Cs [140, 204, 205]. My work has shown that it also works for K and so we can now build a next generation apparatus using a pyramid source which will lead to better vacuum lifetimes in the science cell.

For ^{39}K^{133}Cs single molecules one can cool down ^{133}Cs atom simultaneously along with ^{39}K at the same science chamber. The trapping light is provided by three independent retro-reflected counter-propagating MOT beams from three orthogonal directions as presented in [197]. For cooling and trapping ^{39}K and ^{133}Cs atoms in a 3D-MOT with 852 nm and 767 nm beam, and the paths are regulated and controlled individually.

7.1.1 Single atom trapping

For a single atom experiment, the MOT size or the number of atoms within the MOT need not be huge; only 10^5 numbers of atoms are more than sufficient. Therefore, trapping of a single-atom like experiment requires a laser with very little output power in the order of a few mW for cooling and repump beams. The tweezers or micro trap is created by focusing a far-off resonant Gaussian laser light with species-specific wavelengths for specific atomic species as presented [206].

For micro trap and fluorescence detection, we in our lab used a high numerical aperture (NA) objective lens, the lens from special optics with NA = 0.55. The objective lens is diffraction limited at 767, 780, 852, and 1064 nm. The tweezer beams have a Gaussian intensity profile, and the trapped light focused at the position of the atoms has a waist of $\sim$1 μm. The same high numerical aperture (NA) lens accumulates the fluorescence photons to produce an image on a electron-multiplying charge-coupled device camera as presented in figure 7.1.

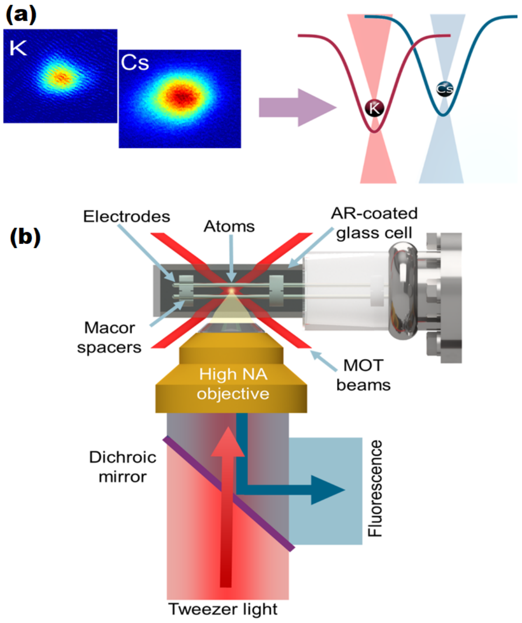

Figure 7.1: In figure 7.1(a) two individual atoms trapped side-by-side from two individual 3D-MOT (here we present an ideal scenario, at the time of writing only Cs MOT in our chamber). 7.1(b) Both tweezer beams are combined on a dichroic mirror and focussed by an objective lens. The position of the trap in the focal plane move by changing the driver frequency of an upstream acoustic-optical deflector (AOD). The figure is taken from our current experimental optical setup made by one of our PhD student Vincent Brooks [206].

In figure 7.1 (a) shown schematic of trapped, ^{39}K and ^{133}Cs MOT side-by-side, two individual atom trap by tweezer laser beam separately (at the time of writing only Cs MOT in our chamber and ^{39}K will be trap in the near future), it is also possible to manipulate a single ^{39}K Rydberg atom in the micro trap. In figure 7.1 (b), the tweezer light enters through a dichroic, and atomic fluorescence is also separated from the tweezer light using the same dichroic and detected using an Andor iXon 897 Ultra EMCCD, providing a great spatial resolution of the atom. The science cell is made up of an AR-coated glass cell and the electrodes shown in the figure. After trapping the single atom in a micro-optical trap for single-molecule experiments or Rydberg excitation, the trapped atom need to cool down to the ground state; therefore, in the next section, we present a short description of how one can

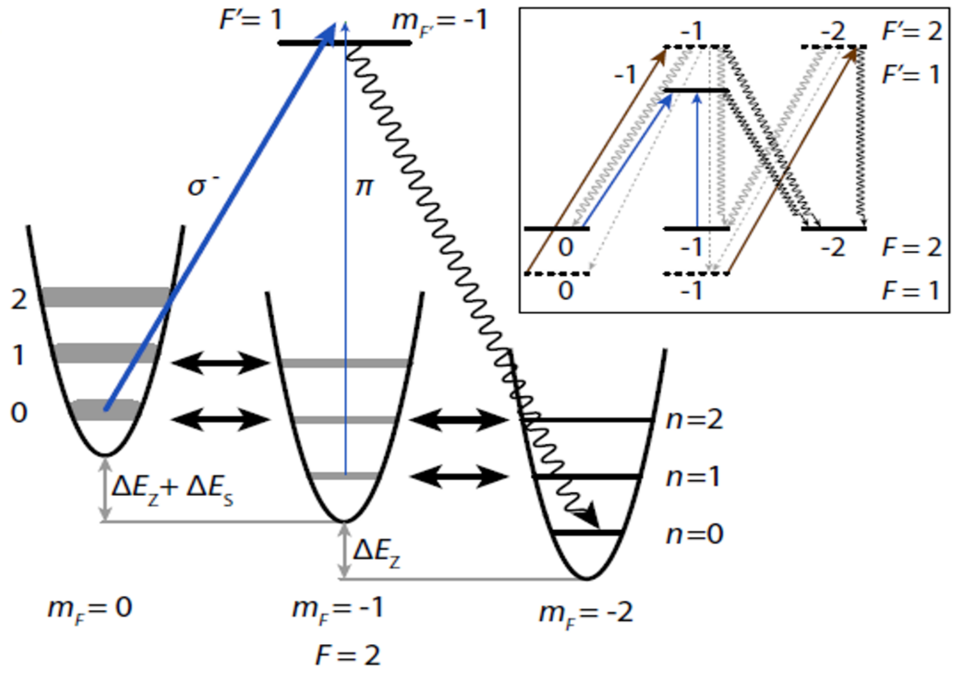

Figure 7.2: Cooling Scheme of DRSC on the D_1 transition on ^{39}K atomic species. An individual cooling cycle consists of double two-photon Raman transitions as exhibited by a double-sided arrow in between vibrational and magnetic states. The degeneracy lifted by the external magnetic field (ΔE_Z) and optical pumping via the $|F^{'} = 1, m_{F'} = -1\rangle$ state as shown by one side single blue arrow. The strong pumping beam with σ^- broadens and shift (ΔE_S) the energy levels. The brown arrows symbolize the repump beam; the wiggled grey line indicates spontaneous collapse into $F = 2$ states. The dashed grey represents the spontaneous decay transitions to $F = 1$ the lower ground states, and one wiggled black involves the decay into the dark state. This figure is adapted from [207].

cool down the ensemble of atom in their ground state.

7.2 Degenerate Raman sideband cooling

Before loading atom in the optical tweezers, the ensemble of ^{39}K atoms need to be in the ground state, the degenerate Raman Sideband cooling (DRSC) method is a very efficient process as presented in figure 7.2. In the DRSC process, the cloud of atoms transfers from its high-lying vibrational energy level v to its low-lying vibrational ground state. The degenerate Raman sideband cooling of ^{39}K is rightly presented in [207].

The main difference between the DRSC scheme for bosonic K and the more standard scheme is the possibility of spontaneous decay to the wrong hyperfine ground state, a repump beam is required to repopulate the ground state. Figure 7.2 shows three separate magnetic hyperfine sublevels m_F state; the sublevel shifted from each other due to applied offset magnetic field to get nth vibrational sublevel to degenerate $(n-1)$th vibrational sublevel, which is the next m_F state as presented in the figure i.e $|F=2, m_F=-2, n=2\rangle$ with $|2,-1,1\rangle$. The degenerate 2-photon stimulated Raman transitions prompted by lights coupled to degenerate states. The pumping beam is represented as blue arrows to drive $|F=2\rangle \rightarrow |F^{'}=1\rangle$ pump transition. The pumping beams consist a strong σ^- and a weak π component. Initially atoms inhabit high−lying vibrational states n. Then the atoms are shifted from the $|2,-2,n\rangle$ to the $|2,0,n-2\rangle$ state after one cooling cycle due to the double two−photon Raman operation, which changes the spin projection and atomic vibrational states. For one complete cooling cycle, the atoms get shifted by the σ^- polarized beam into the $|2,-2,n-2\rangle$ state. And the cooling carry on with as indicated above until atoms achieve either the $|2,-2,0\rangle$ or $|2,-1,0\rangle$ state. After that using a weak π component of the polarizer beam with $|2,-1,0\rangle$ state, we transfer all the atoms in the $|2,-2,0\rangle$ state as presented in figure 7.2.

7.3 Feshbach Resonances

For accurate control of atomic interaction, the Feshbach resonances remain an indispensable mechanism in atomic and molecular science. To produce ultracold molecules from ultracold atoms, coherently transfer atom set toward bound state molecules by a familiar procedure called magneto-association [32], which is governed by Feshbach resonances. The exceptional power of the atomic interactions provided by Feshbach resonances rigorously applied to produce bright solitons [208] or quantum droplets [209]. Notably, the Feshbach resonances remained necessary for the investigation of the BEC−BCS crossover within Fermi gases [210].

In the scattering event, the entrance channels and closed channels related to a specific set of quantum states in which atoms are permitted or prohibited respectively, develop from a scattering effect by energy conservation. Then any channel with energy $E < E_{tot}$ is described as an entrance channel, and any channel with $E > E_{tot}$ is named a closed channel, where E_{tot} is the total energy of the incoming atoms. Feshbach resonances occur when the entrance channel's total energy matches a bound state's energy in a closed channel, as shown in fig. 7.3 (a). And this entrance channel usually matches the ground state potential of pair of atoms, including at a sizeable inter-nuclear distance (R), the potential asymptotically addresses two free atoms' ground state.

The smaller the difference between the atoms' energy in the exit and entrance channels, the larger the collisional cross-section changes. The sign of the scattering length also depends on the bound state's position relative to the entrance channel's energy. If the energy of the entrance channel (E_{ent}) less than the bound state energy, which implies the negative scattering length, i.e. the attractive interaction in nature. However, V_c does also hold bound molecular states in close proximity of the entrance channel.

Any Feshbach resonance only happens if the energy of an incoming allowable elastic channel is magnetically tuned so that it coincides with that of a molecular bound state of an energetically closed channel. This tuning can be accomplished when the two channels maintain different total magnetic moments and therefore experience a differential Zeeman shift under the condition of an external applied magnetic field. The hyperfine interaction of alkali atoms provides several new channels forming multiple crossings as a magnetic field function. Therefore, near the proximity of coupling among those two potentials, the channels' intense mixing occurs.

In the region of a Feshbach resonance, the scattering length a be regulated by the external B-field is conventionally expressed by [211],

$$a(B) = a_{bg}\left(1 - \frac{\Delta}{B - B_0}\right), \tag{7.1}$$

where a_{bg} define as background scattering length, the magnetic field strength define as B, the resonance position define as B_0 where $a \to \infty$ i.e. divergence of scattering length also Δ is the resonance width. The Feshbach resonances only happen at the crossing of the atom-molecule states at the

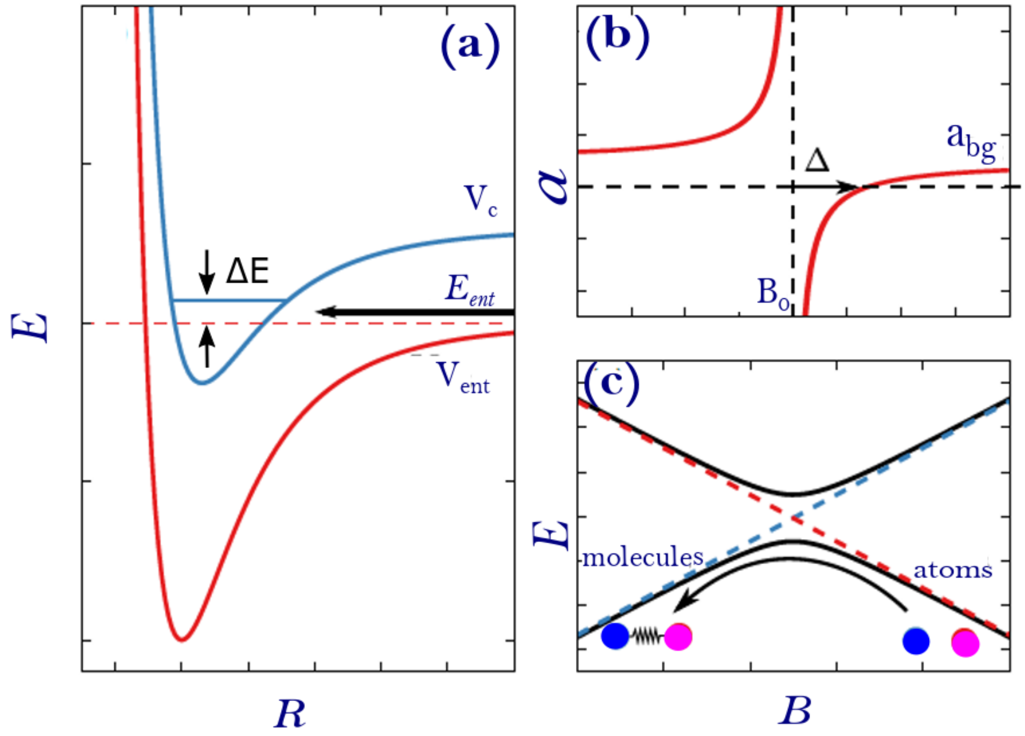

Figure 7.3: The basic model for a typical Feshbach resonance. (a) Graphic description of the entrance channel with energy E_{ent} represented by red and closed channel define by blue curve respectively. The energy ΔE of a molecular bound state can be modified to resonantly couple the two channels by tuning the magnetic field. (b) The red curve represents the interparticle scattering length. The Feshbach resonance can be described by its position B_0 and its width Δ. The scattering length decreases from the higher energy to smaller than its background estimation a_{bg} and leads to negative while it addresses the bound state's atomic threshold. (c) The atomic and molecular bound states coupling offers an avoided crossing. After sweeping the magnetic field adiabatically over the avoided crossing, the colliding atoms transfer toward weakly bound Feshbach molecules.

scattering length, which occurs at a magnetic field of $B_0 + \Delta$. This character for the scattering length is presented in Figure 7.3 (b). In the trap, the three-body loss rate scaling as a^4 [212] leads to inelastic losses from the trap. This intensified loss also can be computed at the positions of Feshbach resonances in ultracold gases. Therefore Feshbach resonances allow the feasibility after regulating the scattering length, which directly indicate the inter-atomic interactions can be manipulated in this process. I think you mean Feshbach resonances provide experimentalists an important control knob for manipulating ultracold atomic gases. Alternatively, by utilizing the radio-frequencies, oscillating B-fields [213] or even optical fields [214] one can tune the scattering length and couple the atoms and molecules.

7.3.1 Magnetoassociation

By attuning the magnetic field near a Feshbach resonance, one can associate atoms and form molecules called magneto-association. As shown by the colour dashed lines in figure 7.3 (c), the coupling among atomic and molecular states at a Feshbach resonance started in order to avoid the crossing. By ramping the magnetic field adiabatically [215, 216] one can avoid crossing, then colliding atom couples are united and form Feshbach molecules [32].

The magneto-association technique practices for actual molecular bound states where $\Delta E < 0$ as presented in figure 7.3 (b) while the B - field changing from high to low values. Other than $E = 0$, i.e., the scattering continuum, the molecular bonding is very weak, therefore dissociating quickly into respective atoms. A prudent selection of B - field ramps needs to apply to drive the spectrum to tune the Feshbach associations. Thus, below the threshold coupling among the molecular bound states drives in order to bypassed crossings within the molecular energy spectrum. In the beginning, when the Feshbach molecules formed, their binding energies are extremely low; because of that, the molecules are enormous in the order of the scattering length. At the trap, the inelastic collision between molecule - molecule or atom - molecule seriously limits the trapping lifetime of bosonic Feshbach molecules to several milliseconds [217]. More recently, a more efficient way to form Feshbach molecules by using optical lattice, where an individual atom of individual species trap in per lattice site [218], theoretically; with this single lattice process, one can achieve nearly 100 % association efficiency.

After weakly bound Feshbach molecules formed, then weakly bound molecules need to transfer into the deeply bound rovibrational ground state molecules by adopting Stimulated Raman adiabatic passage (STIRAP). The transfer efficiency to the ground state also depends on the initial molecular state. Also, in complex molecular energy levels have many avoided crossings. Which can be applied to assign the molecule in a different state, obtained by regulating the Landau−Zener tunnelling at avoided crossings after employing ramping magnetic field [219] or employing RF transitions [220].

7.4 Summary

In summary, with the knowledge of a pioneer work at Harvard with NaCs [201–203], we will develop a similar experiment to achieve a single ground state ^{39}K^{133}Cs molecule in an optical tweezer, which is not studied till now and also array of Rydberg single atom will be a very interesting experiment from the point of fundamental physics. Therefore, to produce a single ^{39}K^{133}Cs molecules, one can start with trapping both ^{39}K and ^{133}Cs species in 3D-MOT side-by-side, then load it into two individual optical tweezer trap, after that, it needs to cool-down the trapped atom into their ground state via Raman sideband cooling (RSC) mechanism [221]. Then for single-molecule experiments, one can merge ^{39}K and ^{133}Cs atoms into a single optical trap and form weakly bound molecule applying Feshbach association, then weakly bound molecule transfer to its ground state using STIRAP process. And on the other hand, it is not necessary to cool- down to the ground state for Rydberg excitation, but there are advantages to being in the ground state as indicated [31].

7.5 Outlook

The outstanding prospect of investigations with polar molecules in our group is brilliant and also have several different objectives which are believed to accomplish in the coming future. As we presented a single ^{39}K^{133}Cs ground state molecule can possible to achieve where two spices are bosonic, it will be interesting to achieve fermionic and bosonic combination ground state single ^{41}K^{133}Cs molecule in an optical tweezer.

Also, quantum gas microscopes experiments are pretty interesting, which are competent in imaging atoms in an individual plane of an optical lattice with single-site and single-atom resolution as presented in [222]. Similarly, one can make a single ^{39}K^{133}Cs molecule in the individual lattice. This experiment can address the disclosure of the new quantum phases prophesied for polar molecules in optical lattices where spatial relationships are anticipated [223]. Also, the microscope makes it possible to address the individual molecules in the lattice.

Array of Rydberg atoms distributed by a few micrometers makes the atoms more interacting. Due to increased lifetime and large dipole moments at the system, it can be useful and interesting for quantum simulations [12, 20, 21] or even for quantum gates [22, 23].

7.6 Concluding Remarks

The thesis started by describing the necessary background theory needed to understand the essential cooling and trapping mechanism for any alkali metal in the chapter 2. In the next chapter, atom-light interaction via four-wave mixing process in the hot thermal vapour cell for modulation transfer spectroscopy to lock and stabilise the laser system in chapter 3. We studied the experimental apparatus, as well as the experimental results, was also described with particular focus on the pyramid MOT for ^{39}K isotope in chapter 4 and 5, respectively. In the next chapter 6, we did spectroscopic experiments with a 405 nm transition of potassium-39 and motivated towards the inverted ladder-type Rydberg excitation scheme. In outlook, we present a future direction.

This thesis includes a techniques for creating and optically trapping ultracold polar molecules, and manageable quantum states clearly define Rydberg excitation for quantum simulations. The methods shown here describe a move ahead for our ^{39}K^{133}Cs experiment towards the long-term aim to create a single ground state polar molecules in an optical tweezer, and it is a fascinating experience to be a member of the domain of ultracold atoms along with Rydberg excitation, and our current research in Durham is one of the first few to examine in this field of physics.

Appendix

Appendix A

All the theory and calculations throughout on a simplistic two-level outline of an atomic system with a near resonance light field as displayed in the figure A.1.

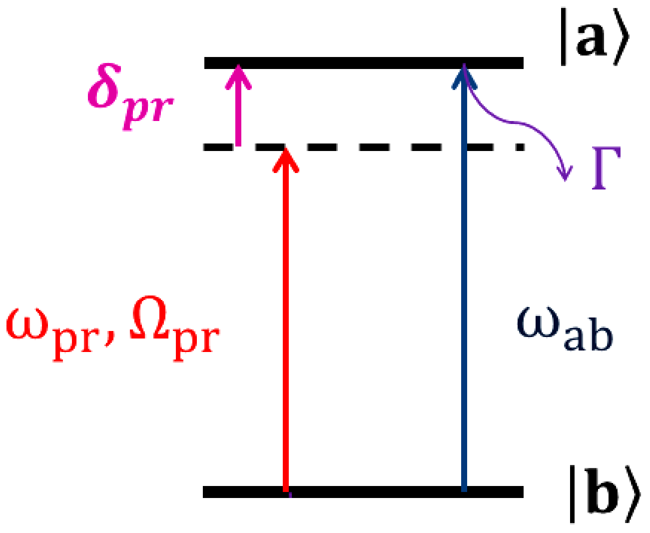

Figure A.1: A two level atomic system, where two levels are separated by $\hbar\omega_{\mathrm{ab}}$ amount of energy. The atoms interact with a monochromatic light beam with frequency Ω_{pr}. In this process two key parameters dictate the dynamics of atom−light interaction, which are the detuning $\delta_{\mathrm{pr}} = \omega_{\mathrm{ab}} - \omega_{\mathrm{pr}}$ and the Rabi frequency Ω_{pr}.

The level is presented as ground state $|b\rangle$ and an excited state $|a\rangle$ and the separation energy between this two levels is $\hbar\omega_{ab}$. The probe laser field with frequency ω_{pr} interact with the atom, the detuning from the excited state is denoted as δ_{pr}. The interaction strength of the probe light beam and the atoms defined by Rabi frequency Ω_{pr} [224], where $\Omega_{\mathrm{pr}} = -\frac{\langle \mathrm{b}|\mathrm{d.E_{pr}}|\mathrm{a}\rangle}{\hbar}$, here d represent the atomic dipole and the E_{pr} is laser electric field respectively, and finally Γ the linewidth of excited states. Because we consider closed transitions, so the decay rate (linewidth) is almost zero. Although in practical life its not completely closed, still small amount of atoms can decay to other states.

A.1 The density matrix representation

Here we consider an ensemble of atoms in an equal superposition state. The state of atom can be completely described by the wave function which is below,

$$|\psi\rangle = \frac{1}{\sqrt{2}}(|\mathrm{b}\rangle + |\mathrm{a}\rangle). \tag{A.1}$$

If we consider N atoms within a beam, then the beam can be thought of as a product of these wave functions,

$$|\psi_{\mathrm{beam}}\rangle = (|\psi\rangle)^{\mathrm{N}}. \tag{A.2}$$

This state is known as a pure state. If the consists with atoms which are randomly in one state or the another, then the beam is consist of a statistical mixture of two states, which cannot be described by wave function at all, this kind of state is known as the mixed state. Such kind of atomic system can be represented by density matrix [225]. And here ρ is density matrix operator. For pure state ρ can be represented as,

$$|\rho\rangle = |\psi\rangle\langle\psi|, \tag{A.3}$$

where

$$|\psi\rangle = C_{\mathrm{a}}|a\rangle + C_{\mathrm{b}}|b\rangle. \tag{A.4}$$

Above equations can be represented in a more convenient way in terms of matrix formalism for our two level system which is following,

$$\rho = \begin{pmatrix} \rho_{\mathrm{aa}} & \rho_{\mathrm{ab}} \\ \rho_{\mathrm{ba}} & \rho_{\mathrm{bb}} \end{pmatrix} = \begin{pmatrix} C_a C_a^* & C_a C_b^* \\ C_b C_a^* & C_b C_b^* \end{pmatrix}. \tag{A.5}$$

The diagonal element of the above matrix represents the population of the states, whereas off-diagonal define coherences between states. And every element in the density matrix is probability amplitudes.

The density matrix for the mixed state can be define as following way,

$$|\rho\rangle = \sum_i P_i |\psi_i\rangle\langle\psi_i|, \tag{A.6}$$

where P_i is the classical probability of being in state i. For a completely mixed state the density matrix is always diagonal.

A.1.1 Liouville equation

In principle, Schrödinger equation describe how the states evolve over time within the individual pure state, and this idea is also applicable to many-particle systems too. Consider a state $|\psi(t_0)\rangle$ after some time t the state evolved to $|\psi(t)\rangle$, from which we can construct the following relation,

$$|\psi(t)\rangle = U(t,t_0)|\psi(t_0)\rangle, \tag{A.7}$$

where

$$U(t=t_0,t_0) = 1. \tag{A.8}$$

After equation A.7 applied into the Schrödinger equation we get,

$$|\dot{\psi}\rangle = -\frac{i}{\hbar} H|\psi\rangle. \tag{A.9}$$

Here we obtain,

$$i\hbar\left[\frac{\partial U(t,t_0)}{\partial t}|\psi(t_0)\rangle + U(t,t_0)\frac{\partial|\psi(t_0)\rangle}{\partial t}\right] = |\psi(t_0)\rangle HU(t,t_0)+U(t,t_0)H|\psi(t_0)\rangle \tag{A.10}$$

Hence

$$i\hbar\frac{\partial U(t,t_0)}{\partial t} = HU(t,t_0) \tag{A.11}$$

From equation A.9 and A.11 we can find

$$U(t,t_0) = exp\left[-\frac{i}{\hbar}H(t-t_0)\right]. \tag{A.12}$$

Now if we consider Θ a variable which evolves when $|\psi(t)\rangle$ evolves as per equation A.7 then,

$$\langle\psi(t)|\Theta|\psi(t)\rangle = \langle\psi(t_0)|U^\dagger\Theta U|\psi(t_0)\rangle = \langle\psi(t_0)|\Theta_0|\psi(t_0)\rangle. \tag{A.13}$$

Since

$$U^\dagger\Theta U = \Theta_0. \tag{A.14}$$

as we know

$$U^\dagger U = 1 \tag{A.15}$$

Then

$$\Theta = U\Theta_0 U^\dagger. \tag{A.16}$$

Now equation A.16 differentiating with respect to t and we get,

$$\frac{d\Theta}{dt} = U\Theta_0\frac{\partial U^\dagger}{\partial t} + U\frac{\partial\Theta_0}{\partial t}U^\dagger + \frac{\partial U}{\partial t}\Theta_0 U^\dagger \tag{A.17}$$

$$= \frac{1}{i\hbar}(H\Theta - \Theta H) + U\frac{\partial\Theta_0}{\partial t}U^\dagger \tag{A.18}$$

$$\Rightarrow \frac{d\Theta}{dt} = \frac{1}{i\hbar}[H,\Theta] + \frac{\partial\Theta}{\partial t} \tag{A.19}$$

Now we can replace Θ with the density matrix ρ and we get,

$$\dot{\rho} = \frac{i}{\hbar}[\rho, H] + \frac{\partial\rho}{\partial t}. \tag{A.20}$$

We can rewrite 2nd term of above equation as follows,

$$\frac{\partial \rho}{\partial t} = -\Gamma \rho \tag{A.21}$$

$$\Rightarrow \dot{\rho} = \frac{i}{\hbar}\left[\rho, H\right] - \Gamma \rho \tag{A.22}$$

This last equation A.22 known as Liouville equation and its density matrix formalism is equivalent to Schrödinger equation. Here Γ represent decay rate from the excited states.

A.1.2 The optical Bloch equations

In the previous sub−section, we ended up with Liouville equation which is equivalent to Schrödinger picture. From there we can write density matrix equation for the evolution as follows,

$$\dot{\rho} = \frac{i}{\hbar}[\rho, H] - \begin{pmatrix} -\Gamma \rho_{\mathrm{aa}} & \frac{\Gamma}{2}\rho_{\mathrm{ba}} \\ \frac{\mathit{\Gamma}}{2}\rho_{\mathrm{ab}} & \Gamma \rho_{\mathrm{bb}} \end{pmatrix} \tag{A.23}$$

The diagonal term in equation A.23 represents the time evolution populations because of spontaneous emission which is described mathematically in the following way,

$$\frac{d\rho_{\mathrm{aa}}}{dt} = -\frac{d\rho_{\mathrm{bb}}}{dt} = -\Gamma \rho_{\mathrm{aa}}. \tag{A.24}$$

The off−diagonal term represent the coherence population decay due to spontaneous emission which is less obvious,

$$\frac{d\rho_{\mathrm{ab}}}{dt} = -\frac{\Gamma}{2}\rho_{\mathrm{ab}}, \frac{d\rho_{\mathrm{ba}}}{dt} = -\frac{\Gamma}{2}\rho_{\mathrm{ba}}. \tag{A.25}$$

Here we have just included results and referred to the standard literature [224] for justification.

Here we have use time−dependent Hamiltonian for two level systems [226] that is discussed below,

$$H = \frac{\hbar}{2}\begin{pmatrix} 0 & \Omega \\ \Omega & -2\delta_{\mathrm{pr}} \end{pmatrix}. \tag{A.26}$$

Now from equation A.23 and A.24 we can compute the following equation,

$$\frac{d\rho}{dt} = \frac{i}{2}\left[\rho H - H\rho\right] - \begin{pmatrix} -\Gamma\rho_{\mathrm{aa}} & \frac{\Gamma}{2}\rho_{\mathrm{ba}} \\ \frac{\varGamma}{2}\rho_{\mathrm{ab}} & \Gamma\rho_{\mathrm{bb}} \end{pmatrix}. \tag{A.27}$$

From equation A.27 it is quite straight forward to show following coupled differential equations,

$$\dot{\rho}_{\mathrm{bb}} = \frac{i\Omega}{2}(\rho_{\mathrm{ba}} - \rho_{\mathrm{ab}}) + \Gamma\rho_{\mathrm{aa}} \tag{A.28}$$

$$\dot{\rho}_{\mathrm{aa}} = -\frac{i\Omega}{2}(\rho_{\mathrm{ba}} - \rho_{\mathrm{ab}}) - \Gamma\rho_{\mathrm{aa}} \tag{A.29}$$

$$\dot{\rho}_{\mathrm{ba}} = -\frac{i\Omega}{2}(\rho_{\mathrm{aa}} - \rho_{\mathrm{bb}}) - i\delta_{\mathrm{pr}}\rho_{\mathrm{ba}} - \frac{\Gamma}{2}\rho_{\mathrm{ba}} \tag{A.30}$$

$$\dot{\rho}_{\mathrm{ab}} = \frac{i\Omega}{2}(\rho_{\mathrm{aa}} - \rho_{\mathrm{bb}}) + i\delta_{\mathrm{pr}}\rho_{\mathrm{ab}} - \frac{\Gamma}{2}\rho_{\mathrm{ab}} \tag{A.31}$$

This equations are known as Optical Bloch Equations. Their exact numerical solution [227] has been studied extensively in the last few years but their analytical solutions are only possible for few cases.

In steady state,

$$\dot{\rho}_{\mathrm{ab}} = \dot{\rho}_{\mathrm{aa}} = \dot{\rho}_{\mathrm{bb}} = 0. \tag{A.32}$$

In the two level close transition,

$$\rho_{\mathrm{aa}} + \rho_{\mathrm{bb}} = 1. \tag{A.33}$$

So the optical Bloch equations reduce to,

$$\Gamma\rho_{\mathrm{aa}} = \frac{i\Omega_{\mathrm{pr}}}{2}\left(\rho_{\mathrm{ab}} - \rho_{\mathrm{ba}}\right) \tag{A.34}$$

$$\left(\frac{\Gamma}{2} - i\delta_{\mathrm{pr}}\right)\rho_{\mathrm{ab}} = \frac{i\Omega_{\mathrm{pr}}}{2}(\rho_{\mathrm{aa}} - \rho_{\mathrm{bb}}) \tag{A.35}$$

substituting equation A.33 into equation A.35 and we get,

$$\rho_{\mathrm{ab}} = \frac{i\Omega_{\mathrm{pr}}}{2(\Gamma/2 - i\delta_{\mathrm{pr}})}(2\rho_{\mathrm{aa}} - 1). \tag{A.36}$$

After replacing equation A.36 and its complex conjugate into equation A.34, and we will be able to get a solution for ρ_{aa} which is as follows,

$$\rho_{\mathrm{aa}} = \frac{1}{2} \cdot \frac{\Omega_{\mathrm{pr}}^2/2}{\Omega_{\mathrm{pr}}^2/2 + (\Gamma/2)^2 + \delta_{\mathrm{pr}}^2}. \tag{A.37}$$

We get the steady-state solution for coherence within two levels by substituting A.37 on A.36,

$$\rho_{\mathrm{ab}} = \frac{\Omega_{\mathrm{pr}}}{2}\left(\frac{\delta_{\mathrm{pr}} - i(\Gamma/2)}{\Omega_{\mathrm{pr}}^2/2 + (\Gamma/2)^2 + \delta_{\mathrm{pr}}^2}\right) \tag{A.38}$$

Another great way to represent the optical Bloch equation is in the form of vector component which is much more appropriate in terms of physical significance. The component of Bloch vector are,

$$\tilde{u} = \frac{\rho_{\mathrm{ab}} + \rho_{\mathrm{ba}}}{2} = \frac{\Omega_{\mathrm{pr}}}{2}\frac{\delta_{\mathrm{pr}}}{\delta_{\mathrm{pr}}^2 + (\Gamma/2)^2 + \Omega_{\mathrm{pr}}^2/2} \tag{A.39}$$

$$\tilde{v} = \frac{\rho_{\mathrm{ba}} - \rho_{\mathrm{ab}}}{2} = \frac{\Omega_{\mathrm{pr}}}{2}\frac{\Gamma/2}{\delta_{\mathrm{pr}}^2 + (\Gamma/2)^2 + \Omega_{\mathrm{pr}}^2/2} \tag{A.40}$$

and

$$\tilde{w} = \frac{\rho_{\mathrm{aa}} - \rho_{\mathrm{bb}}}{2} \tag{A.41}$$

Since w represent half way within the populations of $|a\rangle$ and $|b\rangle$ so,

$$\tilde{w} + \frac{1}{2} = \rho_{\mathrm{aa}} = \frac{1}{2}\frac{\Omega_{\mathrm{pr}}^2/2}{\delta_{\mathrm{pr}}^2 + (\Gamma/2)^2 + \Omega_{\mathrm{pr}}^2/2} \tag{A.42}$$

Above equation A.39, A.40 and A.42 represent steady state solutions of Bloch vector.

A.1.3 Complex electric susceptibility

Frequency reliant electric susceptibility of a dielectric medium is $\chi(\delta_{\mathrm{pr}})$ which can be connected with macroscopic polarization P with a applied electric field E. The dispersive properties can be written as real part of $\chi_{\mathrm{R}}(\delta_{\mathrm{pr}})$ and imaginary part $\chi_{\mathrm{I}}(\delta_{\mathrm{pr}})$, which is absorption properties of the medium [228].

The classical macroscopic polarization P of the medium can be given by [228],

$$\mathrm{P} = \epsilon_0 \chi(\delta_{\mathrm{pr}}) \mathrm{E} = \mathrm{N_D} \langle \partial \rangle \tag{A.43}$$

where ϵ_0 is the permittivity of the medium, $\mathrm{N_D}$ is the number of dipoles in unit volume, which is number density and $\langle \partial \rangle$ is average dipole moment.

We can write polarization in terms of electric field and complex susceptibility as,

$$\mathrm{P} = \frac{1}{2}\epsilon_0 \mathrm{E}(\chi \mathrm{e}^{-\mathrm{i}\omega \mathrm{t}} + \chi^* \mathrm{e}^{\mathrm{i}\omega \mathrm{t}}). \tag{A.44}$$

In general, the expectation value of any operator can be written as following way [229],

$$\langle \partial \rangle = \mathrm{Tr}(\rho \partial) = \partial_{\mathrm{ab}}(\rho_{\mathrm{ba}} + \rho_{\mathrm{ab}}). \tag{A.45}$$

Now using slow variable from [224], we can say that the average dipole moment become,

$$\langle \partial \rangle = \partial_{\mathrm{ab}}(\tilde{\rho}_{\mathrm{ba}} \mathrm{e}^{\mathrm{i}\omega_{\mathrm{pr}} \mathrm{t}} + \tilde{\rho}_{\mathrm{ab}} \mathrm{e}^{-\mathrm{i}\omega_{\mathrm{pr}} \mathrm{t}}). \tag{A.46}$$

Now using equation A.52, A.53 and A.55 we can write as,

$$\mathrm{N_D} \partial_{\mathrm{ab}}(\tilde{\rho}_{\mathrm{ba}} \mathrm{e}^{\mathrm{i}\omega_{\mathrm{pr}} \mathrm{t}} + \tilde{\rho}_{\mathrm{ab}} \mathrm{e}^{-\mathrm{i}\omega_{\mathrm{pr}} \mathrm{t}}) = \frac{1}{2}\epsilon_0 \mathrm{E}(\chi \mathrm{e}^{-\mathrm{i}\omega \mathrm{t}} + \chi^* \mathrm{e}^{\mathrm{i}\omega \mathrm{t}}). \tag{A.47}$$

Now after taking dot product with equation A.56 and we know $\hbar\Omega_{\mathrm{pr}} = -\partial_{\mathrm{ab}} \cdot \mathrm{E}$, which leads to us,

$$\mathrm{N_D} \partial_{\mathrm{ab}}^2(\tilde{\rho}_{\mathrm{ba}} \mathrm{e}^{\mathrm{i}\omega_{\mathrm{pr}} \mathrm{t}} + \tilde{\rho}_{\mathrm{ab}} \mathrm{e}^{-\mathrm{i}\omega_{\mathrm{pr}} \mathrm{t}}) = -\frac{1}{2}\epsilon_0 \hbar \Omega_{\mathrm{pr}}(\chi \mathrm{e}^{-\mathrm{i}\omega \mathrm{t}} + \chi^* \mathrm{e}^{\mathrm{i}\omega \mathrm{t}}). \tag{A.48}$$

Now equating the coefficient of $e^{-i\omega t}$ give us,

$$\chi = -2 \cdot \frac{\mathrm{N_D}\partial^2_{\mathrm{ba}}}{\epsilon_0 \hbar \Omega_{\mathrm{pr}}} \tilde{\rho}_{\mathrm{ab}}. \tag{A.49}$$

The density matrix of the above equation can be written using equation A.39 and A.40 in the following way,

$$\tilde{\rho}_{\mathrm{ab}} = u - iv. \tag{A.50}$$

Substituting equation A.59 into equation A.58 and using the steady state solutions for u and v in equations A.39 and A.40 we end up with,

$$\chi = -\frac{\mathrm{N_D}\partial^2_{\mathrm{ba}}}{\epsilon_0 \hbar} \left(\frac{\delta_{\mathrm{pr}}}{\delta^2_{\mathrm{pr}} + (\Gamma/2)^2 + \Omega^2_{\mathrm{pr}}/2} - \mathrm{i} \frac{\Gamma/2}{\delta^2_{\mathrm{pr}} + (\Gamma/2)^2 + \Omega^2_{\mathrm{pr}}/2} \right). \tag{A.51}$$

After equating imaginary and real part we get,

$$\chi_{\mathrm{R}} = -\frac{\mathrm{N_D}\partial^2_{\mathrm{ba}}}{\epsilon_0 \hbar} \left(\frac{\delta_{\mathrm{pr}}}{\delta^2_{\mathrm{pr}} + (\Gamma/2)^2 + \Omega^2_{\mathrm{pr}}/2} \right) \tag{A.52}$$

$$\chi_{\mathrm{I}} = \frac{\mathrm{N_D}\partial^2_{\mathrm{ba}}}{\epsilon_0 \hbar} \left(\frac{\Gamma/2}{\delta^2_{\mathrm{pr}} + (\Gamma/2)^2 + \Omega^2_{\mathrm{pr}}/2} \right) \tag{A.53}$$

Now χ_{R} and χ_{I} are the real and imaginary part of complex susceptibility respectively.

A.2 Transmission intensity

The electromagnetic−wave can be represented as $\mathrm{E} = \mathrm{E_0} \exp[\mathrm{i}(\mathrm{k_{pr}z} - \omega_{\mathrm{pr}}\mathrm{t})]$ passing through a dielectric medium with refractive index n and length L_Z along Z direction, the frequency remain unchanged but the propagation wave vector $\mathrm{k_{pr}}$ modified by $\mathrm{k_n} = \mathrm{nk_{pr}}$. Now the refractive index which consists of real and imaginary part we see before which leads us to the electric field (E) and the intensity (I) which is as following,

$$\mathrm{E} = \mathrm{E_0} \mathrm{e}^{-\mathrm{k_{pr}n_I L_z}} \mathrm{e}^{\mathrm{i}(\mathrm{k_{pr}n_R L_z} - \omega_{\mathrm{pr}}\mathrm{t})}, \tag{A.54}$$

and

$$\mathrm{I} = \mathrm{I_0 e^{-2k_{pr}n_I L_z}}. \tag{A.55}$$

The above equation can be written as following way,

$$\mathrm{I(z)} = \mathrm{I_0 e^{-\alpha L_z}}. \tag{A.56}$$

The above equation known as Beer−Lambert law. Where $\alpha(\delta_{\mathrm{pr}})$ is the absorption coefficient of the medium, which is also the function of detuning δ_{pr} with Lorentzian line shape,

$$\alpha(\delta_{\mathrm{pr}}) = 2\mathrm{n_I}(\delta_{\mathrm{pr}})\mathrm{k_{pr}}. \tag{A.57}$$

Now $\mathrm{n_R}(\delta_{\mathrm{pr}}) - \mathrm{n_0}$ gives us dispersion profile of the medium but at atomic vapours $\mathrm{n_0} \simeq 1$, then the dispersion profile become $\mathrm{n_R}(\delta_{\mathrm{pr}}) - 1$.

A.2.1 Frequency axis calibration

To compare the experimental data with theory using a computer program called ElecSus. To analyze data with ElecSus, the data must be normalized and the time scale needs to be converted in terms of frequency, which will be discussed in great detail. In figure A.2 shown a typical oscilloscope output, in the figure black, red and blue data point corresponding to the voltage product from the PD, the Fabry−Perot cavity and the gradient voltage provided to the piezoelectric stack sequentially. Special black data point corresponding to the left axis and the red and blue data point corresponding to the right axis.

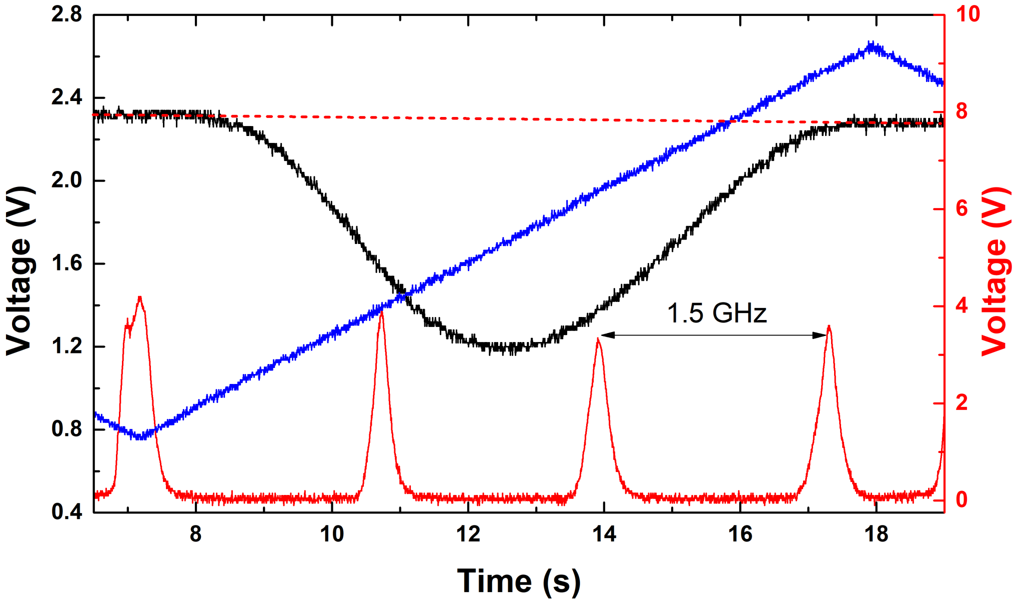

Figure A.2: A standard oscilloscope producing when transmission spectra were registered. In order to normalise the spectrum, the red broken line is a straight fit to the sides of the transmission spectra. The red data shows the cavity peaks and the blue input is the grade voltage utilised to the piezoelectric stack, both of them corresponding to the right y-axis.

The Thorlabs SA200−3B scanning Fabry−Perot cavity with a free spectral range of 1.50 ± 0.01 GHz used for frequency calibration. The total separation between first and last cavity peak in terms of GHz is divided by the time difference in between first and last cavity peak, which give us frequency/time. Now if we multiply the time axis with this frequency/time, we will get our x-axis in terms of frequency. To normalize the transmission spectra, a straight fit was made to the wings of the spectrum as recorded in the red dashed line. The data was then shared by the straight fit to normalized the spectra.

Bibliography

[1] A. L. Schawlow and C. H. Townes, Phys. Rev. **112**, 1940 (1958).

[2] T. H. Maiman, nature **187**, 493 (1960).

[3] S. Chu, Rev. Mod. Phys. **70**, 685 (1998).

[4] C. N. Cohen-Tannoudji, Rev. Mod. Phys. **70**, 707 (1998).

[5] W. D. Phillips, Rev. Mod. Phys. **70**, 721 (1998).

[6] I. M. Georgescu, S. Ashhab, and F. Nori, Rev. Mod. Phys. **86**, 153 (2014).

[7] A. Ashkin, Phys. Rev. Lett. **24**, 156 (1970).

[8] N. Schlosser, G. Reymond, I. Protsenko, and P. Grangier, Nature **411**, 1024 (2001).

[9] H. Bernien, S. Schwartz, A. Keesling, H. Levine, A. Omran, H. Pichler, S. Choi, A. S. Zibrov, M. Endres, M. Greiner, *et al.*, Nature **551**, 579 (2017).

[10] S. Ebadi, T. T. Wang, H. Levine, A. Keesling, G. Semeghini, A. Omran, D. Bluvstein, R. Samajdar, H. Pichler, W. W. Ho, *et al.*, Nature **595**, 227 (2021).

[11] A. Browaeys and T. Lahaye, Nature Physics , 1 (2020).

[12] F. Nogrette, H. Labuhn, S. Ravets, D. Barredo, L. Béguin, A. Vernier, T. Lahaye, and A. Browaeys, Phys. Rev. X **4**, 021034 (2014).

[13] M. Saffman, Journal of Physics B: Atomic, Molecular and Optical Physics **49**, 202001 (2016).

[14] D. Barredo, S. de Léséleuc, V. Lienhard, T. Lahaye, and A. Browaeys, Science **354**, 1021 (2016), https://science.sciencemag.org/content/354/6315/1021.full.pdf .

[15] K.-N. Schymik, V. Lienhard, D. Barredo, P. Scholl, H. Williams, A. Browaeys, and T. Lahaye, Phys. Rev. A **102**, 063107 (2020).

[16] J. Smith, A. Lee, P. Richerme, B. Neyenhuis, P. W. Hess, P. Hauke, M. Heyl, D. A. Huse, and C. Monroe, Nature Physics **12**, 907 (2016).

[17] A. M. Kaufman, M. E. Tai, A. Lukin, M. Rispoli, R. Schittko, P. M. Preiss, and M. Greiner, Science **353**, 794 (2016), https://science.sciencemag.org/content/353/6301/794.full.pdf .

[18] P. Richerme, Z.-X. Gong, A. Lee, C. Senko, J. Smith, M. Foss-Feig, S. Michalakis, A. V. Gorshkov, and C. Monroe, Nature **511**, 198 (2014).

[19] N. Goldman, J. C. Budich, and P. Zoller, Nature Physics **12**, 639 (2016).

[20] T. M. Graham, M. Kwon, B. Grinkemeyer, Z. Marra, X. Jiang, M. T. Lichtman, Y. Sun, M. Ebert, and M. Saffman, Phys. Rev. Lett. **123**, 230501 (2019).

[21] A. D. King, J. Carrasquilla, J. Raymond, I. Ozfidan, E. Andriyash, A. Berkley, M. Reis, T. Lanting, R. Harris, F. Altomare, *et al.*, Nature **560**, 456 (2018).

[22] D. Jaksch, J. I. Cirac, P. Zoller, S. L. Rolston, R. Côté, and M. D. Lukin, Phys. Rev. Lett. **85**, 2208 (2000).

[23] L.-M. Duan, M. D. Lukin, J. I. Cirac, and P. Zoller, Nature **414**, 413 (2001).

[24] A. Gaëtan, Y. Miroshnychenko, T. Wilk, A. Chotia, M. Viteau, D. Comparat, P. Pillet, A. Browaeys, and P. Grangier, Nature Physics **5**, 115 (2009).

[25] E. Urban, T. A. Johnson, T. Henage, L. Isenhower, D. Yavuz, T. Walker, and M. Saffman, Nature Physics **5**, 110 (2009).

[26] L. Isenhower, E. Urban, X. L. Zhang, A. T. Gill, T. Henage, T. A. Johnson, T. G. Walker, and M. Saffman, Phys. Rev. Lett. **104**, 010503 (2010).

[27] H. Labuhn, D. Barredo, S. Ravets, S. De Léséleuc, T. Macrì, T. Lahaye, and A. Browaeys, Nature **534**, 667 (2016).

[28] J. Zeiher, P. Schauß, S. Hild, T. Macrì, I. Bloch, and C. Gross, Phys. Rev. X **5**, 031015 (2015).

[29] P. Schauß, J. Zeiher, T. Fukuhara, S. Hild, M. Cheneau, T. Macrì, T. Pohl, I. Bloch, and C. Groß, Science **347**, 1455 (2015).

[30] D. Barredo, H. Labuhn, S. Ravets, T. Lahaye, A. Browaeys, and C. S. Adams, Phys. Rev. Lett. **114**, 113002 (2015).

[31] N. Lorenz, L. Festa, L.-M. Steinert, and C. Gross, SciPost Phys. **10**, 52 (2021).

[32] T. Köhler, K. Góral, and P. S. Julienne, Rev. Mod. Phys. **78**, 1311 (2006).

[33] M. A. Baranov, A. Micheli, S. Ronen, and P. Zoller, Phys. Rev. A **83**, 043602 (2011).

[34] J. J. Hudson, D. M. Kara, I. Smallman, B. E. Sauer, M. R. Tarbutt, and E. A. Hinds, Nature **473**, 493 (2011).

[35] L. Pollet, J. D. Picon, H. P. Büchler, and M. Troyer, Phys. Rev. Lett. **104**, 125302 (2010).

[36] D. DeMille, Phys. Rev. Lett. **88**, 067901 (2002).

[37] J. W. Park, Z. Z. Yan, H. Loh, S. A. Will, and M. W. Zwierlein, Science **357**, 372 (2017), https://science.sciencemag.org/content/357/6349/372.full.pdf .

[38] V. Zhelyazkova, A. Cournol, T. E. Wall, A. Matsushima, J. J. Hudson, E. A. Hinds, M. R. Tarbutt, and B. E. Sauer, Phys. Rev. A **89**, 053416 (2014).

[39] L. W. Cheuk, L. Anderegg, Y. Bao, S. Burchesky, S. S. Yu, W. Ketterle, K.-K. Ni, and J. M. Doyle, Phys. Rev. Lett. **125**, 043401 (2020).

[40] S. K. Tokunaga, W. Skomorowski, P. S. Żuchowski, R. Moszynski, J. M. Hutson, E. Hinds, and M. Tarbutt, The European Physical Journal D **65**, 141 (2011).

[41] M. Zeppenfeld, B. G. Englert, R. Glöckner, A. Prehn, M. Mielenz, C. Sommer, L. D. van Buuren, M. Motsch, and G. Rempe, Nature **491**, 570 (2012).

[42] J. R. Bochinski, E. R. Hudson, H. J. Lewandowski, G. Meijer, and J. Ye, Phys. Rev. Lett. **91**, 243001 (2003).

[43] E. Narevicius and M. G. Raizen, Chemical reviews **112**, 4879 (2012).

[44] R. Fulton, A. I. Bishop, M. N. Shneider, and P. F. Barker, Nature Physics **2**, 465 (2006).

[45] M. H. Steinecker, D. J. McCarron, Y. Zhu, and D. DeMille, ChemPhysChem **17**, 3664 (2016), https://onlinelibrary.wiley.com/doi/pdf/10.1002/cphc.201600967 .

[46] S. Truppe, H. Williams, M. Hambach, L. Caldwell, N. Fitch, E. Hinds, B. Sauer, and M. Tarbutt, Nature Physics **13**, 1173 (2017).

[47] I. Kozyryev, L. Baum, K. Matsuda, B. L. Augenbraun, L. Anderegg, A. P. Sedlack, and J. M. Doyle, Phys. Rev. Lett. **118**, 173201 (2017).

[48] A. L. Collopy, S. Ding, Y. Wu, I. A. Finneran, L. Anderegg, B. L. Augenbraun, J. M. Doyle, and J. Ye, Phys. Rev. Lett. **121**, 213201 (2018).

[49] J. A. Devlin and M. R. Tarbutt, New Journal of Physics **18**, 123017 (2016).

[50] J. P. Covey, S. A. Moses, M. Gärttner, A. Safavi-Naini, M. T. Miecnikowski, Z. Fu, J. Schachenmayer, P. S. Julienne, A. M. Rey, D. S. Jin, *et al.*, Nature communications **7**, 1 (2016).

[51] P. K. Molony, P. D. Gregory, A. Kumar, C. R. Le Sueur, J. M. Hutson, and S. L. Cornish, ChemPhysChem **17**, 3811 (2016).

[52] P. K. Molony, A. Kumar, P. D. Gregory, R. Kliese, T. Puppe, C. R. Le Sueur, J. Aldegunde, J. M. Hutson, and S. L. Cornish, Phys. Rev. A **94**, 022507 (2016).

[53] P. D. Gregory, J. Aldegunde, J. M. Hutson, and S. L. Cornish, Phys. Rev. A **94**, 041403 (2016).

[54] T. Takekoshi, L. Reichsöllner, A. Schindewolf, J. M. Hutson, C. R. Le Sueur, O. Dulieu, F. Ferlaino, R. Grimm, and H.-C. Nägerl, Phys. Rev. Lett. **113**, 205301 (2014).

[55] P. K. Molony, P. D. Gregory, Z. Ji, B. Lu, M. P. Köppinger, C. R. Le Sueur, C. L. Blackley, J. M. Hutson, and S. L. Cornish, Phys. Rev. Lett. **113**, 255301 (2014).

[56] K. M. Jones, E. Tiesinga, P. D. Lett, and P. S. Julienne, Rev. Mod. Phys. **78**, 483 (2006).

[57] M. Viteau, A. Chotia, M. Allegrini, N. Bouloufa, O. Dulieu, D. Comparat, and P. Pillet, Science **321**, 232 (2008), https://science.sciencemag.org/content/321/5886/232.full.pdf .

[58] J. Deiglmayr, A. Grochola, M. Repp, K. Mörtlbauer, C. Glück, J. Lange, O. Dulieu, R. Wester, and M. Weidemüller, Phys. Rev. Lett. **101**, 133004 (2008).

[59] H. J. Patel, C. L. Blackley, S. L. Cornish, and J. M. Hutson, Phys. Rev. A **90**, 032716 (2014).

[60] M. Gröbner, P. Weinmann, E. Kirilov, H.-C. Nägerl, P. S. Julienne, C. R. Le Sueur, and J. M. Hutson, Phys. Rev. A **95**, 022715 (2017).

[61] P. K. Molony, P. D. Gregory, Z. Ji, B. Lu, M. P. Köppinger, C. R. Le Sueur, C. L. Blackley, J. M. Hutson, and S. L. Cornish, Phys. Rev. Lett. **113**, 255301 (2014).

[62] K.-K. Ni, S. Ospelkaus, M. H. G. de Miranda, A. Pe'er, B. Neyenhuis, J. J. Zirbel, S. Kotochigova, P. S. Julienne, D. S. Jin, and J. Ye, Science **322**, 231 (2008), https://science.sciencemag.org/content/322/5899/231.full.pdf .

[63] T. Tiecke, University of Amsterdam, The Netherlands, Thesis , 12 (2010).

[64] W. Xu and B. DeMarco, Phys. Rev. A **93**, 011801 (2016).

[65] G. Unnikrishnan, M. Gröbner, and H.-C. Nägerl, SciPost Phys. **6**, 47 (2019).

[66] T. Hänsch and A. Schawlow, Optics Communications **13**, 68 (1975).

[67] D. Wineland and H. Dehmelt, in *Bulletin of the American Physical Society*, Vol. 20 (AMER INST PHYSICS CIRCULATION FULFILLMENT DIV, 500 SUNNYSIDE BLVD, WOODBURY , 1975) pp. 637–637.

[68] D. J. Wineland and W. M. Itano, Phys. Rev. A **20**, 1521 (1979).

[69] I. G. Hughes and M. J. Pritchard, Physics Education **42**, 27 (2006).

[70] J. Dalibard, *The role of fluctuations in the dynamics of an atom coupled to the electromagnetic field*, Ph.D. thesis, Universite Pierre et Marie Curie-Paris VI (1986).

[71] P. D. Lett, W. D. Phillips, S. L. Rolston, C. E. Tanner, R. N. Watts, and C. I. Westbrook, J. Opt. Soc. Am. B **6**, 2084 (1989).

[72] S. KEMP *et al.*, *Laser cooling and optical trapping of ytterbium*, Ph.D. thesis, Durham University (2017).

[73] H. J. Metcalf and P. van der Straten, "Laser cooling and trapping of neutral atoms," in *The Optics Encyclopedia* (American Cancer Society, 2007)

https://onlinelibrary.wiley.com/doi/pdf/10.1002/9783527600441.oe005
.

[74] S. Chu and C. Wieman, J. Opt. Soc. Am. B **6**, 2020 (1989).

[75] M. Landini, S. Roy, L. Carcagní, D. Trypogeorgos, M. Fattori, M. Inguscio, and G. Modugno, Phys. Rev. A **84**, 043432 (2011).

[76] P. Tierney, *Magnetic trapping of an ultracold (ˆ 87) Rb-(ˆ 133) Cs atomic mixture*, Ph.D. thesis, Durham University (2009).

[77] P. D. Lett, R. N. Watts, C. I. Westbrook, W. D. Phillips, P. L. Gould, and H. J. Metcalf, Phys. Rev. Lett. **61**, 169 (1988).

[78] J. Dalibard and C. Cohen-Tannoudji, J. Opt. Soc. Am. B **6**, 2023 (1989).

[79] P. J. Ungar, D. S. Weiss, E. Riis, and S. Chu, J. Opt. Soc. Am. B **6**, 2058 (1989).

[80] D. S. Weiss, E. Riis, Y. Shevy, P. J. Ungar, and S. Chu, J. Opt. Soc. Am. B **6**, 2072 (1989).

[81] C. J. Pethick and H. Smith, *Bose-Einstein condensation in dilute gases* (Cambridge university press, 2008).

[82] C. J. Cooper, G. Hillenbrand, J. Rink, C. G. Townsend, K. Zetie, and C. J. Foot, Europhysics Letters (EPL) **28**, 397 (1994).

[83] A. Bambini and A. Agresti, Phys. Rev. A **56**, 3040 (1997).

[84] D. A. Steck, "Cesium d line data," (2003).

[85] R. L. D. Campbell, *Thermodynamic properties of a Bose gas with tuneable interactions*, Ph.D. thesis, University of Cambridge (2012).

[86] G. Breit and I. I. Rabi, Phys. Rev. **38**, 2082 (1931).

[87] S. Upadhyay, U. Dargyte, V. D. Dergachev, R. P. Prater, S. A. Varganov, T. V. Tscherbul, D. Patterson, and J. D. Weinstein, Phys. Rev. A **100**, 063419 (2019).

[88] T. G. Tiecke (2011).

[89] G. W. Thomson, Chemical Reviews **38**, 1 (1946), https://doi.org/10.1021/cr60119a001 .

[90] C. Alcock, V. Itkin, and M. Horrigan, Canadian Metallurgical Quarterly **23**, 309 (1984).

[91] Y. Singh, D. K. Nandy, and B. K. Sahoo, Phys. Rev. A **86**, 032509 (2012).

[92] S. Falke, E. Tiemann, C. Lisdat, H. Schnatz, and G. Grosche, Phys. Rev. A **74**, 032503 (2006).

[93] H. J. Metcalf and P. Straten, *Laser cooling and trapping of neutral atoms* (Wiley Online Library, 2007).

[94] S. Uetake, K. Hayasaka, and M. Watanabe, Japanese Journal of Applied Physics **42**, L332 (2003).

[95] H. D. Do, G. Moon, and H.-R. Noh, Phys. Rev. A **77**, 032513 (2008).

[96] K. L. Corwin, Z.-T. Lu, C. F. Hand, R. J. Epstein, and C. E. Wieman, Appl. Opt. **37**, 3295 (1998).

[97] D. J. McCarron, I. G. Hughes, P. Tierney, and S. L. Cornish, Review of Scientific Instruments **78**, 093106 (2007), https://doi.org/10.1063/1.2785157 .

[98] I. Lindsay, P. Groß, C. Lee, B. Adhimoolam, and K.-J. Boller, Opt. Express **14**, 12341 (2006).

[99] H.-R. Noh, S. E. Park, L. Z. Li, J.-D. Park, and C.-H. Cho, Opt. Express **19**, 23444 (2011).

[100] F. Bertinetto, P. Cordiale, G. Galzerano, and E. Bava, IEEE Transactions on Instrumentation and Measurement **50**, 490 (2001).

[101] J. Zhang, D. Wei, C. Xie, and K. Peng, Opt. Express **11**, 1338 (2003).

[102] L. Zhe Li, S. Eon Park, H.-R. Noh, J.-D. Park, and C.-H. Cho, Journal of the Physical Society of Japan **80**, 074301 (2011), https://doi.org/10.1143/JPSJ.80.074301 .

[103] D. Sun, C. Zhou, L. Zhou, J. Wang, and M. Zhan, Opt. Express **24**, 10649 (2016).

[104] L. Mudarikwa, K. Pahwa, and J. Goldwin, Journal of Physics B: Atomic, Molecular and Optical Physics **45**, 065002 (2012).

[105] G. Salomon, L. Fouché, P. Wang, A. Aspect, P. Bouyer, and T. Bourdel, EPL (Europhysics Letters) **104**, 63002 (2013).

[106] T. W. Hänsch, A. L. Schawlow, and G. W. Series, *The spectrum of atomic hydrogen* (WH Freeman and Company, 1979).

[107] W. Demtröder, *Laser spectroscopy: vol. 2: experimental techniques*, Vol. 2 (Springer Science & Business Media, 2008).

[108] S. E. Park and H.-R. Noh, Opt. Express **21**, 14066 (2013).

[109] A. R. Edmonds, *Angular momentum in quantum mechanics* (Princeton university press, 2016).

[110] J. Sagle, R. K. Namiotka, and J. Huennekens, Journal of Physics B: Atomic, Molecular and Optical Physics **29**, 2629 (1996).

[111] D. J. McCarron, S. A. King, and S. L. Cornish, Measurement Science and Technology **19**, 105601 (2008).

[112] M. A. Zentile, J. Keaveney, L. Weller, D. J. Whiting, C. S. Adams, and I. G. Hughes, Computer Physics Communications **189**, 162 (2015).

[113] A. Lindgård and S. E. Nielsen, Atomic data and nuclear data tables **19**, 533 (1977).

[114] D. MCCARRON *et al.*, *A Quantum Degenerate Mixture of Rb and Cs*, Ph.D. thesis, Durham University (2011).

[115] M. KOPPINGER *et al.*, *Creation of ultracold RbCs molecules*, Ph.D. thesis, Durham University (2014).

[116] M. L. Harris, *Realisation of a cold mixture of rubidium and caesium*, Ph.D. thesis, Durham University (2008).

[117] I. Nosske, L. Couturier, F. Hu, C. Tan, C. Qiao, J. Blume, Y. H. Jiang, P. Chen, and M. Weidemüller, Phys. Rev. A **96**, 053415 (2017).

[118] C. Slowe, L. Vernac, and L. V. Hau, Review of Scientific Instruments **76**, 103101 (2005).

[119] A. Paris-Mandoki, M. D. Jones, J. Nute, J. Wu, S. Warriar, and L. Hackermüller, Review of Scientific Instruments **85**, 113103 (2014), https://doi.org/10.1063/1.4900577 .

[120] K. Dieckmann, R. J. C. Spreeuw, M. Weidemüller, and J. T. M. Walraven, Phys. Rev. A **58**, 3891 (1998).

[121] J. Schoser, A. Batär, R. Löw, V. Schweikhard, A. Grabowski, Y. B. Ovchinnikov, and T. Pfau, Phys. Rev. A **66**, 023410 (2002).

[122] Y. B. Ovchinnikov, Optics Communications **249**, 473 (2005).

[123] J. Ramirez-Serrano, N. Yu, J. M. Kohel, J. R. Kellogg, and L. Maleki, Opt. Lett. **31**, 682 (2006).

[124] P. Cren, C. Roos, A. Aclan, J. Dalibard, and D. Guéry-Odelin, The European Physical Journal D-Atomic, Molecular, Optical and Plasma Physics **20**, 107 (2002).

[125] J. R. Kellogg, D. Schlippert, J. M. Kohel, R. J. Thompson, D. C. Aveline, and N. Yu, Applied Physics B **109**, 61 (2012).

[126] S. J. Park, J. Noh, and J. Mun, Optics Communications **285**, 3950 (2012).

[127] H. Chen and E. Riis, Applied Physics B **70**, 665 (2000).

[128] R. Conroy, Y. Xiao, M. Vengalattore, W. Rooijakkers, and M. Prentiss, Optics Communications **226**, 259 (2003).

[129] S. Chaudhuri, S. Roy, and C. S. Unnikrishnan, Phys. Rev. A **74**, 023406 (2006).

[130] S. Weyers, E. Aucouturier, C. Valentin, and N. Dimarcq, Optics communications **143**, 30 (1997).

[131] L. Cacciapuoti, A. Castrillo, M. De Angelis, and G. Tino, The European Physical Journal D-Atomic, Molecular, Optical and Plasma Physics **15**, 245 (2001).

[132] W. Wohlleben, F. Chevy, K. Madison, and J. Dalibard, The European Physical Journal D-Atomic, Molecular, Optical and Plasma Physics **15**, 237 (2001).

[133] Z. T. Lu, K. L. Corwin, M. J. Renn, M. H. Anderson, E. A. Cornell, and C. E. Wieman, Phys. Rev. Lett. **77**, 3331 (1996).

[134] E. Donley, T. Heavner, and S. Jefferts, IEEE Transactions on Instrumentation and Measurement **54**, 1905 (2005).

[135] J. Arlt, O. Marago, S. Webster, S. Hopkins, and C. Foot, Optics communications **157**, 303 (1998).

[136] R. S. W. III, P. A. Voytas, R. T. Newell, and T. Walker, Opt. Express **3**, 111 (1998).

[137] A. Camposeo, A. Piombini, F. Cervelli, F. Tantussi, F. Fuso, and E. Arimondo, Optics communications **200**, 231 (2001).

[138] J. M. Kohel, J. Ramirez-Serrano, R. J. Thompson, L. Maleki, J. L. Bliss, and K. G. Libbrecht, J. Opt. Soc. Am. B **20**, 1161 (2003).

[139] N. Lundblad, D. C. Aveline, R. J. Thompson, J. M. Kohel, J. Ramirez-Serrano, W. M. Klipstein, D. G. Enzer, N. Yu, and L. Maleki, J. Opt. Soc. Am. B **21**, 3 (2004).

[140] M. L. Harris, P. Tierney, and S. L. Cornish, Journal of Physics B: Atomic, Molecular and Optical Physics **41**, 035303 (2008).

[141] E. Imhof, B. K. Stuhl, B. Kasch, B. Kroese, S. E. Olson, and M. B. Squires, Phys. Rev. A **96**, 033636 (2017).

[142] R. Conroy, Y. Xiao, M. Vengalattore, W. Rooijakkers, and M. Prentiss, Optics Communications **226**, 259 (2003).

[143] J. Arlt, O. Maragò, S. Webster, S. Hopkins, and C. Foot, Optics Communications **157**, 303 (1998).

[144] K. I. Lee, J. A. Kim, H. R. Noh, and W. Jhe, Opt. Lett. **21**, 1177 (1996).

[145] E. Kochkina, *Stigmatic and astigmatic gaussian beams in fundamental mode: impact of beam model choice on interferometric pathlength signal estimates*, Ph.D. thesis, Technische Informationsbibliothek und Universitätsbibliothek Hannover (TIB . . . (2013).

[146] R. Paschotta, Encyclopedia of Laser Physics and Technology (2011).

[147] D. McCarron, (2007).

[148] J. C. B. Kangara, A. J. Hachtel, M. C. Gillette, J. T. Barkeloo, E. R. Clements, S. Bali, B. E. Unks, N. A. Proite, D. D. Yavuz, P. J. Martin, J. J. Thorn, and D. A. Steck, American Journal of Physics **82**, 805 (2014), https://doi.org/10.1119/1.4867376 .

[149] R. A. Nyman, G. Varoquaux, B. Villier, D. Sacchet, F. Moron, Y. Le Coq, A. Aspect, and P. Bouyer, Review of Scientific Instruments **77**, 033105 (2006), https://doi.org/10.1063/1.2186809 .

[150] R. S. W. III, P. A. Voytas, R. T. Newell, and T. Walker, Opt. Express **3**, 111 (1998).

[151] P. F. Griffin, *Laser cooling and loading of Rb into a large period, quasi-electrostatic, optical lattice*, Ph.D. thesis, Durham University (2005).

[152] S. Turner, (1999), 10.5170/CERN-1999-005.99.

[153] R. Grinham and D. A. Chew, Applied Science and Convergence Technology **26**, 95 (2017).

[154] D. S. Jin, M. R. Matthews, J. R. Ensher, C. E. Wieman, and E. A. Cornell, Phys. Rev. Lett. **78**, 764 (1997).

[155] C. J. Myatt, E. A. Burt, R. W. Ghrist, E. A. Cornell, and C. E. Wieman, Phys. Rev. Lett. **78**, 586 (1997).

[156] C. Monroe, W. Swann, H. Robinson, and C. Wieman, Phys. Rev. Lett. **65**, 1571 (1990).

[157] T. E. Barrett, S. W. Dapore-Schwartz, M. D. Ray, and G. P. Lafyatis, Phys. Rev. Lett. **67**, 3483 (1991).

[158] M. Landini, S. Roy, L. Carcagní, D. Trypogeorgos, M. Fattori, M. Inguscio, and G. Modugno, Phys. Rev. A **84**, 043432 (2011).

[159] A. Lampis, *Coherent light-matter interactions with potassium atoms*, Ph.D. thesis, University of Birmingham (2018).

[160] A. Ratkata, *A Two-Species Magneto-Optical Trap Using 39K and 133Cs*, Ph.D. thesis, Durham University (2017).

[161] R. S. Williamson, *Magneto-optical trapping of potassium isotopes*, Ph.D. thesis, University of Wisconsin–Madison (1997).

[162] T. Opdam, V. Lebedev, and S. Lepoutre, Report of a **36** (2012).

[163] R. A. Culver, *Collective strong coupling of cold potassium atoms in an optical ring cavity*, Ph.D. thesis, University of Birmingham (2017).

[164] S. Ravenhall, B. Yuen, and C. Foot, arXiv preprint arXiv:2102.00251 (2021).

[165] S. Ravenhall, *A compact, high-flux source of cold atoms*, Ph.D. thesis, University of Oxford (2018).

[166] L. Mudarikwa, K. Pahwa, and J. Goldwin, Journal of Physics B: Atomic, Molecular and Optical Physics **45**, 065002 (2012).

[167] M. Fleischhauer and M. D. Lukin, Phys. Rev. A **65**, 022314 (2002).

[168] D. Budker, D. F. Kimball, S. M. Rochester, V. V. Yashchuk, and M. Zolotorev, Phys. Rev. A **62**, 043403 (2000).

[169] P. Siddons, C. S. Adams, C. Ge, and I. G. Hughes, Journal of Physics B: Atomic, Molecular and Optical Physics **41**, 155004 (2008).

[170] G. Modugno, G. Ferrari, G. Roati, R. J. Brecha, A. Simoni, and M. Inguscio, Science **294**, 1320 (2001), https://science.sciencemag.org/content/294/5545/1320.full.pdf .

[171] G. Salomon, L. Fouché, P. Wang, A. Aspect, P. Bouyer, and T. Bourdel, EPL (Europhysics Letters) **104**, 63002 (2013).

[172] D. C. McKay, D. Jervis, D. J. Fine, J. W. Simpson-Porco, G. J. A. Edge, and J. H. Thywissen, Phys. Rev. A **84**, 063420 (2011).

[173] J. E. Sansonetti, Journal of Physical and Chemical Reference Data **37**, 7 (2008), https://doi.org/10.1063/1.2789451 .

[174] C. J. Foot *et al.*, *Atomic physics*, Vol. 7 (Oxford University Press, 2005).

[175] E. Arimondo, M. Inguscio, and P. Violino, Rev. Mod. Phys. **49**, 31 (1977).

[176] J. Jiang and J. Mitroy, Phys. Rev. A **88**, 032505 (2013).

[177] D. A. Smith and I. G. Hughes, American Journal of Physics **72**, 631 (2004), https://doi.org/10.1119/1.1652039 .

[178] R. K. Hanley, P. D. Gregory, I. G. Hughes, and S. L. Cornish, Journal of Physics B: Atomic, Molecular and Optical Physics **48**, 195004 (2015).

[179] D. McKay, "Potassium 5p line data," (2009).

[180] B. E. Sherlock and I. G. Hughes, American Journal of Physics **77**, 111 (2009), https://doi.org/10.1119/1.3013197 .

[181] P. J. Mohr, B. N. Taylor, and D. B. Newell, Journal of Physical and Chemical Reference Data **37**, 1187 (2008), https://doi.org/10.1063/1.2844785 .

[182] Y. Ralchenko, A. Kramida, J. Reader, *et al.*, "Nist atomic spectra database (version 3.1. 5)," (2008).

[183] U. I. Safronova and M. S. Safronova, Phys. Rev. A **78**, 052504 (2008).

[184] A. Sieradzan, R. Stoleru, W. Yei, and M. D. Havey, Phys. Rev. A **55**, 3475 (1997).

[185] P. Siddons, C. S. Adams, C. Ge, and I. G. Hughes, Journal of Physics B: Atomic, Molecular and Optical Physics **41**, 155004 (2008).

[186] C. J. Sansonetti and C. J. Lorenzen, Phys. Rev. A **30**, 1805 (1984).

[187] S. Pucher, P. Schneeweiss, A. Rauschenbeutel, and A. Dareau, Phys. Rev. A **101**, 042510 (2020).

[188] A. K. Mohapatra, M. G. Bason, B. Butscher, K. J. Weatherill, and C. S. Adams, Nature physics **4**, 890 (2008).

[189] H. Kübler, J. Shaffer, T. Baluktsian, R. Löw, and T. Pfau, Nature Photonics **4**, 112 (2010).

[190] T.-L. Chen, S.-Y. Chang, Y.-J. Huang, K. Shukla, Y.-C. Huang, T.-H. Suen, T.-Y. Kuan, J.-T. Shy, and Y.-W. Liu, Phys. Rev. A **101**, 052507 (2020).

[191] M. Fleischhauer, A. Imamoglu, and J. P. Marangos, Rev. Mod. Phys. **77**, 633 (2005).

[192] A. Lezama, S. Barreiro, and A. M. Akulshin, Phys. Rev. A **59**, 4732 (1999).

[193] A. M. Akulshin, S. Barreiro, and A. Lezama, Phys. Rev. A **57**, 2996 (1998).

[194] J. A. Gordon, C. L. Holloway, A. Schwarzkopf, D. A. Anderson, S. Miller, N. Thaicharoen, and G. Raithel, Applied Physics Letters **105**, 024104 (2014).

[195] A. K. Mohapatra, T. R. Jackson, and C. S. Adams, Phys. Rev. Lett. **98**, 113003 (2007).

[196] M. Landini, S. Roy, G. Roati, A. Simoni, M. Inguscio, G. Modugno, and M. Fattori, Phys. Rev. A **86**, 033421 (2012).

[197] M. Gröbner, P. Weinmann, F. Meinert, K. Lauber, E. Kirilov, and H.-C. Nägerl, Journal of Modern Optics **63**, 1829 (2016), https://doi.org/10.1080/09500340.2016.1143051 .

[198] T. Weber, J. Herbig, M. Mark, H.-C. Nägerl, and R. Grimm, Science **299**, 232 (2003), https://science.sciencemag.org/content/299/5604/232.full.pdf .

[199] C. Sheng, J. Hou, X. He, K. Wang, R. Guo, J. Zhuang, B. Mamat, P. Xu, M. Liu, J. Wang, and M. Zhan, "Defect-free arbitrary-geometry assembly of mixed-species atom arrays," (2021), arXiv:2106.06144 [physics.atom-ph] .

[200] R. Guo, X. He, C. Sheng, J. Yang, P. Xu, K. Wang, J. Zhong, M. Liu, J. Wang, and M. Zhan, Phys. Rev. Lett. **124**, 153201 (2020).

[201] L. R. Liu, J. D. Hood, Y. Yu, J. T. Zhang, K. Wang, Y.-W. Lin, T. Rosenband, and K.-K. Ni, Phys. Rev. X **9**, 021039 (2019).

[202] L. R. Liu, J. D. Hood, Y. Yu, J. T. Zhang, N. R. Hutzler, T. Rosenband, and K.-K. Ni, Science **360**, 900 (2018), https://science.sciencemag.org/content/360/6391/900.full.pdf .

[203] J. T. Zhang, Y. Yu, W. B. Cairncross, K. Wang, L. R. Picard, J. D. Hood, Y.-W. Lin, J. M. Hutson, and K.-K. Ni, arXiv preprint arXiv:2003.07850 (2020), https://arxiv.org/abs/2003.07850.

[204] H. Cho, D. McCarron, D. Jenkin, M. Köppinger, and S. Cornish, The European Physical Journal D **65**, 125 (2011).

[205] D. J. McCarron, H. W. Cho, D. L. Jenkin, M. P. Köppinger, and S. L. Cornish, Phys. Rev. A **84**, 011603 (2011).

[206] R. V. Brooks, S. Spence, A. Guttridge, A. Alampounti, A. Rakonjac, L. A. McArd, J. M. Hutson, and S. L. Cornish, New Journal of Physics **23**, 065002 (2021).

[207] M. Gröbner, P. Weinmann, E. Kirilov, and H.-C. Nägerl, Phys. Rev. A **95**, 033412 (2017).

[208] L. Khaykovich, F. Schreck, G. Ferrari, T. Bourdel, J. Cubizolles, L. D. Carr, Y. Castin, and C. Salomon, Science **296**, 1290 (2002), https://science.sciencemag.org/content/296/5571/1290.full.pdf .

[209] H. Kadau, M. Schmitt, M. Wenzel, C. Wink, T. Maier, I. Ferrier-Barbut, and T. Pfau, Nature **530**, 194 (2016).

[210] C. A. Regal, M. Greiner, and D. S. Jin, Phys. Rev. Lett. **92**, 040403 (2004).

[211] A. J. Moerdijk, B. J. Verhaar, and A. Axelsson, Phys. Rev. A **51**, 4852 (1995).

[212] T. Weber, J. Herbig, M. Mark, H.-C. Nägerl, and R. Grimm, Phys. Rev. Lett. **91**, 123201 (2003).

[213] C. Chin, R. Grimm, P. Julienne, and E. Tiesinga, Rev. Mod. Phys. **82**, 1225 (2010).

[214] M. Theis, G. Thalhammer, K. Winkler, M. Hellwig, G. Ruff, R. Grimm, and J. H. Denschlag, Phys. Rev. Lett. **93**, 123001 (2004).

[215] F. A. van Abeelen and B. J. Verhaar, Phys. Rev. Lett. **83**, 1550 (1999).

[216] F. H. Mies, E. Tiesinga, and P. S. Julienne, Phys. Rev. A **61**, 022721 (2000).

[217] T. Mukaiyama, J. R. Abo-Shaeer, K. Xu, J. K. Chin, and W. Ketterle, Phys. Rev. Lett. **92**, 180402 (2004).

[218] G. Thalhammer, K. Winkler, F. Lang, S. Schmid, R. Grimm, and J. H. Denschlag, Phys. Rev. Lett. **96**, 050402 (2006).

[219] M. Mark, F. Ferlaino, S. Knoop, J. G. Danzl, T. Kraemer, C. Chin, H.-C. Nägerl, and R. Grimm, Phys. Rev. A **76**, 042514 (2007).

[220] F. Lang, P. vd Straten, B. Brandstätter, G. Thalhammer, K. Winkler, P. S. Julienne, R. Grimm, and J. H. Denschlag, Nature Physics **4**, 223 (2008).

[221] A. M. Kaufman, B. J. Lester, and C. A. Regal, Phys. Rev. X **2**, 041014 (2012).

[222] W. S. Bakr, J. I. Gillen, A. Peng, S. Fölling, and M. Greiner, Nature **462**, 74 (2009).

[223] C. Weitenberg, M. Endres, J. F. Sherson, M. Cheneau, P. Schauß, T. Fukuhara, I. Bloch, and S. Kuhr, Nature **471**, 319 (2011).

[224] R. Loudon, *The quantum theory of light* (OUP Oxford, 2000).

[225] K. Blum, *Density matrix theory and applications*, Vol. 64 (Springer Science & Business Media, 2012).

[226] M. Jones, "Atom light interactions," .

[227] M. E. Crenshaw, M. Scalora, and C. M. Bowden, Phys. Rev. Lett. **68**, 911 (1992).

[228] M. Fox, American Journal of Physics **70**, 1269 (2002), https://doi.org/10.1119/1.1691372 .

[229] T. Berggren, Physics Letters B **373**, 1 (1996).